Properties of multilayered and multicomponent nitride alloys from first principles

Dissertation

zur Erlangung des Grades

des Doktors der Ingenieurwissenschaften

der Naturwissenschaftlich-Technischen Fakultät

der Universität des Saarlandes

von

Fei Wang

Saarbrücken

2018

Tag des Kolloquiums	28 February 2018
Dekan	Prof. Dr. rer. nat Guido Kickelbick
Berichterstatter	Prof. Dr. -Ing. Frank Mücklich
	Prof. Dr. Michael Springborg
	Assoc. Prof. Dr. Ferenc Tasnádi
Vorsitz	Prof. Dr. Lars Ojamäe
Akad. Mitarbeiter	Dr. -Ing. Flavio Soldera
Weitere Mitglieder	Prof. Dr. Levente Vitos
	Prof. Dr. Ulf Jansson
	Prof. Dr. Claudia Draxl

To my family

Abstract

This thesis is a theoretical exploration of properties of multilayered and multicomponent nitride alloys, in particular their mixing thermodynamics and elastic behaviors. Systematic investigation of properties of a large class of materials, such as the multicomponent nitride solid solutions, is in line with the modern approach of high-throughput search of novel materials. In this thesis we benchmark and utilize simple but efficient methodological frameworks in predicting mixing thermodynamics, Young's moduli distribution of multilayer alloys and the linear thermal expansion of quaternary nitride solid solutions.

We demonstrate by accurate ab-initio calculations that $Ti_{1-x}Al_xN$ solid solution is stabilized by interfacial effects if it is coherently sandwiched between TiN layers along (001). For TiN/AlN and ZrN/AlN multilayers we show higher thermodynamic stability with semicoherent interfaces than with isostructural coherent ones.

Accurate 0 Kelvin elastic constants of cubic $Ti_xX_yAl_{1-x-y}N$ (X=Zr, Hf, Nb, V, Ta) solid solutions and their multilayers are derived and an analytic comparison of strengths and ductility are presented to reveal the potential of these materials in hard coating applications. The Young's moduli variation of the bulk materials has provided a reliable descriptor to screen the Young's moduli of coherent multilayers.

The Debye model is used to reveal the high-temperature thermodynamics and spinodal decomposition of $Ti_xNb_yAl_{1-x-y}N$. We show that though the effect of vibration is large on the mixing Gibbs free energy the local spinoal decomposition tendencies are not altered. A quasi-harmonic Debye model is benchmarked against results of molecular dynamics simulations in predicting the thermal expansion coefficients of $Ti_xX_yAl_{1-x-y}N$ (X=Zr, Hf, Nb, V, Ta).

Sammanfattning

Denna avhandling är en teoretisk undersökning av egenskaperna hos multilager och multikomponentlegeringar av nitrider, särskilt deras blandningstermodynamik och elastiska egenskaper. Systematiska undersökningar av egenskaperna hos en stor materialfamilj, såsom fasta lösningar av multikomponentnitrider, ligger i linje med den moderna angreppsvinkeln av massundersökningar i sökandet efter nya material. I denna avhandling utvärderar och använder vi enkla men effektiva metodologiska ramverk för att förutsäga blandningstermodynamik, fördelning av Young's moduli multilager och den linjära termiska expansionen i kvaternära fasta lösningar av nitrider.

Vi visar med precisa ab-initio-beräkningar att en fast lösning av $Ti_{1-x}Al_xN$ stabiliseras av gränssnittseffekter om den placeras koherent mellan TiN-skikt längs med (001). För multilager av TiN/AlN och ZrN/AlN påvisar vi högre termodynamisk stabilitet med semikoherenta gränsskikt än med isostrukturella koherenta. Precisa elastiska konstanter vid 0 K för kubiska fasta lösningar av $Ti_xX_yAl_{1-x-y}N$ (X=Zr, Hf, Nb, V, Ta) och deras multilager beräknas och en analytisk jämförelse av deras hållfasthet och duktilitet presenteras för att visa dessa materials potential som hårda beläggningar. Variationen av Young's moduli materialen i bulk har gett en pålitlig deskriptor för att undersöka Young's moduli koherenta multilager.

Debye-modellen används för att undersöka hög-temperatur-termodynamiken och spinodalt sönderfall hos $Ti_xNb_yAl_{1-x-y}N$. Vi visar att trots att vibrationers effekt på Gibbs fria energi för blandning är stor påverkas inte de lokala tendenserna för spinodalt sönderfall. En kvasiharmonisk Debye-modell jämförs med resultat från molekyldynamiksimuleringar för att förutsäga utvidgningskoefficienter för $Ti_xX_yAl_{1-x-y}N$ (X=Zr, Hf, Nb, V, Ta).

Zusammenfassung

Diese Arbeit ist eine theoretische Untersuchung der Eigenschaften von mehrschichtigen und mehrkomponentigen Nitridlegierungen, insbesondere deren Mischungs-Thermodynamik und elastischen Verhalten. Eine systematische Untersuchung von Eigenschaften einer großen Klasse von Materialien, wie zum Beispiel fester Lösungen von Mehrkomponenten-Nitriden, ist im Einklang mit dem zeitgenössischen Hochdurchsatzverfahren für die Suche nach neuen Materialien. In dieser Arbeit benchmarken und nutzen wir einfache, aber effiziente methodische Frameworks zur Vorhersage der Mischungs-Thermodynamik, der Verteilung des Elastizitätsmoduls von Mehrschichtlegierungen und der linearen thermischen Ausdehnung von festen, quaternären Nitrid-Lösungen. Wir zeigen durch genaue Ab-initio-Berechnungen, dass $Ti_{1-x}Al_xN$ Mischkristalle durch Grenzflächenwirkungen stabilisiert werden, wenn sie kohärent zwischen TiN Schichten entlang (001) sandwichartig angeordnet sind. Die genauen elastischen Konstanten von kubischen $Ti_xX_yAl_{1-x-y}N$ (X = Zr, Hf, Nb, V, Ta) Mischkristallen und deren Mehrfachschichten bei 0 Kelvin werden abgeleitet und ein analytischer Vergleich der Festigkeit und Duktilität zeigt das Potential dieser Materialien in Hartbeschichtungsanwendungen. Das Debye-Modell wird verwendet, um die Hochtemperatur-Thermodynamik und die spinodale Entmischung von $Ti_xNb_yAl_{1-x-y}N$ aufzudecken. Wir zeigen, dass sich die lokale Tendenzen zur spinodalen Entmischung nicht ändern, obwohl die Wirkung von Vibrationen auf die Gibbs-Energie großist. Ein quasi-harmonisches Debye-Modell wird gegen die Ergebnisse von Moleküldynamik-Simulationen gebenchmarkt, um die thermische Ausdehnungskoeffizienten von $Ti_xX_yAl_{1-x-y}N$ (X=Zr, Hf, Nb, V, Ta) vorherzusagen.

Populärvetenskaplig sammanfattning

Industrin kräver ständig utveckling inom materialbearbetning för att utveckla innovativa produkter och stärka sin marknadsposition. Beläggningsmaterials hög temperaturprestanda har en enorm påverkan påskärverktygsindustrin. Ett materials hårdhet, strukturella stabilitet vid höga temperaturer och oxidationsmotstånd är nyckelstorheter för att det ska kunna användas i krävande miljöer. Moderna hårda beläggningsmaterial förväntas ha en hårdhet omkring 30-40 GPa och vara strukturellt stabila upp till en arbetstemperatur på $1200-1500\,^{\circ}\mathrm{C}$. Övergångsmetallnitrider(TiN, ZrN, HfN, NbN, VN, TaN) och deras legeringar definierar materialklassen med potential som hårda beläggningar.

Alla systematiska teoretiska undersökningar av utformningsstragier i klassen övergångsmetallnitrider använder datorer i ett slags "test och försök", med bonusen att fysiken bakom resultaten blottläggs. Detta är i linje med det moderna mass undersöknings-baserade sökandet efter nya material. Kemisk utformning såsom multikomponentlegering tillåter en att använda kombinationer av grundämnen från det periodiska systemet. Strukturell formgivning såsom att göra multilager innebär att material läggs mellan varandra vilket leder till att termisk stabilitet och materialets elasticitet kan förändras av ömsesidig växelverkan mellan materialen.

I min forskning har mitt mål varit att hitta och förklara trender i termisk stabilitet och elastiska egenskaper hos multilager och multikomponentlegeringar av nitrider. Jag har undersökt högtemperaturtermodynamiken i $\mathrm{Ti}_x\mathrm{Nb}_y\mathrm{Al}_{1-x-y}\mathrm{N}$. Genom att använda en koherent multilagerstruktur av TiN och $\mathrm{Ti}_{1-x}\mathrm{Al}_x\mathrm{N}$ har jag visat att gränsskiktseffekter stabiliserar $\mathrm{Ti}_{1-x}\mathrm{Al}_x\mathrm{N}$-legeringen. Jag har beräknat de elastiska konstanterna för kubiska legeringar av $\mathrm{Ti}_x\mathrm{X}_y\mathrm{Al}_{1-x-y}\mathrm{N}$ (X=Zr, Hf, Nb, V, Ta) och deras multilager och gjort en analytisk jämförelse av hållfasthet och duktilitet för att utforska dessa materials potential som hårda beläggningar. Pågrund av dessa uppgifters komplexitet behövde jag utvärdera och använda enkla metoder istället för tids- och resurskrävande molekyldynamiksimuleringar. Jag har visat att en linjär elastisk modell av multilager är tillräcklig för att diskutera

hållfastheten hos nitrid-multilager med olika ytorienteringar. Vidare har en kvasi-harmonisk approximation av atomiska vibrationer visat sig vara tillräcklig för att förutsäga den termiska expansionen av multikomponentnitridlegeringar.

Min avhandling visar att moderna atomistiska simuleringsmetoder kombinerade med kontrollerade fysiska approximationer för teoretiska undersökningar till framkanten av utformningen av nyskapande teknologiska material för att befästa mottot "Rätt material för rätt tillämpning".

Preface

This thesis is a result of my doctoral studies carried out in Theoretical Physics Division at the Department of Physics, Chemistry, and Biology at Linköping University(Sweden) and Functional Materials Division at the Department of Material Science and Engineering at Saarland University(Germany) from Oct,2012 to Feb,2018. During this time, I have spent more than 6 months in Saarland University.

My work was part of the Joint European Doctoral Programme in Material Science and Engineering(DocMASE). The research was also partially supported by the Swedish Foundation for Strategic Research (SSF) project SRL Grant No. 10-0026.

All the theoretical calculations have been carried out using supercomputer resources provided by the Swedish National Infrastructure for Computing(SNIC) at the National Supercomputer Center(NSC) and the Center for High-Performance Computing(PDC).

Acknowledgements

- My supervisor, *Dr. Ferenc Tasnádi*, for giving me the oppotunity to do this journey, for the help with the start, for all the support and guidance during my studies. It has been a fantastic experience to work with you!
- My co-supervisor, *Prof. Igor Abrikosov*, for your support, encouragement and guidance, for sharing enormous amount of knowledge and invaluable contributions in different projects.
- My supervisor at Saarland University, *Prof. Frank Mücklich*, for providing me the oppotunity to live and work in wonderful Saarbrücken.
- *Prof. Magnus Odén*, for all the support in understanding materials science from experimental point of view and suggestions over these years.
- *Dr. Flavio Soldera* for solving all the problems in Saarbrücken, for having many unforgettable DocMASE summer schools.
- Special thanks to all my coauthors who I have had the pleasure to work with, especially *Dr. Kumar Yalamanchili*, *Dr. Jianqiang Zhu*, for your knowledge in experimental matters and our fruitful discussion and collaboration.
- All the colleagues in *Theoretical Physics group* and *Nanostructured Materials group*, for always being helpful and open for discussions.
- Warmest thanks to morning coffee group, for providing company and funny topics which were always entertaining, for all the activities we have had. It has been a lot of fun.
- *Aylin Atakan* and *Dr. Isabella Schramm*, for being such great friend with me. I really had a good time with you.

- A distinguished important thank to my parents, who have always supported, encouraged and believed in me; my husband Chao, I would never come to this far without you; My son, Guoguo, who makes me feel really lucky. I am happy to have all of you in my life.

王菲

Fei Wang
Linköping, 2018

Contents

1 Introduction **1**
- 1.1 Theoretical material science . . . 1
- 1.2 Aim of the thesis . . . 2
- 1.3 Outline of the thesis . . . 3

2 Hard coating nitrides **5**
- 2.1 Binary nitrides . . . 6
- 2.2 Ternary pseudo-binary nitride alloys . . . 8
- 2.3 Quaternary nitride alloys . . . 11
- 2.4 Multilayers . . . 11

3 Structure modeling of alloys **13**
- 3.1 Configurational disorder in alloys . . . 13
- 3.2 The special quasi-random structure (SQS) approach . . . 14
  - 3.2.1 Modeling multilayered alloys . . . 15
- 3.3 The Coherent Potential Approximation (CPA) . . . 17

4 Mixing thermodynamics and decomposition **19**
- 4.1 Gibbs free energy . . . 19
- 4.2 Mixing enthalpy in multilayers . . . 20
- 4.3 Gibbs free energy calculated with the Debye model . . . 23
- 4.4 Thermal expansion coefficient (TEC) . . . 25

5 Elastic properties **27**
- 5.1 Elastic properties of isotropic solids . . . 27
- 5.2 Elastic stiffness tensor . . . 28
- 5.3 Elastic moduli of polycrystalline materials . . . 29
- 5.4 Elastic properties of cubic disordered structures . . . 30
- 5.5 Elastic Young's modulus of multilayers . . . 31

6 Density Functional Theory **33**
6.1 Hohenberg-Kohn theorems 34
6.2 Kohn-Sham equation 35
6.3 Exchange-correlation functionals 36
6.4 Basis sets 36

7 Results **39**
7.1 Thermodynamics stability 39
7.1.1 Mixing thermodynamics of cubic $Ti_{1-x}Al_xN$/TiN(001) multilayers 39
7.1.2 Thermal stability of TiN/AlN and ZrN/AlN 41
7.2 Elastic properties 43
7.2.1 Alloys 43
7.2.2 Multilayers 44
7.3 Application of Debye model on multicomponent nitride alloys . . . 45
7.3.1 $Ti_xNb_yAl_zN$ alloys 45
7.3.2 Thermal expansion coefficients of $Ti_{1-x-y}X_yAl_xN$ (X = Zr, Hf, Nb, V, Ta) 48

8 Conclusions and Outlook **49**

Bibliography **51**

List of included publications and my contribution **61**

Related, not included publications **63**

Paper I **65**

Paper II **73**

Paper III **83**

Paper IV **97**

Paper V **115**

Paper VI **127**

CHAPTER 1

Introduction

1.1 Theoretical material science

Materials have always been imperative for humans to advance civilization. The material of choice is used to mark prehistorical periods, such as Stone Age, Bronze Age, Iron Age, and Steel Age. Evolving originally from metallurgy, material science became a scientific branch of its own. During the 19th and 20th centuries, it became a leading field of science with incorporating physics, chemistry, and engineering. Nowadays, on the basis of all the sophisticated technologies, when we are talking about materials, we also think of material's multi-functionality for next generation applications. It is motivated by the fact that the functionality of modern tools and devices, such as surface coatings, electrical and optical devices etc., are determined to a large extent by the material's properties on nanometer (10^{-9} m) or atomic scale.

Through electronic-structure simulations, atomistic and quantum mechanical modeling of complex materials have became an important tool in the material's exploration, for example, the Material's Genome [1], Novel Materials Discovery (NOMAD) [2] etc. Experimental investigations are expensive and time consuming. The power of computer simulation, is that it can interpret and predict the properties of materials at arbitrary physical conditions (pressure, temperature). Of course, such theoretical studies have also limitations, (i) we investigate mostly perfect materials (not with the imperfections, defects) (ii) the solution of the quantum mechanical many-body problem requires approximations. Density-functional theory (DFT) has reached an appropriate level for many questions, but it is not completed yet. Nevertheless researchers have achieved great success in achieving thermodynamics accuracy, bridging length-scales and overcoming time-scales limitations. Modern theoretical material science faces with two main challenges:

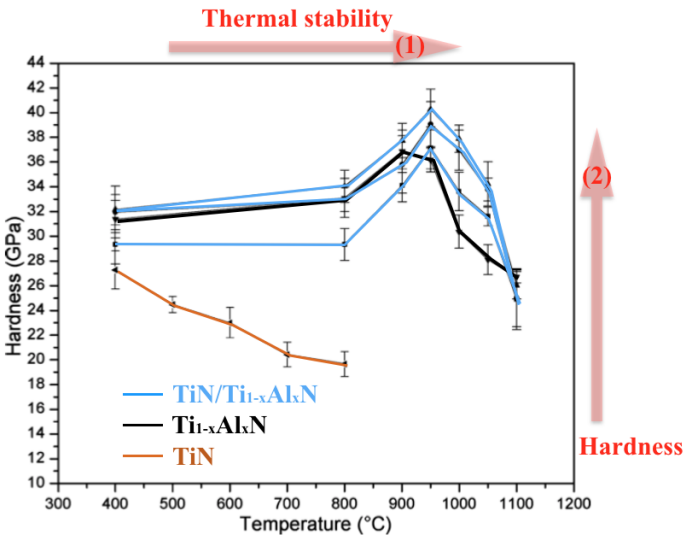

Figure 1.1. Hardness values of the as-deposited and heat treated monolithic and multilayered coatings. This figure is an adopted version of the figure in J. Appl. Phys. 108, 044312 (2010)

(A) It aims to provide a fundamental understanding of microscopic and macroscopic properties of materials, it wants to explain the experimentally observed properties and phenomena. For example, the mechanical properties of TiN, such as hardness is enhanced by alloying element Al or through a multilayer design [3]. The detailed arrangement and the movement of atoms and electrons (chemical bonds, phonons) brings insight on the experimental observation through a statistical description.

(B) It is utilized to discover novel materials or predict accurately and quantitatively the properties of systems that have not been investigated experimentally so far or cannot be investigated by experiments directly. For instance, the structure and properties of iron have been modeled theoretically at Earth-core conditions (around 300-350 GPa and 5000-6000 K) [4].

1.2 Aim of the thesis

Figure 1.1 plots the material's hardness (materials resistance against external force) of TiN, $Ti_{1-x}Al_xN$ and $TiN/Ti_{1-x}Al_xN$ [001] multilayers (x is a fraction of AlN) versus annealing temperature. It shows that the hardness of TiN decreases monotonously with the annealing temperature. In contrast the hardness of $Ti_{1-x}Al_xN$ alloy increases with the annealing temperature up to around 900 °C. Around 900 °C an anomalous increase of hardness is observed which is explained by the material's altered microstructure resulted by a (lattice) coherent spinodal decomposition. Cubic B1 $Ti_{1-x}Al_xN$ coherently decomposes into cubic AlN and

cubic TiN phases. The hardness value decreases at higher temperatures as the cubic AlN phase transforms into the ground state hexagonal (wurtzite) structure [5]. Therefore an increased thermal stability of the cubic phase of AlN with respect its wurtzite phase is assumed to result in higher hardness value of the decomposed $Ti_{1-x}Al_xN$ at higher ($> 1000\,^{\circ}C$) temperatures. This hypothetical extension of hardness is shown with arrow (2) in Figure 1.1, both multicomponent alloying and artificial multilayer structuring might change the thermodynamic stability of the materials phases and result in altered hardness vs. temperature behavior. Materials elastic properties have indirect impact on hardness and therefore they are of distinct interest in searching for novel hard materials. The objective of this thesis is to give a fundamental exploration of thermodynamics and elastic properties of multilayered and multicomponent nitride alloys from three perspectives:

- What is the effect of lattice coherency and interfacial chemistry on the thermodynamics of multilayers. How interfacial effects influence the decomposition process of $Ti_{1-x}Al_xN$ if it is confined in a multilayer architecture.
- How multicomponent alloying improves material's thermal stability and elastic properties.
- Since the elastic energy distribution influences the microstructure of the decomposing solid solution through the anisotropic elastic (stiffness) constants, one has to develop an overview of the single crystal and polycrystalline elasticity of multicomponent nitrides alloys and for some of their multilayers.

The material class we focus on in this thesis is restricted to nitride solid solutions and multilayers with high potential for cutting tool applications. We investigate AlN, XN, $X_{1-x}Al_xN$, $X_{1-x}Ti_xN$, $Ti_xX_yAl_{1-x-y}N$ (X=Ti, Zr, Hf, V, Nb, Ta), TiN/AlN and $Ti_{1-x}Al_xN$/TiN etc.

1.3 Outline of the thesis

This thesis includes chapters with a comprehensive overview of the investigated materials, the applied theoretical approaches and the obtained results.

- Chapter 1 gives a brief overview of theoretical material science and the aim of this work.
- Chapter 2 provides an introduction to hard coating materials, as well as the ones of interest for this work: the binary nitrides, titanium nitride based ternary and quaternary nitride alloys and alloys in multilayers.
- Chapter 3 describes the applied methods for the structural modeling of random alloys and alloys in multilayers.
- Chapter 4 explains the mixing thermodynamics of alloys and multilayers.
- Chapter 5 explores the calculations of elastic properties in disordered alloys and alloys in multilayers.

- Chapter 6 presents a short overview of the underlying approach of electronic structure calculations, which is density functional theory (DFT).
- Chapter 7 contains a summary of results presented in the included papers.
- Chapter 8 presents a short conclusion and an outlook for future research.
- The papers are included in the end of the thesis.

CHAPTER 2

Hard coating nitrides

Coatings are usually micron (10^{-6} m) thick layers on the surface of machining tools (drills, gears, etc.) and other devices. The purpose of applying coatings might be functional and decorative, or both. Coatings are applied to functionalize the surface properties of the raw material, such as thermal and electrical conductivity, optical reflectivity or corrosion and wear resistance. Since manufacturing industries have become increasingly dependent on automation, the critical demand for wear- and corrosion- resistant coatings has also expanded. In today's industries, the protective coatings, also known as hard coatings, were developed and used to improve the operational efficiency, reliability and the life time of cutting and machining tools. The global market for these coating systems is rising.

In 1969, a few microns thick titanium carbide TiC coatings were developed using chemical vapor deposition (CVD) technique to prevent the cutting tools start to oxidize at low temperatures [6]. During the last three decades transition metal nitrides and carbides have been developed as prominent hard coating materials as they offer extremely hard surfaces, low friction coefficient, excellent adhesion, favorable sliding characteristics, and relatively high electrical and thermal conductivity. These extraordinary properties could be explained after understanding the thermodynamic, the crystallographic and microstructural characteristics of these materials in connection with their microscopic electronic properties.

The industrial scaled PVD (physical vapor deposition) deposited TiN High Speed Steel (HSS) drill bits were introduced in 1982 [6]. Using physical vapor deposition one solved problems appeared in CVD grown coatings, such as the poor transverse rupture strength and toughness. However, the oxidation resistance of the achieved coatings were not satisfactory. In 1986 the first PVD Ti-Al-N coatings were reported with improved oxidation resistance and superior cutting performance compared to TiN [7], because of a peak in the hardness value around 900 °C [3]. This age hardening phenomena starts to disappear rapidly at 950 °C

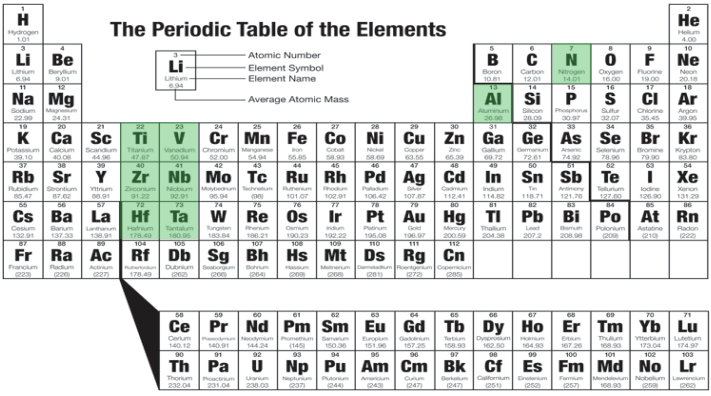

Figure 2.1. The periodic table of elements. Elements marked in green have been investigated in this work.

and above, which is the actual operation temperature of high-speed cutting tools for 10-15 minutes. This phenomenon of age hardening at elevated temperature is triggered by the self-organized nanostructuring of the solid solution as a result of spinodal decomposition. The metastable cubic Ti-Al-N decomposes coherently into cubic TiN and cubic AlN. At higher temperatures the ground state hexagonal phase of AlN phase hinders the presence of the cubic phase, which results in a significant hardness drop [5].

Multicomponent alloys and their multilayers as coatings have become highly interests in the past decades by their promise in fulfilling the need of cutting and machining tool industry for increased productivity and reliability. The physical properties of hard coating alloys can be engineered by altering the composition or making an artificial structuring of various phases on a microscopic scale. For example, in a multilayer form with different interface orientation.

2.1 Binary nitrides

The lattice parameters of the bellow described binary nitrides with cubic and hexagonal structures are summarized in Table 2.1.

Aluminum nitride (AlN) is a wide band gap (6.2 eV) semiconductor material, mainly used in optical and electronic device applications [8]. The thermodynamically stable (hexagonal, B4) structure of AlN is illustrated in Figure 2.2 (a). It has lattice parameters a = 3.11 Å and c = 4.98 Å [9]. AlN stabilizes in cubic structure with lattice parameter a = 4.05 Å at high pressure (16.6 GPa) and temperature [10, 11]. Cubic AlN phase can be grown as epitaxial film on Si substrates [12] or stabilized in the multilayer structure TiN/AlN(001) [13]. It appears as metastable phase during the spinodal decomposition of cubic B1 $Ti_{1-x}Al_xN$ solid solution, which process is responsible for the age hardening of Ti-Al-N coatings [3, 5, 14, 15].

Table 2.1. The lattice parameters a(Å) of binary nitrides with cubic and hexagonal structures

structure	a (Å)
cubic (B1) AlN	4.05
hexagonal (B4) AlN	$a = 3.11$, $c = 4.98$
cubic (B1) TiN	4.24
cubic (B1) ZrN	4.58
cubic (B1) HfN	4.53
cubic (B1) VN	4.14
hexagonal V_2N	$a = 2.84$, $c = 4.54$
cubic (B1) NbN	4.39
hexagonal Nb_2N	$a = 3.05$, $c = 5.01$
cubic (B1) TaN	4.36
hexagonal Ta_2N	$a = 5.19$, $c = 2.91$

Titanium nitride (TiN) is an extremely hard material with cubic B1 structure as shown in Figure 2.2 (b), it has a lattice parameter a = 4.24 Å [16]. It has high hardness ∼26-30 GPa [3, 17] and offers excellent protection against abrasive wear. Therefore, TiN has been one of the first coating materials used in the cutting tools industry since 1970's. It is moreover used as diffusion barriers in semiconductor devices and decorative coatings because of its goldish color. The material can be deposited as hard or protective coating by using PVD or CVD techniques.

Zirconium nitride (ZrN) is a hard material similar to TiN with cubic B1 crystal structure and has lattice parameter a = 4.58 Å [18], which is larger than that of TiN and AlN. ZrN grown by PVD shows a light gold color slightly brighter than TiN. ZrN has similar mechanical properties as TiN but exhibits lower friction coefficient [19, 20]. The hardness of arc-evaporated ZrN is 21-27 GPa [21, 22].

Hafnium nitride (HfN) has cubic B1 crystal structure with a lattice parameter a = 4.53 Å [23]. Compared to other elements in the transition metal nitride family, HfN has the highest melting point(T_m = 3300 °C), largest negative heat of formation and highest elastic moduli [24, 25]. It can be used as a good coating material for cutting tools and has been recently attracted attention as a buffer layer to enable epitaxial growth of GaN on Si [26, 27] and as a back contact to enhance light extraction from optical devices [28].

Vanadium nitride (VN) crystallizes with the cubic B1 crystal structure with lattice parameter a = 4.14 Å [29] and belongs to the class of refractory-metal compounds. The V_2N phase with hexagonal structure can be formed along with VN during nitriding. VN has recently drawn intense interest due to the strongly enhanced spin susceptibility when its composition approaches stoichiometry [30]. VN is also a promising electrode material for electrochemical supercapacitors [31, 32].

The equilibrium phase of niobium nitride is the hexagonal Nb_2N structure. With thin film deposition approaches it is possible to synthesize the metastable

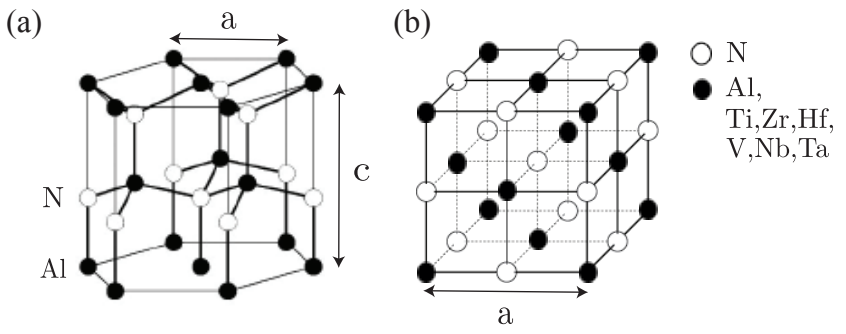

Figure 2.2. (a)The wurtzite structure (B4) (b)The rock-salt (NaCl) structure (B1)

B1 cubic NbN at room temperature [33]. The lattice parameter of cubic B1 NbN is 4.39 Å [34]. The as-deposited film shows a hardness of 42 GPa [33] and even at room temperature, NbN has higher hardness than TiN which makes it promising for protective coating application. Furthermore, it is a material candidate for tunnel junction electrode due to its thermal cyclability and large superconducting energy gap [35].

Tantalium nitride has two phases, the Ta_2N with hexagonal structure and the TaN with cubic B1 structure, the lattice parameter of B1 cubic TaN is 4.36 Å [36]. TaN has been used effectively in semiconductor industry because of high melting point and good resistivity. Recently it is utilized as diffusion barrier layers for Cu wiring of Si semiconductor devices due to the excellent thermal stability [37]. It is also applied as high-speed thermal printing head [38] and thin film resistors [39]. At 0 K, VN, NbN and TaN with cubic B1 structure are dynamical instable [40].

2.2 Ternary pseudo-binary nitride alloys

Figure 2.3 shows the ab-initio calculated 0 Kelvin isostructural mixing enthalpies of different ternary nitride alloys as a function of the AlN content. Positive energy of mixing value means that the solid solution is unstable at 0 Kelvin with respect to the reference binary materials and the solid solution will decompose. Despite this instability the alloys can be deposited in a metastable form using low temperature thin film deposition techniques. Higher energy of mixing value indicates higher "thermodynamic" tendency towards decomposition. According to the figure, one says that all the shown binary nitride solid solutions are unstable. Compared to $Ti_{1-x}Al_xN$, $Zr_{1-x}Al_xN$ and $Hf_{1-x}Al_xN$ have rather higher mixing enthalpies, which means that mixing HfN and ZrN with AlN is exceptionally difficult. $Nb_{1-x}Al_xN$ shows similar values of the mixing enthalpy as $Ti_{1-x}Al_xN$. $Ta_{1-x}Al_xN$ shows the lowest mixing enthalpy.

Ti-Al-N system is a well-established protective coating of cutting tools because of the excellent mechanical properties and oxidation resistance at elevated

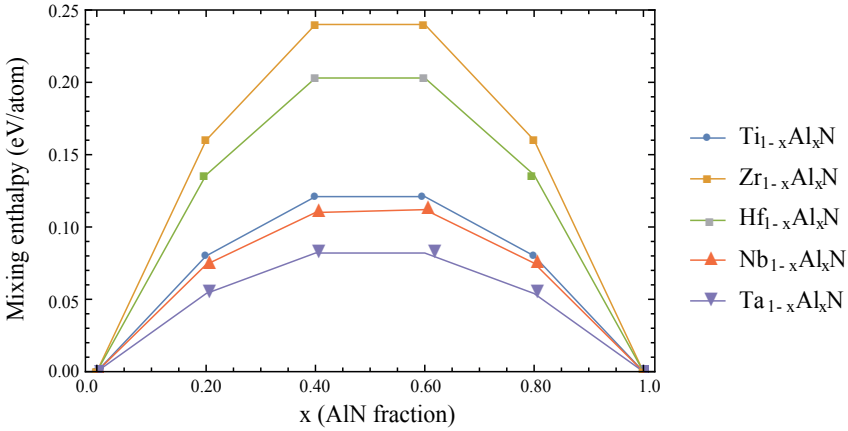

Figure 2.3. Calculated isostructural mixing enthalpy for cubic B1 $Ti_{1-x}Al_xN$, $Zr_{1-x}Al_xN$, $Hf_{1-x}Al_xN$, $Nb_{1-x}Al_xN$ and $Ta_{1-x}Al_xN$. The data is from Journal of Applied Physics 113, 113510 (2013).

temperatures [41, 42]. Cubic solid solution of Ti-Al-N can be deposited by PVD techniques with Al content up to 70 atomic %. At higher Al contents the hexagonal (wurtzite) phase becomes thermodynamicaly stable [5, 43, 44]. As long as the metastable cubic structure can be maintained, the mechanical properties and the oxidation resistance increase with the Al content. At elevated temperatures the metastable cubic Ti-Al-N phase decomposes coherently into strained c-TiN and c-AlN enriched domains [45, 46]. The step is understood as an iso-structural spinodal decomposition [47] and explained by thermodynamic calculations through the observed miscibility gap and the negative second derivative of Gibbs free energy (see Chapter 4) [48–50]. Age hardening of the coating has also been reported and attributed to the coherent spinodal decomposition [3, 45, 47, 51]. Hörling et al. [47] found that the addition of Al increases the tool's life time however at higher Al content, the appearing thermodynamically stable wurtzite phase of AlN makes the life time drastically shorter, which correlates with the materials decreased hardness, shown in Figure 1.1. Therefore, controlling the formation of the wurtzite phase of AlN has been the main research focus on the development of Ti-Al-N coatings.

Zr-Al-N system is a highly immiscible material system with the highest mixing enthalpy among the ternary transition metal aluminum nitrides, see Figure 2.3. The large lattice mismatch between c-ZrN and c-AlN (see Table 2.1) has been used to explain the fact that smaller (max. 40%) amount of c-AlN can be solved in the cubic Zr-Al-N system [52–54]. When the Al content is high ($x > 0.70$), the wurtzite hexagonal structure is stable. For intermediate Al contents, the structure is a mixture of cubic, hexagonal nano-crystallites and amorphous regions [54–56]. Zr-Al-N coatings with 36 at. % Al was shown to form self-organized semi-coherent nanostructures at 900 °C [57].

In $Hf_{1-x}Al_xN$, the spinodal decomposition has recently been observed in experiments [25]. The chemical driving force for the isostructural decomposition into binary cubic nitrides is high since the mixing enthalpy is almost twice as big as in $Ti_{1-x}Al_xN$, see Figure 2.3 [58, 59]. The maximum amount of AlN soluble in $Hf_{1-x}Al_xN$ is reported to be $x \approx 0.5$ [25, 60, 61]. From X-ray diffraction patterns, it is found that the cubic phase is maintained up to $x = 0.33$, then an amorphous or nanocrystalline material is obtained between $x = 0.38$ and 0.71, while from $x = 0.77$ wurtzite single phase field is formed [59]. Alloying HfN with AlN gives rise to an increased hardness caused by nanostructured compositional modulations as a result of the onset of spinodal decomposition [25].

Few publications have been dedicated to $V_{1-x}Al_xN$, $Nb_{1-x}Al_xN$, $Ta_{1-x}Al_xN$ coatings and solid solutions. $V_{1-x}Al_xN$ coatings have shown excellent mechanical properties, such as high hardness (up to 35GPa) and good adhesion to the steel substrates [62]. $V_{0.48}Al_{0.52}N$ coating was even found superhard (> 40GPa) [63]. Whereas, spinodal decomposition in $V_{1-x}Al_xN$ is not indicated, which may be related to the lower mixing enthalpy of $V_{1-x}Al_xN$, decomposition by nucleation and growth is observed [64]. The maximum amount of AlN soluble in $V_{1-x}Al_xN$ is observed as $x = 0.62$, and below it stabilizes in the metastable B1 structure [63]. A variety of crystallographic phases can be formed for NbN, see section 2.1, which means a higher complexity for investigating solubility in $Nb_{1-x}Al_xN$. The cubic B1 structure was confirmed by experiments [65–68]. It was shown that B1 NbN could be retained up to an Al concentration of $x = 0.45 - 0.56$ by cathodic arc-evaporation [68] and $x \approx 0.6$ by reactive sputtering [65]. Ab-initio calculations revealed that the B1 structure is (thermodynamically) stable in the composition range $x \approx 0.14 - 0.7$, and the wurtzite phase is favored at $x > 0.7$ [69]. $Nb_{0.73}Al_{0.27}N$ has shown a maximum hardness value 33.5 GPa [68]. Concerning $Ta_{1-x}Al_xN$ alloys, only $Ta_{0.89}Al_{0.11}N$ was investigated [70]. It has shown a single-phased cubic B1 solid solution in the as-deposited state, and has been found to be stable until 1100 °C. The measured hardness in the as-deposited state is around 30 GPa.

Pseudo-ternary $Ti_{1-x}Zr_xN$, $Ti_{1-x}Hf_xN$, $Ti_{1-x}V_xN$, $Ti_{1-x}Nb_xN$, $Ti_{1-x}Ta_xN$ coatings (no Al content) have also gained special attention as alternatives for high temperature cutting and machining tools. Generally they have higher hardness than their binary nitride components [71–76]. It has been shown that $Ti_{1-x}X_xN$ (X= Zr, Hf, V, Nb, Ta) can form solid solution over the whole x range ($0 < x < 1$) and are thermodynamically stable in the rocksalt structure [77, 78]. $Ti_{1-x}Zr_xN$ has been well studied by experiments and calculations [72, 73, 79, 80]. The hardness vales have been found between 32 and 35 GPa for the as-deposited films, while after annealing at $1100 - 1200$ °C the samples have shown a reduced $24 - 30$ GPa hardness [72]. An increase of hardness has been reported with increasing Zr content [73] and explained by a dominant solid-solution hardening effect [72]. For $Ti_{1-x}Nb_xN$, the material's hardness also increases with increasing Nb content and a maximum value of 31 ± 2.4 GPa is found for x(Nb)= 0.77 [74]. $Ti_{1-x}Ta_xN$ films have shown to be good conductors with varying density of conduction [76, 81, 82] and excellent mechanical properties with hardness as high as 42 GPa for $x = 0.69$ [76].

2.3 Quaternary nitride alloys

As summarized in the previous chapter, significant efforts are concentrated on advancing both, the microstructural and compositional design of alloys to achieve higher hardness and extended thermal stability [83]. A novel concept of multicomponent alloying has been established by mixing CrN and $Ti_{1-x}Al_xN$ [84, 85]. The substantial improvement of thermal stability of quasi-ternary (TiCrAl)N alloys in respect with the characteristic thermal stability of Ti-Al-N, has been explained by the occurence of a novel metastable cubic phase of $Cr_{1-x}Al_xN$. It has extended the increased interest for metastable materials. The 0 K thermodynamics of quaternary transition metal nitride (Ti-Al-X-N, X=Zr,Hf,V,Nb,Ta) alloys has recently been investigated by Holec using *ab initio* simulations [86]. Zr improves the oxidation resistance and the as deposited hardness of $Ti_{1-x}Al_xN$ [87, 88]; Hf leads to an inferior oxidation resistance of $Ti_{1-x}Al_xN$ and promotes the formation of cubic domains, however it retards the formation of stable wurtzite AlN during thermal annealing [89, 90]; The addition of V to $Ti_{1-x}Al_xN$ hard coatings enables lubricating effects based on oxidation resistance and improves the overall wear resistance [91–93]; Nb and Ta are also favored due to combining outstanding mechanical properties with good oxidation resistance [94–96].

In paper V we present a study of the thermal stability as well as structure and stress evolution of cubic $Ti_xNb_yAl_{1-x-y}N$ coatings during annealing. Paper IV gives a comprehensive overview of the elasticity in cubic quaternary transition metal nitride $Ti_xX_yAl_{1-x-y}N$ alloys where X is Zr, Hf, V, Nb or Ta and analyzes the possible multicomponent alloying strategies to engineer the strength and ductility of quaternary solid solution.

2.4 Multilayers

Materials can be repeatedly deposited on top of each other to compose nanoscale multilayer structures. Coherent, semi- and incoherent interfaces can be formed and thermodynamic stabilization can be observed. The concept of forming coherent multilayers is offered as an alternative to extend the wear resistance and hardness of monolithic bulk materials [3]. Therefore multilayer coatings have rised the interest of cutting tool industry in the beginning of 1980's.

The altered thermodynamics of $Ti_{1-x}Al_xN$ in the form of $Ti_{1-x}Al_xN$/TiN superlattice has been investigated experimentally [3, 15, 97]. Through electron microscopy and atom probe tomography combined with phase field simulations, the occurence of surface directed spinodal decomposition [98] has been shown. In our work the study of multilayers is motivated by the approximation that during the coherent spinodal decomposition of the alloys, the microstruture can locally be described as coherent multilayers with different interfacial orientations. Paper II discusses the mixing thermodynamics of cubic (B1) $Ti_{1-x}Al_xN$/TiN(001) multilayers and shows that interfacial effects suppress the mixing enthalpy of $Ti_{1-x}Al_xN$ compared to the monolithic case, suggesting that the multilayer structure has a stabilization effect. Furthermore, Paper III with experiments and *ab initio* calculations demonstrate that forming semicoherent interfaces during film growth

might offer higher thermal stability. Paper IV predicts the Young's modulus of the quaternary transition metal nitride multilayers with the [001] and [111] interfacial direction and reveals the materials local Young's modulus distribution affects the microstructure evolution which indicates an effect on the hardness of the materials.

CHAPTER 3

Structure modeling of alloys

3.1 Configurational disorder in alloys

The degree of disorder in alloys influences the thermodynamic properties of the alloys to a great extent. The translational symmetry of the lattice results in pure elements and ordered compounds that an unit cell is sufficient to simulate material's properties. Long-range ordering in a single crystal can be observed by X-ray diffraction technique to obtain the pair correlation function, see Figure 3.1 (a). The arrangement of atoms is regularly repeated at any distance from an atom. This results in the periodically repeated peaks in the pair correlation function in Figure 3.1 (a). In alloys the configurational disorder breaks this regularity in pair correlation function, only short range order is observed with highly broaden peaks, see Figure 3.1 (b). Repeated supercells of the underlying lattice symmetry in each direction can be used to simulate the disorder in alloys. A sufficiently large structure on which the atoms can be appropriately distributed is needed, thereafter supercells can be used for disordered alloys, impurities, defects and even treating interfacial boundary effects.

In my work two of the most successful modeling disordered alloys approaches were used. One is the construction of "special quasirandom structures" (SQS) [99] by the principle of close reproduction of the perfectly random network for the first few shells around each site. It is an elegant technique with the advantage of an access to atomic forces. Its drawback is the extra computational costs. The second one is based on creating an effective medium that describes the analytical averaging over the disordered configurations. The Coherent Potential Approximation (CPA) [100] is an improved scheme for creating the effective medium, it provides the same scattering properties of the one-component effective medium as the average of alloy components, embedded in this effective medium.

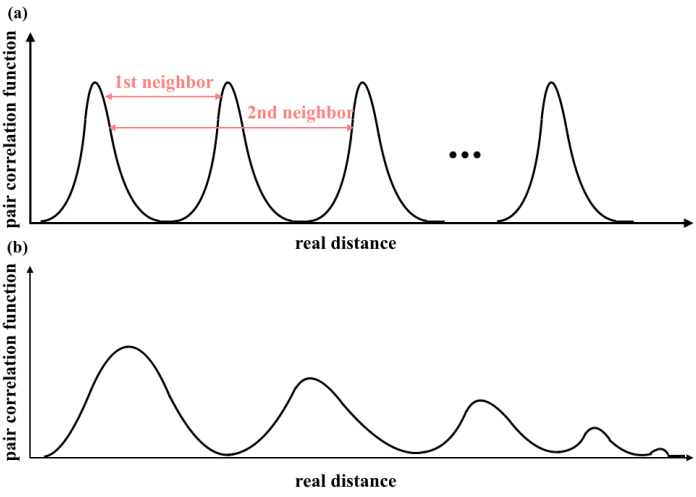

Figure 3.1. Illustration of pair correlation function of (a) Single crystals (b) Alloys.

3.2 The special quasi-random structure (SQS) approach

The special quasirandom structure (SQS) approach as suggested by Zunger *et al* [99] is introduced for a binary $A_{1-x}B_x$ solid solutions. During the SQS algorithm one uses spin variables σ_i to describe the atomic occupation, if the ith site is occupied by atom A, σ_i is $+1$, otherwise it equals -1. The atomic configuration of an alloy with N sites can be given by the vector $\sigma = \{\sigma_1, \sigma_2, ..., \sigma_N\}$. Then one can define a characteristic function $\Phi_f^{(n)}(\sigma)$ for a given n-site in clusters f by the product of the spin variables of f:

$$\Phi_f^{(n)}(\sigma) = \prod_{i \in f} \sigma_i. \tag{3.1}$$

These functions form a complete and orthonormal set, with the inner product between two functions:

$$\langle \Phi_f^{(n)}(\sigma), \Phi_g^{(n)}(\sigma) \rangle = \frac{1}{2^N} \sum_{\sigma} \Phi_f^{(n)}(\sigma) \Phi_g^{(n)}(\sigma) = \delta_{f,g}. \tag{3.2}$$

where the sum runs over all the atomic configurations on the N sites. The function equals to 1 only if two clusters are the same in the crystal, otherwise it is 0. This means that one can expand any function of configuration in this basis set:

$$F(\sigma) = \sum_f F_f^{(n)} \Phi_f^{(n)}(\sigma). \tag{3.3}$$

The expansion coefficients are

$$F_f^{(n)} = \langle F(\sigma), \Phi_f^{(n)}(\sigma) \rangle. \tag{3.4}$$

As for the total energy of an alloy, the expansion coefficients are so-called effective cluster interactions (ECI), given by

$$V_f^{(n)} = \langle E_{tot}(\sigma), \Phi_f^{(n)}(\sigma) \rangle. \tag{3.5}$$

The total energy of an alloy can then be calculated with arbitrary configuration, given by

$$E_{tot} = \sum_f V_f^{(n)} \xi_f^{(n)}. \tag{3.6}$$

where $\xi_f^{(n)}$ is the n-site correlation function for the cluster f, defined as the average value of the symmetrically identical characteristic function, $\xi_f^{(n)} = \langle \Phi_f^{(n)} \rangle$.

In the case of a completely random alloy, $\xi_f^{(n)}$ equals to zero and can be expressed with the help of the Warren-Cowlley short range order (SRO) parameters [101]. For a binary $A_{1-x}B_x$ alloy, the SRO parameters of A and B atoms within a sublattice can be optimized towards a random distribution of A and B that they are close to zero for as many coordination shells as possible. Due to the limitation of the supercell size, it is not practically possible to obtain zero value of the SRO parameters for all coordination shells, E_{tot} could affect predictions of some properties. For example, the total energy needs to be converged with respect to the supercell size [102] and therefore the accuracy of using the SQS method must be weighed against the computational cost. With today's supercomputers, SQS approach can excellently reproduce the total energy of a random alloy. However, there are still limitations. One of the limitations is modeling tensorial properties. The problem with the SQS approach is that it breaks inherently the point symmetry of the underlying crystal lattice. Thus the tensorial properties can differ from experimental values with the chosen SQS model. A symmetry-based projection technique was introduced [103, 104] to extract the closest approximation of the elastic tensor components. This technique was used in Paper IV to derive the elastic properties of transition metal alloys. More details will be shown in Chapter 5. In Paper I, we point out the limitations and methodological corrections for the application of SQS approach in studies of advanced properties of alloys and multilayers.

3.2.1 Modeling multilayered alloys

It is shown by Ruban *et al* [102] that in inhomogeneous systems such as multilayer alloys, the structral SRO parameters should depend on the layer index. The interaction and the large relaxation of the interfacial atoms renormalise the effective cluster interactions(ECI) [102] so that layer dependent cluster expansion has to be applied. Therefore, all properties have to be indexed with the layer number (λ) with keeping the homogeneity only in the two periodic directions (x and y) [102]. In Paper I and Paper II, We use a composition profile through the interfaces by

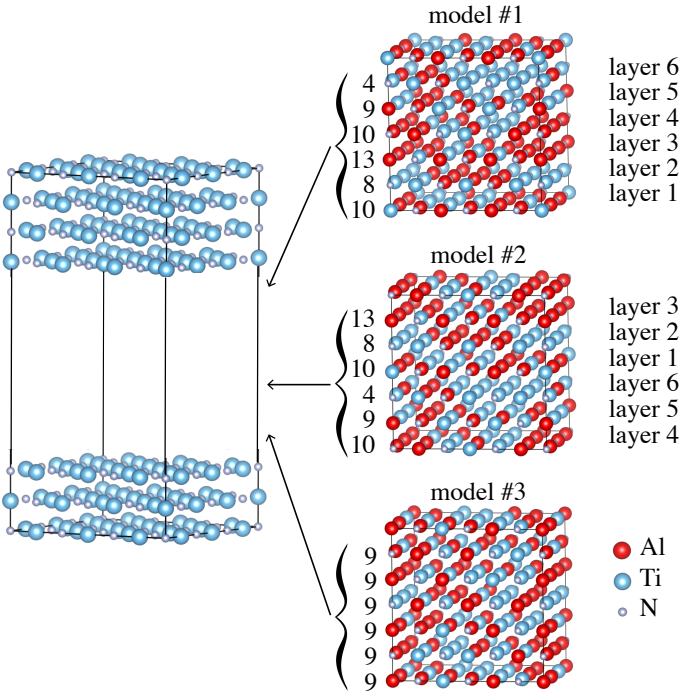

Figure 3.2. Three different bulk SQS models of $Ti_{0.5}Al_{0.5}N$ to build the multilayer of $TiN/Ti_{0.5}Al_{0.5}N$.

keeping the same composition in each layer of the SQS model to obtain results relevant for simulations of disordered multilayers.

The total energy density of the multilayer can be written as

$$e^{\mathrm{ML}} = \sum_i y_i e_i^{\mathrm{bulk}} + e^{\mathrm{interface}}(\{y_i\}) + e^{\mathrm{strain}}(\{y_i\}), \tag{3.7}$$

where y_i are the content ratios and e_i^{bulk} denote the unstrained bulk energies of the components in the multilayer, $e^{\mathrm{interface}}$ and e^{strain} stand for the interfacial and constituent strain energies per surface area [105]. The last two terms can strongly depend on the atomic arrangement in a finite size model.

In Paper I, we aim to underline the dependence of the derived mixing enthalpy values on the chosen SQS supercell in the multilayers. We generate three different bulk $Ti_{0.5}Al_{0.5}N$ with a size of $(3 \times 3 \times 3)$ and sandwiched them between the TiN layers, as shown in Figure 3.2. The model #1 was created by minimizing the bulk Warren-Cowlley SRO parameters up to the seventh shell without constraining the composition profile. Model #2 was obtained from model #1 by a layer shift. The model #3 has also been created by minimizing the bulk Warren-Cowlley SRO parameters up to the seventh shell but with keeping the same composition $x_\lambda = 0.5$ in each layer. The derived in-plane SRO parameters of all the three

Table 3.1. The layer composition x_λ and the layer Warren-Cowlley SRO parameters of three SQS models.

	x_λ	1st	2nd	3rd	4th	5th	6th	7th
	model #1 and #2							
layer 1	0.56	-0.01	-0.01	-0.13	-0.01	-0.01	-0.35	-0.13
layer 2	0.44	0.21	0.10	-0.24	-0.24	0.10	-0.35	-0.24
layer 3	0.72	0.17	-0.11	-0.11	-0.11	-0.11	-0.38	-0.11
layer 4	0.56	-0.01	0.10	-0.24	-0.01	0.10	-0.35	-0.24
layer 5	0.50	-0.22	-0.22	0.22	0.11	-0.22	-0.56	0.22
layer 6	0.22	0.20	-0.13	-0.13	-0.13	-0.13	-0.29	-0.13
	model #3							
layer 1	0.50	0.00	-0.22	0.00	0.11	-0.22	-0.56	0.00
layer 2	0.50	0.00	0.00	-0.22	0.00	0.00	-0.11	-0.22
layer 3	0.50	0.00	0.00	-0.22	0.00	0.00	-0.11	-0.22
layer 4	0.50	-0.44	0.22	0.22	-0.22	0.22	-0.11	0.22
layer 5	0.50	0.11	0.22	-0.22	-0.22	0.22	-0.56	-0.22
layer 6	0.50	0.00	-0.33	0.11	0.00	-0.33	-0.11	0.11

supercells are listed in Table 3.1. The most relevant difference between the three models are the compositions x_λ, especially at the interface with TiN. Model #3 has the proper constrained value $x_\lambda = 0.5$ in each layer so that it also represents bulk randomness, which corresponds to the proper treatment of inhomogeneous systems [102].

3.3 The Coherent Potential Approximation (CPA)

The concept of effective medium with keeping the translational symmetry of the underlying lattice is designed to average out the disorder. Coherent potential approximation (CPA) makes use of the one-electron Green's function, which is a self-averaging quantity. The method aims to find a one-component effective medium with a Green's function that has translational symmetry of the underlying lattice. It was originally introduced by Soven [100] for the electronic structure problem and by Taylor [106] to deal with phonons of disordered alloys. The CPA was reformulated with the multiple-scattering theory of Korringa-Kohn-Rostoker (KKR) [107, 108] by Györffy [109], and since then it was widely used. The objective of the CPA is to provide the same scattering properties of the one-component effective medium as the average of alloy components, which is schematically illustrated in Figure 3.3. With the single site approximation, the advantage of CPA against the SQS method is that one does not need to build large supercells to ensure the randomness, therefore disordered alloys can be treated with less demanding calculations. However, the single site character does not take into account other effects such as local environment effects, short and long-range order effects, charge transfer, etc. One has to apply additional models and do extra calculations beyond the CPA calculations. For example, to take into account the effect of charge transfer

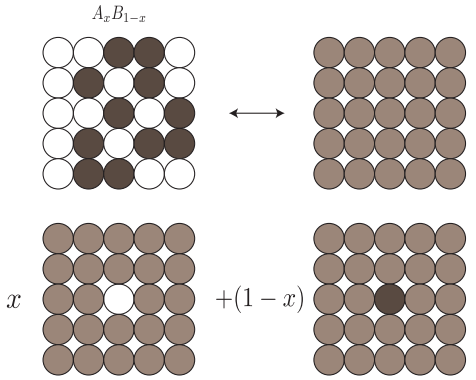

Figure 3.3. Schematic representation of the principle of CPA approximation for a disordered binary alloy A_xB_{1-x}. See the text for details.

between components, one can use the screened impurity model(SIM), where each atom is treated as an impurity in the effective CPA medium and the net charge is screened by the first coordination shell of the nearest neighbor [110]. To estimate the local relaxations, the effective tetrahedron method (ETM) [111] which considers the effect of a local volume relaxation is proven to work accurate.

In Paper V, we modeled $Ti_xNb_yAl_{1-x-y}N$ alloy (B1 crystal structure) with four lattice sites in the unit cell, one metal, one nitrogen and two empty spheres were included to improve the space filling in the atomic sphere approximation (ASA) [112]. Through the use of the independent sublattice model (ISM) [50], the additional relaxation effect of the nitrogen and metal atoms relative to each other has been considered and the local relaxation energy was calculated as:

$$E_{rel} = E_{tot} - E_{unrel}, \tag{3.8}$$

where E_{tot} is the total energy of a disordered alloy with fully relaxed ionic positions and E_{unrel} is the total energy of the same system with the ideal B1 crystal lattice positions. To calculate E_{rel} one only needs to consider relaxations of nitrogens, because of the shown negligible displacement of the metallic atoms [50]. One can derive an expression for E_{rel} for N atoms in c-$Ti_xNb_yAl_{1-x-y}N$ as:

$$E_{rel} = 6(\nu_{TiAl}\rho_{TiAl} + \nu_{NbAl}\rho_{NbAl} + \nu_{TiNb}\rho_{TiNb}). \tag{3.9}$$

where ν_{TiAl}, ν_{NbAl} and ν_{TiNb} are the relaxation energies and ρ_{TiAl}, ρ_{NbAl} and ρ_{TiNb} are the probabilities of a nitrogen atom being surrounded by the corresponding two metal atoms in one direction. The relaxation energy parameters were determined by supercell calculations with and without atomic relaxations. The supercells were built using the Special Quasirandom Structure (SQS) approach introduced before. The supercell calculations resulted in ν_{TiAl} = -0.0321061 eV/atom, ν_{NbAl} = -0.116299 eV/atom and ν_{TiNb} = -0.010324 eV/atom to the relaxation energies.

CHAPTER 4

Mixing thermodynamics and decomposition

4.1 Gibbs free energy

To predict the thermodynamic phase diagram of a binary solid solution, see Figure 4.1, one has to calculate Gibbs free energy. Gibbs free energy G, is a thermodynamic potential of system at constant pressure p and temperature T with a constant number of particles.

$$G(p,T) = E + pV - TS = H - TS = F + pV, \tag{4.1}$$

where E is the total (internal) energy calculated through electronic structure calculations, H is the enthalpy, S denotes the entropy and F is Helmholtz free energy. When $T = 0$ K and $p = 0$ GPa, $G = E$.

To determine whether a solid solution is thermodynamically stable or not, one has to calculate the Gibbs free energy of mixing ΔG as,

$$\Delta G = G_{solution} - \sum_i x_i G_i. \tag{4.2}$$

Here $G_{solution}$ is the Gibbs free energy of the solid solution, x_i and G_i are the concentration and the Gibbs free energy of the components or reference materials. Moreover, ΔG is expressed as

$$\Delta G = \Delta H - T\Delta S. \tag{4.3}$$

where ΔH and ΔS are defined as mixing enthalpy and mixing entropy, respectively. If $\Delta G < 0$, the solution is stable with respect to their competing components and will be formed spontaneously. If $\Delta G > 0$, then the solution is unstable (or metastable) and phase separation should occur.

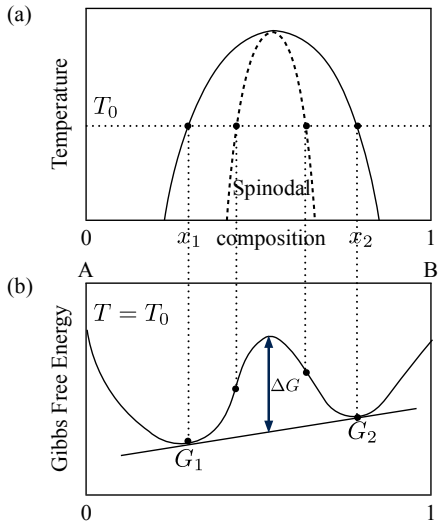

Figure 4.1. Illustration of the phase diagram and the Gibbs free energy curve of a binary alloy. (a) A schematic phase Temperature-compositon(x) diagram of an alloy. The solid line shows the binodal curve, while the dashed one is the spinodal curve. (b) The free energy as a function of composition for the phase separation. Mixing Gibbs free energy ΔG is minimized by a common tangent construction.

Spinodal decomposition happens if the phase separation occurs spontaneously in the system without nucleation and growth. The range of spinodal decomposition is shown in Figure 4.1(b) and defined as

$$\frac{\partial^2 G}{\partial^2 x} < 0. \tag{4.4}$$

For a multicomponent alloy with more than two components, such as $Ti_xNb_yAl_zN$ in Paper V, the second directional derivative is calculated as

$$\frac{\partial^2 G}{\overrightarrow{\Delta R}^2} = \frac{G(\mathbf{R} + \overrightarrow{\Delta R}) + G(\mathbf{R} - \overrightarrow{\Delta R}) - 2G(\mathbf{R})}{|\overrightarrow{\Delta R}^2|}. \tag{4.5}$$

In direction $\overrightarrow{\Delta R} = (\Delta x, \Delta y, \Delta z)$ at the composition plane point $\mathbf{R} = (x, y, z)$. Interpolation is used to derive the mixing energy and its second directional derivatives.

4.2 Mixing enthalpy in multilayers

In this section, we explain the thermodynamic mixing of $Ti_{1-x}Al_xN$ in the superlattice $Ti_{1-x}Al_xN$/TiN(001) in comparison with the one of bulk $Ti_{1-x}Al_xN$. Figure 4.2 shows a schematic way of calculating the coherent phase separation in

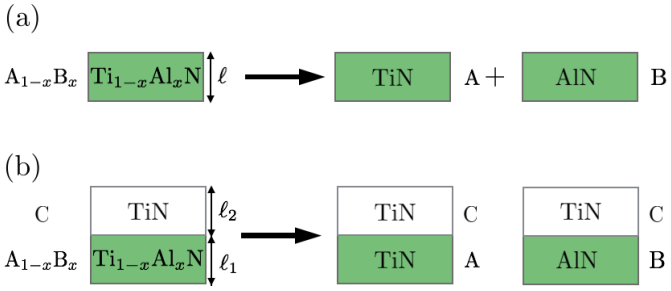

Figure 4.2. Schematic diagram of the phase separation of (a) $Ti_{1-x}Al_xN$ bulk and (b) $Ti_{1-x}Al_xN$/TiN multilayer.

cubic B1 $Ti_{1-x}Al_xN$ bulk and $Ti_{1-x}Al_xN$/TiN(001) multilayer. With using the figure, the mixing enthalpy is written as

$$\Delta H^{\mathrm{Ti}_{1-x}\mathrm{Al}_x\mathrm{N}}(x) = \frac{1}{N}\left(E_\ell^{\mathrm{Ti}_{1-x}\mathrm{Al}_x\mathrm{N}}(x) - (1-x)E_\ell^{\mathrm{TiN}} - xE_\ell^{\mathrm{AlN/TiN}}\right), \tag{4.6}$$

for bulk $Ti_{1-x}Al_xN$ and

$$\Delta H^{\mathrm{Ti}_{1-x}\mathrm{Al}_x\mathrm{N/TiN}}(x,\ell_1,\ell_2) = \frac{1}{N}\left(E_{\ell_1/\ell_2}^{\mathrm{Ti}_{1-x}\mathrm{Al}_x\mathrm{N/TiN}}(x) - (1-x)E_{\ell_1/\ell_2}^{\mathrm{TiN}} - xE_{\ell_1/\ell_2}^{\mathrm{AlN/TiN}}\right). \tag{4.7}$$

for the multilayer. N is the total number of atoms in the $Ti_{1-x}Al_xN$ slab, E_ℓ^A denotes the equilibrium total energy of material A with ℓ layers along the crystallographic (001) direction. If ΔH is positive, $Ti_{1-x}Al_xN$ will decompose to TiN and AlN and if it is negative, the structure is stable.

For the $Ti_{1-x}Al_xN$/TiN(001) multilayer, the end components are pure TiN and AlN/TiN(001). The mixing enthalpy $\Delta H^{\mathrm{Ti}_{1-x}\mathrm{Al}_x\mathrm{N/TiN}}$ can be further divided into two terms: (i) the in-plane lattice matching or strain effects and (ii) the remaining so called chemical interaction of $Ti_{1-x}Al_xN$ and TiN through the (001) interface.

$$\Delta H^{\mathrm{Ti}_{1-x}\mathrm{Al}_x\mathrm{N/TiN}}(x,\ell_1,\ell_2) = \Delta H_{\mathrm{strain}}^{\mathrm{Ti}_{1-x}\mathrm{Al}_x\mathrm{N/TiN}} + \Delta H_{\mathrm{chemical}}^{\mathrm{Ti}_{1-x}\mathrm{Al}_x\mathrm{N/TiN}}. \tag{4.8}$$

To quantify the effect of strain on the mixing enthalpy, two methods are presented and compared in this thesis. The first approach is the constituent strain method proposed by Ozoliņš *et al* [105]. The constituent strain energy $E_{\mathrm{const}}^{\mathrm{AB/C}}$ in AB/C multilayer is defined by

$$E_{\mathrm{const}}^{\mathrm{AB/C}} = \min_a \left[y\Delta E^{\mathrm{AB}}(a) + (1-y)\Delta E^{\mathrm{C}}(a)\right]. \tag{4.9}$$

Here, $y = \ell_1/(\ell_1+\ell_2)$ denotes the relative thickness of the AB layer and

$$\Delta E^\alpha(a) = \min_c E^\alpha(a,c) - E_0^\alpha, \tag{4.10}$$

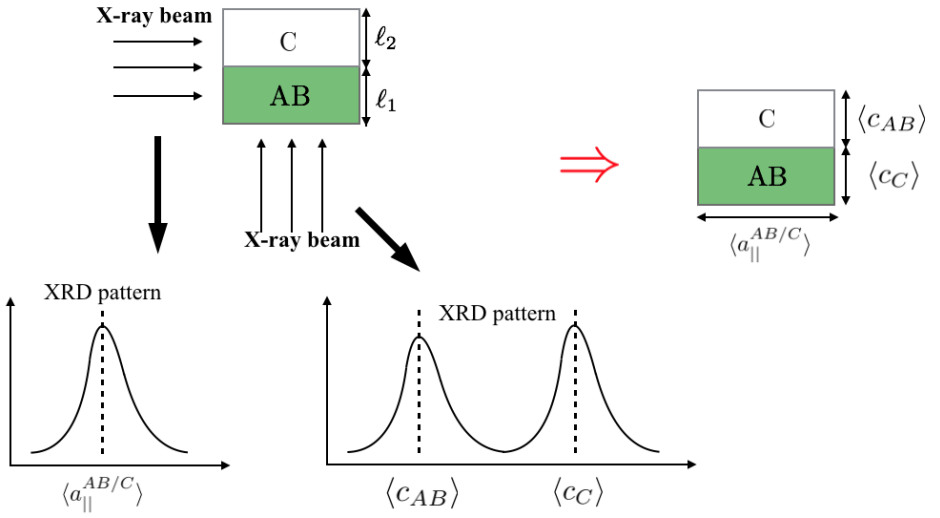

Figure 4.3. Schematic drawing of experimental way of obtaining structural data.

stands for the epitaxial strain energy, a and c denote the in-plane and out-of-plane lattice parameters and E_0^α is the equilibrium energy of layer α. Using E_0^α from Eq.(4.10) and substituting it into Eq.(4.9) one obtains E_{const} for each system. Further with the help of Eq.(4.7), the constituent strain contribution to the mixing enthalpy can be derived as:

$$\begin{aligned}\Delta H_{\text{const}}^{\text{AB/C}}(x,\ell_1,\ell_2) = \frac{1}{N}\Bigg(\\ \min_a \left[y\bar{E}^{\text{AB}}_{\ell_1/\ell_2}(a) + (1-y)\bar{E}^{\text{C}}_{\ell_1/\ell_2}(a) \right] - \\ (1-x)\min_a \left[y\bar{E}^{\text{A}}_{\ell_1/\ell_2}(a) + (1-y)\bar{E}^{\text{C}}_{\ell_1/\ell_2}(a) \right] - \\ x\min_a \left[y\bar{E}^{\text{B}}_{\ell_1/\ell_2}(a) + (1-y)\bar{E}^{\text{C}}_{\ell_1/\ell_2}(a) \right] \Bigg).\end{aligned} \tag{4.11}$$

and the remaining contributions come from the interface chemistry.

Another way of making the energy partitioning into a strain and chemical contributions implements the experimentally available structural data of the multilayers. It is based on the coherent in-plane lattice parameter of the full system and the averaged inter-layer distances along the [001] growth direction. Therefore, we call this method coherency strain approach. According to Figure 4.3, in an AB/C multilayer one assumes two strong diffraction peaks in the growth direction what correspond to the interlayer distance in material AB and C, respectively. Therefore one can introduce an energy expression

$$\mathcal{E}^{\text{AB/C}}_{\ell_1+\ell_2}(x) = yE^{\text{AB}}_{\ell_1+\ell_2}(x, a_{||}^{\text{AB/C}}, \langle c_{\text{AB}} \rangle) + (1-y)E^{\text{C}}_{\ell_1+\ell_2}(a_{||}^{\text{AB/C}}, \langle c_{\text{C}} \rangle), \tag{4.12}$$

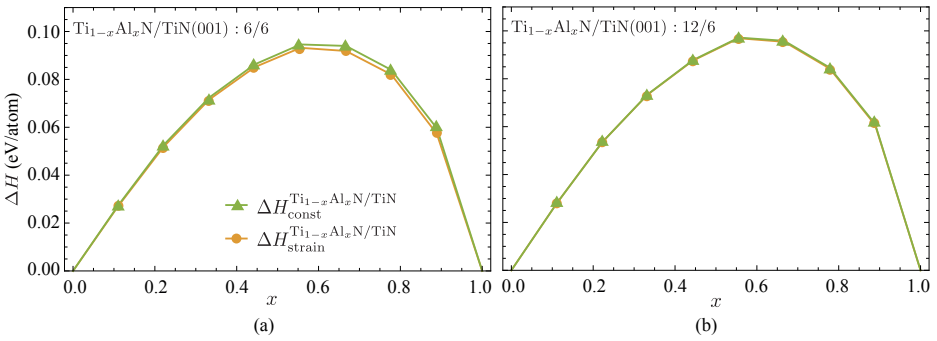

Figure 4.4. The mixing enthalpy with the constituent strain and coherency strain effect of (a)6 layers $Ti_{1-x}Al_xN$/6 layers TiN multilayer (b)12 layers $Ti_{1-x}Al_xN$/6 layers TiN multilayer.

where $a_{||}^{\mathrm{AB/C}}$ is the coherent in-plane lattice parameter and $\langle c^{\mathrm{AB}}\rangle$, $\langle c^{\mathrm{C}}\rangle$ are the averaged out-of-plane lattice parameters. Then, the strain contribution in the mixing enthalpy is defined as

$$\Delta H_{\mathrm{strain}}^{\mathrm{AB/C}} = \frac{1}{N}\left(\mathcal{E}_{\ell_1/\ell_2}^{\mathrm{AB/C}}(x) - (1-x)\mathcal{E}_{\ell_1/\ell_2}^{\mathrm{A/C}} - x\mathcal{E}_{\ell_1/\ell_2}^{\mathrm{B/C}}\right). \tag{4.13}$$

This expression might reflect the meaning of strain contribution in experimental studies.

The calculated mixing enthalpy values of both methods are shown in Figure 4.4. One sees that the coherency strain contribution agrees well with the constituent strain contribution. Though, in the coherency strain method one includes certain chemical effect through the interface, by the coherent lattice parameter, the contribution is negligible. In Paper II, we base our description on the concept of coherency strain rather than the constituent one because it allows us to connect the results of the simulations to an experimental interpretation. More details about the comparison of mixing enthalpy of $Ti_{1-x}Al_xN$ bulk and $Ti_{1-x}Al_xN$/TiN multilayers are presented in Chapter 7.

4.3 Gibbs free energy calculated with the Debye model

At finite temperature, the Gibbs free energy G is written as

$$G(p,T) = F_{chemical} + F_{vib} + F_{mag} + pV, \tag{4.14}$$

using the Helmholtz free energy F

$$F = E_{chemical} + E_{vib} + E_{mag} - T(S_{chemical} + S_{vib} + S_{mag}). \tag{4.15}$$

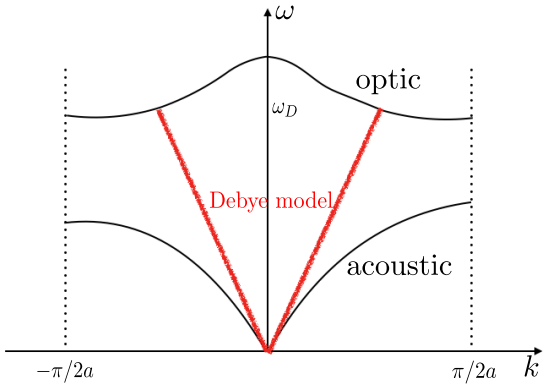

Figure 4.5. The Debye approximation to the dispersion relation. The upper branch is called the optical and the lower branch is the acoustic.

The total energy $E_{chemical}$ is calculated using Density Functional Theory (DFT), see Chapter 6. The material systems discussed in this thesis are non-magnetic and therefore, the magnetic contribution is neglected.

For a completely random disordered solid solution, the configurational entropy S_{conf} is calculated using the mean field approximation,

$$S_{conf} = -k_B \sum_i x_i ln(x_i). \tag{4.16}$$

where k_B is Boltzmann's constant and x_i is the concentration of ith type atoms. S_{conf} is temperature independent.

In this thesis, the vibrational energy and entropy is approximated using the Debye model. The model is explained in Figure 4.5. It treats the atomic vibrations of the lattice with a linear dispersion relation $\omega = ck$ and deals only with the acoustic branches. The Debye temperature θ_D can be related to the maximum frequency ω_D,

$$k_B \theta_D = \hbar \omega_D, \tag{4.17}$$

The average sound velocity, $\overline{s}$, can be defined by Christoffel equation [113] for sound velocities as

$$\frac{3}{\overline{s}^3} = \sum_\lambda \int \frac{1}{s_\lambda^3(\Omega)} \frac{d\Omega}{4\pi}. \tag{4.18}$$

where $s_\lambda(\Omega)$ is the phase velocity of the long wavelength acoustic phonons and the integral means an average over the propagation direction. If $\overline{s}$ is isotropic, for the longitudinal (L) and the two degenerate transverse (T) branches, then

$$\frac{3}{\overline{s}_{ic}^3} = \frac{1}{s_L^3} + \frac{2}{s_T^3}. \tag{4.19}$$

here s_L and s_T are related with the elastic constants and the mass density ρ,

$$s_L = \sqrt{[C_{11} + \frac{2}{5}(2C_{44} + C_{12} - C_{11})]/\rho},$$
$$s_T = \sqrt{[C_{44} - \frac{1}{5}(2C_{44} + C_{12} - C_{11})]/\rho}, \tag{4.20}$$

The Debye temperature θ_D can be expressed as

$$\theta_D = \frac{\hbar}{k_B}(6\pi N/V)^{1/3}\overline{s}_{ic} = \frac{\hbar}{k_B}(6\pi N\rho/M)^{1/3}\overline{s}_{ic}, \tag{4.21}$$

M is the mass of a mole of the material. Then at temperature T, one calculates the vibrational energy and entropy as

$$E_{vib}(T) = \frac{9}{8}N\hbar\omega_D + \frac{9N\hbar}{\omega_D^3}\int_0^{\omega_D}\frac{\omega^3}{exp(\hbar\omega/k_BT) - 1}d\omega,$$
$$S_{vib}(T) = \frac{12Nk_B}{\omega_D^3}\int_0^{\omega_D}\frac{\hbar\omega^3/(k_BT)d\omega}{exp(\hbar\omega/k_BT) - 1} - 3Nk_B\ln[1 - exp(-\hbar\omega_D/k_BT)] \tag{4.22}$$

Substituting these expressions into equation (4.14) and (4.15), the Gibbs free energy with the vibration contribution can be obtained. In Paper V, we investigate the mixing Gibbs free energy of $Ti_xNb_yAl_{1-x-y}N$ at usual cutting operation temperature.

4.4 Thermal expansion coefficient (TEC)

The linear thermal expansion coefficient (TEC) is calculated as

$$\alpha(T) = \sum_r \frac{1}{3B}(\frac{\partial S_r}{\partial V})_T. \tag{4.23}$$

where T is the temperature, B is the isothermal bulk modulus, S_r stands for the different entropy contributions and V denotes the volume. The volume dependence of each entropy term can be written with the help of the Grüneisen parameter γ_r and the heat capacity at constant volume $(C_V)_r$. Considering electronic (el.) and phononic (phon.) entropies one has

$$\alpha(T) = \frac{\gamma_{\text{el.}}(C_V)_{\text{el.}}}{3BV} + \frac{\gamma_{\text{phon.}}(C_V)_{\text{phon.}}}{3BV}. \tag{4.24}$$

The heat capacity which is the ratio of the heat added or removed within the temperature change, are approximated through the Debye model as

$$(C_V)_{\text{phon.}}(T) = 9Nk_B(\frac{T}{\theta_D})^3\int_0^{\theta_D/T}\frac{x^4exp^x}{(exp^x - 1)^2}dx,$$
$$(C_V)_{\text{el.}}(T) = \frac{2\pi^2}{3}k_B^2T \times DOS(\epsilon_F). \tag{4.25}$$

Then the thermal expansion coefficients that describes how the materials volume is altered by expansion with a change in temperature can be approximated. In Paper VI, the thermal expansion coefficients of $Ti_{1-x-y}X_yAl_xN$ (X=Zr, Hf, Nb, V, Ta) solid solutions were predicted by the Debye model.

CHAPTER 5

Elastic properties

The elastic parameters of materials are classified as elastic moduli for polycrystals and elastic stiffness or compliance for single crystals [114]. Elastic moduli are calculated using effective medium theories, such as the Reuss (lower bound, uniform strain) and Voigt (upper bound, uniform stress) averaging approaches [115, 116]. Hereby, a scheme is proposed to distinguish these elastic parameters [114]:

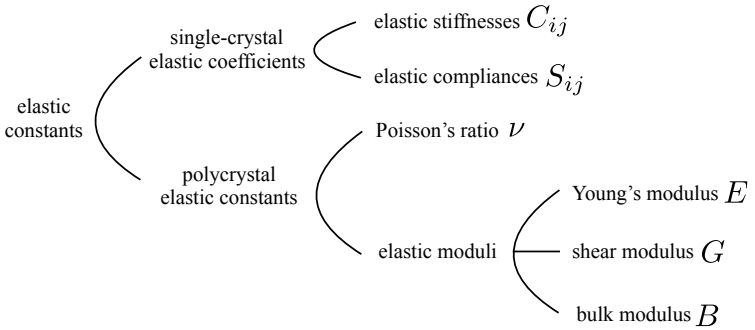

5.1 Elastic properties of isotropic solids

Deformation of materials changes the material's internal mechanical state. These changes are described by the strain and stress tensors; $\epsilon(\mathbf{r})$, $\sigma(\mathbf{r})$. ϵ defines the local distortion field in the material by

$$\mathbf{r} \rightarrow \mathbf{r}' = (\mathbb{1} + \epsilon(\mathbf{r}))\mathbf{r}. \tag{5.1}$$

and σ describes the induced local internal forces per unit area $\mathbf{f}$ via

$$f_i = \sum_{j=x,y,z} \sigma_{ij} n_j, \quad i = \{x, y, z\}, \tag{5.2}$$

where $\mathbf{n}$ is the normal vector of an arbitrary plane. The diagonal elements of σ are called normal (or longitudinal, uniaxial) stresses while the off-diagonals are the shear ones. The eigenvalues of the stress tensor are called principal stresses. Hydrostatic or the isotropic stress condition is defined if $\sigma = p\mathbb{1}$, where the scalar p is the mean stress or hydrostatic pressure. Any stress tensor can be split into a hydrostatic and a residual deviatoric component.

In the elastic (or linear) regime one defines the Young's (E) and shear (G) moduli of a material as

$$\begin{aligned} \sigma_{ii} &= E\epsilon_{ii}, \\ \sigma_{ij} &= G\epsilon_{ij} \quad i \neq j \quad i, j = \{x, y, z\} \end{aligned} \tag{5.3}$$

Young's modulus (E) can be calculated also by $(F/A)/(dL/L_0)$, where F is the applied force, A is the cross area of the material with length L_0. dL is the expansion of the material by the applied force. Thereby this modulus is commonly used as a measure of strength in engineering. Hydrostatic pressure causes a volume change ΔV of the material and then one defines the bulk modulus B by

$$p = B(-\Delta V/V). \tag{5.4}$$

Beyond the ratio of B/G introduced by Pugh [117] one plots an Ashby map [118] showing the material strength defined as E/ρ versus G/B to classify materials from mechanical engineering point of view, where ρ is the materials density. The material is characterized as brittle if $G/B > 0.57$ otherwise one says that the material is ductile (non-brittle).

5.2 Elastic stiffness tensor

The components of stress σ_{ij} and strain ϵ_{ij} tensors are commonly written in 3×3 matrix form using Voigt's notation

$$\sigma_{ij} = \begin{bmatrix} \sigma_1 & \sigma_6 & \sigma_5 \\ \sigma_6 & \sigma_2 & \sigma_4 \\ \sigma_5 & \sigma_4 & \sigma_3 \end{bmatrix}, \quad \varepsilon_{ij} = \begin{bmatrix} \epsilon_1 & 2\epsilon_6 & 2\epsilon_5 \\ 2\epsilon_6 & \epsilon_2 & 2\epsilon_4 \\ 2\epsilon_5 & 2\epsilon_4 & \epsilon_3 \end{bmatrix}. \tag{5.5}$$

In case of elastic distortions Hook's law says that the stress is linearly related to the strain

$$\sigma_{ij} = \sum_{k\ell} C_{ijk\ell} \epsilon_{k\ell}. \tag{5.6}$$

and the corresponding coefficient $C_{ijk\ell}$ is the 2nd-order elasticity stiffness tensor. The inverse of $C_{ijk\ell}$ is called the elastic compliance tensor. In the most general

case of no symmetry, the number of elements in the elastic tensor is 21. The amount of work made by an infinitesimal distortion $d\epsilon_i$ is written by

$$dU = \sigma_i d\epsilon_i = V \sum_j C_{ij}\epsilon_j d\epsilon_i. \tag{5.7}$$

Therefore

$$C_{ij} = \frac{1}{V}\frac{\partial}{\partial \varepsilon_j}\frac{\partial U}{\partial \varepsilon_i}, \tag{5.8}$$

which confirms also the symmetry of

$$C_{ij} = C_{ji}. \tag{5.9}$$

One writes the symmetric elastic tensor in a 6×6 matrix form using Voigt's notation as,

$$\begin{pmatrix} C_{11} & C_{12} & C_{13} & C_{14} & C_{15} & C_{16} \\ & C_{22} & C_{23} & C_{24} & C_{25} & C_{26} \\ & & C_{33} & C_{34} & C_{35} & C_{36} \\ & & & C_{44} & C_{45} & C_{46} \\ & & ... & & C_{55} & C_{56} \\ & & & & & C_{66} \end{pmatrix}. \tag{5.10}$$

This full matrix is for the triclinic crystal symmetry class, which has only one symmetry operation, the unitary operation.

Based on Eq.(5.7), the elastic energy of a solid can be given by

$$U = \frac{V}{2}\sum_{i=1}^{6}\sum_{j=1}^{6} C_{ij}\varepsilon_i\varepsilon_j = \frac{V}{2}\sum_{i=1}^{6}\sum_{j=1}^{6} S_{ij}\sigma_i\sigma_j. \tag{5.11}$$

5.3 Elastic moduli of polycrystalline materials

In the Voigt [116] approximation one assumes that the single crystal fibres are parallel to the stress axis subject to the same strain but with non-uniform stress, while the Reuss's assumption[115] means that the single crystal platelets are arranged in layers perpendicular to the stress axis with the uniform stress and non-uniform strain. The following expressions were obtained for the isotropic Polycrystalline elastic moduli:

$$\begin{aligned} B_V &= (1/3)(L + 2M), \\ G_V &= (1/5)(L - M + 3N). \end{aligned} \tag{5.12}$$

where

$$\begin{aligned} L &= (1/3)(C_{11} + C_{22} + C_{33}), \\ M &= (1/3)(C_{12} + C_{23} + C_{13}), \\ N &= (1/3)(C_{44} + C_{55} + C_{66}). \end{aligned} \tag{5.13}$$

and

$$\begin{aligned} B_R &= 1/(L^{'} + 2M^{'}), \\ G_R &= 5/(4L^{'} - 4M^{'} + 3N^{'}). \end{aligned} \tag{5.14}$$

where

$$\begin{aligned} L^{'} &= (1/3)(S_{11} + S_{22} + S_{33}), \\ M^{'} &= (1/3)(S_{12} + S_{23} + S_{13}), \\ N^{'} &= (1/3)(S_{44} + S_{55} + S_{66}). \end{aligned} \tag{5.15}$$

Furthermore, the Young's Modulus is defined as

$$E = \frac{9BG}{3B + G}. \tag{5.16}$$

The Poisson ratio ν is written as

$$\nu = \frac{3B - 2G}{6B + 2G}. \tag{5.17}$$

In fact, the real physical value of these moduli should lie between the Voigt and Reuss averages [115, 116]. Therefore an arithmetic average the Hill average is proposed [119].

$$\begin{aligned} B_H &= \frac{B_V + B_R}{2}, \\ G_H &= \frac{G_V + G_R}{2}. \end{aligned} \tag{5.18}$$

5.4 Elastic properties of cubic disordered structures

The substitutional disorder used in the SQS approach (Chapter 3) breaks, in general, the point group symmetry of the underlying lattice. However, experimental investigations show that the symmetry of anisotropic materials quantities may not be altered by subtitutional alloying, or one measures polycrystalline constants, because one has ceramics that are polycrystalline. For example, the elastic stiffness tensor of c-TiAlN solid solution preserves the cubic symmetry of the parent materials, c-TiN and c-AlN. A symmetry based projection technique has been suggested [103, 120] to derive accurate prediction of the elastic tensor of substitutional alloys. For example, the symmetry projected cubic elastic stiffness constants are calculated as arithmetic averages:

$$\begin{aligned} \bar{C}_{11} &= \frac{C_{11} + C_{22} + C_{33}}{3}, \\ \bar{C}_{12} &= \frac{C_{12} + C_{13} + C_{23}}{3}, \\ \bar{C}_{44} &= \frac{C_{44} + C_{55} + C_{66}}{3}, \end{aligned} \tag{5.19}$$

based on nine independent tensor elements: $C_{11}, C_{22}, C_{33}, C_{23}, C_{13}, C_{12}, C_{44}, C_{55}$ and C_{66}. A criterion for mechanical (not dynamical) stability of the crystal lattice is obtained from the condition that the energy density can be represented by

a quadratic form defined positive so that the energy increases with any small deformation. Thus, the stability criteria of cubic crystals are given by:

$$\bar{C}_{44} > 0,\ \bar{C}_{11} > |\bar{C}_{12}|,\ \bar{C}_{11} + 2\bar{C}_{12} > 0. \tag{5.20}$$

Cauchy relations are known as the relations between elastic constants [121]. In cubic case, it is $\bar{C}_{12} = \bar{C}_{44}$. The deviation from Cauchy relations indicates the deviation from the assumption of central forces.

A measure of elastic anisotropy can be given by:

$$\bar{A} = 2\bar{C}_{44}/(\bar{C}_{11} - \bar{C}_{12}). \tag{5.21}$$

and the directional dependence of the Young's modulus [122] is written as

$$\frac{1}{\bar{E}_{\ell_1\ell_2\ell_3}} = \bar{S}_{11} - 2(\bar{S}_{11} - \bar{S}_{12} - \frac{1}{2}\bar{S}_{44})(\ell_1^2\ell_2^2 + \ell_2^2\ell_3^2 + \ell_1^2\ell_3^2). \tag{5.22}$$

The 3-tuple(ℓ_1, ℓ_2, ℓ_3) stands for the directional cosines to the x, y and z coordinate axes.

For cubic crystals, the polycrystalline elastic moduli are calculated using the expressions:

$$\begin{aligned}
&B_V = B_R = \frac{\bar{C}_{11} + 2\bar{C}_{12}}{3}, \quad B_H = \frac{B_V + B_R}{2},\\
&G_V = \frac{(\bar{C}_{11} - \bar{C}_{12} + 3\bar{C}_{44})}{5}, \quad G_R = \frac{5\bar{C}_{44}(\bar{C}_{11} - \bar{C}_{12})}{4\bar{C}_{44} + 3(\bar{C}_{11} - \bar{C}_{12})}, \quad G_H = \frac{G_V + G_R}{2},\\
&E = \frac{9B_HG_H}{3B_H + G_H}, \quad \nu = \frac{3B_H - 2G_H}{6B_H + 2G_H}.
\end{aligned} \tag{5.23}$$

5.5 Elastic Young's modulus of multilayers

A linear-elasticity model of multilayers has been established with neglecting the interfacial heterogeneity [123]. Within our sharp interface approximation (see section 3.2), an analytic formula can be derived for the elastic stiffness constants of superlattices C_{ij}^{SL}. We assume that the superlattice is built from the materials denoted by 1 and 2. The fractions of materials 1 and 2 in the superlattice are written as f_1 and f_2. The stress and strain of the superlattice can be expressed as a function of the stress and strain of the individual layers:

$$\sigma = f_1\sigma_1 + f_2\sigma_2, \mu = f_1\mu_1 + f_2\mu_2, \tag{5.24}$$

The constituent relations in each layer are

$$\sigma_i = C_i\mu_i, i = 1, 2. \tag{5.25}$$

The effective elastic constant matrix of the superlattice is defined as

$$\sigma = C\mu. \tag{5.26}$$

Thus, the elastic stiffness constants of the superlattice are:

$$C^{\mathrm{SL}} = (f_1 \bar{C}_1^{\vec{n}} M + f_2 \bar{C}_2^{\vec{n}})(f_1 M + f_2 I)^{-1}, \tag{5.27}$$

where the interface normal vector is $\vec{n}$,

$$M = P_1^{-1} P_2, \quad P_\alpha = \begin{pmatrix} 1 & 0 & 0 & 0 & 0 & 0 \\ 0 & 1 & 0 & 0 & 0 & 0 \\ & & \left(\bar{C}_\alpha^{\vec{n}} \right)_{\substack{31\cdots36 \\ 41\cdots46 \\ 51\cdots56}} & & & \\ 0 & 0 & 0 & 0 & 0 & 1 \end{pmatrix}_{6\times6} \tag{5.28}$$

The Young's modulus of the multilayer in the normal direction to the interface is then given by

$$E_{\vec{n}} = 1/S_{33}^{\mathrm{SL}} = \frac{C_{33}^{\mathrm{SL}}(C_{11}^{\mathrm{SL}} + C_{12}^{\mathrm{SL}}) - 2C_{13}^{\mathrm{SL}} C_{13}^{\mathrm{SL}}}{C_{11}^{\mathrm{SL}} + C_{12}^{\mathrm{SL}}}. \tag{5.29}$$

CHAPTER 6

Density Functional Theory

Density functional theory (DFT) is an exact approach to solve the quantum mechanical many body problem. The non-relativistic time-dependent Schrödinger equation

$$i\frac{\mathrm{d}\Psi}{\mathrm{d}t} = \hat{H}\Psi \tag{6.1}$$

gives the description of the dynamical behavior of a quantum system. $\hat{H}$ is the Hamiltonian of the system which is written in the case of a system of electrons and nuclei as

$$\hat{H} = -\frac{1}{2}\sum_i \nabla_i^2 - \sum_I \frac{1}{2M_I}\nabla_I^2 + \frac{1}{2}\sum_{i\neq j}\frac{1}{|\mathbf{r}_i - \mathbf{r}_j|} + \frac{1}{2}\sum_{I\neq J}\frac{Z_I Z_J}{|\mathbf{R}_I - \mathbf{R}_J|} - \sum_{i,I}\frac{Z_I}{|\mathbf{r}_i - \mathbf{R}_I|}. \tag{6.2}$$

where the terms represent the kinetic energy of the electrons and the nuclei as well as the Coulomb interactions between electrons, nuclei and between electrons and nuclei. M_I denotes the mass of the nuclei. $\mathbf{r}_i$ are the positions for the electrons. $\mathbf{R}_I$ and Z_I stand for the positions and the charge number of the nuclei. For this Hamiltonian, the state of the system, the wave function is written as

$$\Psi = \Psi(\mathbf{r}_1, \mathbf{r}_2, \mathbf{r}_3, ..., \mathbf{r}_N, \sigma_1, \sigma_2, \sigma_3, ..., \sigma_N, \mathbf{R}_1, \mathbf{R}_2, \mathbf{R}_3, ..., \mathbf{R}_N, t). \tag{6.3}$$

where σ_i are the spin variables of the electrons.

The stationary states of the system are the eigen solutions of the time-independent Schrödinger equation, which can be written as

$$\hat{H}\Psi = E\Psi. \tag{6.4}$$

Eq.(6.2) has too many variables to solve it exactly and therefore approximations are essential in order to simplify the task. Since the nuclei are much heavier than

the electrons, they move much slower and can be considered as "frozen" particles. This approximation is called Born-Oppenheimer approximation [124], in which one decouples the electronic freedoms from the freedoms of nuclei motion. Then the kinetic energy of the nuclei is constant and the Coulomb interactions between nuclei contribute as a constant term, which we can exclude when solving Eq.(6.4). The electron-nuclei interaction is then treated as an external field for the electrons. Therefore, the Hamiltonian of the electrons is given as

$$\hat{H}_{elec} = -\frac{1}{2}\sum_i \nabla_i^2 + \frac{1}{2}\sum_{i\neq j}\frac{1}{|\mathbf{r}_i - \mathbf{r}_j|} - \sum_{i,I}\frac{Z_I}{|\mathbf{r}_i - \mathbf{R}_I|}. \tag{6.5}$$

In case of periodical systems, the wave function solutions to the Shrödinger equation has the form

$$\psi_{n\mathbf{k}}(\mathbf{r}) = e^{i\mathbf{k}\cdot r}u_{n\mathbf{k}}(\mathbf{r}). \tag{6.6}$$

where n is the quantum number, k is a reciprocal vector, $e^{i\mathbf{k}\cdot r}$ describes a plane wave and $u_{n\mathbf{k}}(\mathbf{r})$ is a function with the periodicity of the lattice. Even though the many body problem has been much simplified with all these approximations, solving the Schrödinger equation directly is still not practical. Hence, more reformulation of the problem should be done.

6.1 Hohenberg-Kohn theorems

The general idea of density functional theory (DFT) is to use the real electron density $n(\mathbf{r})$ as a basic variable instead of the complex wave function Eq.(6.3). The first attempt is known as Thomas-Fermi theory [125, 126], which was based on the density of a homogeneous electron gas for the kinetic energy and neglected both exchange and correlations among the electrons. Although Dirac extended the method with an approximation for the exchange [127], the theory was still inaccurate in most applications. In 1964, Hohenberg and Kohn [128] formulated two theorems, that have established the basis of modern density functional theory. The two theorems are stated as follows:

Theorem 1 *For any system of interacting particles in an external potential $V_{ext}(\mathbf{r})$, the potential $V_{ext}(\mathbf{r})$ is uniquely determined, except an additive constant, by the ground state particle density $n_0(\mathbf{r})$.*

Theorem 2 *A universal functional for the energy $E[n]$ in terms of the density $n(\mathbf{r})$ can be defined, valid for any external potential $V_{ext}(\mathbf{r})$. For any particular $V_{ext}(\mathbf{r})$, the exact ground state energy of the system is the global minimum value of this functional, and the density $n(\mathbf{r})$ that minimizes the functional is the exact ground state density $n_0(\mathbf{r})$.*

It is clear that the energy functional $E[n]$ determines the exact ground state energy and density, then the external potential on individual electrons is also obtained and with that all properties of the system can be derived. Therefore all that is needed is the energy functional $E[n]$. Its general form is written as:

$$E[n] = T[n] + E_{int}[n] + \int d\mathbf{r}V_{ext}(\mathbf{r})n(\mathbf{r}) + E_{ion-ion}. \tag{6.7}$$

where the terms on the right are the kinetic energy of the electrons, the interaction energy between the electrons, the Coulomb interaction energy of electron density $n(\mathbf{r})$ with the external potential and the interaction energy between the nuclei. However, the forms of $T[n]$ and $E_{int}[n]$ are not known and a practical scheme is needed to solve the problem.

6.2 Kohn-Sham equation

Kohn and Sham [129] proposed replacing the interacting many-body system with non-interacting particles that move in an effective external field and have the same ground state density as the real system. The total energy of this non-interacting particles can be expressed with the density:

$$E_{KS}[n] = T_s[n] + \int d\mathbf{r} V_{ext}(\mathbf{r}) n(\mathbf{r}) + E_{Hartree}[n] + E_{xc}[n] + E_{ion-ion}. \tag{6.8}$$

where $T_s[n]$ is the kinetic energy of the non-interacting particles, given by:

$$T_s[n] = -\frac{1}{2}\sum_{i=1}^{N}\langle\psi_i|\nabla^2|\psi_i\rangle. \tag{6.9}$$

The electron density $n(\mathbf{r})$ in a system with N non-interacting electrons can be calculated as:

$$n(\mathbf{r}) = \sum_{i=1}^{N}|\psi_i(\mathbf{r})|^2. \tag{6.10}$$

The effective potential acting on the non-interacting particles is

$$V_{eff}(\mathbf{r}) = V_{ext}(\mathbf{r}) + \int d\mathbf{r}' \frac{n(\mathbf{r}')}{|\mathbf{r}-\mathbf{r}'|} + V_{xc}(\mathbf{r}). \tag{6.11}$$

The first term is the external potential, the second term is the Hartree potential describing the Coulomb interaction of an electron with a charge distribution $n(\mathbf{r})$, and the last term is the exchange-correlation potential:

$$V_{xc}(\mathbf{r}) = \frac{\delta E_{xc}[n(\mathbf{r})]}{\delta n(\mathbf{r})}. \tag{6.12}$$

ψ_i are the solutions of the single-particle Schödinger-like equation:

$$(-\frac{1}{2}\nabla^2 + V_{eff}(\mathbf{r}))\psi_i(\mathbf{r}) = \epsilon_i\psi_i(\mathbf{r}). \tag{6.13}$$

where ϵ_i is the eigenvalue of the non-interacting single particle.

$E_{Hartree}[n]$ is the Coulomb electrostatic potential energy of the electron density $n(\mathbf{r})$ with itself:

$$E_{Hartree}[n] = \frac{1}{2}\int\int d\mathbf{r}d\mathbf{r}' \frac{n(\mathbf{r})n(\mathbf{r}')}{|\mathbf{r}-\mathbf{r}'|}. \tag{6.14}$$

The trick is that those terms that vanish in a non-interacting, independent particle system are collected into an energy functional called exchange-correlation energy $E_{xc}[n]$.

6.3 Exchange-correlation functionals

The simplest form of the exchange-correlation functional is the Local Density Approximation (LDA), first suggested in the original paper by Kohn and Sham. [129] The basic assumption is that the exchange-correlation energy at each spatial point $\mathbf{r}$ in space is equal to the exchange-correlation energy of a homogenous electron gas with the density $\epsilon_{xc}^{hom}(n(\mathbf{r}))$. The LDA exchange-correlation functional is thus calculated as:

$$E_{xc}^{LDA}[n] = \int d\mathbf{r} n(\mathbf{r}) \epsilon_{xc}^{hom}(n(\mathbf{r})). \tag{6.15}$$

LDA is very accurate for the system with spatially slowly varying densities [130]. However, a weakness of LDA calculations is the overestimate of $E_{xc}[n(\mathbf{r})]$ for many systems resulting in underestimated lattice parameters, which may give rise to erroneous predictions of the ground state structure. The most cited failure of LDA is for Fe, the prediction of the ground state structure is non-magnetic face-centered cubic (fcc), while in fact from experiments it is ferromagnetic body-centered cubic (bcc) [131]. Furthermore, LDA does not work for weak induced dipole-dipole interactions, such as Van der Waal's interactions.

An improvement of the LDA approximation is the Generalized Gradient approximation (GGA) [132],

$$E_{xc}^{GGA}[n] = \int d\mathbf{r} n(\mathbf{r}) \epsilon_{xc}(n(\mathbf{r}), \nabla n(\mathbf{r})). \tag{6.16}$$

which takes into account not only the density $n(\mathbf{r})$ but also the density gradient ∇n. The GGA approximation tends to underbind and it usually gives larger lattice constants compared to those obtained from experiments.

6.4 Basis sets

To solve the Kohn-Sham equations Eq.(6.13) numerically, the single-particle wavefunctions $\psi_i(\mathbf{r})$ need to be represented by a basis set. For crystalline solids, the atomic structure is periodic, a suitable choice of basis set is plane waves. However, $\psi_i(\mathbf{r})$ changes rapidly near the nuclei which requires a huge number of plane waves with high cutoff energy resulting in a very expensive computational cost.

The pseudopotential method [133, 134] is one attempt to solve the problem. The idea is to substitute the strong Coulomb potential by an effective ionic potential acting on the valence electrons, thus reducing the basis set size and computational time. The pseudopotential is constructed to provide the scattering properties of the core region and outside some cutoff radius, both the behavior of the valence wave functions and the effective potentials have to be the same as the exact ones. Norm-conserving [135] and Ultrasoft [136] pseudopotentials are two common used pseudopotentials.

An extension of the pseudopotential approach is the projector augmented wave (PAW) method, originally introduced by Blöchl [137] and further expanded by

Kresse [138]. It is an all-electron method which retains the wave functions of the core states as well as applying the frozen core approximation. The full real electron wave function $\psi_i(\mathbf{r})$ is still available for total energy evaluations, the reliability and transferability of the potentials is thus increased.

In connection with the Coherent potential approximation (CPA), see Chapter 3, the Linear Muffin-Tin Orbital (LMTO) method [139] is used. The energy linearization of the Muffin-Tin Orbitals is put into a Hamiltonian formalism. The localized LMTO basis set, so called tight binding-LMTO was introduced by Andersen *et al* in 1984 [140]. The minimal basis produces a small Hamiltonian matrix, which makes calculations more efficient.

CHAPTER 7

Results

7.1 Thermodynamics stability

7.1.1 Mixing thermodynamics of cubic $Ti_{1-x}Al_xN$/TiN(001) multilayers

Experimental results show extended age hardening by the spinodal decomposition of $Ti_{1-x}Al_xN$, the role of lattice coherency and interfacial chemistry on the driving force of this decomposition process is unexplored. Motivated by this, we choose cubic (B1) $Ti_{1-x}Al_xN$/TiN(001) multilayers as an example to investigate the mixing thermodynamics. Modeling alloys in multilayers and the calculation of mixing enthalpy in the $Ti_{1-x}Al_xN$/TiN(001) multilayer are introduced in details in Chapter 3.2,1 and 4.2. Here we discuss the multilayers with two different periodicities: 6 layers of $Ti_{1-x}Al_xN$ followed by 6 layers of TiN and 12 layers of $Ti_{1-x}Al_xN$ followed by 6 layers of TiN.

The calculated mixing enthalpy values of $Ti_{1-x}Al_xN$ in multilayers (MLs) are shown in Figure 7.1, compared with the values obtained for the monolithic, bulk $Ti_{1-x}Al_xN$ case. The values are positive indicating a thermodynamic driving force towards phase separation. The ML curves show the same asymmetric tilting to higher compositions as in bulk $Ti_{1-x}Al_xN$. The multilayer mixing enthalpies are significantly suppressed with respect to bulk values, which means that the multilayer structure has a stabilization effect on $Ti_{1-x}Al_xN$. The decrease in the thicker 12/6 multilayer is smaller as the overall system is closer to bulk $Ti_{1-x}Al_xN$. We propose that the stabilization effect can be split into a strain and an interfacial (or chemical) contribution, and both contributions are significant.

A method of calculating coherency strain effect on the mixing enthalpy is proposed, both the coherent in-plane lattice parameters and the modified lattice struc-

ture along the (001) growth direction are considered. The mixing enthalpy with the coherency strain effect is shown in Figure 7.1. It is clear that the strain effect stabilizes the alloy, but does not give the full decrease of the mixing enthalpy. The rest of the stabilization effect is defined as the local interfacial or chemical contribution.

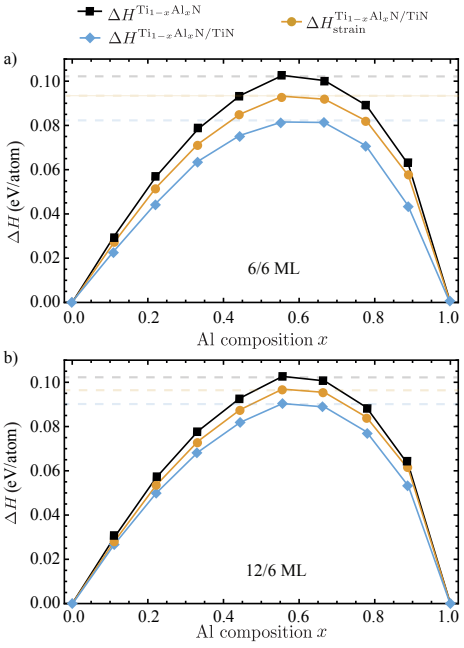

Figure 7.1. The mixing enthalpy of bulk $Ti_{1-x}Al_xN$(*ab initio*), the mixing enthalpy with the coherency strain effect and the mixing enthalpy(*ab initio*) of $Ti_{1-x}Al_xN/TiN$ multilayer(ML). (a)6/6 ML (b)12/6 ML. The horizontal dashed lines show the maximum of the mixing enthalpy values for the bulk and the different multilayer cases.

The atomic relaxations were calculated and compared to the situation in bulk to see the effect of interfaces. With altered relaxations one expects a change in the effective cluster interactions. Figure 7.2 shows the relaxations of the N atoms along the z directions in each layer. The z coordinate is chosen because it is the interface orientation. The N atoms are distinguished by the different first neighborhood: Al-N-Al, Ti-N-Al, and Ti-N-Ti. The average shift of the relative distortions, shown by red line, gives that the TiAlN slab shrinks along z, while the TiN slab expands. The internal, sub-plane with the N atoms surrounded only by Al atoms (noted as Al-N-Al) has the largest shift. The Ti atoms in the TiN slab scatter wider in z direction than in x direction. The average relaxation of the Ti atoms does not follow the common trend which is the fitted straight line. For example, the Ti atoms in the last layer of the TiAlN slab have an increased amount of Ti first neighbors from layer 7 (TiN slab), which results in a stronger binding between the two layers via the Ti-d orbitals. Figure 7.3 shows the Ti-site d-orbital partial

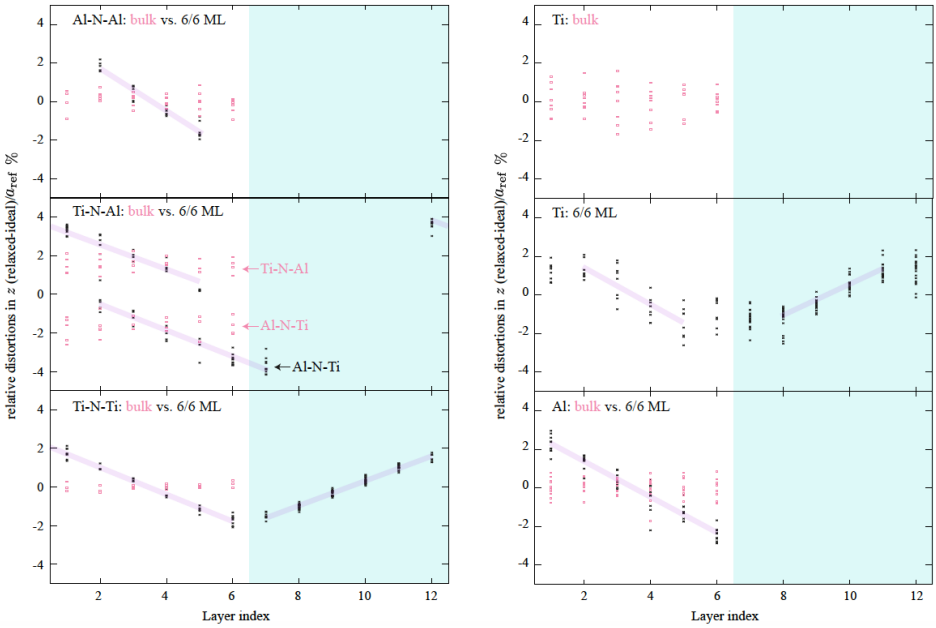

Figure 7.2. The atomic relaxations of the N atoms with different type of neighbors(Al-N-Al, Ti-N-Al, Ti-N-Ti)d and the relaxations of the Ti and Al atoms along z direction. The atomic relaxations are with respect to the ideal positions in each layer for x= 0.55 of bulk $Ti_{1-x}Al_xN$ and 6/6 ML.

density of states (PDOS) at the Fermi energy of the $Ti_{1-x}Al_xN$ slabs in the 6/6 ML compared with the ones obtained in the bulk. In the multilayer form, one has lower PDOS values which means an increased Ti-Ti hybridization. Compared to the bulk, the electronic stabilization effect in the multilayer increases more with increasing the Al content, which correlates with the decreased tendency toward decomposition.

7.1.2 Thermal stability of TiN/AlN and ZrN/AlN

To explore the effect of forming semicoherent interfaces during film growth on the thermodynamic stability of multilayers, we propose to grow TiN or ZrN on AlN within different interfaces: cubic-(100)//cubic-(100), cubic-(110)//wurtzite-(10-10), cubic-(111)//cubic-(111) and cubic-(111)//wurtzite-(0001). Figure 7.4 shows that for both TiN/AlN and ZrN/AlN, the relative energy difference is low between isostructural coherent interfaces c-(100)//c-(100) and c-(111)//c-(111). The semicoherent interface, c-(110)//w-(10-10) is favorable for ZrN/AlN but not for TiN/AlN. c-(111)//w-(0001) is energetically the most favorable interface for both material systems. Compared to isostructural coherent interfaces, the semicoherent interfaces have higher thermodynamic stability for ZrN/AlN, which matches the experimental observation of a high thermal stability of the film containing

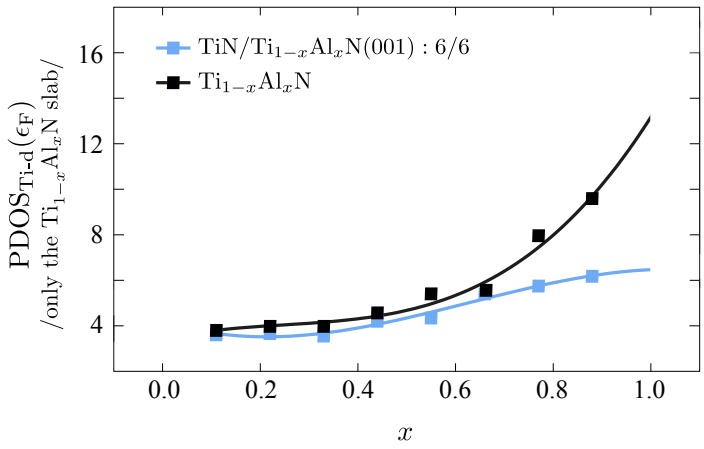

Figure 7.3. Bulk and the 6/6 multilayer *d*-orbital partial density of states (PDOS) at the Fermi energy (ϵ_F) of the Ti atoms from only the $Ti_{1-x}Al_xN$ slab.

semicoherent interfaces.

We also find that for TiN/AlN, the strain values are largest in case of c-(110)//w-(10-10) and smallest for c-(111)//w-(0001). For ZrN/AlN, the largest strain is found for isostructural c-(100)//c-(100) and c-(111)//c-(111) interfaces, followed by c-(110)//w-(10-10) and smallest for c-(111)//w-(0001) interface. One can conclude that the higher thermodynamic stability of c-(111)//w-(0001) interface is related to the lower misfit strain, and the fact that AlN is in the stable wurtzite structure.

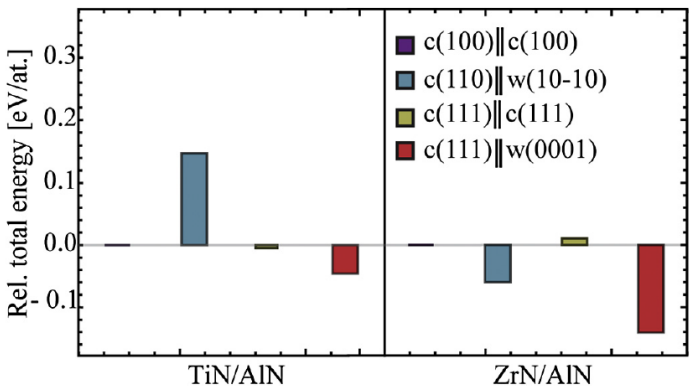

Figure 7.4. Ab-initio calculated total energy divided by 192 atoms (eV/atom) relative to c-(100)[001]//c-(100)[001] for TiN/AlN and ZrN/AlN multilayer.

7.2 Elastic properties

7.2.1 Alloys

In Chapter 5, the symmetry projected cubic elastic stiffness constants are introduced and the polycrystalline elastic moduli can be calculated. Cauchy pressure ($\bar{C}_{12} - \bar{C}_{44}$) indicates the character of atomic bonds, if it is negative the bonding is directional, while a positive value means delocalized rather metallic bonds. Figure 7.5 shows G/B values and Cauchy pressure map of ternary $X_{0.5}Al_{0.5}N$ (1), $X_{0.5}Ti_{0.5}N$ (3) and quaternary alloys $X_{0.33}Ti_{0.33}Al_{0.33}N$ (2) where X can be Zr, Hf, V, Nb and Ta. Cubic AlN has covalent bonding and highly brittle behavior while cubic TaN is found as metallic and ductile material. Increased ductility is observed along the (0)-(2)-(3) lines and it is more clear for X from the VB metals than for IVB ones. The same behavior is noticed along the (0)-(2)-XN lines. Furthermore, ductility increases with the monotonous increase of the period number which means 3*d* valence orbitals to 5*d* ones. Decreasing Cauchy pressure indicates tendency toward stronger covalency in the atomic bonds, which results in increased resistance against shearing. The changes of shear modulus values G correlate with the Cauchy pressure values.

To have a vivid picture of the elastic anisotropy, the directional dependence of the Young's modulus in each quaternary alloy is shown in Figure 7.6. A totally isotropic system would have a spherical shape, and the degree of geometric deviation from a sphere indicates the degree of anisotropy in a specific property of the system. The shapes of $Zr_{0.33}Ti_{0.33}Al_{0.33}N$, $Hf_{0.33}Ti_{0.33}Al_{0.33}N$, $V_{0.33}Ti_{0.33}Al_{0.33}N$ are a sphere, while there are deviations from sphere for the other phases. Such a feature of the E shapes can be explained from considering significant difference in the nature of bonding behaviors with different components in the system.

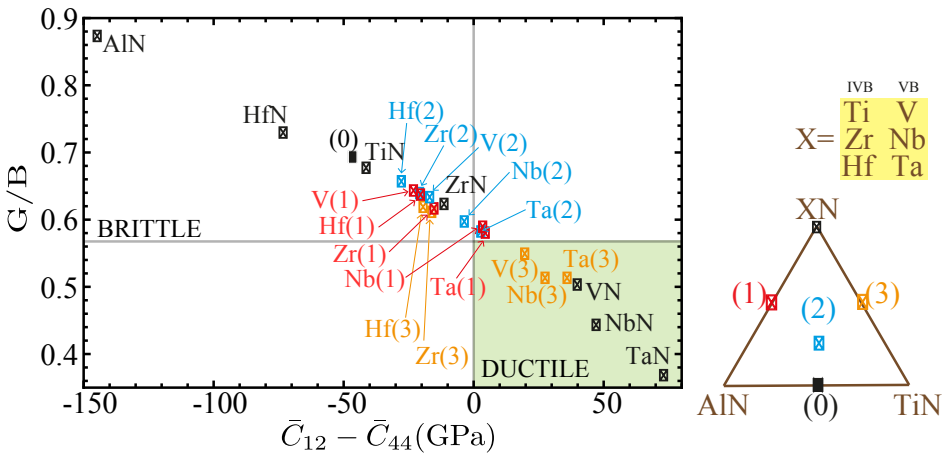

Figure 7.5. The G/B vs. Cauchy pressure map of quaternary $X_yTi_{(1-x-y)}Al_xN$ alloys where X is Zr, Hf, V, Nb and Ta.

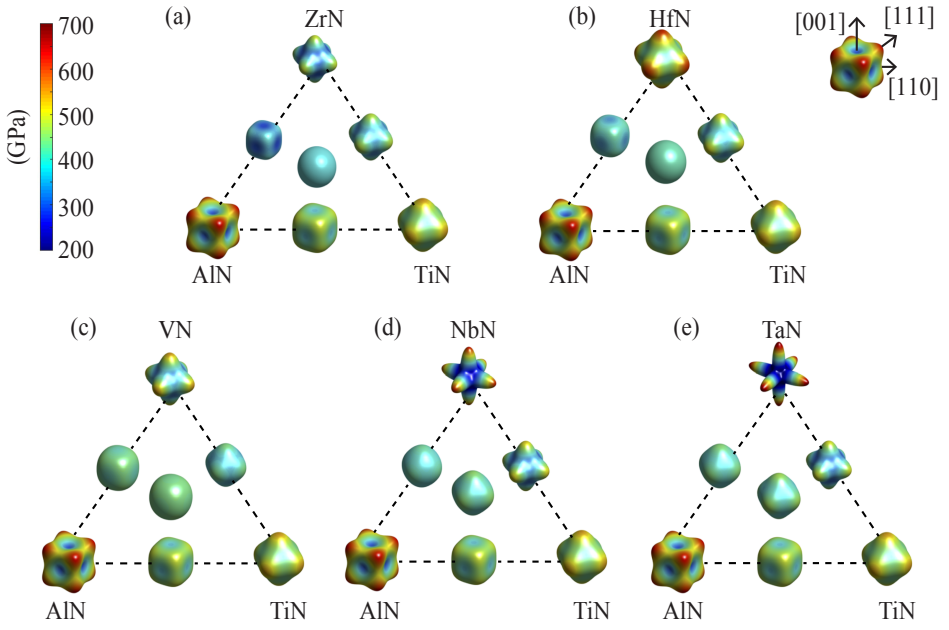

Figure 7.6. Three dimensional distribution of the Young's modulus in the quaternary $X_yTi_{(1-x-y)}Al_xN$ alloys where X is Zr, Hf, V, Nb and Ta.

7.2.2 Multilayers

The elastic constants of a multilayer are derived using the linear-elasticity model of superlattices in Chapter 5.5. The Young's modulus in the normal direction to the interface $E_{\vec{n}}$ of ternary and quaternary alloys coherently multilayered with TiN and ZrN binaries is shown in Figure 7.7. The values are for 1:1 fraction of the materials in the multilayer. $E_{\vec{n}}$ correlate with the ones in Figure 7.6 for all alloys and for both interfaces. The alloys multilayered with ZrN has lower Young's modulus values than the alloys multilayered with TiN. Due to the largest Young's modulus of HfN along [111] in Figure 7.6, HfN contained alloys in the (111) multilayers behave distinguished. Furthermore, $E_{\vec{n}}$ decreases with increasing TiN content with [111] interfacial orientation while it increases with increasing TiN content in [001] oriented multilayers. The high Young's modulus of all the transition metal nitrides in the dominant [001] direction determines the strength of the multilayers and therefore Young's modulus values are high for (001) multilayers, which we can conclude that one can estimate the variation of $E_{\vec{n}}$ based on Figure 7.6. Moreover, the multilayers with [111] orientations become more ductile with increasing TiN content while the increase of the $E_{\vec{n}}$ values with the TiN content in the (001) multilayers results in larger G/B values, which predicts increased brittleness.

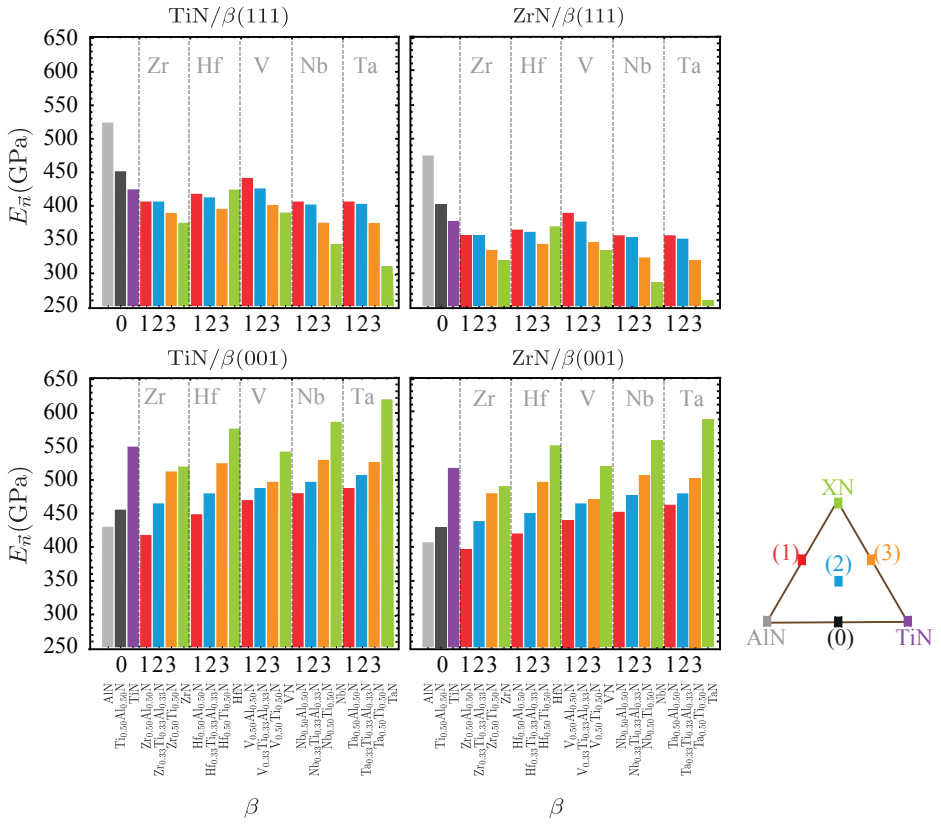

Figure 7.7. The Young's modulus perpendicular to the interface in coherent (001) and (111) directional TiN/XTiAlN and ZrN/XTiAlN multilayers where X is Zr, Hf, V, Nb and Ta. The values are give in GPa.

7.3 Application of Debye model on multicomponent nitride alloys

7.3.1 $Ti_xNb_yAl_zN$ alloys

With the method introduced in Chapter 3.3 and Chapter 4.3, the effect of NbN alloying on the high temperature behavior of $Ti_{0.5}Al_{0.5}N$ thin films is investigated. The mixing Gibbs free energy of cubic $Ti_xNb_yAl_zN$ (where $z = 1 - x - y$) alloys is calculated relative to the cubic B1 phases of TiN, NbN, and AlN at 1100 K, which is shown in Figure 7.8. The mixing free energy of NbAlN and TiAlN is positive for all compositions, while it is negative for TiNbN, which indicates that NbAlN and TiAlN alloys are thermodynamically unstable and TiNbN is thermodynamically stable. The fact that NbAlN is unstable with a maximum in the Al rich end and TiNbN is stable with a minimum at equal Nb and Ti contents, determines the topology of the mixing Gibbs free energy surface. The mixing Gibbs free energy

has a small positive value and it is in between two distinct free energy regions with positive and negative values of the mixing free energy. In this particular region the thermodynamic driving force (energy difference - chemical potential) is the same but with distinguished local environment or second derivative (topology). It is also clear from Figure 7.8 (a) that the inclusion of the vibrational contribution stabilizes the solid solution.

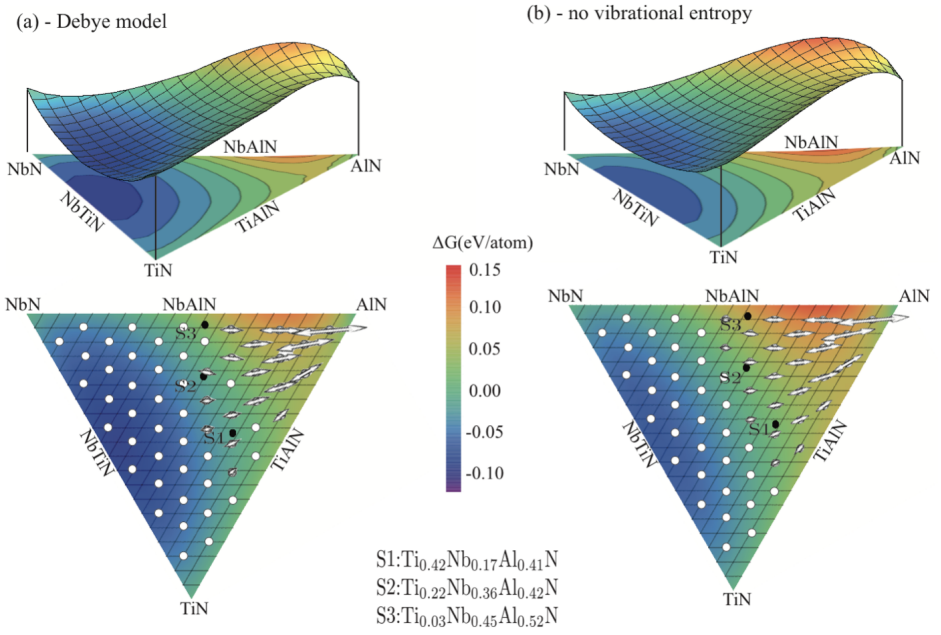

Figure 7.8. The mixing free energy surface ΔG with arrows showing the local tendencies for spinodal decomposition in cubic $Ti_xNb_yAl_zN$ at 1100 K. (a) shows ΔG with the inclusion of phonon contribution approximated through the Debye model while (b) displays ΔG with configurational entropy only. The arrows represent the most favorable directions of local spinodal decomposition. The lengths of the arrows are proportional to the magnitudes of the second derivatives, which indicate the strength of the decomposition. In the low Al content part of the diagram where the alloy is stable, there is no driving force for spinodal decomposition, which is marked by open circles.

For multicomponent alloys, to predict their mixing thermodynamics at high temperature, one needs an effective approach. Figure 7.9 shows the mixing energetics of $Ti_{1-x}Al_xN$ solid solutions calculated at 1500 K. In a) one sees a comparison of the Gibbs free energy obtained by TDEP (the temperature dependent effective potential method which includes the effects of anharmonicity) and by the quasi-harmonic Debye model using elastic constants calculated for x = 0.0, 0.5 and 1.0 at 0 K. In b) one sees the vibrational contribution to G_{mix} in both, TDEP and the quasi-harmonic Debye model. It underlines that Debye model can be assumed to greatly increase the efficiency of simulations and work fine for the class of multicomponent nitride coatings.

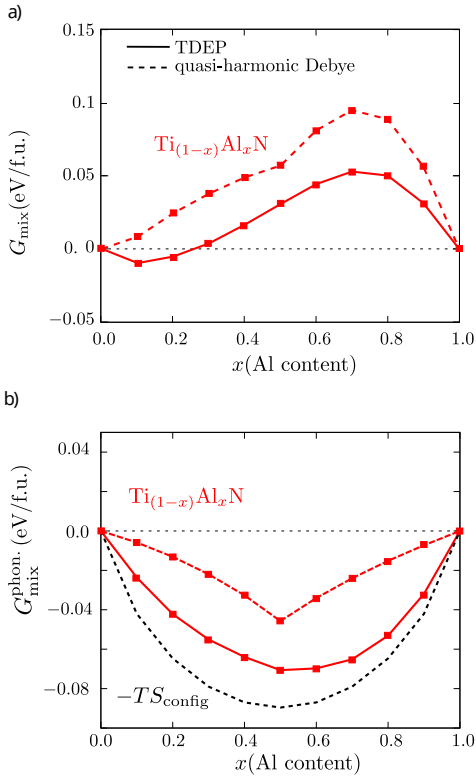

Figure 7.9. Mixing energetics of $Ti_{1-x}Al_xN$ solid solutions calculated at 1500 K. a) shows G_{mix} obtained by TDEP method with solid lines and the dashed lines show the results of the quasi-harmonic Debye model. In b) the lines display the vibration contribution to G_{mix} in both, TDEP and the present quasi-harmonic Debye model with elastic constants calculated for $x = 0.0$, 0.5 and 1.0.

Spinodal decomposition will occur if the second derivative of Gibbs free energy is negative. For a ternary alloy, a two-dimensional second directional derivative should be considered for determining the local spinodal decomposition behavior and the decomposition will start in the direction with the largest negative value of the second derivative. The spinodal decomposition trends of $Ti_xNb_yAl_zN$ alloys are shown in Figure 7.8 with arrows. It is interesting that vibrational contribution strongly affects the thermodynamic stability of the solution phases, but not the favorable local tendencies for the spinodal decomposition. Three experimental samples, S1: $Ti_{0.42}Nb_{0.17}Al_{0.41}N$, S2: $Ti_{0.22}Nb_{0.36}Al_{0.42}N$, S3: $Ti_{0.03}Nb_{0.45}Al_{0.52}N$ were deposited in the interesting region. The arrows sizes are slowly changing in the vicinity of S1 while they show a more significant variations around S3. It suggests different thermal stabilities against spinodal decomposition for the samples. The calculations indicate that rapid low temperature spinodal decomposition should occur in S3, which results in significant age hardening though with low temperature stability. For S1 high temperature stability is predicted, higher than for

S2 and S3. Furthermore, no TiN and NbN are expected during the decomposition.

7.3.2 Thermal expansion coefficients of $Ti_{1-x-y}X_yAl_xN$ (X = Zr, Hf, Nb, V, Ta)

In Paper VI, the thermal expansion coefficients (TEC) of multicomponent cubic nitride alloys $Ti_{1-x-y}X_yAl_xN$ (X=Zr, Hf, Nb, V, Ta) are predicted with the quasi-harmonic Debye approximation of phonons through the ab initio calculated 0K elastic constants. A direct benchmark of the approximation against TDEP in predicting TEC has been shown with TiN and $Ti_{1-x}Al_xN$.

The linear thermal expansion coefficients of cubic quaternary $Ti_{1-x-y}Hf_yAl_xN$ and $Ti_{1-x-y}Ta_yAl_xN$ solid solutions at 600, 900 and 1200K with the quasi-harmonic Debye approximation are shown in Figure 7.10. The values increase with the temperature and present a monotonous increase with X amount at all temperatures in $Ti_{1-x-y}Ta_yAl_xN$. For $Ti_{1-x-y}Hf_yAl_xN$ alloys, the highest value of TEC is shown in the Al rich vicinity of $Hf_{0.5}Al_{0.5}N$.

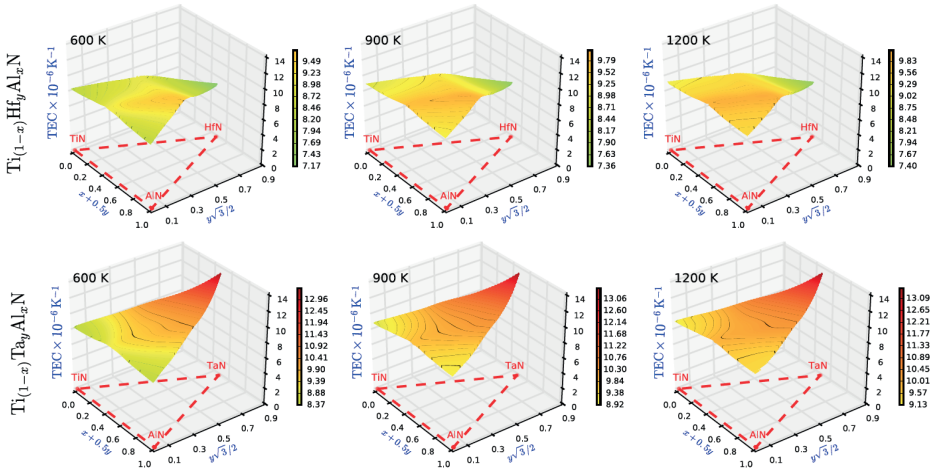

Figure 7.10. The linear thermal expansion coefficients (TEC) of cubic quaternary $Ti_{1-x-y}Hf_yAl_xN$ and $Ti_{1-x-y}Ta_yAl_xN$ solid solutions at 600, 900 and 1200K with the Debye approximation.

CHAPTER 8

Conclusions and Outlook

My research presented here has explored the most important properties of nitride alloys for high-temperature industrial cutting applications. I illustrated the power of theoretical investigations as guidance to tailor design novel materials and consolidate the motto "The right material for right application".

We demonstrate that $Ti_{1-x}Al_xN$ solid solution is stabilized by interfacial effects if it is coherently sandwiched between TiN layers along (001). Motivated by this, I would investigate the thermodynamics in case of semicoherent multilayers.

The Debye model is used in this thesis to reveal the high-temperature thermodynamics and spinodal decomposition of $Ti_xNb_yAl_{1-x-y}N$ and predict the thermal expansion coefficients of $Ti_xX_yAl_{1-x-y}N$ (X=Zr, Hf, Nb, V, Ta). The impact of phonons on the mixing energetics and the thermal expansion of multilayers are expected to be captured with reasonable (for industry) accuracy by the efficient quasi-harmonic Debye model. A fairly complex project would be to establish a simulation framework in which one considers a finite interfacial thickness (2-3 nm) with compositional profile that is observed by atom probe tomography.

We also calculated the elastic constants of cubic $Ti_xX_yAl_{1-x-y}N$ (X=Zr, Hf, Nb, V, Ta) solid solutions and their multilayers. An analytic comparison of strengths and ductility is presented to reveal the potential of these materials in hard coating applications. A linear-elasticity model of superlattices instead of performing computationally demanding calculations is proposed to derive the elastic constants and obtain the Young's modulus, which is one of the important engineering parameter for experiments. In the next step, this method could be applied to other superlattices. It is also possible to develop a further model on multilayers including disordered alloys.

Bibliography

[1] Materials Genome Initiative. 2011. URL: https://www.mgi.gov/.

[2] Novel Materials Discovery. 2015. URL: https://www.nomad-coe.eu/.

[3] A. Knutsson et al. "Thermally enhanced mechanical properties of arc evaporated $Ti_{0.34}Al_{0.66}N$/TiN multilayer coatings". In: *J. Appl. Phys.* 108.4 (2010), p. 044312.

[4] Jeffrey H. Nguyen and Neil C. Holmes. "Melting of iron at the physical conditions of the Earth's core". In: *Nature* 427 (2004), pp. 339–342.

[5] A. Hörling et al. "Thermal stability of arc evaporated high aluminum-content $Ti_{1-x}Al_xN$ thin films". In: *J. Vac. Sci. Technol. A Vacuum, Surfaces, Film.* 20.5 (2002), p. 1815.

[6] Staffan Söderberg. "Advances in coating technology for metal cutting tools". In: *Met. Powder Rep.* 56.4 (2001), pp. 24–30.

[7] Wolf-Dieter Münz. "Titanium aluminum nitride films: A new alternative to TiN coatings". In: *J. Vac. Sci. Technol. A Vacuum, Surfaces, Film.* 4.6 (1986), p. 2717.

[8] I. Vurgaftman, J. R. Meyer, and L. R. Ram-Mohan. "Band parameters for III-V compound semiconductors and their alloys". In: *J. Appl. Phys.* 89.11 I (2001), pp. 5815–5875.

[9] M A Moram and M E Vickers. "X-ray diffraction of III-nitrides". In: *Reports Prog. Phys.* 72.3 (2009), p. 036502.

[10] A Siegel, K Parlinski, and U Wdowik. "Ab initio calculation of structural phase transitions in AlN crystal". In: *Phys. Rev. B* 74.10 (2006), pp. 1–6.

[11] N E Christensen and I Gorczyca. "Optical and structural properties of III-V nitrides under pressure". In: *Phys. Rev. B* 50.7 (1994), pp. 4397–4415.

[12] Wen Tai Lin et al. “Epitaxial growth of cubic AlN films on (100) and (111) silicon by pulsed laser ablation”. In: *Appl. Phys. Lett.* 66.16 (1995), pp. 2066–2068.

[13] A. Madan et al. “Stabilization of Cubic AlN in Epitaxial AlN/TiN Superlattices”. In: *Phys. Rev. Lett.* 78.9 (1997), pp. 1743–1746.

[14] F. Adibi et al. “Defect structure and phase transitions in epitaxial metastable cubic $Ti_{0.5}Al_{0.5}N$ alloys grown on MgO(001) by ultra-high-vacuum magnetron sputter deposition”. In: *J. Appl. Phys.* 69.9 (1991), pp. 6437–6450.

[15] A. Knutsson et al. “Machining performance and decomposition of TiAlN/TiN multilayer coated metal cutting inserts”. In: *Surf. Coatings Technol.* 205.16 (2011), pp. 4005–4010.

[16] “Powder diffraction files 03-065-0565 (TiN)”. In: *International center for diffraction data* (2007).

[17] A Flink, T Larsson, and J. Sjölén. “Influence of Si on the microstructure of arc evaporated (Ti, Si) N thin films; evidence for cubic solid solutions and their thermal stability”. In: *Surf. Coatings Technol.* 200.5-6 (2005), pp. 1535–1542.

[18] “Powder diffraction files 00- 035-0753 (ZrN)”. In: *International center for diffraction data* (2007).

[19] H Holleck. “Metastable coatings - Prediction of composition and structure”. In: *Surf. Coatings Technol.* 36.1-2 (1988), pp. 151–159.

[20] S.H. Sheng, R.F. Zhang, and S. Veprek. “Phase stabilities and thermal decomposition in the $Zr_{1-x}Al_xN$ system studied by ab initio calculation and thermodynamic modeling”. In: *Acta Mater.* 56.5 (2008), pp. 968–976.

[21] K.A. Gruss et al. “Characterization of zirconium nitride coatings deposited by cathodic arc sputtering”. In: *Surf. Coatings Technol.* 107.2-3 (1998), pp. 115–124.

[22] E. W. Niu et al. “Influence of substrate bias on the structure and properties of ZrN films deposited by cathodic vacuum arc”. In: *Mater. Sci. Eng. A* 460-461 (2007), pp. 135–139.

[23] “Powder diffraction files 00-033-0592 (HfN)”. In: *International center for diffraction data* (2007).

[24] H. S. Seo et al. “Epitaxial and polycrystalline Hf Nx ($0.8 \leq x \leq 1.5$) layers on MgO(001): Film growth and physical properties”. In: *J. Appl. Phys.* 97.8 (2005), pp. 0–9.

[25] B. Howe et al. “Growth and physical properties of epitaxial metastable $Hf_{1-x}Al_xN$ alloys deposited on MgO(001) by ultrahigh vacuum reactive magnetron sputtering”. In: *Surf. Coatings Technol.* 202.4-7 (2007), pp. 809–814.

[26] R. Armitage et al. “Lattice-matched HfN buffer layers for epitaxy of GaN on Si”. In: *Appl. Phys. Lett.* 81.8 (2002), pp. 1450–1452.

[27] X. Xu et al. "Epitaxial condition and polarity in GaN grown on a HfN-buffered Si(111) wafer". In: *Appl. Phys. Lett.* 86.18 (2005), pp. 1–3.

[28] Anna Delin et al. "Optical properties of the group-IVB refractory metal compounds." In: *Phys. Rev. B. Condens. Matter* 54.3 (1996), pp. 1673–1681.

[29] "Powder diffraction files 00-035-0768 (VN". In: *International center for diffraction data* (2007).

[30] F I Ajami and R K Maccrone. "Magnetic Susceptibility and Superconductivity of Cubic Vanadium Nitrides". In: *J. Phys. Chem. Solids* 36 (1975), pp. 7–15.

[31] Daiwon Choi, George E. Blomgren, and Prashant N. Kumta. "Fast and reversible surface redox reaction in nanocrystalline vanadium nitride supercapacitors". In: *Adv. Mater.* 18.9 (2006), pp. 1178–1182.

[32] Xiaoping Zhou et al. "Study on the electrochemical behavior of vanadium nitride as a promising supercapacitor material". In: *J. Phys. Chem. Solids* 70.2 (2009), pp. 495–500.

[33] V.N. Zhitomirsky et al. "Structure and mechanical properties of vacuum arc-deposited NbN coatings". In: *Thin Solid Films* 326.1-2 (1998), pp. 134–142.

[34] "Powder diffraction files 03-065-5011 (NbN)". In: *International center for diffraction data* (2007).

[35] Zhen Wang et al. "Superconducting properties and crystal structures of single-crystal niobium nitride thin films deposited at ambient substrate temperature". In: *J. Appl. Phys.* 79.10 (1996), pp. 7837–7842.

[36] "Powder diffraction files 03-065-9404 (TaN)". In: *International center for diffraction data* (2007).

[37] M. H. Tsai et al. "Comparison of the diffusion barrier properties of chemical-vapor-deposited TaN and sputtered TaN between Cu and Si". In: *J. Appl. Phys.* 79.9 (1996), pp. 6932–6938.

[38] S. Shibata, K. Murasugi, and K. Kaminishi. "New Type Thermal Printing Head Using Thin Film". In: *IEEE Trans. Parts, Hybrids, Packag.* 12.3 (1976), pp. 223–230.

[39] Kazuo Eda et al. "Miniature hybrid microwave IC's using a novel thin-film technology". In: *IEEE Trans. Microw. Theory Tech.* 38.12 (1990), pp. 1949–1956.

[40] E. I. Isaev et al. "Phonon related properties of transition metals, their carbides, and nitrides: A first-principles study". In: *J. Appl. Phys.* 101.12 (2007), p. 123519.

[41] Hermann A. Jehn et al. "Morphology and properties of sputtered (Ti,Al)N layers on high speed steel substrates as a function of deposition temperature and sputtering atmosphere". In: *J. Vac. Sci. Technol. A Vacuum, Surfaces, Film.* 4.6 (1986), p. 2701.

[42] O. Knotek, M. Böhmer, and T. Leyendecker. "On structure and properties of sputtered Ti and Al based hard compound films". In: *J. Vac. Sci. Technol. A Vacuum, Surfaces, Film.* 4.1986 (1986), p. 2695.

[43] U. Wahiström et al. "Crystal growth and microstructure of polycrystalline $Ti_{1-x}Al_xN$ alloy films deposited by ultra-high-vacuum dual-target magnetron sputtering". In: *Thin Solid Films* 235.1-2 (1993), pp. 62–70.

[44] Min Zhou et al. "Phase transition and properties of Ti-Al-N thin films prepared by r.f.-plasma assisted magnetron sputtering". In: *Thin Solid Films* 339.1-2 (1999), pp. 203–208.

[45] Paul H. Mayrhofer et al. "Self-organized nanostructures in the Ti-Al-N system". In: *Appl. Phys. Lett.* 83.10 (2003), p. 2049.

[46] B Alling et al. "Comparison of thermodynamic properties of cubic $Cr_{1-x}Al_xN$ and $Ti_{1-x}Al_xN$ from first-principles calculations". In: *J. Appl. Phys.* 102.4 (2007), p. 044314.

[47] A. Hörling et al. "Mechanical properties and machining performance of $Ti_{1-x}Al_xN$-coated cutting tools". In: *Surf. Coatings Technol.* 191.2-3 (2005), pp. 384–392.

[48] P H Mayrhofer, D Music, and J M Schneider. "Ab initio calculated binodal and spinodal of cubic $Ti_{1-x}Al_xN$". In: *Appl. Phys. Lett.* 88.7 (2006), p. 071922.

[49] RF Zhang and S Veprek. "Metastable phases and spinodal decomposition in $Ti_{1-x}Al_xN$ system studied by ab initio and thermodynamic modeling, a comparison with the TiN-Si_3N_4 system". In: *Mater. Sci. Eng. A* 448.1-2 (2007), pp. 111–119.

[50] B. Alling et al. "Mixing and decomposition thermodynamics of c-$Ti_{1-x}Al_xN$ from first-principles calculations". In: *Phys. Rev. B* 75.4 (2007), p. 045123.

[51] R Rachbauer et al. "Decomposition pathways in age hardening of Ti-Al-N films". In: *J. Appl. Phys.* 110.2 (2011), p. 023515.

[52] Hiroyuki Hasegawa, Masahiro Kawate, and Tetsuya Suzuki. "Effects of Al contents on microstructures of $Cr_{1-x}Al_xN$ and $Zr_{1-x}Al_xN$ films synthesized by cathodic arc method". In: *Surf. Coatings Technol.* 200.7 (2005), pp. 2409–2413.

[53] R Lamni et al. "Microstructure and nanohardness properties of Zr-Al-N and Zr-Cr-N thin films". In: *J. Vac. Sci. Technol. A* 23.4 (2005), pp. 593–598.

[54] L. Rogström et al. "Influence of chemical composition and deposition conditions on microstructure evolution during annealing of arc evaporated ZrAlN thin films". In: *J. Vac. Sci. Technol. A Vacuum, Surfaces, Film.* 30.3 (2012), p. 031504.

[55] L. Rogström et al. "Thermal stability and mechanical properties of arc evaporated ZrN/ZrAlN multilayers". In: *Thin Solid Films* 519.2 (2010), pp. 694–699.

[56] L. Rogström et al. "Age hardening in arc-evaporated ZrAlN thin films". In: *Scr. Mater.* 62.10 (2010), pp. 739–741.

[57] Naureen Ghafoor et al. "Nanolabyrinthine ZrAlN thin films by self-organization of interwoven single-crystal cubic and hexagonal phases". In: *APL Mater.* 1.2 (2013), p. 022105.

[58] Björn Alling, A Karimi, and I.A. Abrikosov. "Electronic origin of the isostructural decomposition in cubic $M_{1-x}Al_xN$ (M=Ti, Cr, Sc, Hf): A first-principles study". In: *Surf. Coatings Technol.* 203.5-7 (2008), pp. 883–886.

[59] David Holec et al. "Phase stability and alloy-related trends in Ti-Al-N , Zr-Al-N and Hf-Al-N systems from first principles". In: *Surf. Coat. Technol.* 206.7-5 (2011), pp. 1698–1704.

[60] R. Franz et al. "Investigation on structure and properties of arc-evaporated HfAlN hard coatings". In: *J. Vac. Sci. Technol. A Vacuum, Surfaces, Film.* 28.4 (2010), p. 528.

[61] B.M. Howe et al. "Real-time control of AlN incorporation in epitaxial $Hf_{1-x}Al_xN$ using high-flux, low-energy (10-40eV) ion bombardment during reactive magnetron sputter deposition from a $Hf_{0.7}Al_{0.3}$ alloy target". In: *Acta Mater.* 59.2 (2011), pp. 421–428.

[62] Szilárd Kolozsvári et al. "Deposition and characterization of hard coatings in the material system V-Al-N by reactive magnetron sputter deposition". In: *Plasma Process. Polym.* 6 (2009), pp. 146–151.

[63] Ping Zhu et al. "Microstructure, chemical states, and mechanical properties of magnetron co-sputtered $V_{1-x}Al_xN$ coatings". In: *Surf. Coatings Technol.* 232 (2013), pp. 311–318.

[64] Florian Rovere et al. "Experimental and computational study on the phase stability of Al-containing cubic transition metal nitrides". In: *J. Phys. D. Appl. Phys.* 43.3 (2010), p. 035302.

[65] TI Selinder et al. "Phase formation and microstructure of $Nb_{1-x}Al_xN$ alloy films grown on MgO (001) by reactive sputtering: a new ternary phase". In: *Vacuum* 46.12 (1995), pp. 1401–1406.

[66] Harish C. Barshilia et al. "Structure and properties of reactive direct current magnetron sputtered niobium aluminum nitride coatings". In: *J. Mater. Res.* 23.05 (2008), pp. 1258–1268.

[67] R. Franz et al. "Tribological Properties of Arc-Evaporated NbAlN Hard Coatings". In: *Tribol. Lett.* 45.1 (2012), pp. 143–152.

[68] R. Franz et al. "Structure, mechanical properties and oxidation behaviour of arc-evaporated NbAlN hard coatings". In: *Surf. Coatings Technol.* 204.15 (2010), pp. 2447–2453.

[69] David Holec et al. "Structure and stability of phases within the NbN-AlN system". In: *J. Phys. D. Appl. Phys.* 43.14 (2010), p. 145403.

[70] C.M. Koller et al. "Thermal stability and oxidation resistance of arc evaporated TiAlN, TaAlN, TiAlTaN, and TiAlN/TaAlN coatings". In: *Surf. Coatings Technol.* 259 (2014), pp. 599–607.

[71] O. Knotek, W. Burgmer, and C. Stoessel. "Arc-evaporated Ti-V-N thin films". In: *Surf. Coatings Technol.* 54-55 (1992), pp. 249–254.

[72] A. Hoerling et al. "Thermal stability, microstructure and mechanical properties of $Ti_{1-x}Zr_xN$ thin films". In: *Thin Solid Films* 516.18 (2008), pp. 6421–6431.

[73] V.V. Uglov et al. "Structural and mechanical stability upon annealing of arc-deposited Ti-Zr-N coatings". In: *Surf. Coatings Technol.* 202.11 (2008), pp. 2394–2398.

[74] K. Vasu, M. Ghanashyam Krishna, and K. A. Padmanabhan. "Effect of Nb concentration on the structure, mechanical, optical, and electrical properties of nano-crystalline $Ti_{1-x}Nb_xN$ thin films". In: *J. Mater. Sci.* 47.8 (2012), pp. 3522–3528.

[75] I Grimberg et al. "Multicomponent Ti-Zr-N and Ti-Nb-N coatings deposited by vacuum arc". In: *Surf. Coatings Technol.* 108-109 (1998), pp. 154–159.

[76] G. Abadias et al. "Reactive magnetron cosputtering of hard and conductive ternary nitride thin films: Ti-Zr-N and Ti-Ta-N". In: *J. Vac. Sci. Technol. A Vacuum, Surfaces, Film.* 28.4 (2010), p. 541.

[77] G. M. Matenoglou et al. "Structure, stability and bonding of ternary transition metal nitrides". In: *Surf. Coatings Technol.* 204.6-7 (2009), pp. 911–914.

[78] M.A. Roldán, M.D. Alcalá, and C. Real. "Characterisation of ternary $Ti_x V_{1-x}N_y$ nitride prepared by mechanosynthesis". In: *Ceram. Int.* 38.1 (2012), pp. 687–693.

[79] O. Knotek. "Industrial deposition of binary, ternary, and quaternary nitrides of titanium, zirconium, and aluminum". In: *J. Vac. Sci. Technol. A Vacuum, Surfaces, Film.* 5.4 (1987), p. 2173.

[80] V.V. Uglov et al. "Stability of Ti-Zr-N coatings under Xe-ion irradiation". In: *Surf. Coatings Technol.* 204.12-13 (2010), pp. 2095–2098.

[81] L. E. Koutsokeras et al. "Conducting transition metal nitride thin films with tailored cell sizes: The case of δ-$Ti_xTa_{1-x}N$". In: *Appl. Phys. Lett.* 93.1 (2008), p. 011904.

[82] G. M. Matenoglou et al. "Structure and electronic properties of conducting, ternary $Ti_xTa_{1-x}N$ films". In: *J. Appl. Phys.* 105.10 (2009), p. 103714.

[83] Paul H. Mayrhofer et al. "Microstructural design of hard coatings". In: *Prog. Mater. Sci.* 51.8 (2006), pp. 1032–1114.

[84] H Lind et al. "Improving thermal stability of hard coating films via a concept of multicomponent alloying". In: *Appl. Phys. Lett.* 99.9 (2011), p. 091903.

[85] Rikard Forsén et al. "Decomposition and phase transformation in TiCrAlN thin coatings". In: *J. Vac. Sci. Technol. A Vacuum, Surfaces, Film.* 30.6 (2012), p. 061506.

[86] David Holec et al. "Alloying-related trends from first principles: An application to the Ti-Al-X-N system". In: *J. Appl. Phys.* 113.11 (2013), p. 113510.

[87] Li Chen et al. "Influence of Zr on structure, mechanical and thermal properties of Ti-Al-N". In: *Thin Solid Films* 519.16 (2011), pp. 5503–5510.

[88] S.A. Glatz et al. "Thermal stability and mechanical properties of arc evaporated Ti-Al-Zr-N hard coatings". In: *Surf. Coatings Technol.* 266 (2015), pp. 1–9.

[89] R Rachbauer et al. "Effect of Hf on structure and age hardening of Ti-Al-N thin films". In: *Surf. Coatings Technol.* 206.10 (2012), pp. 2667–2672.

[90] Yu X. Xu et al. "Influence of Hf on the structure, thermal stability and oxidation resistance of Ti-Al-N coatings". In: *Thin Solid Films* 565 (2014), pp. 25–31.

[91] K. Kutschej et al. "A new low-friction concept for $Ti_{1-x}Al_xN$ based coatings in high-temperature applications". In: *Surf. Coatings Technol.* 188-189.2004 (2004), pp. 358–363.

[92] M Pfeiler et al. "The influence of bias voltage on structure and mechanical/tribological properties of arc evaporated Ti-Al-V-N coatings". In: *Surf. Coatings Technol.* 202.4-7 (2007), pp. 1050–1054.

[93] Robert Franz and Christian Mitterer. "Vanadium containing self-adaptive low-friction hard coatings for high-temperature applications: A review". In: *Surf. Coatings Technol.* 228 (2013), pp. 1–13.

[94] R. Rachbauer, D. Holec, and P.H. Mayrhofer. "Increased thermal stability of Ti-Al-N thin films by Ta alloying". In: *Surf. Coatings Technol.* 211 (2012), pp. 98–103.

[95] Richard Rachbauer et al. "Electronic origin of structure and mechanical properties in Y and Nb alloyed Ti-Al-N thin films". In: *Int. J. Mater. Res.* 102.6 (2011), pp. 735–742.

[96] M. Pfeiler et al. "Arc Evaporation of Ti-Al-Ta-N Coatings: The Effect of Bias Voltage and Ta on High-temperature Tribological Properties". In: *Tribol. Lett.* 30.2 (2008), pp. 91–97.

[97] A. Knutsson et al. "Thermal decomposition products in arc evaporated TiAlN/TiN multilayers". In: *Appl. Phys. Lett.* 93.14 (2008), p. 143110.

[98] A. Knutsson et al. "Microstructure evolution during the isostructural decomposition of TiAlN-A combined in-situ small angle x-ray scattering and phase field study". In: *J. Appl. Phys.* 113.21 (2013), p. 213518.

[99] Alex Zunger et al. "Special quasirandom structures". In: *Phys. Rev. Lett.* 65.3 (1990), pp. 353–356.

[100] Paul Soven. "Coherent-Potential Model of Substitutional Disordered Alloys". In: *Phys. Rev.* 156.3 (1967), pp. 809–813.

[101] J. M. Cowley. "An Approximate Theory of Order in Alloys". In: *Phys. Rev.* 77.5 (1990), pp. 669–675.

[102] A V Ruban and I A Abrikosov. "Configurational thermodynamics of alloys from first principles: effective cluster interactions". In: *Reports Prog. Phys.* 71.4 (2008), p. 046501.

[103] Maher Moakher and Andrew N. Norris. "The Closest Elastic Tensor of Arbitrary Symmetry to an Elasticity Tensor of Lower Symmetry". In: *J. Elast.* 85.3 (2006), pp. 215–263.

[104] Ferenc Tasnádi, M. Odén, and Igor A. Abrikosov. "Ab initio elastic tensor of cubic $Ti_{0.5}Al_{0.5}N$ alloys: Dependence of elastic constants on size and shape of the supercell model and their convergence". In: *Phys. Rev. B* 85.14 (2012), p. 144112.

[105] V. Ozoliiņš, C Wolverton, and Alex Zunger. "Effects of anharmonic strain on the phase stability of epitaxial films and superlattices: Applications to noble metals". In: *Phys. Rev. B* 57.8 (1998), pp. 4816–4828.

[106] D W Taylor. "Vibrational Properties of Imperfect Crystals with Large Defect Concentrations". In: *Phys. Rev.* 156.3 (1967), pp. 1017–1029.

[107] J Korringa. "On the calculation of the energy of a Bloch wave in a metal". In: *Physica* 13.6-7 (1947), pp. 392–400.

[108] W. Kohn and N. Rostoker. "Solution of the Schrödinger Equation in Periodic Lattices with an Application to Metallic Lithium". In: *Phys. Rev.* 94.5 (1954), pp. 1111–1120.

[109] B. L. Györffy. "Coherent-Potential Approximation for a Nonoverlapping-Muffin-Tin-Potential Model of Random Substitutional Alloys". In: *Phys. Rev. B* 5.6 (1972), pp. 2382–2384.

[110] A. V. Ruban and H. L. Skriver. "Screened Coulomb interactions in metallic alloys. I. Universal screening in the atomic-sphere approximation". In: *Phys. Rev. B* 66.2 (2002), p. 024201.

[111] A. V. Ruban et al. "Local lattice relaxations in random metallic alloys: Effective tetrahedron model and supercell approach". In: *Phys. Rev. B* 67.21 (2003), p. 214302.

[112] A.V. Ruban and H.L. Skriver. "Calculated surface segregation in transition metal alloys". In: *Comput. Mater. Sci.* 15.2 (1999), pp. 119–143.

[113] R.E. Newnham. *Properties of materials, Anisotropy, symmetry, Structure*. Oxford University Press, 2005.

[114] Göran Grimvall. *Thermophysical properties of materials*. ELSEVIER SCIENCE, 1999.

[115] A Reuss. "Berechnung der Fließgrenze von Mischkristallen auf Grund der Plastizitätsbedingung für Einkristalle". In: *Z. Angew Math. Phys.* 9.49 (1929).

[116] N Voigt. "Ueber adiabatische Elasticitätsconstanten". In: *Ann. Phys. (Leipz.)* 38.573 (1889).

[117] S.F. Pugh. "Relations between the elastic moduli and the plastic properties of polycrystalline pure metals". In: *Philos. Mag. Ser. 7* 45.367 (1954), pp. 823–843.

[118] William Art Counts et al. "Ab Initio Guided Design of bcc Ternary Mg-Li-X (X = Ca, Al, Si, Zn, Cu) Alloys for Ultra-Lightweight Applications". In: *Adv. Eng. Mater.* 12.7 (2010), pp. 572–576.

[119] R Hill. "The Elastic Behaviour of a Crystalline Aggregate". In: *Proc. Phys. Soc. Sect. A* 65.5 (1952), pp. 349–354.

[120] Jules Thomas Browaeys and Sébastien Chevrot. "Decomposition of the elastic tensor and geophysical applications". In: *Geophys. J. Int.* 159.2 (2004), pp. 667–678.

[121] K.Huang and M.Born. *Dynamical theory of crystal lattices*. Oxford University Press, London, 1954.

[122] John F Nye. *Physical properties of crystals*. Oxford Clarendon, 1985.

[123] M. Grimsditch. "Effective elastic constants of superlattices". In: *Phys. Rev. B* 31.10 (1985), pp. 6818–6819.

[124] M. Born and R. Oppenheimer. "Zur Quantentheorie der Molekeln". In: *Ann. Phys.* 389.20 (1927), pp. 457–484.

[125] L. H. Thomas. "The calculation of atomic fields". In: *Math. Proc. Cambridge Philos. Soc.* 23.05 (1927), p. 542.

[126] E. Fermi. "Un metodo statistico per la determinazione di alcune priorietà dell'atome". In: *Rend. Accad. Naz. Lincei* 6 (1927), pp. 602–607.

[127] P. A. M. Dirac. "Note on Exchange Phenomena in the Thomas Atom". In: *Math. Proc. Cambridge Philos. Soc.* 26.03 (1930), p. 376.

[128] P. Hohenberg and W. Kohn. "Inhomogeneous Electron Gas". In: *Phys. Rev.* 136.3B (1964), B864–B871.

[129] W. Kohn and L. J. Sham. "Self-Consistent Equations Including Exchange and Correlation Effects". In: *Phys. Rev.* 140.4A (1965), A1133–A1138.

[130] Kieron Burke, John P Perdew, and Matthias Ernzerhof. "Why semilocal functionals work: Accuracy of the on-top pair density and importance of system averaging". In: *J. Chem. Phys.* 109.10 (1998), pp. 3760–3771.

[131] C. S. Wang, B. M. Klein, and H. Krakauer. "Theory of Magnetic and Structural Ordering in Iron". In: *Phys. Rev. Lett.* 54.16 (1985), pp. 1852–1855.

[132] John P. Perdew, Kieron Burke, and Matthias Ernzerhof. "Generalized Gradient Approximation Made Simple". In: *Phys. Rev. Lett.* 78.7 (1997), pp. 1396–1396.

[133] H. Hellmann. "A New Approximation Method in the Problem of Many Electrons". In: *J. Chem. Phys.* 3.1 (1935), pp. 61–61.

[134] H. Hellmann and W. Kassatotschkin. "Metallic Binding According to the Combined Approximation Procedure". In: *J. Chem. Phys.* 4.5 (1936), pp. 324–325.

[135] D. R. Hamann, M. Schlüter, and C. Chiang. "Norm-Conserving Pseudopotentials". In: *Phys. Rev. Lett.* 43.20 (1979), pp. 1494–1497.

[136] David Vanderbilt. "Soft self-consistent pseudopotentials in a generalized eigenvalue formalism". In: *Phys. Rev. B* 41.11 (1990), pp. 7892–7895.

[137] P. E. Blöchl. "Projector augmented-wave method". In: *Phys. Rev. B* 50.24 (1994), pp. 17953–17979.

[138] G. Kresse and D. Joubert. "From ultrasoft pseudopotentials to the projector augmented-wave method". In: *Phys. Rev. B* 59.3 (1999), pp. 1758–1775.

[139] O. K. Andersen. "Simple approach to the band-structure problem". In: *Solid State Communications* 13.2 (1973), pp. 133–136.

[140] O. K. Andersen and O. Jepsen. "Explicit, First-Principles Tight-Binding Theory". In: *Phys. Rev. Lett.* 53 (1984), pp. 2571–2574.

List of included publications and my contribution

[I] **Special quasirandom structure method in application for advanced properties of alloys: A study on $Ti_{0.5}Al_{0.5}N$ and $TiN/Ti_{0.5}Al_{0.5}N$ multilayer**
Ferenc Tasnádi, Fei Wang, Magnus Odén, Igor A. Abrikosov.
Computational Materials Science, **103**, 194-199 (2015).

I took part in performing some calculations, did some data analysis, participated in part of the evaluation and interpretation of the results.

[II] **Coherency effects on the mixing thermodynamics of cubic $Ti_{1-x}Al_xN$ /TiN(001) multilayers**
Fei Wang, Igor A. Abrikosov, Sergei I. Simak, Magnus Odén, Frank Mücklich, Ferenc Tasnádi.
PHYSICAL REVIEW B, **93**, 174201 (2016).

I took part in planning of the project, performed all the calculations, did all the data analysis, participated in the evaluation and interpretation of the results, and wrote the manuscript.

[III] **Growth and thermal stability of TiN/ZrAlN: Effect of internal interfaces**
Kumar Yalamanchili, Fei Wang, Hisham Aboulfadl, Jenifer Barrirero, Lina Rogström, Emilio Jiménez-Pique, Frank Mücklich, Ferenc Tasnádi, Magnus Odén, Naureen Ghafoor.
Acta Materialia, **121**, 396-406 (2016),

I took part in part of planning of the project, performed all the calculations, did all the data analysis of calculations, participated part of the evaluation

and interpretation of the results, and wrote part of the manuscript.

[IV] **Systematic *ab initio* investigation of the elastic modulus in quaternary transition metal nitride alloys and in their coherent multilayers**
Fei Wang, David Holec, Magnus Odén, Frank Mücklich, Igor A. Abrikosov, Ferenc Tasnádi.
Acta Materialia, **127**, 124-132 (2017).

I took part in planning of the project, performed all the calculations, did all the data analysis, participated in the evaluation and interpretation of the results, and wrote the manuscript.

[V] **High temperature thermodynamics of spinodal decomposition in arc deposited $\mathbf{Ti}_x\mathbf{Nb}_y\mathbf{Al}_z\mathbf{N}$ coatings**
Ferenc Tasnádi, Lina Rogström, Jianqiang Zhu, Fei Wang, T.-W. Hsu, Hans Lind, Igor A. Abrikosov, M. P. Johansson-Jõesaar, Magnus Odén.
Submitted to Materials and Design.

I took part in part of planning of the project, performed all the calculations, did all the data analysis of calculations, participated part of the evaluation and interpretation of the results.

[VI] **Thermal expansion of quaternary nitride coatings**
Ferenc Tasnádi, Fei Wang, Magnus Odén, Igor A. Abrikosov.
Submitted to APL materials.

I performed some calculations, did some data analysis of calculations, participated part of the evaluation and interpretation of the results.

Related, not included publications

[I] **Exploring the high entropy alloy concept in (AlTiVNbCr)N**
K. Yalamanchili, Fei Wang, Isabella Schramm, J. M. Andersson, Mats P. Johansson Jöesaar, Ferenc Tasnádi, Frank Mücklich, Naureen Ghafoor and Magnus Odén.
Thin Solid Films, **636**, 346-352 (2017).

[II] **Effects of configurational disorder on the elastic properties of icosahedral boron-rich alloys based on B_6O, $B_{13}C_2$, and B_4C, and their mixing thermodynamics.**
A. Ektarawong, S. I. Simak, L. Hultman, J. Birch, F. Tasnádi, F. Wang and B. Alling.
The Journal of Chemical Physics, **144**, 134503 (2016).

I

Paper I

Special quasirandom structure method in application for advanced properties of alloys: A study on $Ti_{0.5}Al_{0.5}N$ and $TiN/Ti_{0.5}Al_{0.5}N$ multilayer

Ferenc Tasnádi
Fei Wang
Magnus Odén
Igor A. Abrikosov

Computational Materials Science, **103**, 194-199 (2015)

Computational Materials Science 103 (2015) 194–199

Contents lists available at ScienceDirect

Computational Materials Science

journal homepage: www.elsevier.com/locate/commatsci

Special quasirandom structure method in application for advanced properties of alloys: A study on $Ti_{0.5}Al_{0.5}N$ and $TiN/Ti_{0.5}Al_{0.5}N$ multilayer

Ferenc Tasnádi [a,*], Fei Wang [a,b], Magnus Odén [a], Igor A. Abrikosov [a,c,d]

[a] Department of Physics, Chemistry and Biology (IFM), Linköping University, SE-581 83 Linköping, Sweden
[b] Functional Materials, Materials Science and Engineering Department (MSE), Saarland University, P.O. Box 151150, 66041 Saarbrücken, Germany
[c] Materials Modeling and Development Laboratory, NUST "MISIS", 119049 Moscow, Russia
[d] LACOMAS Laboratory, Tomsk State University, 634050 Tomsk, Russia

ARTICLE INFO

Article history:
Received 21 November 2014
Received in revised form 11 March 2015
Accepted 22 March 2015
Available online 11 April 2015

Keywords:
Modelling alloys
Special quasirandom structure approach
Elastic constants
Vacancy formation energy
Multilayers

ABSTRACT

The special quasirandom structure (SQS) approach is a successful technique for modelling of alloys, however it breaks inherently the point symmetry of the underlying crystal lattice. We demonstrate that monocrystalline and polycrystalline elastic moduli can scatter significantly depending on the chosen SQS model and even on the supercell orientation in space. Also, we demonstrate that local disturbances, such as vacancies or interfaces change the SQS configuration in a way, that significantly affects the values of the calculated physical properties. Moreover, the diversity of local environments in random alloys results in a large variation of the calculated local properties. We underline that improperly chosen, generated or handled SQS may result in erroneous theoretical findings. The challenges of the SQS method are discussed using bulk $Ti_{0.5}Al_{0.5}N$ alloy and $TiN/Ti_{0.5}Al_{0.5}N$ multilayer as model systems. We present methodological corrections for the mindful application of this approach in studies of advanced properties of alloys.

1. Introduction

Computer simulations play an increasing role in materials science. They allow one to explain experimental findings and predict novel, extraordinary properties of materials using atomistic modelling [1]. Sophisticated approaches based on quantum mechanical laws are utilised by efficient program packages (VASP, Quantum Espresso, Abinit, [2–4] etc.) to simulate materials relevant for fundamental science, as well as for industrial applications. Moreover, a dramatic increase of the available supercomputer power allows one to develop high-throughput computational approaches in tailor-designing novel materials with a serious speed up of the development process [5,6].

In connection to this success it has been realised that with multiscale computational simulations one can achieve industrial conditions, in terms of length and time scales. The need to obtain more insight about the impact of microstructure on materials mechanical properties, such as hardness, has been addressed in the hard coatings industry [7]. In addition, novel approaches have been developed to extract more advanced materials properties. For example, high temperature elastic constant [8], vacancy formation energy calculations or even large time scale diffusion simulations [9] have been performed beyond the zero temperature ground state properties calculations. Not only the calculated properties but also the simulated materials have become more complex, as inhomogeneous or low dimensional structures can originate a variety of novel physical phenomena (magnetic, optical or structural). The simulation of interfaces, multilayers or defects in alloys require the inclusion of many more atoms in the model and the system size is further increased in case of finite temperature simulations.

The description of complex materials at realistic conditions requires a computationally efficient and accurate atomistic, structural modelling. The special quasirandom structure (SQS) approach [10] is an elegant technique to model alloys with a computationally less demanding finite size supercell. The piezoelectric properties of ScAlN alloys [11,12], or the elasticity of TiAlN [13,14] have been successfully predicted using SQS supercells. Mayrhofer et al. have investigated the impact of the atomic configuration on the structural, elastic properties, and phase stability in TiAlN [15]. The phase diagrams of ZrAlN, HfAlN [16] and the alloying trends in quaternary Ti-Al-X-N systems [17] have been derived using the SQS approach. Significant configurational dependence of the piezoelectric constant has been obtained in B-doped wurtzite AlN

* Corresponding author at: Campus Valla, Linköping University, SE-581 83 Linköping, Sweden. Tel.: +46 13 285709.
E-mail address: tasnadi@ifm.liu.se (F. Tasnádi).

http://dx.doi.org/10.1016/j.commatsci.2015.03.030
0927-0256/

[18] and the nonlinear macroscopic polarisation in III–V nitride alloys with wurtzite symmetry have been discussed [19].

Beside the tremendous success of the SQS approach it is important to understand some of its shortcomings. The accuracy of the method is fully determined by the range and the magnitude of interactions relevant for the description of the particular physical property in the system [20]. Furthermore, supercell models of alloys break inherently the point symmetry of the underlying crystal lattice. As finite size effect, local disturbances, such as vacancies or interfaces change the overall configurational setup of the supercell, what can significantly affect the value of the physical quantity that the calculation is aiming for. Therefore, improperly chosen or handled SQS supercells may result in a large discrepancy between theory and experiment or in erroneous theoretical findings.

In this paper we discuss these challenges of the SQS method using bulk $Ti_{0.5}Al_{0.5}N$ and $TiN/Ti_{0.5}Al_{0.5}N$ multilayer as model systems. We present correction schemes that allow one to establish the mindful application of this efficient technique.

2. SQS approach and some of its limitations

The special quasirandom structure (SQS) approach [10] is developed to predict self-averaging quantities of alloys using finite size supercells. Self-averaging means that the relative variance of a physical quantity Q vanishes

$$\frac{\langle Q^2\rangle - \langle Q\rangle^2}{\langle Q\rangle^2} \to 0, \tag{1}$$

with the inclusion of more and more configurational realisations [21]. $\langle\ \rangle$ stands for mean value. Using the nominator from Eq. (1) for a binary $A_{1-x}B_x$ alloy one can formulate the SQS algorithm as minimising

$$\sum_f w_f D_f \left[(2x-1)^{k_f} - \bar{P}_f(\sigma)\right] \tag{2}$$

where $\bar{P}_f(\sigma)$ is the lattice average of the spin products with atomic configuration σ, D_f is the degeneracy for figure f, k_f stand for the number of vertices and w_f are the interaction parameters in f. In case of pair interactions P_f can be expressed with the help of the Warren–Cowlley short range order (SRO) parameters [22]. In practice the bracketed term is minimised with respect the atomic configuration for the chosen figures. For more details see Refs. [10,20,23].

With the assumption of a finite length scale correlation between the atomic sites, range of relevant interactions in Eq. (2), one could attempt to derives a finite size structural model without the knowledge of w_f. However, in this case converging the obtained results with respect to the number of included SRO parameters, or in other words with respect to the supercell size, is a crucial and necessary task.

Beyond the extensive thermodynamic quantities, that are self-averaging, the SQS approach due to its relatively low computational demand has become an ultimate technique in modelling tensorial properties and also in determining local properties of alloys, such as vacancy formation energy. However, the SQS approach does not aim to generate structures with a proper point symmetry of the system. Therefore, predicting the elastic, piezoelectric constants of alloys within the SQS approach requires extra considerations. Besides, a general tensorial extension of the cluster expansion has been developed [24]. Recently, a symmetry based projection technique has been suggested to predict elasticity of alloys [14].

For modelling vacancy formation in alloys a local cluster expansion has been developed based on the help of point symmetry [25,26]. In a finite supercells approach calculating vacancy formation energy sounds as a straightforward computational task: remove atoms. However, an SQS supercell contains many different local environments to represent the structural disorder on the average. Therefore, in this approach the vacancy formation energy varies from site to site [27,28]. Moreover, because of the finite size of the used SQS supercell, the removal of an atom changes not only the concentration but also the configuration or the SRO parameters of the model. As it will be shown in Section 4, though, these small changes have negligible effects on the extensive (self-averaging) quantities, it alters significantly the value of local quantities, such as the vacancy formation energy.

In inhomogeneous systems, such as multilayers containing alloys, the interaction and the large relaxation of the interfacial atoms can renormalise the effective cluster interactions [20] (ECI) to such a degree that layer dependent cluster expansion has to be applied. In addition, the one particle ECIs – the segregation energies, become extremely important. This rescaled diversity of the local environmental effects has to be handled on a pure structural level in using the SQS approach. The interfacial energy is self-averaging as it is an extensive quantity with respect to the interface area. If the in-plane size of the supercell is large enough to include sufficient amount of different local environments (configurations), then the total energy of the multilayer can be written as

$$e^{\mathrm{ML}} = \sum_i y_i e_i^{\mathrm{bulk}} + e^{\mathrm{interface}}(\{y_i\}) + e^{\mathrm{strain}}(\{y_i\}), \tag{3}$$

where y_i are the content ratios and e_i^{bulk} denote the unstrained bulk energies of the components in the multilayer, $e^{\mathrm{interface}}$ and e^{strain} stand for the interfacial and constituent strain energies per surface area [29]. Clearly, in a finite size model the last two terms can strongly depend on the atomic arrangement. Therefore creating supercell models for calculating the interfacial energy or the mixing enthalpy with a common energy alignment of epitaxial substrate-alloy interfaces or metal-alloy multilayers is not a straightforward task.

The multilayer breaks the periodicity along the direction perpendicular to the layers (z). Thereby all properties have to be indexed with the layer number (λ) with keeping the homogeneity only in the two periodic directions (x and y) [20]. In Section 5 it will be shown that one has to take care of a composition profile through the interfaces and to ensure the same composition in all the layers of the SQS model to obtain results relevant for simulations of uniformly disordered multilayers.

3. Effective elastic properties of cubic TiAlN

In cubic systems the threefold rotation around the [1 1 1] direction transforms the canonical crystallographic direction [1 0 0] into [0 1 0] and [0 0 1] and accordingly the set of elastic constants (C_{11}, C_{12}, C_{44}) into (C_{33}, C_{13}, C_{66}) and (C_{22}, C_{23}, C_{55}). The SQS approach in general breaks the point group symmetry of the lattice [14]. Therefore, in general the elastic tensor of an SQS model has a symmetry class that is lower than what the simulated alloy. Indeed, the three sets of elastic constants (or the corresponding crystallographic directions) are not equivalent and thereby the consideration of only one set of them is inappropriate. Note that, an averaging technique was introduced in Refs. [14,30] to extract the symmetry averaged elastic tensor components.

To underline this directional variation of the elastic moduli for monocrystals, as well as for polycrystals we analyse the effective elastic constants of $Ti_{0.5}Al_{0.5}N$ derived in Ref. [14] and summarized in Table 1 for three different supercells shown in Fig. 1, an ordered $L1_0$ structure and two SQS supercells with size $(2\times2\times3)$ and $(4\times4\times4)$ in terms of the face-centered cubic (fcc) unit vectors. Elastic properties of polycrystalline materials, such as TiAlN, are

Table 1
Elastic constants of $Ti_{0.5}Al_{0.5}N$ using three structural models; the ordered $L1_0$ and two generated SQS supercells [14]. All quantities are in GPa.

SQS	C_{11}	C_{22}	C_{33}	C_{12}	C_{13}	C_{23}	C_{44}	C_{55}	C_{66}
$L1_0$	409	409	332	183	197	197	100	100	120
$(2\times2\times3)$	429	388	443	173	164	169	187	203	188
$(4\times4\times4)$	457	462	444	149	156	156	202	203	200
	$\overline{C}_{11}$			$\overline{C}_{12}$			$\overline{C}_{44}$		
$L1_0$	384			193			107		
$(2\times2\times3)$	420			169			193		
$(4\times4\times4)$	454			154			202		

most important for their technological applications. They are usually discussed in terms of effective elastic constants using the Reuss (G_R), Voigt (G_V) and Hill (G_H) averaging [31–33].

The isotropic elastic moduli G_R, G_V and G_H of polycrystalline $Ti_{0.5}Al_{0.5}N$ together with the derived bulk modulus B using the three different SQS models and the three sets of elastic constants are listed in Table 2. In addition, Table 2 shows the convergence of the bulk modulus B, the isotropic polycrystalline elastic moduli $G_{R/V/H}, E$ and A, together with the convergence of their direction dependent values. Note that values of the elastic tensor components for monocrystalline $Ti_{0.5}Al_{0.5}N$ simulated with $(4\times4\times4)$ SQS are well converged [14]. Therefore, we can consider the corresponding moduli calculated from symmetry averaged elastic tensor component for this supercell as references to measure the accuracy of other SQS models. The values indicated with Δ express the deviations of respective elastic moduli from this reference values. One can see, for instance, that the polycrystalline elastic moduli calculated for $(4\times4\times4)$ supercell show very small directional dependence.

On the contrary, the use of the ordered $L1_0$ structure to simulate the elastic moduli of the random alloy results, both in the large directional dependence of all the effective materials constants and in huge deviations with respect to the converged results. For instance, in case of G_R one gets almost 50% deviation (Δ) in [0 0 1] from the converged value. Smaller, but still significant directional variations are obtained in case of the $(2\times2\times3)$ structure. The Zener's elastic anisotropy shows extreme directional dependence in both cases. One can see from Table 2 that even for the $(2\times2\times3)$ SQS that simulate a random rather than the ordered alloy, the error in calculated elastic anisotropy can get to ≈40% if an unfortunate direction of the supercell is chosen for the simulation. Note that the use of the symmetrization technique [14] for this SQS brings the deviations of all the polycrystalline elastic moduli within 10% from the converged value and the Zener's elastic anisotropy within 15%.

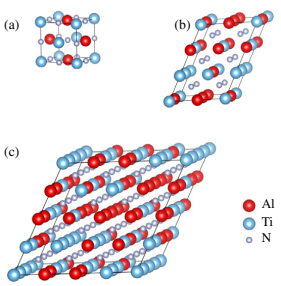

Fig. 1. Structural models to simulate $Ti_{0.5}Al_{0.5}N$. (a) Is the ordered $L1_0$ structure, (b and c) show SQS structures with a size of $(2\times2\times3)$ and $(4\times4\times4)$ in terms of the face-centered cubic unit vectors.

Thus, different SQS break the point symmetry differently of the simulated alloy, what might result in large directional variation of the calculated effective elastic moduli. These discrepancies vanish with increased system size by including larger amount of different local environments. This fact together with the better convergence of all the isotropic elastic moduli derived from the projected elastic constants underline the validity of the projection technique.

4. Metal vacancy formation energies in $Ti_{0.5}Al_{0.5}N$

In the thermodynamic limit vacancy formation does not change either the average atomic configuration $\bar{\sigma}$ or the composition x of the alloy. However, in the finite supercell approach the removal of a metal atom alters both, $(\bar{\sigma}_0 \to \bar{\sigma})$ and $(x_0 \to x)$. Therefore, finite size energy corrections have to be introduced, $\delta E_{\text{conc.}}$ for the concentration and $\delta E_{\text{conf.}}$ for the configurational change. The concentration correction can be done by calculating the chemical potential in the alloy. The configurational correction is much more difficult to deal with. Here we propose to determine it by making a cluster expansion in the alloy with and without vacancy and using the bulk effective cluster interactions (ECIs). The alloy ECIs correspond to w_f in Eq. (2) if the alloy energy is expanded as a function of configurations.

In this study the ECIs of TiAlN were taken from Ref. [34]. In the finite size SQS the metal vacancy formation energies in TiAlN can be written as

$$E_{\text{vf}}^{\text{Ti/Al}}(\bar{\sigma},x) = E_{N-1}(\bar{\sigma},x,V) - E_N(\bar{\sigma},x,V) + \frac{E_N^{\text{Ti/Al}}(V)}{N} \tag{4}$$

where the correction is applied on the host alloy supercell with N metal atoms specified by atomic configuration $\bar{\sigma}_0$ and composition x_0,

$$\begin{aligned} E_N(\bar{\sigma},x,V) &= E_N(\bar{\sigma}_0,x,V') + \delta E_{\text{conf.}}(\bar{\sigma},x) \\ &= E_N(\bar{\sigma}_0,x_0,V_0) + \delta E_{\text{conc.}}(\bar{\sigma}_0) + \delta E_{\text{conf.}}(\bar{\sigma},x). \end{aligned} \tag{5}$$

Here $\bar{\sigma}$ is the changed configuration and x is the changed composition obtained by vacancy creation. The Vs denote the optimised volumes at ambient conditions ($T = 0$ K, $p = 0$ GPa).

In modelling the alloy a large $(4\times4\times4)$ SQS supercell, based on the B1 fcc Bravais cell, was generated by optimising the Warren–Cowlley short-range order (SRO) parameters [22] in the seven nearest coordination shells, see Fig. 2(a).

To underline the strong variation of the vacancy formation energies with the local environment we derived the vacancy formation energies of two Al atoms with clearly distinguishable atomic neighbourhoods and using fcc-Al reservoir. The calculations were done using the Quantum Espresso program package [3]. The exchange correlation energy was approximated by the PBE generalized gradient functional [35].

Fig. 2(b) and (c) exhibit the two local environments with different amount of Al atoms and different type of distribution of them. In env. #1 one counts less Al atoms in the 1st and 2nd metallic shells than env. #2. Whereas, env. #2 shows a fairly homogeneous (spherical) distribution of the Al atoms than env. #1. The calculated vacancy formation energies are listed in Table 3.

In both cases we obtained positive vacancy formation energies, what reflects the stability of that Al atoms. However, the two formation energies deviate largely from each other, around 11%. Table 3 gives the value of the corrections, too. Beyond the fact that both corrections are large, $\delta E_{\text{conf.}}$ is about 10% of $E_{\text{vf}}^{\text{Al}}$, the configurational correction has a different sign in the two local environments.

Thus, we conclude the necessity of both corrections and establish the strong variation of the vacancy formation energies with respect to the local environments. Furthermore, the results point

Table 2
The bulk modulus (B), Reuss (G_R), Voigt (G_V) and Hill (G_H) polycrystalline elastic and Young's (E) moduli, the Zener's elastic anisotropy (A) of $Ti_{0.5}Al_{0.5}N$ together with their symmetry averaged values using the three different directions ([100], [001], [010]) of the orders $L1_0$ structure and two SQS supercells. The values are in GPa. The relative deviations (Δ) are calculated with respect the value obtained by the symmetry averaged elastic constants of the $(4 \times 4 \times 4)$ supercell and are read in %.

SQS	$B^{[100]}$	$B^{[001]}$	$B^{[010]}$	$\overline{B}$	$\Delta B^{[100]}$	$\Delta B^{[001]}$	$\Delta B^{[010]}$	$\Delta\overline{B}$
$L1_0$	258	242	268	257	1.71	−4.72	5.38	1.18
$(2 \times 2 \times 3)$	258	257	242	253	1.71	1.18	−4.72	−0.39
$(4 \times 4 \times 4)$	252	252	258	254	−0.92	−0.79	1.576	
	$G_R^{[100]}$	$G_R^{[001]}$	$G_R^{[010]}$	$\overline{G}_R$	$\Delta G_R^{[100]}$	$\Delta G_R^{[001]}$	$\Delta G_R^{[010]}$	$\Delta\overline{G}_R$
$L1_0$	105	92	102	102	−40.91	−48.41	−42.32	−42.37
$(2 \times 2 \times 3)$	158	165	151	159	−11.00	−6.96	−14.70	−10.17
$(4 \times 4 \times 4)$	180	173	180	177	1.24	−2.44	1.20	
	$G_V^{[100]}$	$G_V^{[001]}$	$G_V^{[010]}$	$\overline{G}_V$	$\Delta G_V^{[100]}$	$\Delta G_V^{[001]}$	$\Delta G_V^{[010]}$	$\Delta\overline{G}_V$
$L1_0$	105	99	102	102	−41.94	−45.36	−43.49	−43.65
$(2 \times 2 \times 3)$	163	169	166	166	−9.82	−6.95	−8.61	−8.29
$(4 \times 4 \times 4)$	183	178	183	181	0.88	−1.98	0.99	
	$G_H^{[100]}$	$G_H^{[001]}$	$G_H^{[010]}$	$\overline{G}_H$	$\Delta G_H^{[100]}$	$\Delta G_H^{[001]}$	$\Delta G_H^{[010]}$	$\Delta\overline{G}_H$
$L1_0$	105	95	102	102	−41.43	−46.87	−42.91	−43.02
$(2 \times 2 \times 3)$	161	167	158	162	−10.40	−6.96	−11.62	−9.50
$(4 \times 4 \times 4)$	181	175	181	179	1.06	−2.21	1.10	
	$E^{[100]}$	$E^{[001]}$	$E^{[010]}$	$\overline{E}$	$\Delta E^{[100]}$	$\Delta E^{[001]}$	$\Delta E^{[010]}$	$\Delta\overline{E}$
$L1_0$	277	253	272	271	−36.28	−41.98	−37.45	−37.70
$(2 \times 2 \times 3)$	399	411	390	401	−8.33	−5.51	−10.39	−7.82
$(4 \times 4 \times 4)$	438	427	441	435	0.68	−1.94	1.19	
	$A^{[100]}$	$A^{[001]}$	$A^{[010]}$	$\overline{A}$	$\Delta A^{[100]}$	$\Delta A^{[001]}$	$\Delta A^{[010]}$	$\Delta\overline{A}$
$L1_0$	0.89	1.78	0.94	1.12	−34.29	32.01	−29.95	−17.04
$(2 \times 2 \times 3)$	1.46	1.35	1.85	1.54	8.49	0.07	37.66	14.07
$(4 \times 4 \times 4)$	1.31	1.39	1.33	1.35	−2.60	3.14	−1.48	

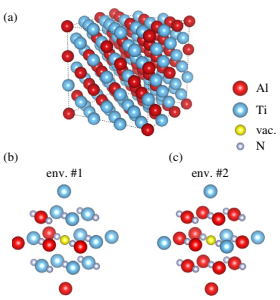

Fig. 2. (a) The $(3 \times 3 \times 3)$ binary SQS supercell with vanishing SROs up to the seventh shell. (b and c) Show two particular environments up to the 2nd metallic coordination shell.

Table 3
Al vacancy formation energies for two particular local environments in $Ti_{0.5}Al_{0.5}N$. All quantities are in eV.

Vacancy	E_{vf}^{Al}	$\delta E_{conc.}$	$\delta E_{conf.}$
env. #1	3.94	−2.63	0.35
env. #2	4.38	−2.63	−0.43

out a request on the interpretation of the several different vacancy formation energies that can be derived from different SQS supercells.

5. Mixing enthalpy of TiN/$Ti_{0.5}Al_{0.5}N$ multilayer

In inhomogeneous systems, such as multilayers with interfaces, an ultimate goal is the prediction of the mixing enthalpy and the spinodal curve with respect the multilayer periodicity, thickness. In terms of Eq. (3) it means an accurate access to the interfacial and the constituent strain energies. Ozoliņš et al. [29] have derived a technique to obtain this quantities for epitaxial films and superlattices. Here we focus ourself on a metal-alloy multilayer, the TiN/$Ti_{0.5}Al_{0.5}N$ system.

Our aim is to underline the dependence of the derived mixing enthalpy values on the chosen SQS supercell in modelling a sharp interface. Thus, we generated three different bulk models with a size of $(3 \times 3 \times 3)$ and sandwiched them between two TiN layers, see Fig. 3. The model #1 was created by optimising the bulk

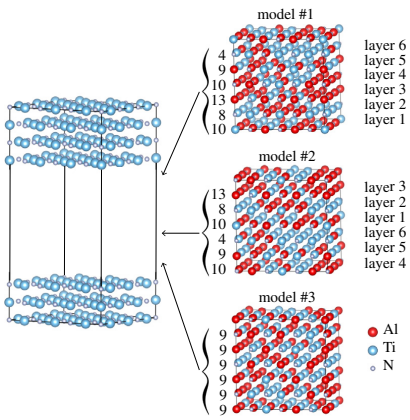

Fig. 3. Three different bulk SQS models of $Ti_{0.5}Al_{0.5}N$ to build the multilayer of TiN/$Ti_{0.5}Al_{0.5}N$.

Warren–Cowlley SRO parameters up to the seventh shell with allowing arbitrary composition profile (homogeneity). Model #2 was obtained from model #1 by a layer shift explained in Fig. 3. The model #3 has also been derived by optimising the bulk Warren–Cowlley SRO parameters up to the seventh shell but with keeping the same composition in each layer, $x_i = 0.5$.

In all the three supercells the final bulk SRO parameters vanish up to the seventh coordination shell. The in-plane (layer) SRO parameters – SRO parameters calculated in the two dimensional atomic layers parallel to the interface, show strong variations shown in Table 4. In model #1 and #2 the SRO parameters are large even in the most important 1st and 2nd shells. We establish that the model #3 model describes the in-plane randomness better than the other two ones, except a mid-layer, layer 4. However, the most relevant difference between the three models are the layer compositions x_i listed also in Table 4, especially at the interface with TiN. Model #3 has the proper constrained value $x_i = 0.5$ in each layer so that it also represents bulk randomness. We underline, that this corresponds to the proper treatment of inhomogeneous systems, see Ref. [20].

Density functional calculations using the Vienna Ab-initio Simulation Package [2] have been performed to derive total energies and the structural parameters of the multilayer models. We used the PBE generalized gradient functional [35] with 400 eV cut-off and a $4 \times 4 \times 2$ sampling of the Brillouin zone [36] for the multilayer structures. Table 5 shows the calculated lattice parameters a and c in Å,the total energies per surface area e in eV/Å^2 unit and the mixing (alloying) enthalpy

$$\Delta H = \frac{E_{\mathrm{TiN/Ti_{0.5}Al_{0.5}N}} - (1/2)E_{\mathrm{TiN}} - (1/2)E_{\mathrm{TiN/AlN}}}{N} \qquad (6)$$

in eV/atom, where N is the total number of atoms in the $Ti_{0.5}Al_{0.5}N$ slab of the multilayer.

Fig. 4 shows the variation of ΔH with the applied SQS supercell model, compared with the corresponding bulk $Ti_{0.5}Al_{0.5}N$ mixing enthalpies. For the comparison the bulk values have to be divided by the $Ti_{0.5}Al_{0.5}N$ content ratio in the multilayer; that is with 2 in our cases.

We see that while all the bulk models give accurately the same bulk mixing enthalpy – 2% deviation, the values for the multilayer (ML) models scatter. Model #2 results in a value that deviates more than 7% from the one obtained by model #3 with constrained in-plane composition. As the obtained lattice parameters of the models are the same we conclude that the strain energy contribution to the total energy in Eq. (3) is the same. Therefore, the reason of this scattering is the different interfacial energy $e^{\mathrm{interface}}$ in the models, what is clearly the consequence of the structural differences.

Table 4
The layer composition x_i and the layer Warren–Cowlley SRO parameters of three SQS models.

	x_i	1st	2nd	3rd	4th	5th	6th	7th
	Model #1 and #2							
Layer 1	0.56	−0.01	−0.01	−0.13	−0.01	−0.01	−0.35	−0.13
Layer 2	0.44	0.21	0.10	−0.24	−0.24	0.10	−0.35	−0.24
Layer 3	0.72	0.17	−0.11	−0.11	−0.11	−0.11	−0.38	−0.11
Layer 4	0.56	−0.01	0.10	−0.24	−0.01	0.10	−0.35	−0.24
Layer 5	0.50	−0.22	−0.22	0.22	0.11	−0.22	−0.56	0.22
Layer 6	0.22	0.20	−0.13	−0.13	−0.13	−0.13	−0.29	−0.13
	Model #3							
Layer 1	0.50	0.00	−0.22	0.00	0.11	−0.22	−0.56	0.00
Layer 2	0.50	0.00	0.00	−0.22	0.00	0.00	−0.11	−0.22
Layer 3	0.50	0.00	0.00	−0.22	0.00	0.00	−0.11	−0.22
Layer 4	0.50	−0.44	0.22	0.22	−0.22	0.22	−0.11	0.22
Layer 5	0.50	0.11	0.22	−0.22	−0.22	0.22	−0.56	−0.22
Layer 6	0.50	0.00	−0.33	0.11	0.00	−0.33	−0.11	0.11

Table 5
Structural parameters and energies of bulk $Ti_{0.5}Al_{0.5}N$ and the multilayer (ML) of TiN/$Ti_{0.5}Al_{0.5}N$. The lattice parameters a and c are in Å, the energy $e = E/a^2$ in eV/Å^2 and the mixing enthalpy per atom, $\Delta H/N$ in unit of eV/atom.

	Size	a	c	e	$\Delta H/N$
Bulk model #1	$(3 \times 3 \times 3)$	12.52		−11.610	0.102
Bulk model #2	$(3 \times 3 \times 3)$	12.52		−11.610	0.102
Bulk model #3	$(3 \times 3 \times 3)$	12.53		−11.600	0.100
ML model #1	$(3 \times 3 \times 6)$	12.66	25.28	−24.560	0.078
ML model #2	$(3 \times 3 \times 6)$	12.66	25.28	−24.539	0.086
ML model #3	$(3 \times 3 \times 6)$	12.65	25.28	−24.580	0.080
TiN	$(3 \times 3 \times 3)$	12.76		−12.986	
AlN	$(3 \times 3 \times 3)$	12.21		−10.538	

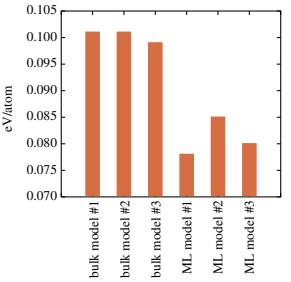

Fig. 4. A comparison of the mixing enthalpy in bulk $Ti_{0.5}Al_{0.5}N$ and the multilayer (ML) of TiN/$Ti_{0.5}Al_{0.5}N$ in unit of eV/atom using three different bulk SQS models.

These draw our attention not only to the fact that the local interfacial interactions have significant effects, which results in different interfacial energies, but also that improper usage of SQS supercells may result in a large discrepancy and erroneous theoretical findings. Furthermore, these results reveal the method of aligning the energy values in calculating composition derivatives, such as the spinodal curve, by constraining the in-plane composition x_i – using model #3.

6. Summary

In this study we discuss the challenges of special quasirandom structure approach in modelling the cubic elastic constants, the vacancy formation energies in cubic B1 $Ti_{0.5}Al_{0.5}N$ and the interfacial effects in TiN/$Ti_{0.5}Al_{0.5}N$. The SQS approach is a successful scheme to model and predict the thermodynamic properties of alloys, yet the technique has to be applied carefully as quantities that are influenced by the global symmetry and/or local chemical environment may converge quite slow with the supercell size, and may depend stronger on the SQS configuration.

Using a symmetry based projection technique one is able to overcome the fact that different SQS supercells break the point symmetry differently and thereby represent the elastic behaviour of the simulated system distinctly. Here, we demonstrated the strong dependence of the polycrystalline cubic elastic moduli of $Ti_{0.5}Al_{0.5}N$ on the used supercell and underlined the directional dependence of the calculated effective isotropic elastic constants with respect to the SQS model. We illustrated the validity of the projection technique in extracting the elastic properties of alloys.

In a finite size SQS model the vacancy formation changes not only the composition but also the SQS configuration. Therefore, correction techniques are required. We showed on the example of Al vacancies in $Ti_{0.5}Al_{0.5}N$, that these corrections are large and environment dependent, that is the vacancy formation energies correlate strongly with the local environments. Furthermore, we

pointed out the need of interpreting the several different vacancy formation energies that can be obtained from different SQS supercells.

The interface in TiN/$Ti_{0.5}Al_{0.5}N$ affects the decomposition thermodynamics of the $Ti_{0.5}Al_{0.5}N$ slab. While the different SQS models can agree accurately in the mixing enthalpy value of bulk $Ti_{0.5}Al_{0.5}N$, they might represent the interfacial effects differently and therefore result in different values. We emphasise that in multilayers all properties have to be indexed with the layer number (λ). Therefore, SQS supercells have to be generated with keeping the compositional homogeneity in each layers. This establishes the way of making an alignment of the SQS models with keeping the same composition in each layer in calculating derivatives of the mixing enthalpy, such as the spinodal curve.

In summary, in this manuscript we discussed some challenges of the SQS approach and suggested methodological corrections for the safe application of this efficient technique.

Acknowledgemnts

Prof. Sergei Simak at Linköping University is acknowledged for the help in generating the different SQS supercells used in this study. This work was supported by the SSF project Designed Multicomponent coatings, MultiFilms and the Swedish Research Council (VR). The calculations were performed at Swedish National Infrastructure for Computing (SNIC). F. Wang acknowledges the Erasmus Mundus Programme of the European Commission within the Doctoral Programme DocMASE for financial support. I.A. Abrikosov acknowledges the support from the Grant of Ministry of Education and Science of the Russian Federation (Grant No. 14.Y26.31.0005) and The Tomsk State University Academic D.I. Mendeleev Fund Program.

References

[1] Materials Genome Initiative for Global Competitiveness, 2011, <www.materialsproject.org>.
[2] G. Kresse, J. Furthmüller, Comput. Mater. Sci. 6 (1996) 15–50.
[3] P. Giannozzi, S. Baroni, N. Bonini, M. Calandra, R. Car, C. Cavazzoni, D. Ceresoli, G.L. Chiarotti, M. Cococcioni, I. Dabo, et al., J. Phys.: Condens. Matter 21 (2009) 395502.
[4] B. Amadon, P.-M. Anglade, J.-M. Beuken, F. Bottin, P. Boulanger, F. Bruneval, D. Caliste, R. Caracas, M. Cote, T. Deutsch, L. Genovese, Ph. Ghosez, M. Giantomassi, S. Goedecker, D.R. Hamann, P. Hermet, F. Jollet, G. Jomard, S. Leroux, M. Mancini, S. Mazevet, M.J.T. Oliveira, G. Onida, Y. Pouillon, T. Rangel, G.-M. Rignanese, D. Sangalli, R. Shaltaf, M. Torrent, M.J. Verstraete, G. Zerah, J.W. Zwanziger, Comput. Phys. Commun. 180 (2009) 2582–2615.
[5] A. Jain, S.P. Ong, G. Hautier, W. Chen, W.D. Richards, S. Daeck, S. Cholia, D. Gunter, D. Skinner, G. Ceder, K.A. Persson, APL Mater. 1 (2013) 011002.
[6] H. Lind, F. Tasnádi, I.A. Abrikosov, New. J. Phys. 15 (2013) 095010.
[7] P. Mayrhofer, C. Mitterer, L. Hultman, H. Clemens, Prog. Mater. Sci. 51 (2006) 1032.
[8] P. Steneteg, O. Hellman, O.Y. Vekilova, N. Shulumba, F. Tasnádi, I.A. Abrikosov, Phys. Rev. B 87 (2013) 094114.
[9] D.G. Sangiovanni, D. Edström, D. Edström, L. Hultman, I. Petrov, J.E. Green, V. Chirita, Surf. Sci. 624 (2014) 25.
[10] A. Zunger, S.-H. Wei, L. Ferreira, J. Bernard, Phys. Rev. Lett. 65 (1990) 353.
[11] F. Tasnádi, B. Alling, C. Höglund, G. Wingqvist, J. Birch, L. Hultman, I.A. Abrikosov, Phys. Rev. Lett. 104 (2010) 137601.
[12] G. Wingqvist, F. Tasnádi, A. Zukauskaite, J. Birch, H. Arwin, L. Hultman, Appl. Phys. Lett. 97 (2010) 112902.
[13] F. Tasnádi, I.A. Abrikosov, L. Rogström, J. Almer, M.P. Johansson, M. Oden, Appl. Phys. Lett. 97 (2010) 231902.
[14] F. Tasnádi, M. Odén, I.A. Abrikosov, Phys. Rev. B. 85 (2012) 144112.
[15] P.H. Mayrhofer, D. Music, J.M. Schneider, J. Appl. Phys. 100 (2006) 094906.
[16] D. Holec, R. Rachbauer, L. Chen, L. Wang, D. Luef, P.H. Mayrhofer, Surf. Coat. Technol. 206 (2011) 1698.
[17] D. Holec, L. Zhou, R. Rachbauer, P.H. Mayrhofer, J. Appl. Phys. 113 (2013) 113510.
[18] F. Tasnádi, I.A. Abrikosov, I. Katardjiev, Appl. Phys. Lett. 94 (2009) 151911.
[19] F. Bernardini, V. Fiorentini, Phys. Rev. B 64 (2001) 085207.
[20] A.V. Ruban, I.A. Abrikosov, Rep. Prog. Phys. 71 (2008) 046501.
[21] D.P. Landau, K. Binder, A Guide to Monte Carlo Simulations in Statistical Physics, third ed., Cambridge University Press, 2009.
[22] J. Cowley, Phys. Rev. 77 (1950) 669.
[23] K. Mäder, A. Zunger, Phys. Rev. B 51 (1995) 10462.
[24] A. van de Walle, Nat. Mater. 7 (2008) 455.
[25] D. Morgan, D.J. Althoff, D. Fontaine, J. Phase Equilibr. 19 (1998) 559.
[26] A. Van der Ven, G. Ceder, Phys. Rev. B. 71 (2005) 054102.
[27] M. Muzyk, D. Nguyen-Manh, K.J. Kurzydłowski, N.L. Baluc, S.L. Dudarev, Phys. Rev. B 84 (2011) 104115.
[28] J.B. Piochaud, T.P.C. Klaver, G. Adjanor, P. Olsson, C. Domain, C.S. Becquart, Phys. Rev. B 89 (2014) 024101.
[29] V. Ozoliņš, C. Wolverton, A. Zunger, Phys. Rev. B 57 (1998) 4816.
[30] M. Moakher, A.N. Norris, J. Elast. 85 (2006) 215.
[31] W. Woigt, Lehrburch der Kristallphysik Teubner Leipzig, 1928.
[32] A. Reuss, Z. Angew. Math. Mech. 9 (1929) 49.
[33] R. Hill, Proc. Phys. Soc. London 65 (1952) 396.
[34] B. Alling, A. Ruban, A. Karimi, L. Hultman, I. Abrikosov, Phys. Rev. B 83 (2011) 104203.
[35] J.P. Perdew, K. Burke, M. Ernzerhof, Phys. Rev. Lett. 77 (1996) 3865.
[36] H. Monkhorst, J. Pack, Phys. Rev. B 13 (1976) 5188.

Paper II

Coherency effects on the mixing thermodynamics of cubic $Ti_{1-x}Al_xN$ /TiN(001) multilayers

Fei Wang
Igor A. Abrikosov
Sergei I. Simak
Magnus Odén
Frank Mücklich
Ferenc Tasnádi

PHYSICAL REVIEW B, **93**, 174201 (2016)

PHYSICAL REVIEW B **93**, 174201 (2016)

Coherency effects on the mixing thermodynamics of cubic $Ti_{1-x}Al_xN$/TiN(001) multilayers

Fei Wang,[1,2,*] Igor A. Abrikosov,[1,3,4] Sergei I. Simak,[1] Magnus Odén,[1] Frank Mücklich,[2] and Ferenc Tasnádi[1]

[1]*Department of Physics, Chemistry and Biology (IFM), Linköping University, SE-581 83 Linköping, Sweden*

[2]*Functional Materials, Materials Science and Engineering Department (MSE), Saarland University, P.O. Box 151150, 66041 Saarbrücken, Germany*

[3]*Materials Modeling and Development Laboratory, NUST "MISIS," 119049 Moscow, Russia*

[4]*LACOMAS Laboratory, Tomsk State University, 634050 Tomsk, Russia*

(Received 7 January 2016; revised manuscript received 1 April 2016; published 9 May 2016)

In this work, we discuss the mixing thermodynamics of cubic (B1) $Ti_{1-x}Al_xN$/TiN(001) multilayers. We show that interfacial effects suppress the mixing enthalpy compared to bulk $Ti_{1-x}Al_xN$. The strongest stabilization occurs for compositions in which the mixing enthalpy of bulk $Ti_{1-x}Al_xN$ has its maximum. The effect is split into a strain and an interfacial (or chemical) contribution, and we show that both contributions are significant. An analysis of the local atomic structure reveals that the Ti atoms located in the interfacial layers relax significantly different from those in the other atomic layers of the multilayer. Considering the electronic structure of the studied system, we demonstrate that the lower Ti-site projected density of states at ϵ_F in the $Ti_{1-x}Al_xN$/TiN multilayers compared to the corresponding monolithic bulk explains a decreased tendency toward decomposition.

DOI: 10.1103/PhysRevB.93.174201

I. INTRODUCTION

Superhard materials have been synthesized in the form of superlattices, such as TiN/V(Nb)N [1–3] and ZrN/CN [4], or as nanocomposites, ZrN-SiN [5], etc. Three major effects—the lattice strain (coherency) and elastic mismatch [6] and the interfacial chemistry—are generally attributed to the observed interfacial strengthening [7]. It has been shown that in multilayers with coherent interfaces, the relevant one is the coherency strain effect [8]. However, one should stress that decoupling the strain or lattice mismatch effects from the chemical ones is not straightforward.

Ozoliņš *et al.* [9] have developed a theoretical approach to discuss the *ab initio* thermodynamics of immiscible superlattices. In this technique, one splits the superlattice formation energy into a constituent strain and interfacial or chemical contribution, which allows for a separation of the strain effects from the chemical ones. Crystallographic investigations (diffraction-based techniques such as XRD, TEM, etc.) of multilayers access lattice parameters and interlayer distances that are affected by the interfacial chemistry. Therefore, the extracted coherency strain is not equal to the derived theoretical constituent strain.

In $Ti_{1-x}Al_xN$/TiN(001) multilayers, extended age hardening is observed [10,11] by the spinodal decomposition of $Ti_{1-x}Al_xN$ [12]. Understanding the role of lattice coherency and interfacial chemistry on the driving force of this decomposition process is unexplored. However, modeling multilayers built from alloys is a theoretical challenge [13]. Van de Walle used the cluster expansion technique to predict the compositional profile in Samarium-doped coherent Ceria superlattices [14], and convergence was achieved with the inclusion of 70 000 atoms. Advanced theoretical investigations based on the special quasirandom structure (SQS) approach [15] have exposed the electronic origin of the thermodynamic instability in $Ti_{1-x}Al_xN$ alloys [12]. Recent molecular-dynamics simulations confirm the high positive value of the mixing free energy in $Ti_{1-x}Al_xN$ alloys at elevated temperature [16].

In this work, we investigate the effect of lattice coherency on the mixing thermodynamics in cubic (B1) $Ti_{1-x}Al_xN$/TiN(001) multilayers. We extend the method by Ozoliņš *et al.* [9] to multilayers with alloys, and we introduce a decomposition of the observed effect into strain and chemical (interfacial) contributions. We base our description on the concept of coherency strain rather than the constituent one because it allows us to connect the results of the simulations to an experimental interpretation. We propose that both strain and interface chemistry contribution are important, and we show that the chemical effect gives rise to a displacement from the ideal positions of the Ti atoms on both sides of the interface. By calculating the Ti-site partial density of states, we reveal the electronic contribution to the stabilization of $Ti_{1-x}Al_xN$/TiN(001) multilayers.

II. CALCULATIONAL DETAILS

The multilayer (ML) structures were generated by sandwiching ℓ_1 monolayers of B1 $Ti_{1-x}Al_xN$ between ℓ_2 monolayers of B1 TiN periodically along the [001] orientation. The two cubic slabs form a coherent interface. The in-plane size of the models was (3×3) based on the B1 conventional cell. We generated multilayers with two different periodicities, i.e., ℓ_1/ℓ_2 was either 6/6 or 12/6. The alloys were modeled within the special quasirandom structure approach [15] with an Al mole fraction (x) grid starting from 0 up to 1 using steps of 1/9. The atomic configurations in the $Ti_{1-x}Al_xN$ supercells were obtained by minimizing the Warren-Cowley pair short-range-order (SRO) [17,18] parameters up to the seventh nearest-neighboring shells in the metal sublattice while demanding the same Al concentration in each monolayer [13]. This provides an alignment of the ML models for different x. The assumption of a sharp compositional interfacial region is valid if the interface thickness is negligible with respect to the slab thicknesses of both $Ti_{1-x}Al_xN$ and TiN. Furthermore,

*feiwa@ifm.liu.se

Chu and Barnett [19] have investigated superlattices with finite interface width using a phenomenological model that provided quantitative agreements with experiments for nitride superlattices. They predicted larger interfacial strengthening for sharper interfaces.

The mixing enthalpy in the $Ti_{1-x}Al_xN$/TiN(001) multilayer is calculated by the energy difference

$$\Delta H^{\mathrm{Ti}_{1-x}\mathrm{Al}_x\mathrm{N}/TiN}(x,\ell_1,\ell_2) = \frac{1}{N}\left(E^{\mathrm{Ti}_{1-x}\mathrm{Al}_x\mathrm{N}/\mathrm{TiN}}_{\ell_1/\ell_2}(x) - (1-x)E^{\mathrm{TiN}}_{\ell_1/\ell_2} - xE^{\mathrm{AlN}/\mathrm{TiN}}_{\ell_1/\ell_2}\right), \quad (1)$$

where N is the total number of atoms in the $Ti_{1-x}Al_xN$ slab; E^A_ℓ denotes the total energy of material A with ℓ layers along (001), which is taken for the calculated equilibrium volume for each specific system and composition.

The total energy calculations were performed within density functional theory (DFT) using the projector augmented wave (PAW) [20] approach implemented in the Vienna Ab initio Simulation Package (VASP) [21–23]. The exchange-correlation energy was approximated by the Perdew-Burke-Ernzerhof generalized gradient functional (PBE-GGA) [24,25]. In the calculations, we applied a plane-wave cutoff energy of 400 eV, and reciprocal-space integration was performed within the Monkhorst-Pack scheme [26] using k-meshes of $(4\times4\times2)$ for $\ell_1/\ell_2 = 6/6$ and $(3\times3\times1)$ in the case of $\ell_1/\ell_2 = 12/6$. These parameters result in ≈ 1 meV/at accuracy in the mixing enthalpy. The structural parameters of the SQS supercells were relaxed while keeping the tetragonal cell shape. The total and projected density-of-states calculations were done on the relaxed structures using a higher k-mesh: $(6\times6\times3)$ for the 6/6 multilayer and $(6\times6\times6)$ for bulk. The energy cutoff was then changed to 520 eV.

III. RESULTS AND DISCUSSION

Figure 1 shows the calculated mixing enthalpies of $Ti_{1-x}Al_xN$ in multilayers (MLs) compared with its monolithic (bulk) form. The bulk values match well with other literature [12]. All the mixing enthalpy values are positive, indicating a thermodynamic driving force toward phase separation. The ML mixing enthalpies are significantly suppressed with respect to the bulk values, which means that in the multilayer structure the coherent TiN confinement has a stabilization effect on the $Ti_{1-x}Al_xN$ slab. It confirms the differential scanning calorimetry observation that $Ti_{1-x}Al_xN$ slabs in multilayers have an improved thermal stability [10]. The stabilization effect is smaller in the thicker 12/6 ML as the overall system is more similar to the bulk alloy. However, this decrease is not just an arithmetic consequence of having twice as many atoms in the 12/6 ML; see the dashed lines in Fig. 1.

Furthermore, the ML curves maxima show the same asymmetric shift to higher compositions as in the bulk. Comparing the 6/6 and 12/6 MLs, one sees that this tilting toward higher compositions is lower in the 12/6 case, which suggests a compositionally increasing term that is gradually decreasing with increased periodicity. A quantity that behaves in this way is the in-plane lattice mismatch (strain) shown in Fig. 2. It provides evidence of the in-plane strain effects on the mixing enthalpy.

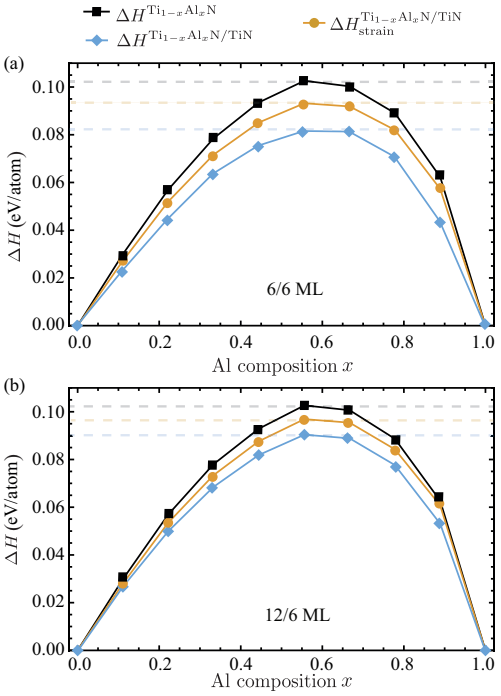

FIG. 1. The mixing enthalpy of bulk $Ti_{1-x}Al_xN$ (*ab initio*), the mixing enthalpy with the coherency strain effect, and the mixing enthalpy (*ab initio*) of $Ti_{1-x}Al_xN$/TiN multilayer (ML). (a) 6/6 ML and (b) 12/6 ML. The dashed lines show the maximum of the mixing enthalpy values for the bulk and the different ML case.

Figure 2 shows the lattice parameter differences between bulk $Ti_{1-x}Al_xN$ at arbitrary x and the relaxed B1-AlN and B1-TiN lattices (dashed lines). This strain is heavily reduced in the multilayers as the lattice parameter of the B1-AlN/TiN

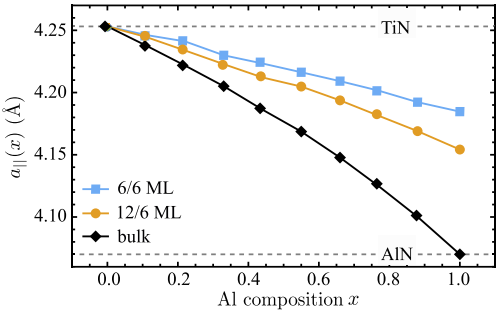

FIG. 2. In-plane lattice parameters of multilayers 6/6 and 12/6: $a_{\mathrm{Ti}_{1-x}\mathrm{Al}_x\mathrm{N}/\mathrm{TiN}}$ and bulk: $a_{\mathrm{Ti}_{1-x}\mathrm{Al}_x\mathrm{N}}$.

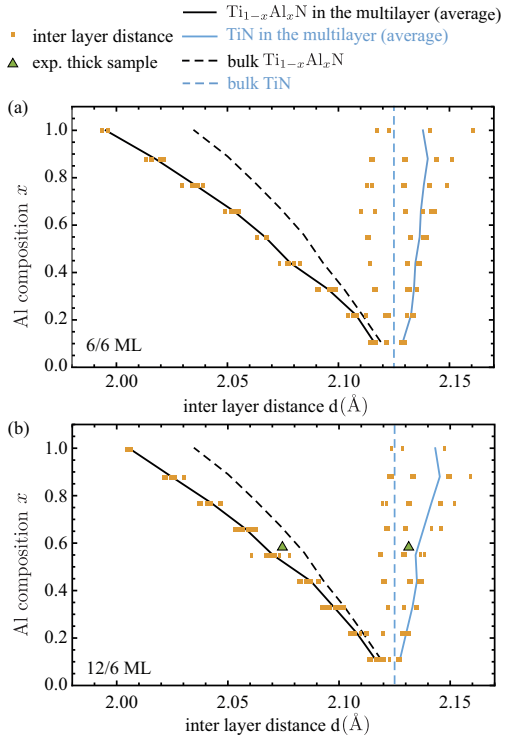

FIG. 3. The calculated averaged interlayer distances d using the fully relaxed structures of both MLs. (a) 6/6 ML and (b) 12/6 ML. The solid lines show the average of the interlayer distance for $Ti_{1-x}Al_xN$ and TiN in the MLs, while the dashed lines show the bulk cases.

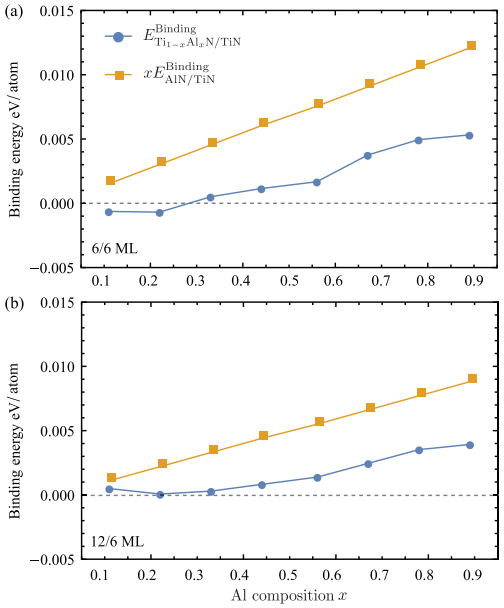

FIG. 4. Comparison of the two chemical effects (normalized binding energy), the one from $Ti_{1-x}Al_xN/TiN$ and the other form AlN/TiN in the mixing enthalpy of the $Ti_{1-x}Al_xN/TiN$ multilayer. (a) shows the 6/6 ML while (b) displays the 12/6 ML.

multilayer is significantly larger than B1-AlN. One also sees that this in-plane lattice mismatch is larger in the 12/6 ML than in the 6/6 ML [higher gradient of $a_{||}(x)$], which correlates with the smaller stabilization effect observed for 12/6 ML in Fig. 1.

Figure 3 shows the calculated averaged interlayer distances d using the fully relaxed structures of the MLs. It is seen that at each composition x one observes mainly three branches of points. Inside the $Ti_{1-x}Al_xN$ slab, the interlayer distance scatter is small while in the TiN slab one finds two branches. The solid lines show the average of the interlayer distance for $Ti_{1-x}Al_xN$ and TiN in the MLs, while the dashed lines plot d in the bulk cases. It is clear that in both multilayers, the $Ti_{1-x}Al_xN$ slab shrinks along the [001] direction with respect to the bulk while the TiN layer expands. A multilayer sample was grown using an industrial reactive cathodic arc evaporation system from Sulzer/Metaplas (MZR-323); see more experimental details in Ref. [27]. The layer distances of the sample with $x = 0.58$, 6.2 μm thickness, and a bilayer period of 37 nm were obtained by measuring the plane spacing in the direction normal to the surface for the 422 lattice planes. The plane spacings of $Ti_{0.42}Al_{0.58}N$ and TiN (normal to surface) are 4.15 and 4.263 Å, respectively. The corresponding interlayer distances are also plotted in Fig. 3(b) as green triangles. Focusing only on the $Ti_{1-x}Al_xN$ slab, one sees that for any x it shrinks less in the 12/6 ML than in the 6/6. This is in accord with that observed in Fig. 2, and therefore the same stabilization argument can be used. The fact that these two figures coherently express the strain effect on the mixing enthalpy of the multilayers suggests that the structural misfit can be used as a partial measure of the relative energetics of the multilayer.

To quantify the full effect of strain on the mixing enthalpy in Eq. (1), one needs to include both the coherent in-plane lattice parameters and the modified lattice structure along the (001) growth direction. One can assume that an experimental structure analysis of the thick multilayers that are grown in practice would result in three peaks for the interlayer distances d along [001]: (i) bulk $Ti_{1-x}Al_xN$, (ii) bulk TiN, and (iii) some averaged interfacial interlayer distances. The presence (or amplitude) of the third peak depends on the amount of material with that interfacial structure. Having all of this crystallographic information, one can write the coherency strain part of the mixing enthalpy $\Delta H^{Ti_{1-x}Al_xN/TiN}$ as

$$\Delta H^{Ti_{1-x}Al_xN/TiN}_{\text{strain}} = \frac{1}{N}\left(\mathcal{E}^{Ti_{1-x}Al_xN/TiN}_{\ell_1/\ell_2}(x) - (1-x)\mathcal{E}^{TiN}_{\ell_1+\ell_2} - x\mathcal{E}^{AlN/TiN}_{\ell_1/\ell_2}\right), \quad (2)$$

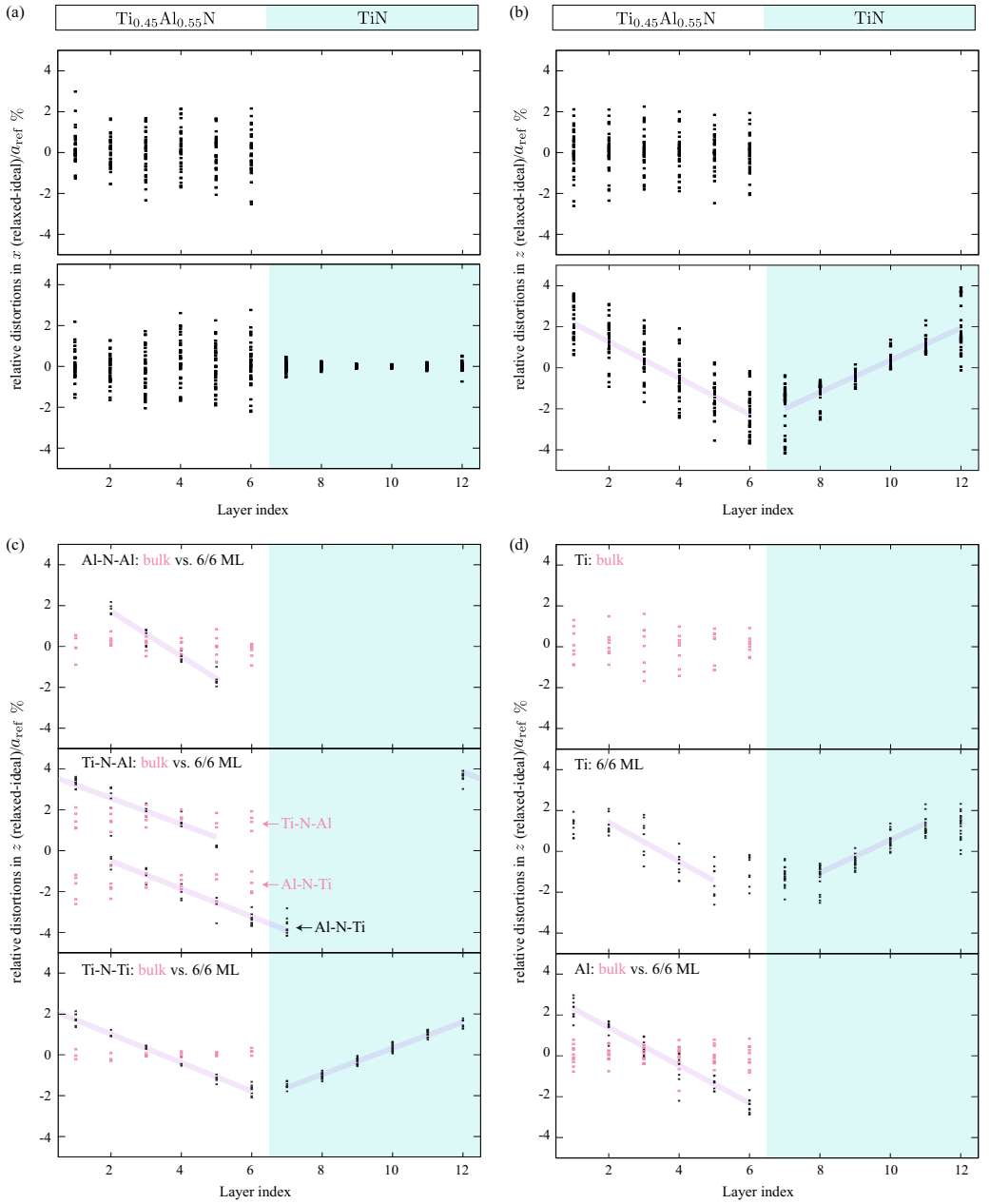

FIG. 5. The atomic relaxations with respect to the ideal positions in each layer for $x = 0.55$ of bulk $Ti_{1-x}Al_xN$ and 6/6 ML (a) in the x direction and (b) in the z direction. (c) The relaxations of the N atoms with different types of neighbors (Al-N-Al, Ti-N-Al, and Ti-N-Ti) along the z direction. (d) The relaxations of the Ti and Al atoms along the z direction. See the text for more details.

with the definition

$$\mathcal{E}^{\mathrm{Ti_{1-x}Al_xN/TiN}}_{\ell_1/\ell_2}(x) = \frac{\ell_1}{\ell_2} E^{\mathrm{Ti_{1-x}Al_xN}}_{\ell_1+\ell_2}\left(x, a_{||}^{\mathrm{Ti_{1-x}Al_xN/TiN}}, \langle c^{\mathrm{Ti_{1-x}Al_xN}}\rangle_{\mathrm{Ti_{1-x}Al_xN/TiN}}\right) + \left(1-\frac{\ell_1}{\ell_2}\right) E^{\mathrm{TiN}}_{\ell_1+\ell_2}\left(a_{||}^{\mathrm{Ti_{1-x}Al_xN/TiN}}, \langle c^{\mathrm{TiN}}\rangle_{\mathrm{Ti_{1-x}Al_xN/TiN}}\right),$$

$$\mathcal{E}^{\mathrm{AlN/TiN}}_{\ell_1/\ell_2}(x) = \frac{\ell_1}{\ell_2} E^{\mathrm{AlN}}_{\ell_1+\ell_2}\left(x, a_{||}^{\mathrm{AlN/TiN}}, \langle c^{\mathrm{AlN}}\rangle_{\mathrm{AlN/TiN}}\right) + \left(1-\frac{\ell_1}{\ell_2}\right) E^{\mathrm{TiN}}_{\ell_1+\ell_2}\left(a_{||}^{\mathrm{AlN/TiN}}, \langle c^{\mathrm{TiN}}\rangle_{\mathrm{AlN/TiN}}\right). \quad (3)$$

Here $\mathcal{E}$ is the energy of a multilayer with a periodicity of ℓ_1/ℓ_2 when using the optimized averaged lattice parameters with no chemical interaction through the interface. E stands for the total energy, $a_{||}^{\mathrm{Ti_{1-x}Al_xN/TiN}}$ and $a_{||}^{\mathrm{AlN/TiN}}$ are the coherent in-plane lattice parameters of the $Ti_{1-x}Al_xN$/TiN and AlN/TiN multilayers, and $\langle c^{\mathrm{Ti_{1-x}Al_xN}}\rangle_{\mathrm{Ti_{1-x}Al_xN/TiN}}$, $\langle c^{\mathrm{TiN}}\rangle_{\mathrm{Ti_{1-x}Al_xN/TiN}}$, $\langle c^{\mathrm{AlN}}\rangle_{\mathrm{AlN/TiN}}$, and $\langle c^{\mathrm{TiN}}\rangle_{\mathrm{AlN/TiN}}$ denote the averaged lattice parameters corresponding to the peaks (1) and (2) in the derived/observed interlayer distances.

Using the averaged interlayer distances (solid lines) from Fig. 3 in Eqs. (2) and (3), one defines the effect of strain on the mixing enthalpy. The calculated $\Delta H^{\mathrm{Ti_{1-x}Al_xN/TiN}}_{\mathrm{strain}}$ values are shown in Fig. 1. It is seen that the strain effect due to the presence of the coherent interfaces with TiN stabilizes the alloy, however it does not account for the full decrease of the mixing enthalpy. The rest of the stabilization effect is defined as the local interfacial or chemical contribution. This chemical contribution is even more significant than the coherency strain effect. By subtracting the strain term [Eq. (3)] from each of the energy terms in Eq. (1), one derives the chemical contribution to $\Delta H^{\mathrm{Ti_{1-x}Al_xN/TiN}}$ including both interfaces: the $Ti_{1-x}Al_xN$/TiN(001) and the AlN/TiN(001). These binding energies Eq. (4) are shown in Fig. 4,

$$E^{\mathrm{binding}}_{\mathrm{Ti_{1-x}Al_xN/TiN}}(x) = E^{\mathrm{Ti_{1-x}Al_xN/TiN}}_{\ell_1+\ell_2}(x) - \mathcal{E}^{\mathrm{Ti_{1-x}Al_xN/TiN}}_{\ell_1/\ell_2}(x),$$
$$E^{\mathrm{binding}}_{\mathrm{AlN/TiN}}(x) = E^{\mathrm{AlN/TiN}}_{\ell_1+\ell_2}(x) - \mathcal{E}^{\mathrm{AlN/TiN}}_{\ell_1/\ell_2}(x). \quad (4)$$

The overall chemical (interfacial) stabilization can be obtained by subtracting the latter one from the former. One should note that the binding energy in $Ti_{1-x}Al_xN$/TiN(001) is mostly positive, which says that it costs extra energy to build the interface. However, this energy is less than what one obtains for the AlN/TiN(001) interface. Therefore, the decomposition of $Ti_{1-x}Al_xN$ interfaced coherently to TiN is also hindered by the interfacial chemistry.

The nonvanishing multilayer binding energy in $Ti_{1-x}Al_xN$/TiN(001) (see Fig. 4) indicates that the atomic coordinates, especially at the interfaces, should show significant deviations from their ideal lattice positions, the so-called atomic relaxations.

The layer-resolved atomic relaxations (scaled, coherent B1 lattice) are shown in Fig. 5. The ideal structures were considered at the volume of the fully relaxed structure for both the bulk and the ML case. The figure shows the relaxations only for $x = 0.55$, and the values are measured in percentage of the lattice parameter of the bulk $Ti_{0.45}Al_{0.55}N$, $a_{\mathrm{ref}} = a_{\mathrm{Ti_{0.45}Al_{0.55}N}} = 4.16$ Å. The horizontal axis is the layer number. Figure 5(a) gives a comparison of the relaxations in the x direction (perpendicular to the growth direction). A very similar dispersion of the relaxations has been obtained in the y direction (which is not shown here). One sees that the relaxations in the $Ti_{0.45}Al_{0.55}N$ slab [bottom part of Fig. 5(a)] are very similar to the bulk case [upper part of Fig. 5(a)], while in the TiN part just the interfacial layers show some distortions, i.e., ±1% wide scattering.

TABLE I. The fitted slopes values (%) of the straight lines and the corresponding shifts of the layers in the ML slabs (Å) (in parentheses).

	$Ti_{0.45}Al_{0.55}N$	TiN
Fig. 5(b)	−0.89 (−0.019)	0.78 (0.016)
Fig. 5(c)		
Al-N-Al	−1.10 (−0.023)	
Ti-N-Al	−0.64 (−0.013)	
Al-N-Ti	−0.68 (−0.014)	
Ti-N-Ti	−0.70 (−0.015)	0.64 (0.013)
Fig. 5(d)		
Ti	−0.96 (−0.020)	0.85 (0.018)
Al	−0.92 (−0.019)	

Along the growth direction, a strong difference between the relaxations in ML and bulk is seen [see Fig. 5(b)]. Although the width of the scatter within each monolayer of $Ti_{0.45}Al_{0.55}N$ agrees well between ML and bulk, a systematic shift of the layers as a whole is observed. The shifts are shown by the straight lines fitted to the relaxations of the individual atoms. The fitted slopes and the corresponding shifts of the layers in the ML slab are summarized in Table I. It is already known from Fig. 3 that the $Ti_{0.45}Al_{0.55}N$ slab shrinks while the TiN one expands. This observation is represented by the distinct slopes of the lines. Using the reference value a_{ref}, one calculates the constant average shifts; see Table I. For example, in the $Ti_{0.45}Al_{0.55}N$ slab one obtains −0.019 Å, which agrees with the value plotted in Fig. 3. In Fig. 5(c), the relaxations of the N atoms with different types of neighbors (Al-N-Al, Ti-N-Al, and Ti-N-Ti) along the growth direction are shown. It is seen that the plane with the N atoms surrounded (from above and below) only by Al atoms has the largest shift, while the other ones, even in the TiN slab, show the same shift around 0.014 Å. Figure 5(d) compares the relaxations of the Al and Ti atoms. One sees that the Ti atoms in the TiN slab scatter wider in the growth direction than in x; see Fig. 5(a). However, the most striking result is the average relaxation of the layers of Ti atoms. In the interfacial layers (layer numbers 1,12 or 6,7), the average relaxation of the Ti atoms breaks the common trend, i.e., they do not sit on the fitted straight lines. The Ti atoms in layer 6 in the multilayer have an increased amount of Ti first neighbors from layer 7 (TiN slab), which results in a stronger binding between the two layers via the Ti-d orbitals. According to the fitted straight lines, the Ti atoms in layer 6 should shift down while in layer 7 they should relax upwards. However, the increased binding results in an increased interlayer distance between layers 5

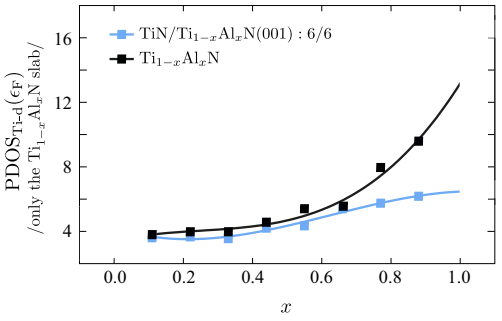

FIG. 6. Bulk and the 6/6 multilayer d-orbital partial density of states (PDOS) at the Fermi energy (ϵ_F) of the Ti atoms from only the $Ti_{1-x}Al_xN$ slab.

and 6 ($Ti_{0.45}Al_{0.55}N$ slab) while it becomes smaller between layers 7 and 8 (TiN slab). These local interfacial relaxations underline the fact that the interactions between the interfacial atoms along the growth directions differ from those in bulk $Ti_{1-x}Al_xN$ alloy. In multilayers one should use layer-resolved effective interactions to express the configurational energetics, and one expects a significant contribution from the on-site interactions; see Ref. [18].

Let us now discuss the electronic structure of the studied system. Figure 6 compares the Ti-site d-orbital partial density of states (PDOS) at the Fermi energy (ϵ_F) of the $Ti_{1-x}Al_xN$ slabs in the 6/6 ML with those in the bulk. The lower PDOS values in the ML mean increased Ti-Ti hybridization, which is explained as the stabilization effect in the bulk [12]. The figure shows that with increasing Al content, this electronic stabilization effect in the ML increases more compared to the bulk, which correlates well with the observed increased multilayer binding energy displayed in Fig. 4. Since the increase of Ti-site projected DOS at ϵ_F with increasing Al content indicates the increased tendency toward decomposition [12] in the bulk, we underline that this effect is clearly suppressed in the ML by means of more $d-d$ hybridization.

IV. CONCLUSIONS

In this study, we investigated the mixing thermodynamics of cubic (B1) $Ti_{1-x}Al_xN$/TiN(001) multilayers, and we showed that the mixing enthalpy is suppressed compared with bulk $Ti_{1-x}Al_xN$ by the interfacial effects. That is, the coherent interface with TiN was shown to stabilize $Ti_{1-x}Al_xN$. We predict the largest effect around the composition where the mixing enthalpy of bulk $Ti_{1-x}Al_xN$ has its maximum. The decrease of the mixing enthalpy in the multilayers was then split into a strain and an interfacial chemical contribution, and both effects are equally important. The in-plane lattice mismatch between $Ti_{1-x}Al_xN$/TiN(001) and AlN/TiN(001) was shown to correlate with the stabilization. The full strain contribution to the suppression was discussed on the basis of the structural properties of the multilayers. The fact that the lattice parameter and interlayer distances coherently expressed the stabilization effect of the structural misfit was suggested as a good partial measure of the relative energetics of the multilayers. We showed that the chemical effects result in large local atomic relaxations, especially for the Ti atoms on both sides of the interface. By calculating the electronic structure for the multilayer, we observe that the increase of Ti-site projected DOS at ϵ_F with increasing Al content, known as the electronic origin of a strong tendency toward the decomposition in the bulk $Ti_{1-x}Al_xN$, is clearly suppressed in the multilayer.

ACKNOWLEDGMENTS

The authors would like to gratefully acknowledge the support from the Swedish Foundation for Strategic Research (SSF) project SRL Grant No. 10-0026 and Multiscale computational-design of novel hard nanostructure coatings. The calculations were carried out through the Swedish National Infrastructure for Computing (SNIC), and they were performed at the Swedish National Supercomputer Center (NSC) for high performance computing. F.W. acknowledges funding received through Erasmus Mundus Joint European Doctoral Programme *DocMASE*. I.A.A. wishes to acknowledge the Swedish Research Council (VR) Grant No. 2015-04391, the Grant of Ministry of Education and Science of the Russian Federation (Grant No. 14.Y26.31.0005), and Tomsk State University Academic D. I. Mendeleev Fund Program (Project No. 8.1.18.2015). M.O. acknowledges the Swedish Research Council (VR) Grant No. 621-2012-4401. The support from Swedish Research Council (VR) (Project No. 2014-4750), LiLi-NFM, and the Swedish Government Strategic Research Area Grant in Materials Science to the AFM research environment at LiU are acknowledged.

[1] M. Shinn, L. Hultman, and S. A. Barnett, J. Mater. Res. **7**, 901 (1992).
[2] U. Helmersson, S. Todorova, S. A. Barnett, J. E. Sundgren, L. C. Markert, and J. E. Greene, J. Appl. Phys. **62**, 481 (1987).
[3] L. Hultman, C. Engström, and M. Odén, Surf. Coat. Technol. **133-134**, 227 (2000).
[4] M.-L. Wu, W.-D. Qian, Y.-W. Chung, Y.-Y. Wang, M.-S. Wong, and W. D. Sproul, Thin Solid Films **308–309**, 113 (1997).
[5] N. Ghafoor, H. Lind, F. Tasnádi, I. A. Abrikosov, and M. Odén, APL Mater. **2**, 046106 (2014).
[6] J. S. Koehler, Phys. Rev. B **2**, 547 (1970).
[7] R. G. Hoagland, T. E. Mitchell, J. P. Hirth, and H. Kung, Philos. Mag. A **82**, 643 (2002).
[8] I. N. Mastorakos, H. M. Zbib, and D. F. Bahr, Appl. Phys. Lett. **94**, 173114 (2009).
[9] V. Ozoliņš, C. Wolverton, and A. Zunger, Phys. Rev. B **57**, 4816 (1998).
[10] A. Knutsson, M. P. Johansson, L. Karlsson, and M. Odén, J. Appl. Phys. **108**, 044312 (2010).
[11] A. Knutsson, M. P. Johansson, L. Karlsson, and M. Odén, Surf. Coat. Technol. **205**, 4005 (2011).

[12] B. Alling, A. V. Ruban, A. Karimi, O. E. Peil, S. I. Simak, L. Hultman, and I. A. Abrikosov, Phys. Rev. B **75**, 045123 (2007).
[13] F. Tasnádi, F. Wang, M. Odén, and I. A. Abrikosov, Comput. Mater. Sci. **103**, 194 (2015).
[14] A. van De Walle and D. E. Ellis, Phys. Rev. Lett. **98**, 266101 (2007).
[15] A. Zunger, S. H. Wei, L. G. Ferreira, and J. E. Bernard, Phys. Rev. Lett. **65**, 353 (1990).
[16] N. Shulumba, O. Hellman, Z. Raza, J. Barrirero, B. Alling, F. Mücklich, I. A. Abrikosov, and M. Odén, arXiv:1503.02459.
[17] I. A. Abrikosov, S. I. Simak, B. Johansson, A. V. Ruban, and H. L. Skriver, Phys. Rev. B **56**, 9319 (1997).
[18] A. V. Ruban and I. A. Abrikosov, Rep. Prog. Phys. **71**, 046501 (2008).
[19] X. Chu and S. Barnett, J. Appl. Phys. **77**, 4403 (1995).
[20] P. E. Blöchl, Phys. Rev. B **50**, 17953 (1994).
[21] G. Kresse and J. Hafner, Phys. Rev. B **47**, 558 (1993).
[22] G. Kresse and J. Hafner, Phys. Rev. B **49**, 14251 (1994).
[23] G. Kresse and J. Furthmüller, Phys. Rev. B **54**, 11169 (1996).
[24] J. Perdew, J. Chevary, S. Vosko, K. Jackson, M. Pederson, D. Singh, and C. Fiolhais, Phys. Rev. B **48**, 4978 (1993).
[25] J. P. Perdew, K. Burke, and M. Ernzerhof, Phys. Rev. Lett. **77**, 3865 (1996).
[26] J. D. Pack and H. J. Monkhorst, Phys. Rev. B **16**, 1748 (1977).
[27] A. Knutsson, I. C. Schramm, K. Asp Grönhagen, F. Mücklich, and M. Odén, J. Appl. Phys. **113**, 114305 (2013).

Paper III

III

Growth and thermal stability of TiN/ZrAlN: Effect of internal interfaces

Kumar Yalamanchili
Fei Wang
Hisham Aboulfadl
Jenifer Barrirero
Lina Rogström
Emilio Jiménez-Pique
Frank Mücklich
Ferenc Tasnádi
Magnus Odén
Naureen Ghafoor

Acta Materialia, **121**, 396-406 (2016)

Acta Materialia 121 (2016) 396–406

Contents lists available at ScienceDirect

Acta Materialia

journal homepage: www.elsevier.com/locate/actamat

Full length article

Growth and thermal stability of TiN/ZrAlN: Effect of internal interfaces

Kumar Yalamanchili [a, c], Fei Wang [a, b], Hisham Aboulfadl [b], Jenifer Barrirero [a, b], Lina Rogström [a], Emilio Jiménez-Pique [c, d], Frank Mücklich [b], Ferenc Tasnadi [a], Magnus Odén [a], Naureen Ghafoor [a, *]

[a] Department of Physics, Chemistry, and Biology (IFM), Linköping University, SE 581 83 Linköping, Sweden
[b] Functional Materials, Department of Materials Science, Campus D3.3, Saarland University, D 66123 Saarbrücken, Germany
[c] Departamento de Ciencia de los Materiales e Ingeniería Metalurgica, Universitat Politècnica de Catalunya, Barcelona, Spain
[d] Center for Research in Nanoengineering, CRnE-UPC, Barcelona, Spain

ARTICLE INFO

Article history:
Received 29 March 2016
Received in revised form
27 June 2016
Accepted 3 July 2016
Available online 16 September 2016

Keywords:
Thermal stability
TM-Al-N multilayer films
Nanostructured materials
Interface energy
Three-dimensional atom probe (3DAP)
Transmission electron microscopy

ABSTRACT

Wear resistant hard films comprised of cubic transition metal nitride (c-TMN) and metastable c-AlN with coherent interfaces have a confined operating envelope governed by the limited thermal stability of metastable phases. However, equilibrium phases (c-TMN and wurtzite(w)-AlN) forming semicoherent interfaces during film growth offer higher thermal stability. We demonstrate this concept for a model multilayer system with TiN and ZrAlN layers where the latter is a nanocomposite of ZrN- and AlN- rich domains. The interfaces between the domains are tuned by changing the AlN crystal structure by varying the multilayer architecture and growth temperature. The interface energy minimization at higher growth temperature leads to formation of semicoherent interfaces between w-AlN and c-TMN during growth of 15 nm thin layers. Ab initio calculations predict higher thermodynamic stability of semicoherent interfaces between c-TMN and w-AlN than isostructural coherent interfaces between c-TMN and c-AlN. The combination of a stable interface structure and confinement of w-AlN to nm-sized domains by its low solubility in c-TMN in a multilayer, results in films with a stable hardness of 34 GPa even after annealing at 1150 °C.

1. Introduction

Development of new materials for wear resistant coatings with high hardness at elevated temperature is a long-standing technological challenge. The current workhorse material for the wear resistant coatings on metal cutting tool inserts is TiAlN with 50–67 at% of Al on the metallic sublattice [1–3]. TiAlN exhibits hardness enhancement at annealing temperatures between 700 and 900 °C due to spinodal decomposition of the supersaturated cubic (*c*)-TiAlN solid solution into *c*-TiN and metastable *c*-AlN [4–9]. The isostructural domains form coherent interfaces contributing to the age hardening. However the lattice coherency breaks down above 900 °C when *c*-AlN transforms to the thermodynamically stable wurtzite (*w*) phase [6]. The resulting incoherent interfaces cause a hardness drop and thus limit the working envelope of the film [6]. Several approaches, such as multicomponent alloying [10–13], multilayering [14,15], and interface coherency strain tuning [16] have been developed to enhance the stability of the metastable *c*-AlN with respect to *w*-AlN. Nevertheless, there is a temperature limit around 1000 °C [15], above which the metastable *c*-AlN assumes its thermodynamically stable wurtzite structure. A volume expansion associated with the transformation leads to structural instability which further deteriorates the mechanical properties of the material [17].

Here, we investigate an alternative material design route to improve the thermal stability of TM-Al-N films, i.e, instead of forming AlN in the metastable cubic phase we propose to grow it in its stable wurtzite structure but with semicoherent interfaces to *c*-TMN. The concept originates from recent experimental studies by us and others showing films consisting *w*-AlN with semicoherent interfaces to display higher hardness similar to the films containing *c*-AlN [18–21]. It exposes the fact that even though *w*-AlN has a lower shear resistance [22], films containing *w*-AlN could be strengthened by growing them such that semicoherent interfaces are formed. The current knowledge of semicoherent growth of *w*-AlN is, however, limited [19,20,23], and their thermal stability is yet

* Corresponding author.
E-mail address: naugh@ifm.liu.se (N. Ghafoor).

http://dx.doi.org/10.1016/j.actamat.2016.07.006
1359-6454/

to be studied. These topics are addressed in this article using TiN/ZrAlN as a model system.

ZrAlN is an immiscible alloy with a maximum enthalpy of mixing around $Zr_{0.4}Al_{0.6}N$, the composition chosen in this study [24,25]. During high temperature growth the alloy segregates to its binaries ZrN and AlN [18]. By adapting a multilayer structure it is known that the crystal structure of AlN can be tuned between the cubic and wurtzite phases by varying the layer thickness [26–28]. Here we combine these phenomena and vary the growth temperature to switch between isostructural (*c*-TMN/*c*-AlN) and hetrostructural (*c*-TMN/*w*-AlN) with coherent or semicoherent interfaces in the magnetron sputtered TiN/ZrAlN multilayers. We probe the thermal stability of hetrostructural semicoherent interfaces by measuring the hardness before and after elevated temperature anneals. The relative thermodynamic stability of isostructural and hetrostructural coherent interfaces are calculated by first principle calculations. The results provide insights in to the interface crystallographic and chemical requirements to enhance the thermal stability of TM-Al-N films to achieve an unaffected high hardness even after annealing to high operational temperatures.

Note the term “interface” is used in the text for both layer interfaces as well as boundaries between chemically segregated domains and collectively all interfaces are referred as “internal interfaces”.

2. Experimental and calculation methods

TiN/$Zr_{0.43}Al_{0.57}N$ multilayer films were deposited on MgO (001) substrates in a high vacuum dual DC magnetron sputter deposition system with a background pressure of 2×10^{-5} Pa. Details of the deposition chamber can be found elsewhere [29]. A 75 mm diameter pure Ti and a pre-alloyed $Zr_{0.4}Al_{0.6}$ target were used. The discharge was obtained at N_2 and Ar partial pressures of 0.06 and 0.5 Pa, respectively. Applied powers of $P_{Ti} = 200$ W (power density ~ 4.5 Wcm^{-2}) and $P_{Zr0.4Al0.6} = 150$ W (power density ~ 3.4 Wcm^{-2}) resulted in deposition rates of 0.15 (TiN) and 0.18 ($Zr_{0.43}Al_{0.57}N$) nm/s, respectively. The individual layers thicknesses (l) of TiN and $Zr_{0.43}Al_{0.57}N$ in the multilayer structure were controlled by shutters in front of each target. The nominal thickness l_{TiN} was kept constant at 15 nm, whereas l_{ZrAlN} was set to 2, 5, 10, 15, and 30 nm in a growth series of five films.

Monolithic films of TiN and $Zr_{0.43}Al_{0.57}N$ (with a 30 nm thick TiN buffer layer) were also deposited for reference. A total film thickness of about 1 μm was achieved for all samples to ensure reliable hardness measurements. All films were grown at a substrate temperature of $T_s = 700$ °C. However, an additional multilayer with $l_{ZrAlN} = 15$ nm was deposited at $T_s = 900$ °C to ensure growth of *w*-AlN with semicoherent interfaces. This film was further annealed at 1150 °C for 2 h under controlled atmosphere of 95% N_2 and 5% H_2 to probe thermal stability.

The composition of the monolithic films was determined by elastic recoil detection analysis (ERDA) using a 40 MeV I^+ beam, having an incident angle of 67.5° with respect to the surface normal, and the recoils were detected at an angle of 45°. The measured ERDA data was converted into relative atomic concentration profiles using the CONTES code [30]. Structural changes were characterized by X-ray diffraction (XRD) with a Panalytical Empyrian diffractometer operated in Bragg-Brentano geometry using Cu-K_α radiation at 40 kV and 40 mA. Transmission electron microscopy (TEM) and scanning transmission electron microscopy (STEM) were performed using a FEI Tecnai G2 TF 20 UT FEG microscope operated at 200 kV, equipped with an energy-dispersive X-ray analysis spectrometer (EDX). For STEM analysis, a high angular annular dark field (HAADF) detector with a camera length of 160 mm was used. Cross section TEM (XTEM) samples were prepared by conventional mechanical polishing followed by ion milling [21].

Atom probe tomography (APT) was used to obtain quantitative information regarding the interface chemistry. APT was performed on four films; $l_{ZrAlN} = 2$ and 15 nm (T_s 700 °C), $l_{ZrAlN} = 15$ nm (T_s 900 °C) in its as-deposited state and after isothermal annealing. Atom probe specimens were prepared in a dual-beam focused ion beam/scanning electron microscopy (SEM) workstation implementing the *in situ* lift out technique [31]. A 200 nm thick Pt layer was electron beam deposited on the film surface to reduce Ga implantation during specimen preparation. The measurements were carried out using a LEAP™ 3000X HR CAMECA™ system operated in laser pulsing mode (532 nm wavelength) with a repetition rate of 160 kHz, base temperatures of 40–50 K, and laser pulse energies of 0.4–0.5 nJ. The data were reconstructed using the standard algorithm developed by Bas et al. [32] and analyzed with the software CAMECA™ IVAS 3.6.8.

First principle calculations were performed to compare the relative thermodynamic stabilities between isostructural and hetrostructural interfaces. The total energy calculations were performed within the density functional theory (DFT) using the projector augmented wave (PAW) approach [33] implemented in the Vienna Ab initio Simulation Package (VASP) [34]. The Perdew-Burke-Ernzerhof generalized gradient functional (PBE-GGA) [35] was used to approximate the exchange and correlation functional. A plane-wave energy cutoff value of 450 eV was used. The reciprocal space integration was performed within the Monkhorst-Pack scheme [36] using a k-mesh of $5\times 5\times 1$. To determine the thermodynamic equilibrium configuration of the multilayers, the in-plane lattice parameter, the c/a ratio, and all the atomic coordinates were relaxed.

Multilayers of TiN/AlN and ZrN/AlN were modeled with different interface structures. Fig. 1 shows the models together with the interfacial matching. The models were built with 1:1 metal-to-metal atomic ratio between the parental slabs (TiN, ZrN and AlN), a condition which results in different slab thicknesses for the different multilayers. The in-plane size and the thicknesses were varied until the relative energy differences between the different multilayers (a-d) were converged. This was achieved for in-plane

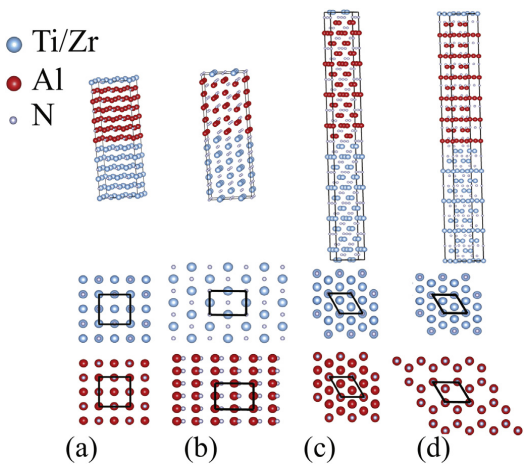

Fig. 1. Multilayer models and the corresponding interfacial matchings (black skeletons). (a) *c*- (100)[001]//*c*-(100)[001], (b) *c*-(110)[001]//*w*-(10-10)[001], (c) *c*-(111)[1–10]//*c*-(111)[1–10], (d) *c*-(111)[1–10]//*w*-(0001)[11–20].

sizes made by the (2 × 2) repetition of the black skeletons shown in Fig. 1. Convergence was achieved using 192 atoms in the models. This means in total 96 metal atoms for the (a), (c) and (d) multilayers. The multilayer (b) does not commensurate with the other three models in terms of the number of metal atoms therefore its total energy was derived by a linear interpolation of the energies calculated with models built from 72 and 168 metal atoms.

Hardness and Young's modulus were obtained using a load-controlled UMIS nano indenter equipped with a Berkovich diamond indenter with a tip radius of approximately 150 nm. An optimum load of 12 mN was selected to avoid substrate effects and obtain load independent mechanical properties. A minimum of 30 indents for each film were used to evaluate the average and standard deviation of the hardness (H) and elastic modulus (E) using the Oliver and Pharr method [37].

3. Results

3.1. Composition

The as deposited monolithic film compositions determined by ERDA were $Zr_{0.43}Al_{0.57}N$ and TiN (±1.5 at%) with a nitrogen to metal ratio close to 1 ± 0.05. Oxygen and carbon impurities account for less than 0.2 at% while the Ar content is 0.8 at% in the films. The Al content in the Zr–Al–N film is lower than that of the target by about 3 at%, which stems from preferential re-sputtering of Al during deposition [21,38]. A comparison of the quantitative compositional analysis between data recorded by APT and ERDA is given in Table 1 using an average of 5 layers in the APT analysis. However, the peak overlap between Zr^{+3} and TiN^{+2} ions in the mass spectrum does not permit precise measurement of the Zr concentration. The composition of the monolithic TiN and ZrAlN samples were measured by ERDA, and for all elements except Zr the results are comparable between the two techniques. Measured error is less than 0.05 at. % for both the techniques. No segregation of the impurities at the multilayer interfaces is observed in APT.

3.2. XRD analysis

Fig. 2 shows X-ray diffractograms of the $Zr_{0.43}Al_{0.57}N$ film, multilayers with l_{ZrAlN} = 2, 10, 15 and 30 nm grown at T_s = 700 °C, and the multilayer l_{ZrAlN} = 15 nm grown at T_s = 900 °C in its as deposited and annealed states. The close lattice-match causes TiN 002 and MgO 002 diffraction peaks to overlap and they cannot be resolved in these diffractograms. The monolithic film shows only one weak and broad diffraction signal around 32.4°, interpreted as *w*-AlN 0002. The peak shift to a slightly lower diffraction angle than pure *w*- AlN is attributed to Zr incorporation in the *w*-AlN, whereas the peak broadening reflects the nanocrystalline nature of the film.

The short period multilayers l_{ZrAlN} = 2 and 5 nm exhibit finite thickness fringes around TiN (MgO) 002 diffraction peak indicative of a superlattice nature of these multilayers. The diffraction signal originates entirely from (002) cubic planes, which indicates epitaxial growth of these short period multilayers.

The appearance of a TiN 111 diffraction peak in l_{ZrAlN} = 10, 15, and 30 nm (hereafter, referred to as long period multilayer) suggests polycrystalline growth. The absence of *c*-ZrN peaks and the appearance of a broad diffraction peak around 32.4° suggest that the $Zr_{0.43}Al_{0.57}N$ layers in the long period multilayers are structurally similar to the monolithic film.

The multilayer, l_{ZrAlN} = 15 nm deposited at T_s = 900 °C shows a distinct diffraction pattern with a single broad peak centered between *c*-ZrN 002 and *w*-AlN 0002 peak positions. Upon annealing at 1150 °C, two broad peaks at 2θ = 35.77° and 39.65° appeared. The phase identification in these films is ambiguous and will be addressed later when combining XRD with TEM investigations.

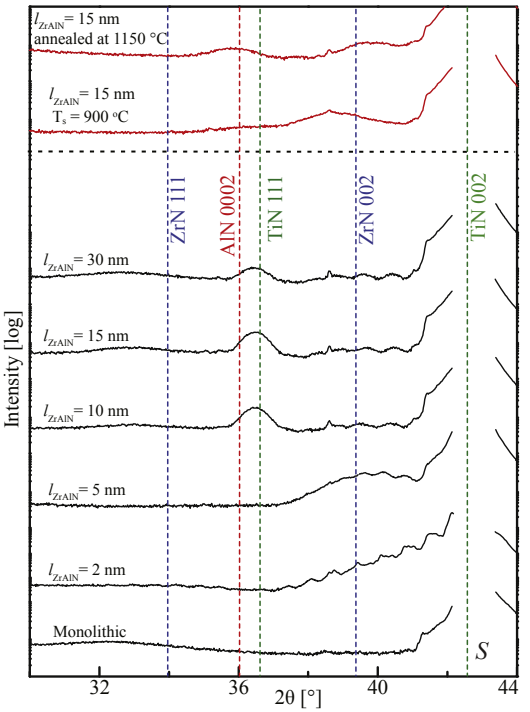

Fig. 2. XRD of monolithic $Zr_{0.43}Al_{0.57}N$ film and TiN/$Zr_{0.43}Al_{0.57}N$ multilayers deposited at T_s = 700 °C (profiles in black), l_{ZrAlN} = 15 nm multilayer deposited at 900 °C and after annealing at 1150 °C (profiles in red).

3.3. Microstructure of as-deposited films

3.3.1. Monolithic $Zr_{0.43}Al_{0.57}N$ film

The cross sectional HAADF-STEM image of $Zr_{0.43}Al_{0.57}N$ monolithic film in Fig. 3a shows contrast variation with a wavelength of ~3 nm, attributed to the formation of ZrN- and AlN-rich domains during growth. The film displays weak columnar contrast in the bright field TEM image (Fig. 3b). The lattice resolved image reveals a preferentially oriented wurtzite crystal structure in the growth direction. A closer analysis of the image shows that the wurtzite lattice repeatedly interrupts about every 2–3 nm with regions that do not display fringes, hereafter referred to as a distorted structure. The wurtzite lattice corresponds to AlN- rich domains, and the

Table 1
Composition of as deposited monolithic and multilayers measured by ERDA and APT analysis.

Technique/Film	Location	Avg. Comp. at. %						
		Ti	Zr	Al	N	O	Ar	C
APT/Multilayer	TiN	49.8	–	0.3	49.5	0.1	0.1	0.01
	ZrAlN	0.2	–	28.2	51.3	0.3	0.25	0.01
ERDA/Monolithic	TiN	49.3	0	0	48.9	0.1	0.5	0.01
	ZrAlN	0	21.6	28.5	48.4	0.1	1	0.01

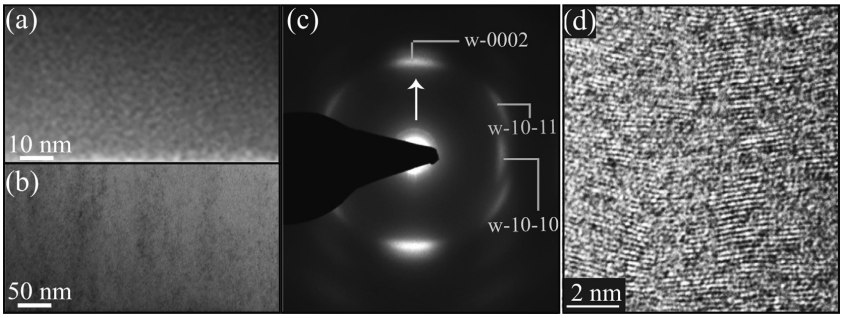

Fig. 3. XTEM images of the monolithic $Zr_{0.43}Al_{0.57}N$ film: (a) STEM-HAADF, (b) BF-TEM, (c) SAED (arrow indicates the growth direction), and (d) HR-TEM.

distorted regions correspond to ZrN-rich domains.

The SAED pattern shows wurtzite reflections with 0002 preferentially orientated in the growth direction and, in agreement with the XRD results, no cubic diffraction peaks are observed. The lattice parameters, a ≈3.66 Å and c ≈ 5.41 Å determined from the SAED are larger than the equilibrium lattice parameter of *w*-AlN [39]. Again, this is in agreement with the XRD 0002 peak being shifted with respect to pure *w*-AlN indicating that AlN-rich domains contain Zr.

These observations suggest that the segregated monolithic $Zr_{0.43}Al_{0.57}N$ film form a nanocomposite with incoherent interfaces where AlN-rich regions assume a preferentially oriented wurtzite structure and ZrN-rich domains assume a distorted structure. Despite the distorted ZrN-rich domains the nanocomposite film displays a crystallographic texture governed by minimization of the surface energy of *w*-AlN, i.e. <0002> orientation in the growth direction.

3.3.2. Short period multilayers and coherent interfaces

In the short period multilayers ($l_{ZrAlN} = 2$ and 5 nm) well defined interfaces between TiN and $Zr_{0.43}Al_{0.57}N$ layers are observed in TEM (Fig. 4). STEM images show bright and dark modulations within the $Zr_{0.43}Al_{0.57}N$ layer that correspond to vertical aligned ZrN- and AlN-rich domains with a wavelength of ~2 nm. The SAED patterns only contain cubic diffraction spots along two different zone axis and no wurtzite phase is observed. The lattice resolved images shows cube-on-cube epitaxy between TiN and $Zr_{0.43}Al_{0.57}N$ layers. It means that the AlN- rich domains assume a metastable cubic crystal structure, forming coherent interfaces with both TiN and ZrN, which leads to a self-aligned and compositionally modulated structure (Fig. 4d). The lattice resolved images (Fig. 4b and e) also show misfit dislocations and the density is higher within the ZrAlN layer, i.e. between the segregated c-ZrN- and c-AlN- rich domains, compared to the interfaces between TiN and ZrAlN layer. This is a consequence of higher misfit strain between c-ZrN and c-AlN (~10%) compared to the misfit strain between the c-TiN and c-ZrAlN layers (~1.5%).

The bright field TEM image shows continues contrast of threading dislocations in the growth direction, more clearly seen for the multilayer of $l_{ZrAlN} = 2$ nm in Fig 4c, which is typical for epitaxial growth. The epitaxial growth causes correlated layer roughness in the growth direction which was also observed in APT reconstruction of $l_{ZrAlN} = 5$ nm multilayers as shown in Fig. 5 inset image.

The 1D concentration profiles from the APT data of the multilayer with $l_{ZrAlN} = 5$ nm (Fig. 5) show an average interface width of ~4 nm between the alternating TiN and $Zr_{0.43}Al_{0.57}N$ layers. This

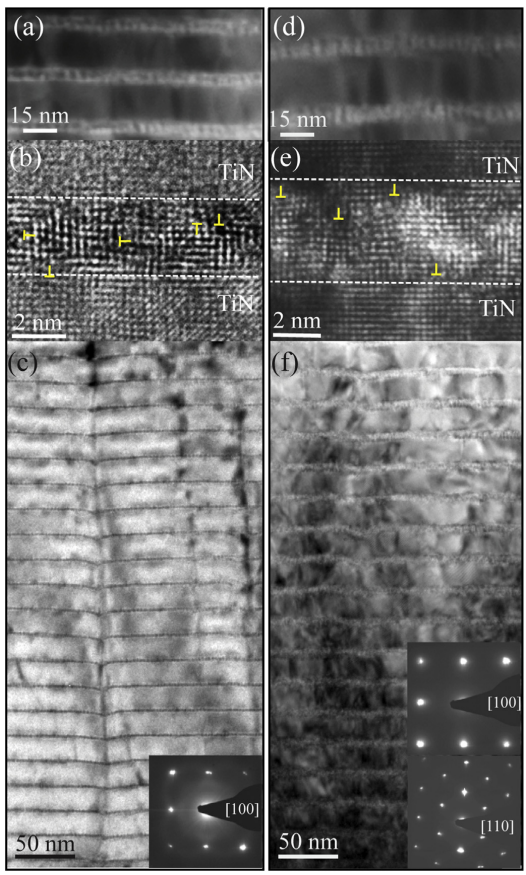

Fig. 4. STEM, HR-TEM, and BF-TEM micrograph with SAED insets of short period multilayers grown at 700 °C: (a–c) $l_{ZrAlN} = 2$ nm, and (d–f) $l_{ZrAlN} = 5$ nm. T symbol in Fig. b, and e indicates dislocations.

implies that the actual $Zr_{0.43}Al_{0.57}N$ layer thickness shrinks to ~1 nm, while the rest of the layer consists of ZrN and AlN- rich domains intermixed with Ti. Thus, in epitaxial $l_{ZrAlN} = 2$ nm

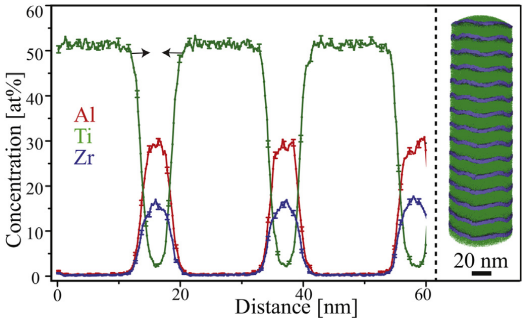

Fig. 5. 1D concentration profile of l_{ZrAlN} = 5 nm (nitrogen not shown here) from a localized volume within the APT reconstruction shown in the inset. Black arrows indicate the region of chemical intermixing between the layers.

multilayer the $Zr_{0.43}Al_{0.57}N$ layers are expected to be fully intermixed with TiN. These observations suggest that the layer composition in short period multilayers significantly deviate from the nominal values and need to be considered when describing metastable phase formation.

3.3.3. *Long period multilayers: interface structure versus growth temperature*

The multilayer with l_{ZrAlN} = 15 nm was chosen for detailed microstructural analysis since all of the long period multilayers show similar X-ray diffractograms. Fig. 6 shows XTEM images of this multilayer grown at 700 °C (a-c), and 900 °C (d-f), respectively. STEM images at low and high magnifications reveal randomly distributed ZrN- and AlN- rich domains in the ZrAlN layers when grown at T_s = 700 °C. The HRTEM micrograph (Fig. 6c) shows a nanocomposite structure of *w*-AlN-rich and distorted ZrN-rich domains similar to what has been observed in the monolithic film (see Fig. 3a). This suggests that the epitaxy associated with the templating effect of TiN is lost for the long period multilayers (l_{ZrAlN} > 10 nm). Similar to the monolithic film, the ZrAlN layers display a weak 0002 diffraction signal from the *w*-AlN-rich domains in Fig. 6a. The ZrN-rich domains are too small and distorted to result in an observable diffraction signal, whereas the *c*-TiN shows nearly continues diffraction ring. These observations suggest that the *w*-AlN forms incoherent interfaces with both ZrN and *c*-TiN.

In contrast, the STEM micrograph of the multilayer grown at 900 °C reveals a compositionally modulated microstructure with vertically aligned domains within the $Zr_{0.43}Al_{0.57}N$ layer (Fig. 6d and e), similar to what is observed for the short period multilayers. The crystallographically aligned wurtzite and cubic reflections in SAED pattern implies that the *w*-AlN-rich domains form semi-coherent interfaces to *c*-ZrN and *c*-TiN. Fast Fourier transform (FFT) of the lattice resolved image in combination with SAED yield a coherency relation of $(110)_{c\text{-}TiN}||(110)_{c\text{-}ZrN}||(10\text{-}10)_{w\text{-}AlN}$ and $[001]_{c\text{-}TiN}||[001]_{c\text{-}ZrN}||[0001]_{w\text{-}AlN}$, here after termed *type I* interfaces. A substrate-film SAED pattern (not shown here) revealed $(100)_{MgO}||(100)_{c\text{-}TiN}$ and $[001]_{MgO}||[001]_{c\text{-}TiN}$.

The lattice resolved image (Fig. 6f) confirms the coherency between *c*-ZrN and *w*-AlN domains, and *c*-ZrN domains and TiN layers. The *type I* interface formation causes an expansion of the *c*-ZrN lattice and a shrinkage of the c-axis of *w*-AlN along the growth direction. This explains the origin of a single broad XRD peak between the *c*-ZrN 002 and *w*-0002 in Fig. 2. The weak cubic 111 reflections in the SAED pattern are signatures of an additional orientation which evolves further after annealing the multilayers

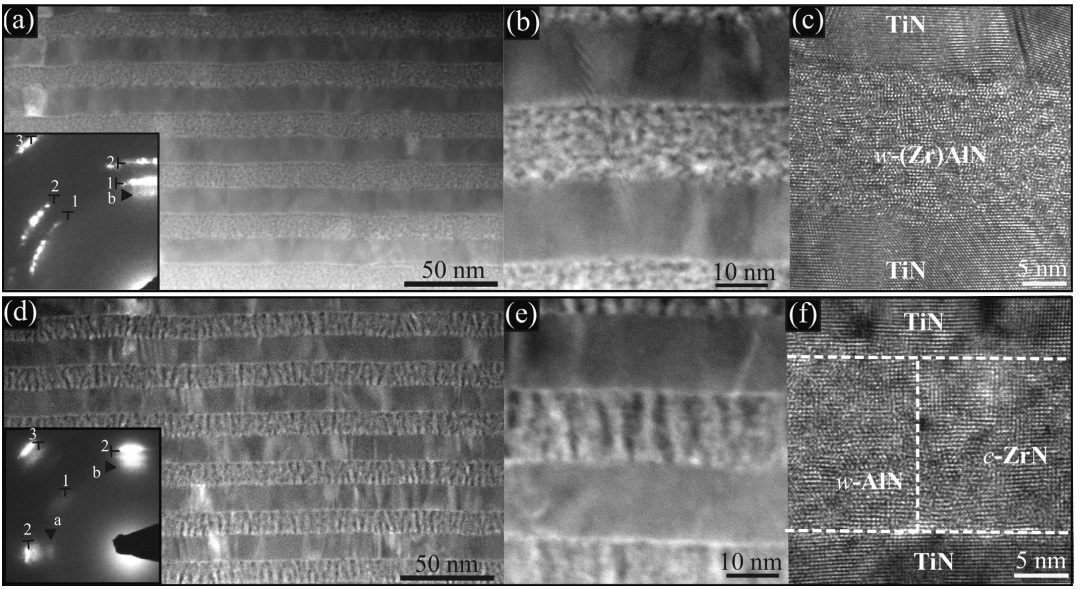

Fig. 6. Cross sectional TEM analysis of l_{ZrAlN} = 15 nm multilayers. Overview STEM images with SAED inset, magnified STEM, and HR-TEM images from left to right for the multilayers grown at 700 °C (a–c) and 900 °C (d–f). SAED annotations, 1, 2 and 3 corresponds to cubic-111, 200, 220 reflections, a and b corresponds to wurtzite-10-10 and 0002. The twin diffraction pattern of cubic phase in (d) corresponds to c-TiN and c-ZrN.

and it will be addressed in Section 3.4.

APT was performed to unveil compositional effects behind the structural variation of l_{ZrAlN} = 15 nm multilayers as a function of growth temperature. Fig. 7a shows 2D Al concentration maps from 1 nm thick virtual slices of $Zr_{0.43}Al_{0.57}N$ layers perpendicular to the growth direction from the multilayers grown at 700 and 900 °C. The more pronounced segregation for T_s = 900 °C is evident by a larger domain size and a higher frequency of AlN-rich domains. The average composition ratios (Al: Zr) evaluated by proximity histogram (not shown here) were 0.9 and 0.3 for the *w*-AlN- and *c*-ZrN-rich domains, respectively. The values indicate that the AlN-rich domains are relatively pure compared to ZrN- rich domains. Previous studies on TiAlN reveal that the segregation on the metallic sublattice has a significant influence on the stability of the metastable cubic phase related to the differences in electronic structure, bond energy, and configurational contribution to the total energy [40].

The APT 1D profiles in Fig. 7b show interface widths of approximately 4 nm in the 700 and 900 °C multilayers. The intermixed layer is comparable to what was observed in short period multilayers and thus, indicates that the interface width is an atomic mixing caused by the ion-bombardment during growth and the difference in growth temperature is too small to affect the intermixing. The interface topography analysis of $Zr_{0.43}Al_{0.57}N$ layers shows that the bottom interface is rougher compared to the top interface in both multilayers, which is likely caused by a faceted columnar growth of TiN layers.

3.4. Interface chemistry and crystallography after annealing

The STEM analysis (Fig. 8a) of the multilayer l_{ZrAlN} = 15 nm (T_s = 900° C) after isothermal annealing at 1150 °C for 2 h shows a lateral coalescence of AlN domains (dark contrast) to approximately 20 nm in size surrounded by ZrN (bright contrast) in the lateral and TiN (grey contrast) in the growth direction. The $Zr_{0.43}Al_{0.57}N$ displays a decrease in the layer thickness from 15 nm in the as-deposited state to 5 nm after annealing. A comparison of EDX line spectra of the as-deposited and annealed film (Fig. 8b) shows that ZrN and TiN interdiffuse. However, due to higher volume fraction of the TiN layer, out diffusion of ZrN is dominant, leaving behind AlN as the main constituent in the original $Zr_{0.43}Al_{0.57}N$ layer, which explains the decrease in layer thickness.

An APT reconstruction in Fig. 8c shows the formation of pure

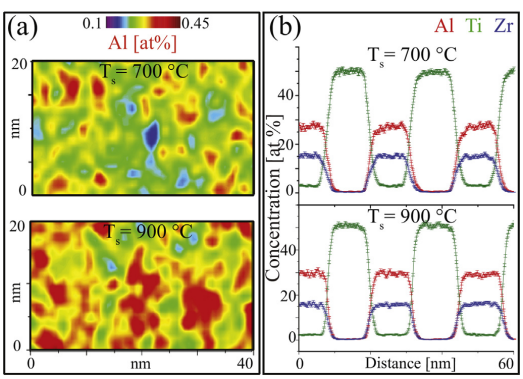

Fig. 7. (a) Plan-view 2D concentration map of Al from the $Zr_{0.43}Al_{0.57}N$ layer in l_{ZrAlN} = 15 nm multilayer from a localized volume within the APT reconstruction, and (b) 1D concentration profiles across the layer interfaces.

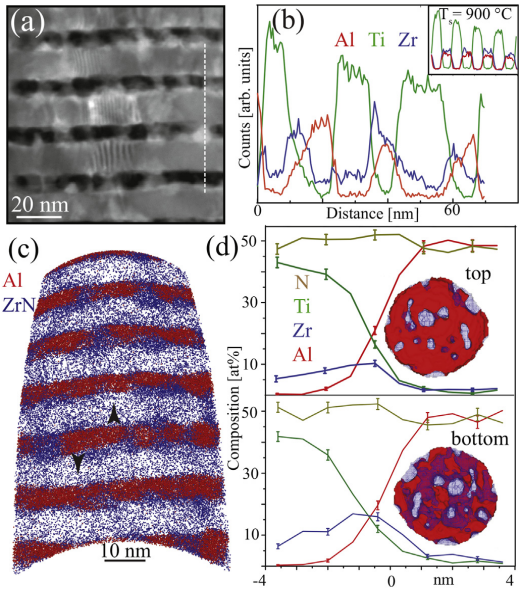

Fig. 8. Analysis of l_{ZrAlN} = 15 nm (900 °C) multilayer after isothermal annealing. (a) STEM image,(b) EDX line profile, inset image shows profile of as-deposited multilayer, (c) reconstructed APT tip, (d), proxigrams of TiN/AlN top and bottom interface, inset images shows isoconcentration surface of Al 30 at% (red, solid) and ZrN 20 at% (blue, wireframe). Black arrows in (c) indicate top and bottom interfaces for proximity histogram construction. (For interpretation of the references to colour in this figure legend, the reader is referred to the web version of this article.)

AlN with intermittent ZrN domains and out diffusion of ZrN from the $Zr_{0.43}Al_{0.57}N$ layer. The AlN (red) domains distribution is presented in the reconstruction with Al ions and the ZrN (blue) domain distribution is presented with ZrN complex ions, respectively, to avoid showing spatial artifacts in the reconstruction originating from minor peak overlaps of Zr^{+3} and TiN^{+2} ions in the mass spectrum. A relatively higher volume fraction of ZrN at the bottom interface is visualized in the reconstruction and also in the isoconcentration surfaces created for the top and bottom interfaces of the $Zr_{0.43}Al_{0.57}N$ layers shown in Fig. 8d. Proximity analysis across the AlN domian interfaces (Fig. 8d), shows concentration gradient of Zr with an average value of 10 ± 1 and 16 ± 1 at%, resulting in $Ti_{0.8}Zr_{0.2}N$ and $Ti_{0.68}Zr_{0.32}N$ compositions at the top and bottom interface respectively (interfaces are marked with arrows). We attribute this to the presence of columnar boundaries near the faceted TiN surface (i.e., bottom interfaces with relatively higher topographical roughness in the as deposited multilayers) providing shorter path for Zr diffusion.

SAED pattern of the annealed multilayer in Fig. 9 shows confined reflections of cubic and wurtzite phases identical to the as deposited multilayer (see Fig. 6d). This is an important result indicating that the semicoherent interfaces of *w*-AlN are stable even after isothermal annealing. The faint c-111 reflections seen in the as-deposited multilayer, however, become intense after annealing. The combination of HRTEM, FFT, SAED pattern, and our previous plan-view image analysis [18] reveal two different interface coherency relations (Fig. 9c–d):

Type I: *c*-ZrN $_{(110)[001]}$ ∥ *w*-AlN $_{(10\text{-}10)[001]}$, exist in both as deposited and annealed multilayers, and.

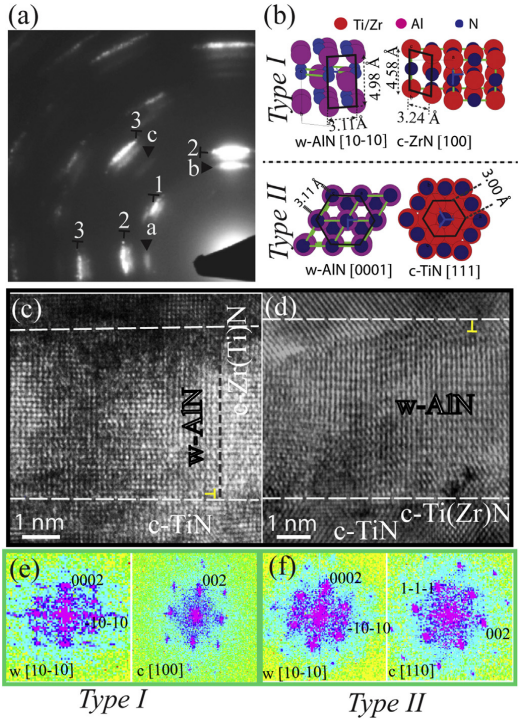

Fig. 9. *Type I* and *Type II* Interface structure of multilayer shown in Fig. 8. (a) SAED pattern, where annotation 1, 2 and 3 mark *c*-111, 200, 220, and a, b and c mark *w*-10-10, 0002, 10–12 reflection. (b) visualization of the two interfaces, (c–d) HR-TEM images and (e–f) corresponding FFT of the two interface types. T symbol in Fig. c, and d indicates dislocations.

Type II: *c*-TiN $_{(111)[1\text{–}10]}$ ‖ *w*-AlN $_{(0001)[11\text{-}20]}$, which forms only in small amounts (faint *c*-111 reflection) during deposition and grows in extent during annealing.

The crystallographic details of the two semicoherent interfaces are visualized in Fig. 9b with *c*-110 ‖*w*-10-10 (*type 1*) and *c*-111 ‖*w*-0001 (*type II*) having the same crystallographic in plane symmetry. The analysis also explains the origins of the XRD-peaks at 35.77° and 39.65° of the annealed multilayer (see. Fig. 2) to be domains with *type II* and *type I* interfaces, respectively. The lattice resolved images display misfit dislocations between the hetrostructural domains (Fig. 9c and d) for both type I and II interfaces, which is expected from the high misfit strain (3.6–8%).

3.5. Ab-initio thermodynamic stability of the interfaces

First-principles calculations were performed to evaluate the interfacial energies of TiN/AlN and ZrN/AlN bicrystals using the multilayer models shown in Fig. 1a–d. The results in Fig. 10 show that the relative energy difference is low between isostructural coherent interfaces with (100) and (111) orientations for both TiN/AlN and ZrN/AlN. For hetrostructural semicoherent interfaces we infer that the *Type I* is favorable for ZrN/AlN interfaces but not for TiN/AlN, whereas *type II* interfaces are energetically the most favorable ones for both material systems. The calculations also reveal that semicoherent *c*-TMN/*w*-AlN structural archetypes have

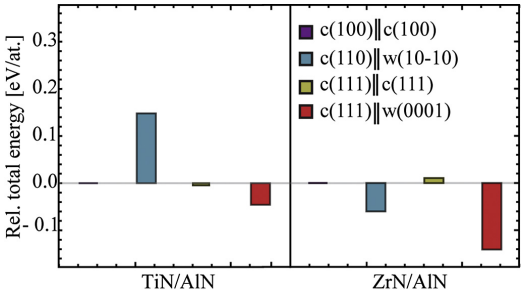

Fig. 10. Ab-initio calculated total energy divided by 192 atoms (eV/atom) relative to *c*-(100)[001]//*c*-(100)[001] for TiN/AlN and ZrN/AlN multilayer.

higher thermodynamic stability compared to isostructural coherent interfaces, i.e. *c*-TMN/*c*-AlN. This underlines the experimental observation of a high thermal stability of the film, $l_{ZrAlN} = 15$ nm, when it contains semicoherent interfaces.

The common in-plane lattice parameter of the multilayer and the strain values calculated in each layer are listed in Table 2. In the case of TiN/AlN, the strain values are largest for *type I*, followed by isostructural interfaces and smallest for *type II* interfaces. For ZrN/AlN, the largest strain is found for isostructural interfaces, followed by *type I* and smallest for *type II* interfaces. It is to be noted that the higher thermodynamic stability of a *type II* interface is related to the lower misfit strain, combined with the fact that the AlN is in its stable wurtzite structure. Accordingly, the structural misfit and the bulk free energy can be suggested as a measure to predict the relative thermodynamic stabilities in chemically modulated structures containing different coherent interface structures.

3.6. Mechanical properties

Fig. 11a shows the variation in H and E of the monolithic and multilayered films as a function of $Zr_{0.43}Al_{0.57}N$ layer thicknesses for $T_s = 700$ °C. The trend for E follows closely the rule-of-mixture of monolithic TiN with a value of 458 ± 15 GPa and $Zr_{0.43}Al_{0.57}N$ with a value of 220 ± 7 GPa. A high hardness is measured for the short period coherenet interface containing multilayers with a maximum value of 35 ± 2 GPa for $l_{ZrAlN} = 5$ nm. In contrast, the long period multilayers with incoherent interfaces display a monotonic hardness drop as a function of $Zr_{0.43}Al_{0.57}N$ layer thickness. However, the multilayer $l_{ZrAlN} = 15$ nm deposited at 900 °C, consisting semicoherent interfaces, shows a higher hardness (Fig. 11b) in its as-deposited state. More importantly, this multilayer display a stable H value of 34 ± 1.5 GPa, after isothermal annealing at 1150 °C. We ascribe the stable hardness of the annealed films to the thermally stable semicoherent interfaces between *w*-AlN and *c*-TiN, *c*-ZrN.

4. Discussion

The current study is an investigation of the crystal and interface structure of TiN/ZrAlN multilayers grown at temperatures between 700 and 900 °C. TiN attains a stable cubic (B1) structure and due to a close lattice match grows epitaxially on MgO [41]. Immiscible $Zr_{0.43}Al_{0.57}N$ on the other hand segregates into ZrN and AlN-rich domains during the growth. Here, the growth temperature corresponds to ~0.4 of the melting temperature, which sets the average adatom diffusion lengths to a few nm for the current deposition rates [42]. This results in a nanocomposite structure of ZrN and AlN.

Table 2
Ab-initio calculated in-plane common lattice parameter and the strain in different layers as a function of interface structure variation for TiN/AlN and ZrN/AlN multilayer.

Interface structure	Common in-plane lattice parameter, Å		% Strain TiN	% Strain AlN	% Strain ZrN	% Strain AlN
	TiN/AlN	ZrN/AlN	TiN/AlN		ZrN/AlN	
c-(100)//c-(100)	4.18	4.45	−1.42	1.46	−2.79	8.01
c-(110)//w-(10-10) Type 1	4.37	4.63	3.07	−12.25	1.14	−7.03
c-(111)//c-(111)	2.94	3.08	−2	0.89	−4.94	5.69
c-(111)//w-(0001) Type 2	3.06	3.2	2	−1.61	−1.23	2.89

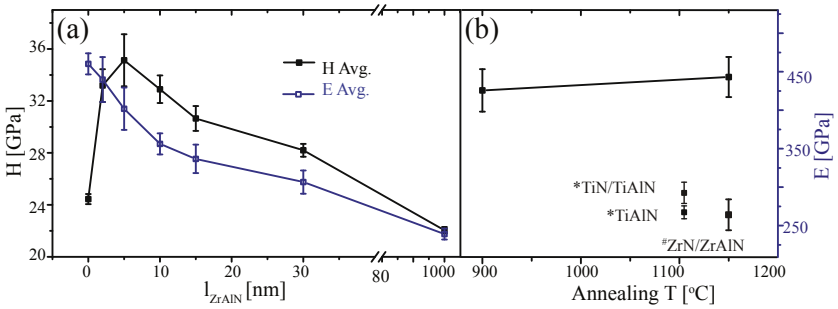

Fig. 11. H, E of monolithic and multilayers. (a) Films grown at 700 °C, (b) multilayers with d_{ZrAlN} 15 nm grown at 900 °C and isothermally annealed at 1150 °C. Ref. values: *TiN/TiAlN, TiAlN [15], #ZrN/ZrAlN [43].

In the TiN/$Zr_{0.43}Al_{0.57}N$ multilayers, the segregated AlN- rich domains form coherent, semicoherent, and incoherent interfaces with TiN and ZrN depending on the thickness of ZrAlN layer and the growth temperature. Interestingly, the semicoherent *w*-AlN/*c*-TMN interfaces display significantly high thermal stability with a stable hardness compared to the monolithic films and multilayers of TiAlN and ZrAlN forming incoherent interfaces [15,43]. The mechanisms governing the different interface structure formation and their effects on thermal and mechanical stability are discussed here.

4.1. Influence of T_s and l_{ZrAlN} on crystal and interface structure

From the APT analysis of the long period multilayers, incorporation of approximately 10 at% Zr in AlN-rich domains and ~30 at% Al in ZrN-rich domains is determined. This suggests that the substrate temperature of 700 °C enables segregation within the $Zr_{0.43}Al_{0.57}N$ layers, however insufficient adatom mobility at the growth front limits the formation of pure binaries. The high solute amount in ZrN- rich domains leads to a distorted structure, whereas the lower solute concentration in the AlN- rich domains enable it to forms its stable wurtzite structure (Fig. 3d). The resulting nanocomposite of *w*-AlN and distorted ZrN forms incoherent interfaces both in monolithic film and in long period multilayers.

The short period multilayers ($l_{ZrAlN} \leq 5$ nm) on the other hand, consist of coherent interfaces. This is a direct consequence of metastable *c*-AlN domain formation. The stabilization of metastable *c*- AlN with a layer thickness between 2 and 5 nm in an epitaxial multilayer structure is attributed to the interface energy dominating the bulk free energy and strain energies [26,44]. The interface energy minimization is achieved by adapting the crystal structure of AlN layer to that of the underlying *c*-TiN layer and thus forming a low energy coherent interface. However, the chemical gradients constitute a significant portion of the multilayer, as observed in the case $l_{ZrAlN} \leq 5$ nm (Fig. 5). This has a favorable effect on the stabilization of metastable *c*-AlN rich domains by reducing the structural misfit with the templating TiN layer and ZrN-rich domains. Hence, we suggest that the metastable phase formation in the short period multilayers is a combined effect of chemical intermixing and epitaxial stabilization. An additional favorable factor is the segregation on the metallic sublattice that reduces the number of Zr–Al bonds which might favor the metastable cubic phase stabilization of ZrAlN similar to what has been shown for TiAlN [40].

Beyond the critical layer thickness i.e. $l_{ZrAlN} > 10$ nm, the template effect is lost and AlN domains assume its stable wurtzite structure with incoherent interfaces to the distorted ZrN domains similar to the monolithic films. This leads to termination of epitaxial growth between the layers of ZrAlN and TiN.

A transition from the incoherent to semicoherent interfaces between *w*-AlN and the cubic phases (TiN and ZrN) in the long period multilayers is obtained by increasing the growth temperature to 900 °C. The semicoherent interfaces form because: (i) higher deposition temperature leads to a more pronounced segregation within the $Zr_{0.43}Al_{0.57}N$ layers (Fig. 7a), which reduces the solute induced distortion causing ZrN-rich domains to attain a cubic crystal structure, and (ii) the higher growth temperature provides sufficient adatom mobility for TiN and ZrN to attain 002 orientation in the growth direction and thus favouring semicoherent interfaces between *c*-ZrN (110) and *w*-AlN (10-10), driven by the interface energy minimization. These two surfaces have similar in plane symmetry (Fig. 9b).

The importance of the material selection to promote semicoherent interfaces with *w*-AlN is noticeable here. For example, studies on TiAlN/MgO (001) performed under similar growth conditions as used in this study showed segregated domains of *c*-TiN and *w*-AlN with incoherent interfaces [45]. Our calculations also confirm higher thermodynamic stability of the coherent interfaces between *w*-AlN (10-10) and *c*- ZrN (110) compared to *c*-TiN (110), as the later one generates relatively higher misfit strain.

In addition, the orientation of *w*-AlN (0001) and *c*-ZrN (002) in

the growth direction, also minimize the growth front (film-vacuum interface) surface energy. Subsequently, the nanoscale domains of *c*-ZrN/*w*-AlN grow simultaneously by adapting a *coupled growth* similar to what has been observed for directionally solidified eutectic systems for a wide range of materials [46]. This results in a chemically modulated structure (Fig. 6e) with non-isostructural semicoherent interfaces between *c*-ZrN and *w*-AlN inherited across the TiN layer and form *type 1* interfaces with a misfit strain of 7%.

Further reduction of the strain energy occur through a competitive *type II* interface formation where the *c*-TiN (111) grows epitaxial to *w*-AlN (0001) with a misfit strain of 4%. The MgO (001) surface promotes *type 1* interfaces and the evolution of *type II* interfaces is attributed to a higher thermodynamic stability in agreement with the theoretical predictions.

4.2. Thermal stability of semicoherent interfaces

The thermal stability is an important criteria to qualify semicoherent interface structural archetype for elevated temperature applications. The competition between the strain and interface energy, bulk free energy sets a critical domain size, above which the semicoherency is likely to breakdown. At elevated temperature, coalescence of *w*-AlN results in larger domains which may lead to semicoherency breakdown to relive the strain energy. For the isostructurally decomposed c-TiN and c-AlN, the critical domain size for coherency breakdown is ~15 nm [47]. This relatively small critical size is an effect of *c*-AlN being a metastable phase with an energy penalty of 0.18 eV/atom with respect to its thermodynamic equilibrium structure [48]. In contrast, for the semicoherent *w*-AlN domains in the TiN/ZrAlN multilayer, the only driving force for the coherency breakdown stems from the strain energy. Therefore, the critical size of *w*-AlN domains to commence coherency breakdown is expected to be significantly larger and consequently results in higher thermal stability of the interfaces.

In short, the retained coherency at the interfaces after isothermal annealing at 1150 °C in the TiN/ZrAlN multilayers is ascribed to: (i) relatively higher thermodynamic stability of semicoherent *type 1* interfaces compared to the isostructural interfaces, (ii) evolution of *type II* interfaces to lower the strain energy of the film, (iii) inter-diffusion between ZrN and TiN generating compositionally graded interfaces to further reduces the misfit strain for *type II* interface as the in-plane lattice parameter misfit between *c*-Ti(Zr)N (111) and *w*-AlN (0001) becomes smaller, and (iv) constrained coalescence of *w*-AlN domains by confining them between the immiscible cubic phases both in the growth and lateral directions, thereby keeping the domains smaller than the critical size.

Previous first principle calculations at 0 K indicate that the TiN–ZrN material system is immiscible with positive enthalpy of mixing in the order of 0.06 eV/atom [49–51] associated with a lattice mismatch of about 7%. However, the current study reveals interdiffusion between TiN and ZrN during elevated temperature annealing. At the annealing temperature of 1150 °C, it is likely that the entropy of mixing (ΔS_{mix}) supersedes the enthalpy of mixing (ΔH_{mix}), such that the miscibility gap closes and provides a thermodynamic drive for the intermixing. This analysis is in line with the recent theoretical predictions [24] and previous observation by Rogström et al. [52].

4.3. Influence of interface structure on the mechanical properties

Monolithic $Zr_{0.43}Al_{0.57}N$ shows significantly lower H and E compared to the rest of the films. The lower hardness is likely caused by a coordinated shear displacement, similar to what has been shown for the nanostructured TMN thin films with incoherent interfaces [53,54]. The lower elastic modulus is a combined effect of higher volume fraction of *w*-AlN phase which has a higher compliance compared to cubic TiN and AlN [22], and also that the distorted ZrN domains cause elastic softening similar to nanostructured metals [55].

The hardness varies systematically in the multilayers upon varying the $Zr_{0.43}Al_{0.57}N$ layer thickness (Fig. 11a). For the short period multilayers consisting coherent interfaces the spatial fluctuation in elastic properties across the layers and within the $Zr_{0.43}Al_{0.57}N$ layer offer Koehler [56] strengthening while the lattice misfit between the isostructural coherent interfaces results in coherency hardening [57]. Both strengthening mechanisms become more prominent for the multilayers with 5 nm l_{ZrAlN}, resulting in the highest H value of 35 ± 2 GPa.

The long period multilayers ($l_{ZrAlN} \geq 10$ nm) display a decrease in H as a function of $Zr_{0.43}Al_{0.57}N$ layer thickness. Here the incoherent interfaces between the nanoscale segregated domains of *w*-AlN and distorted ZrN domains offer relatively lower shear resistance similar to the monolithic $Zr_{0.43}Al_{0.57}N$ film. For the multilayers $l_{ZrAlN} = 15$ nm, grown at 900 °C, the evolution of semicoherent interfaces between *w*-AlN and *c*-TMN domains (Fig. 6f) make them more resistant to the coordinated shear displacement which results in higher hardness (Fig. 11b). The key significance of these multilayer structures is that the hardness (34 ± 1.5 GPa) is stable even after isothermal annealing at experimentally constrained temperature of 1150 °C and further high temperature studies are needed to probe the ultimate thermal endurance limit of the semicoherent structure.

We suggest that the thermally stable semicoherent interfaces between *w*-AlN and *c*-TMN domains offer both Koehler and coherency hardening similar to the isostructural interfaces between *c*-TiN and *c*-AlN. In addition, the non-isostructural semicoherent interfaces provide an additional obstacles to dislocation glide due to the misorientation between the active glide planes *c*-TiN {110} and *w*-AlN $\{0001\},\{10\bar{1}1\}$ [58,59]. A high hardness combined with a relatively low elastic modulus of the *c*-TMN/*w*-AlN structural archetypes is likely to cause superior wear resistance similar to what has been observed for other hard coatings [60].

5. Conclusions

Multilayer structures consisting TiN and $Zr_{0.43}Al_{0.57}N$ nanocomposite layers were grown using magnetron sputtering on MgO (001) substrates. The interfaces between the layers and between ZrN and AlN domains were tuned from coherent, semicoherent to incoherent, by varying the multilayer design and the growth temperature.

AlN-rich domains assume a metastable cubic structure in the multilayers with $l_{ZrAlN} \leq 5$ and the stable wurtzite structure in the multilayers with $l_{ZrAlN} > 10$ nm and in the monolithic film. The metastable phase formation in the short period multilayers is suggested to be a combined effect of chemical intermixing and epitaxial stabilization, yielding multilayers with high hardness.

For the wurtzite phase containing films the growth temperatures around 700 °C are found to be inadequate to obtain complete segregation within ZrAlN layer and the presence of Al in the ZrN-rich domains causes a distorted ZrN structure, which leads to the formation of incoherent interfaces between ZrN domains and the *w*-AlN lattice. Higher growth temperature of 900 °C facilitates pronounced segregation of *w*-AlN and *c*-ZrN domains, and the interface energy minimization of the nanoscale modulated structure leads to evolution of semicoherent interfaces between *w*-AlN and cubic phases (TiN and ZrN). Two types of coherency relations are found, where $c\text{-ZrN}_{(110)[001]} \| w\text{-AlN}_{(10\text{-}10)[001]}$ interfaces are promoted by a MgO (001) template effect and the $c\text{-TiN}_{(111)[10\text{-}1]} \| w$-

$AlN_{(0001)[11\text{-}20]}$ interfaces are promoted by the higher thermodynamic stability.

The semicoherent interfaces offer both Koehler and coherency hardening mechanisms. Due to higher thermodynamic stability of the interface structures and limited domain growth of *w*-AlN provided through confinement between TiN layers and ZrN domains, the coherency and thus the hardness retains at ~34 ± 1.5 GPa after elevated temperature annealing.

These findings show the potential of improving the shear strength of materials by modifying the interface structure between the thermodynamically stable *c*-TMN-*w*-AlN phases. We believe that in parallel to the efforts of improving the stability of metastable phases, the approach of designing thermally stable multiphase materials with tailored interface structures provides a complete new dimension for thin film materials to be used at elevated temperatures.

Acknowledgements

The Swedish Research Council (VR grant no 621-2012-4401), Swedish Foundation for Strategic Research (SSF) through the program MultiFilms (RMA08-0069), Swedish government strategic research area grant in material science AFM – SFO MatLiU (2009-00971), EU's Erasmus Mundus graduate school in Material Science and Engineering (DocMASE), the Swedish Governmental Agency for Innovation Systems (Vinnova grants VINNMer 2011-03464 and M – Era.net 2013-02355), are gratefully acknowledged for their financial support. The EU-funded project AME-Lab (European Regional Development Fund C/4-EFRE-13/2009/Br) is acknowledged for the FIB/SEM use. The APT was financed by the DFG and the federal state government of Saarland (INST 256/298-1 FUGG).

References

[1] W.D. Münz, Titanium aluminum nitride films: a new alternative to TiN coatings, J. Vac. Sci. Technol. A 4 (1986) 2717.
[2] S. Paldey, S.C. Dee, Single layer and multilayer wear resistant coatings of (Ti,Al)N: a review, Mater. Sci. Eng. A 342 (2003) 58–79.
[3] M.I. Yousaf, V.O. Pelenovich, B. Yang, C.S. Liu, D.J. Fu, Effect of bilayer period on structural and mechanical properties of nanocomposite TiAlN/MoN multilayer films synthesized by cathodic arc ion-plating, Surf. Coatings Technol. 282 (2015) 94–102.
[4] P.H. Mayrhofer, D. Music, J.M. Schneider, Ab initio calculated binodal and spinodal of cubic $Ti_{1-x}Al_xN$, Appl. Phys. Lett. 88 (2006) 071922.
[5] A. Höling, L. Hultman, M. Odén, J. Sjölén, L. Karlsson, Thermal stability of arc evaporated high aluminum-content $Ti_{[1-x]}Al_{[x]}N$ thin films, J. Vac. Sci. Technol. A 20 (2002) 1815.
[6] P.H. Mayrhofer, A. Hörling, L. Karlsson, J. Sjölén, T. Larsson, C. Mitterer, L. Hultman, Self-organized nanostructures in the Ti–Al–N system, Appl. Phys. Lett. 83 (2003) 2049.
[7] A. Knutsson, J. Ullbrand, L. Rogström, N. Norrby, L.J.S. Johnson, L. Hultman, J. Almer, M.P. Johansson Jöesaar, B. Jansson, M. Odén, Microstructure evolution during the isostructural decomposition of TiAlN- A combined in-situ small angle x-ray scattering and phase field study, J. Appl. Phys. 113 (2013) 213518.
[8] P.E. Hovsepian, D.B. Lewis, W.D. Münz, Recent progress in large scale manufacturing of multilayer/superlattice hard coatings, Surf. Coatings Technol. 133–134 (2000) 166–175.
[9] D. Music, R.W. Geyer, J.M. Schneider, Recent progress and new directions in density functional theory based design of hard coatings, Surf. Coatings Technol. 286 (2016) 178–190.
[10] H.W. Hugosson, H. Högberg, M. Ahlgren, M. Rodmar, T.I. Selinder, Theory of the effects of substitutions on the phase stabilities of $Ti_{1-x}Al_xN$, J. Appl. Phys. 93 (2003) 4505–4511.
[11] F. Rovere, D. Music, S. Ershov, M. Baben, H. Gerd fuss, P.H. Mayrhofer, J.M. Schneider, Experimental and computational study on the phase stability of Al- containing cubic transition metal nitrides, J. Phys. D. Appl. Phys. 43 (2010) 035302.
[12] L. Chen, D. Holec, Y. Du, P.H. Mayrhofer, Influence of Zr on structure, mechanical and thermal properties of Ti-Al-N, Thin Solid Films 519 (2011) 5503–5510.
[13] R. Rachbauer, A. Blutmager, D. Holec, P.H. Mayrhofer, Effect of Hf on structure and age hardening of Ti-Al-N thin films, Surf. Coatings Technol. 206 (2012) 2667–2672.
[14] F. Wang, I.A. Abrikosov, S.I. Simak, M. Odén, F. Mücklich, F. Tasnádi, Coherency effects on the mixing thermodynamics of cubic $Ti_{1-x}Al_xN$/TiN(001) multilayers, Phys. Rev. B 93 (2016) 174201.
[15] A. Knutsson, M.P. Johansson, L. Karlsson, M. Odén, Thermally enhanced mechanical properties of arc evaporated $Ti_{[0.34]}Al_{[0.66]}N$/TiN multilayer coatings, J. Appl. Phys. 108 (2010) 044312.
[16] R. Forsén, N. Ghafoor, M. Odén, Coherency strain engineered decomposition of unstable multilayer alloys for improved thermal stability, J. Appl. Phys. 114 (2013) 244303.
[17] Q. Xia, H. Xia, A.L. Ruoff, Pressure-induced rocksalt phase of aluminum nitride: a metastable structure at ambient condition, J. Appl. Phys. 73 (1993) 8198.
[18] N. Ghafoor, L.J.S. Johnson, D.O. Klenov, J. Demeulemeester, P. Desjardins, I. Petrov, L. Hultman, M. Odén, Nanolabyrinthine ZrAlN thin films by self-organization of interwoven single-crystal cubic and hexagonal phases, APL Mater 1 (2013) 022105.
[19] A. Karimi, G. Allidi, R. Sanjines, Relative orientation of the constituents on the degree of crystallographic coherence in AlN/TiN superlattices, Surf. Coatings Technol. 201 (2006) 4062–4067.
[20] D. Rafaja, A. Poklad, V. Klemm, G. Schreiber, D. Heger, M. Šíma, M. Dopita, Some consequences of the partial crystallographic coherence between nanocrystalline domains in Ti–Al–N and Ti–Al–Si–N coatings, Thin Solid Films 514 (2006) 240–249.
[21] K. Yalamanchili, I.C. Schramm, E. Jiménez-Piqué, L. Rogström, F. Mücklich, M. Odén, N. Ghafoor, Tuning hardness and fracture resistance of ZrN/$Zr_{0.63}Al_{0.37}N$ nanoscale multilayers by stress-induced transformation toughening, Acta Mater 89 (2015) 22–31.
[22] A.J. Wang, S.L. Shang, Y. Du, Y. Kong, L.J. Zhang, L. Chen, D.D. Zhao, Z.K. Liu, Structural and elastic properties of cubic and hexagonal TiN and AlN from first-principles calculations, Comput. Mater. Sci. 48 (2010) 705–709.
[23] M. Wen, H. Huang, K. Zhang, Q. Meng, X. Li, L. Kong, C. Hu, W. Zheng, The AlN layer thickness dependent coherent epitaxial growth, stress and hardness in NbN/AlN nanostructured multilayer films, Surface, Coatings Technol. 235 (2013) 367–375.
[24] H. Lind, R. Pilemalm, L. Rogström, F. Tasnadi, N. Ghafoor, R. Forsén, L.J.S. Johnson, M.P. Johansson-Jöesaar, M. Odén, I.A. Abrikosov, High temperature phase decomposition in TixZryAlzN, AIP Adv. 4 (2014) 127147.
[25] D. Holec, R. Rachbauer, L. Chen, L. Wang, D. Luef, P.H. Mayrhofer, Surface & coatings technology phase stability and alloy-related trends in Ti – Al – N, Zr – Al – N and Hf – Al – N systems from fi rst principles, Surf. Coat. Technol. 206 (2011) 1698–1704.
[26] A. Madan, I.W. Kim, S.C. Cheng, P. Yashar, V.P. Dravid, S.A. Barnett, Stabilization of cubic AlN in epitaxial AlN -TiN superlattices, Phy. Rev. Let. 78 (1997) 1743–1746.
[27] C. Stampfl, A.J. Freeman, Structure and stability of transition metal nitride interfaces from first-principles: AlN/VN, AlN/TiN, and VN/TiN, Appl. Surf. Sci. 258 (2012) 5638–5645.
[28] M. Schlögl, B. Mayer, J. Paulitsch, P.H. Mayrhofer, Influence of CrN and AlN layer thicknesses on structure and mechanical properties of CrN/AlN superlattices, Thin Solid Films 545 (2013) 375–379.
[29] N. Ghafoor, F. Eriksson, P.O.Å. Persson, L. Hultman, J. Birch, Effects of ion-assisted growth on the layer definition in Cr/Sc multilayers, Thin Solid Films 516 (2008) 982–990.
[30] M.S. Janson, CONTES Conversion of Time-energy Spectra—a Program for ERDA Data/analysis, Internal report, Uppsala University, 2004.
[31] M.K. Miller, K.F. Russell, Atom probe specimen preparation with a dual beam SEM/FIB miller, Ultramicroscopy 107 (2007) 761–766.
[32] P. Bas, A. Bostel, B. Deconihout, D. Blavette, A general protocol for the reconstruction of 3D atom probe data, Appl. Surf. Sci. 87–88 (1995) 298–304.
[33] P.E. Blöchl, Projector augmented-wave method, Phys. Rev. B 50 (1994) 17953–17979.
[34] G. Kresse, Efficient iterative schemes for ab initio total-energy calculations using a plane-wave basis set, Phys. Rev. B 54 (1996) 11169–11186.
[35] J.P. Perdew, K. Burke, M. Ernzerhof, Quantum theory group tulane university, generalized gradient approximation made simple, Phys. Rev. Lett. 77 (1996) 3865–3868.
[36] J.D. Pack, H.J. Monkhorst, Special points for Brillouin-zone integrations, Phys. Rev. B 16 (1977) 1748–1749.
[37] W.C. Oliver, G.M. Pharr, Measurement of hardness and elastic modulus by instrumented indentation: advances in understanding and refinements to methodology, J. Mater. Res. 19 (2011) 3–20.
[38] B.M. Howe, E. Sammann, J.G. Wen, T. Spila, J.E. Greene, L. Hultman, I. Petrov, Real-time control of AlN incorporation in epitaxial $Hf_{1-x}Al_xN$ using high-flux, low-energy (10–40eV) ion bombardment during reactive magnetron sputter deposition from a $Hf_{0.7}Al_{0.3}$ alloy target, Acta Mater 59 (2011) 421–428.
[39] PDF-card No 01-073-7288, JCPDS- International Centre for Diffraction Data, 1998.
[40] P.H. Mayrhofer, D. Music, J.M. Schneider, Influence of the Al distribution on the structure, elastic properties, and phase stability of supersaturated $Ti_{1-x}Al_xN$, J. Appl. Phys. 100 (2006) 094906.
[41] L. Hultman, U. Helmersson, S.A. Barnett, J.E. Sundgren, J.E. Greene, Low-energy ion irradiation during film growth for reducing defect densities in epitaxial TiN(100) films deposited by reactive-magnetron sputtering, J. Appl. Phys. 61 (1987) 552.
[42] D.G. Sangiovanni, D. Edström, L. Hultman, I. Petrov, J.E. Greene, V. Chirita, Ti adatom diffusion on TiN(001): ab initio and classical molecular dynamics simulations, Surf. Sci. 627 (2014) 34–41.

[43] L. Rogström, L.J.S. Johnson, M.P. Johansson, M. Ahlgren, L. Hultman, M. Odén, Thermal stability and mechanical properties of arc evaporated ZrN/ZrAlN multilayers, Thin Solid Films 519 (2010) 694–699.
[44] V. Chawla, D. Holec, P.H. Mayrhofer, Stabilization criteria for cubic AlN in TiN/AlN and CrN/AlN bi-layer systems, J. Phys. D. Appl. Phys. 46 (2013) 045305.
[45] F. Adibi, I. Petrov, L. Hultman, U. Wahlström, T. Shimizu, D. McIntyre, J.E. Greene, J.E. Sundgren, Defect structure and phase transitions in epitaxial metastable cubic $Ti_{0.5}Al_{0.5}N$ alloys grown on MgO(001) by ultra-high-vacuum magnetron sputter deposition, J. Appl. Phys. 69 (1991) 6437–6450.
[46] J. Llorca, V.M. Orera, Directionally solidified eutectic ceramic oxides, Prog. Mater. Sci. 51 (2006) 711–809.
[47] N. Norrby, L. Rogström, M.P. Johansson-Jõesaar, N. Schell, M. Odén, In situ X-ray scattering study of the cubic to hexagonal transformation of AlN in $Ti_{1-x}Al_xN$, Acta Mater 73 (2014) 205–214.
[48] V. Chawla, D. Holec, P.H. Mayrhofer, The effect of interlayer composition and thickness on the stabilization of cubic AlN in AlN/Ti − Al − N superlattices, Thin Solid Films 565 (2014) 94–100.
[49] V. Ivashchenko, S. Veprek, A. Pogrebnjak, B. Postolnyi, First-principles quantum molecular dynamics study of Ti_x Zr_{1-x} N(111)/SiN_y heterostructures and comparison with experimental results, Sci. Technol. Adv. Mater 15 (2014) 025007.
[50] G. Abadias, V.I. Ivashchenko, L. Belliard, P. Djemia, Structure, phase stability and elastic properties in the $Ti_{1-x}Zr_xN$ thin-film system: experimental and computational studies, Acta Mater 60 (2012) 5601–5614.
[51] A. Hörling, J. Sjölén, H. Willmann, T. Larsson, M. Odén, L. Hultman, Thermal stability, microstructure and mechanical properties of $Ti_{1-x}Zr_xN$ thin films, Thin Solid Films 516 (2008) 6421–6431.
[52] L. Rogström, N. Ghafoor, M. Ahlgren, M. Odén, Auto-organizing ZrAlN/ZrAlTiN/TiN multilayers, Thin Solid Films 520 (2012) 6451–6454.
[53] Z.B. Qi, P. Sun, F.P. Zhu, Z.C. Wang, D.L. Peng, C.H. Wu, The inverse Hall-Petch effect in nanocrystalline ZrN coatings, Surf. Coatings Technol. 205 (2011) 3692–3697.
[54] K. Yalamanchili, R. Forsén, E. Jiménez-Piqué, M.P. Johansson Jöesaar, J.J. Roa, N. Ghafoor, M. Odén, Structure, deformation and fracture of arc evaporated Zr–Si–N hard films, Surf. Coatings Technol. 258 (2014) 1100–1107.
[55] P. Sharma, S. Ganti, On the grain-size-dependent elastic modulus of nano-crystalline materials with and without grain-boundary sliding, J. Mater. Res. 18 (2011) 1823–1826.
[56] J.S. Koehler, Attempt to design a strong solid, J. Phys. Rev. B 2 (1970) 547.
[57] J.W. Cahn, Hardening by spinodal decomposition, Acta Metal. 11 (1963) 1275.
[58] M. Odén, H. Ljungcrantz, L. Hultman, Characterization of the induced plastic zone in a single crystal TiN(001) film by nanoindentation and transmission electron microscopy, J. Mater. Res. 12 (1997) 2134–2142.
[59] S.R. Jian, Y.C. Tseng, I.J. Teng, J.Y. Juang, Dislocation energetics and pop-ins in AlN thin films by Berkovich nanoindentation, Materials 6 (2013) 4259–4267.
[60] Y.X. Ou, J. Lin, H.L. Che, J.J. Moore, W.D. Sproul, M.K. Lei, Mechanical and tribological properties of CrN/TiN superlattice coatings deposited by pulsed dc magnetron sputtering, Surf. Coatings Technol. 276 (2015) 152–159.

Paper IV

Systematic *ab initio* investigation of the elastic modulus in quaternary transition metal nitride alloys and in their coherent multilayers

IV

Fei Wang
David Holec
Magnus Odén
Frank Mücklich
Igor A. Abrikosov
Ferenc Tasnádi

Acta Materialia, **127**, 124-132 (2017)

Acta Materialia 127 (2017) 124–132

Contents lists available at ScienceDirect

Acta Materialia

journal homepage: www.elsevier.com/locate/actamat

Full length article

Systematic *ab initio* investigation of the elastic modulus in quaternary transition metal nitride alloys and their coherent multilayers

Fei Wang [a, b, *], David Holec [c], Magnus Odén [a], Frank Mücklich [b], Igor A. Abrikosov [a, d], Ferenc Tasnádi [a]

[a] Department of Physics, Chemistry and Biology (IFM), Linköping University, SE-581 83 Linköping, Sweden
[b] Functional Materials, Materials Science and Engineering Department (MSE), Saarland University, P.O. Box 151150, 66041 Saarbrücken, Germany
[c] Department of Physical Metallurgy and Materials Testing, Montanuniversität Leoben, A-8700 Leoben, Austria
[d] Materials Modeling and Development Laboratory, NUST "MISIS", 119049 Moscow, Russia

ARTICLE INFO

Article history:
Received 9 November 2016
Received in revised form
21 December 2016
Accepted 8 January 2017
Available online 10 January 2017

Keywords:
Ab initio calculations
Elastic properties
Transition metal nitride alloys
Multicomponent
Multilayers

ABSTRACT

We give a comprehensive overview of the elastic properties of cubic quaternary transition metal nitride alloys and coherent nitride multilayers for design of wear resistant hard coatings. The elastic stiffness constants of the alloys are calculated using the special quasirandom structure method. For multilayers with sharp interfaces we prove the applicability of a linear-elasticity approximation and show that it can be used with success instead of performing direct computationally demanding *ab initio* calculations. We explore the trends and the potential of multicomponent alloying in engineering the strength and ductility of both, quaternary alloys and their multilayers. We investigate $X_{(1-x-y)}Ti_xAl_yN$ alloys where X is Zr, Hf, V, Nb or Ta, and present an analysis based on increasing *x*. We show that with increasing Ti content ductility can increase in each alloy. Elastic isotropy is observed only in $(Zr,Hf,V)_{(1-x-y)}Ti_xAl_yN$ alloys in the middle of the compositional triangle, otherwise a high Young's modulus is observed along [001]. We predict that coherent $TiN/X_{(1-x-y)}Ti_xAl_yN$ and $ZrN/X_{(1-x-y)}Ti_xAl_yN$ alloy multilayers with the [111] interfacial direction show increasing ductility with increasing *x*, while the multilayers with the [001] orientation become more brittle. We show that the Young's moduli variation in the parent bulk quaternary nitride alloy provide a reliable descriptor to screen the Young's modulus of coherent multilayers in high-throughput calculations.

1. Introduction

Non-equilibrium materials, such as metastable alloys, have unique properties that are utilized in modern industrial applications. Computational materials science offers an effective approach to tailor explore the potential of such materials. The efficiency of a computational screening is affected by the appropriateness of the applied physics models, as well as a coupling to a 'high-level' physical concept that is defined in hands with the complex technological needs. Based on the enormous success of computational materials science, numerous systematic computational studies have been devoted to develop and validate such concepts [1,2]. The elastic Young's modulus is a measurable material property that has been used in combinatorial high-throughput methods to select thin polymer films [3] or charting the elastic properties of inorganic compounds [4].

Metastable thin film cubic (NaCl-type) B1 $Ti_{(1-x)}Al_xN$ alloys are used as protective coatings in the cutting tools industry because of the material's excellent mechanical properties and oxidation resistance at elevated temperatures [5,6]. Cubic solid solutions can be deposited up to an Al content of 70 atomic % [7,8]. The thermodynamics of the material has been successfully described using sophisticated computational approaches [9–11]. The elastic properties of $Ti_{(1-x)}Al_xN$ [12–14], $Cr_{(1-x)}Al_xN$ [15] and textured $Zr_{(1-x)}Al_xN$ [16] have been investigated and a general symmetry based projection technique has been suggested for predicting the elastic tensor of alloys [13]. The kinetics of the (spinodal) decomposition of $Ti_{(1-x)}Al_xN$ has been simulated by solving the *ab inito* parameterized Cahn-Hilliard equation [17] and the importance of elastic anisotropy in the microstructure evolution has been established. Since anisotropic microstructure hinders the dislocation

* Corresponding author. Department of Physics, Chemistry and Biology (IFM), Linköping University, SE-581 83 Linköping, Sweden.
E-mail address: feiwa@ifm.liu.se (F. Wang).

http://dx.doi.org/10.1016/j.actamat.2017.01.017
1359-6454/

motion through the material, microstructural design has became a strategic approach in developing hard coatings [18]. For example, superhard self-organized ZrAlN nanolabyrinthine [19] and Zr-Si-N nanocomposites [20] have been investigated by electron microscopy and nanoindentation. That is, in transition metal nitride alloys, elastic anisotropy is proved to be related to material hardness through the materials anisotropic microstructure [12,17,21,22].

The concept of multicomponent alloying in hard coatings to improve the materials hardness and thermal stability has been introduced by considering a mixing of CrN and $Ti_{(1-x)}Al_xN$ [23,24]. The basic idea of the concept consists of employing the spinodal decomposition to promote the formation of a metastable cubic phase of $Cr_{(1-x)}Al_xN$. It further underlines the increased interest for metastable phases in nitrides alloys. The zero temperature thermodynamics of quaternary transition metal nitride alloys has been recently investigated by Holec [25]. Though, cubic VN is found dynamically unstable at 0 K [26] the renormalized VN phonon dispersion relations calculated by Mei et al. [27] shows that the elastic constants do not change with the temperature. Since similar level of instability is assumed for NbN and TaN, calculations of the elastic constants at T = 0 K are highly valuable. The high temperature elasticity in TiN [28], CrN [29] and $Ti_{(1-x)}Al_xN$ [14] alloy has been investigated. However, the potential of multicomponent alloying for engineering the materials strength and elastic anisotropy in quaternary alloys has not been discussed yet.

Forming coherent multilayers, such as TiN/V(Nb)N or TiHfN/CrN, is proposed as alternative concept to extend the wear resistance and hardness of bulk monolithic materials, see Ref. [30]. The mixing thermodynamics of TiN/$Ti_{(1-x)}Al_xN(001)$ compared with the one of $Ti_{(1-x)}Al_xN$ has recently been investigated experimentally [31,32] and by *ab initio* calculations [33]. Though electron microscopy and atom probe tomography combined with phase field simulations have predicted the occurrence of surface directed spinodal decomposition [17], it has been found less developed than the bulk-like spinodal decomposition in $Ti_{(1-x)}Al_xN$. During the coherent spinodal decomposition of the alloys, the microstructure can be approximated by local coherent multilayers with different interfacial orientations. Therefore, by predicting the Young's modulus of the multilayers one elaborates the material's local strength distribution which affects the microstructural evolution, and by that the hardness of the material.

This paper is organized as follows. Section 2 is devoted to the computational details and the methodology for calculating elastic stiffness constants of alloys and superlattices of alloys. In Section 3 we present the equilibrium structural parameters of the alloys. Thereafter, the elasticity of quaternary transition metal nitride alloys is discussed. Using increased Ti content we discuss the trends in altering ductility via multicomponent alloying. In the last subsection we investigate the strength (Young's modulus) of multilayers and establish the usage of the bulk alloy Young's modulus values to design wear resistant superlattices using high-throughput screening. Finally, a summary of our work is given in Section 4.

2. Methodology

2.1. Calculation details

Binary nitrides - AlN, TiN and XN, where X = Zr, Hf, V, Nb, Ta, together with their $X_{0.5}Al_{0.5}N$ and $X_{0.5}Ti_{0.5}N$ ternary alloys were modeled with $(4 \times 4 \times 3)$ supercells of 96 atoms. The supercell size was chosen based on the results in Ref. [13] and based on the unit cell of the cubic B1 lattice. The substitutional alloying was modeled using the special quasirandom supercell (SQS) approach by Zunger [34] with minimizing the Warren-Cowley pair short-range order (SRO) [35] parameters up to the seventh nearest neighboring shell in the metal sublattice. $X_{0.33}Ti_{0.33}Al_{0.33}N$ quaternary alloys were simulated by $(3 \times 3 \times 3)$ supercells similarly on the basis of B1 conventional cell with 216 atoms. The total energy calculations were performed within density functional theory (DFT) using the projector augmented wave (PAW) [36] approach implemented in the Vienna Ab initio Simulation Package (VASP) [37]. The exchange-correlation energy was approximated by the Perdew-Burke-Ernzerhof generalized gradient functional (PBE-GGA) [38]. The lattice parameters and all the internal atomic coordinates were relaxed to obtain the ground-state structure. In the elastic constant calculations we applied a plane-wave cutoff energy of 600 eV. The reciprocal-space integration was performed using the Monkhorst-Pack scheme [39] with a *k*-mesh of $(6 \times 6 \times 6)$ except for Nb and Ta related alloys where $(7 \times 7 \times 7)$ was applied.

The TiN/$Ti_{(1-x)}Al_xN(001)$ multilayers were modeled with sharp interfaces using 1:1 materials ratio and 216 metal atoms all together. The models were more detailed explained in Ref. [40]. The elastic constants were calculated with a plane-wave cutoff of 520 eV and a Monkhorst-Pack *k*-mesh of $(5 \times 5 \times 3)$.

2.2. Elastic constants

The elastic stiffness constants

$$C_{ij} = \frac{1}{V_0}\frac{\partial^2 E(\vec{\varepsilon})}{\partial\varepsilon_i \partial\varepsilon_j}\bigg|_{\text{relaxed}} \tag{1}$$

using Voigt notation were extracted through the Taylor expansion of the total energy with respect to lattice distortion [41,42]. We applied strains $\vec{\varepsilon} = \{\varepsilon_1, \ldots, \varepsilon_6\}$ corresponding to ±1% and ±2% lattice distortions of the fully relaxed supercells without volume conservation. $E(\vec{\varepsilon})$ is the total energy of the distorted supercell and V_0 denotes the equilibrium volume of the non-distorted supercell.

The SQS approach in principle breaks the point group symmetry of the alloy and the different supercell models break it in different order. Therefore, inhomogeneous materials quantities of alloys, such as the elastic tensor in Eq. (1), have to be calculated carefully [40]. Recently, a symmetry based projection technique [43,44] has been suggested to derive accurate prediction of the elastic and piezoelectric tensor of substitutional alloys [13,45]. The symmetry projected cubic stiffness constant are calculated as

$$\overline{C}_{11} = \frac{C_{11}+C_{22}+C_{33}}{3}, \overline{C}_{12} = \frac{C_{12}+C_{13}+C_{23}}{3}, \\ \overline{C}_{44} = \frac{C_{44}+C_{55}+C_{66}}{3} \tag{2}$$

based on nine independent tensor elements: $C_{11}, C_{22}, C_{33}, C_{23}, C_{13}, C_{12}, C_{44}, C_{55}$ and C_{66}. The mechanical stability of a cubic crystal is proved by fulfilling the Born stability criteria [46];

$$\overline{C}_{44} > 0, \quad \overline{C}_{11} > |\overline{C}_{12}|, \quad \overline{C}_{11} + 2\overline{C}_{12} > 0. \tag{3}$$

Elastic anisotropy of single crystals can be quantified either by Zener's anisotropy ratio ($\overline{A} = 2\overline{C}_{44}/(\overline{C}_{11} - \overline{C}_{12})$) or by the directional dependence of the Young's modulus [41] which in cubic crystals is written as

$$\frac{1}{\overline{E}_{\ell_1\ell_2\ell_3}} = \overline{S}_{11} - 2\left(\overline{S}_{11} - \overline{S}_{12} - \frac{1}{2}\overline{S}_{44}\right)\left(\ell_1^2\ell_2^2 + \ell_2^2\ell_3^2 + \ell_1^2\ell_3^2\right). \tag{4}$$

here, $\overline{S}_{ij}$ is the elastic compliance coefficients which is the inverse of

elastic tensor $\overline{C}_{ij}$ and the 3-tuple (ℓ_1, ℓ_2, ℓ_3) stands for the directional cosines to the a, b and c axes.

Experimental determination of single-crystal elastic constants is highly limited by the preparation of single crystals in the studied systems. Indeed, physical vapor deposited (PVD) polycrystalline samples are widely available in thin film form and effective medium theories are established for polycrystalline materials. An upper bound on the effective elastic moduli of polycrystalline materials is achieved by the Voigt's (V) constant strain model, while the Reuss's (R) constant stress model gives a lower bound. Their arithmetic middle value is called the Hill's average (H) and used throughout this work because it commonly results to measured values. The polycrystalline Young's (E), shear (G), bulk (B) moduli and Poisson's ratio (ν) are common quantities which measure the materials response to external mechanical impact. They describe the cohesion or strain ratio in solids with respect to uniaxial, shear or hydrostatic loading. All can be expressed in terms of the single crystal stiffness constants $\overline{C}_{ij}$. A comprehensive overview of these elastic constants can be found in Ref. [47]. In the following we summarize the expressions of the polycrystalline elastic moduli using the bar for marking the symmetry projection required in case of alloys.

$$\begin{aligned} B_V = B_R &= \frac{\overline{C}_{11} + 2\overline{C}_{12}}{3}, \quad B_H = \frac{B_V + B_R}{2}, G_V \\ &= \frac{(\overline{C}_{11} - \overline{C}_{12} + 3\overline{C}_{44})}{5}, \quad G_R = \frac{5\overline{C}_{44}(\overline{C}_{11} - \overline{C}_{12})}{4\overline{C}_{44} + 3(\overline{C}_{11} - \overline{C}_{12})}, G_H \\ &= \frac{G_V + G_R}{2}, E = \frac{9B_H G_H}{3B_H + G_H}, \quad \nu = \frac{3B_H - 2G_H}{6B_H + 2G_H} \end{aligned} \tag{5}$$

Grimsditch and Nizzoli established a linear-elasticity model of multilayers with neglecting the interfacial heterogeneity [48]. Friák et al. rediscovered the method for nitride superlattices [49]. Within this sharp interface approximation an analytic formula is derived for the elastic stiffness constants of superlattices C_{ij}^{SL} with arbitrary interface orientations and layer periodicity. It requires only the bulk stiffness constant tensors of the constituent materials in the coordinate system assigned by the interface normal vector $\vec{n}$, that is commonly oriented in the canonical $\hat{z}$ direction. In the following we omit the component indices of the tensors and mark the layer numbers in the superlattice (SL) with 1 and 2. Thus,

$$C^{\mathrm{SL}} = \left(f_1 \overline{C}_1^{\vec{n}} M + f_2 \overline{C}_2^{\vec{n}}\right)(f_1 M + f_2 I)^{-1}, \tag{6}$$

where

$$M = P_1^{-1} P_2, \quad P_\alpha = \begin{pmatrix} 1 & 0 & 0 & 0 & 0 & 0 \\ 0 & 1 & 0 & 0 & 0 & 0 \\ & & \left(\overline{C}_\alpha^{\vec{n}}\right)_{31\cdots36} & & & \\ & & & 41\cdots46 & & \\ & & & & 51\cdots56 & \\ 0 & 0 & 0 & 0 & 0 & 1 \end{pmatrix}_{6\times6} \tag{7}$$

and f_α denotes the fraction of the material α in the multilayer. Having C^{SL} one derives

$$E_{\vec{n}} = 1 \Big/ S_{33}^{\mathrm{SL}} = \frac{C_{33}^{\mathrm{SL}}\left(C_{11}^{\mathrm{SL}} + C_{12}^{\mathrm{SL}}\right) - 2C_{13}^{\mathrm{SL}} C_{13}^{\mathrm{SL}}}{C_{11}^{\mathrm{SL}} + C_{12}^{\mathrm{SL}}} \tag{8}$$

for the Young's modulus of the multilayer (tetragonal symmetry) in the normal direction to the interface [50].

3. Results and discussion

3.1. Quaternary alloys

3.1.1. Structural properties

The equilibrium lattice constants obtained in this work are summarized in Table 1. For comparison, we present also some other theoretical (a_{other}) as well as experimental data ($a_{\mathrm{exp.}}$) available in the literature. One sees a good agreement between our results and a_{other}, $a_{\mathrm{exp.}}$ with deviations smaller than 1.4%. The lattice constants show the order of $a(X_{0.5}Al_{0.5}N) < a(X_{0.33}Ti_{0.33}Al_{0.33}N) < a(X_{0.5}Ti_{0.5}N)$ where X can be Zr, Hf, V, Nb or Ta. This trend is in a good agreement with previous experimental observations [51–57].

3.1.2. Single-crystal stiffness constants and sound velocities

The nine independently calculated elastic stiffness constants and the derived projected cubic elastic constants of all the alloys are summarized in Table 2. The small 1–2 GPa deviations in the $\overline{C}_{ij}$ values of the binary materials indicate the general accuracy of our elastic constants calculations. Much larger differences are obtained for the alloys as a consequence of the broken cubic symmetry [13]. To estimate the elastic constants of the studied multicomponent alloys at an arbitrary composition, we employed the linear fitting of the calculated values. In the fitting procedure, the full compositional triangle is split into four equal sub-triangles using the binary and ternary 50-50% mid-point values. In each of these triangles the $\overline{C}_{ij}$ values are fitted by the plane $a\,x + b\,y + c\,\overline{C}_{ij} = d$, where x and y is the content of Al and X, respectively. The obtained parameters are given in the Supplementary material. For the equiatomic quaternary alloys the fitted values are given in parentheses in Table 2. The linear fitted $\overline{C}_{ij}$ values of the quaternary alloys approximate well with the *ab initio* calculated ones. In general, we encounter $\sim 12\%$ error in the linearly predicted stiffness constants except for $\overline{C}_{12}$ in $Nb_{(1-x-y)}Ti_xAl_yN$ and $\overline{C}_{44}$ in $Ta_{(1-x-y)}Ti_xAl_yN$. Since these errors are comparable with the errors made in experimental determinations we suggest to use these sub-triangle linear fitted approximations to

Table 1
The calculated lattice parameters a(Å) of ternary and quaternary transition metal nitride alloys together with other calculational results (GGA), a_{other}, and experimental obtained ones, $a_{\mathrm{exp.}}$.

	a	a_{other}	$a_{\mathrm{exp.}}$
AlN	4.07	4.07 [25]	4.05 [66]
TiN	4.25	4.25 [25]	4.24 [66]
ZrN	4.60	4.62 [25]	4.58 [66]
HfN	4.53	4.54 [25]	4.53 [66]
VN	4.12	4.13 [25]	4.14 [66]
NbN	4.42	4.43 [25]	4.39 [66]
TaN	4.42	4.43 [25]	4.36 [66]
$Ti_{0.5}Al_{0.5}N$	4.18	4.184 [53]	4.18 [53]
$Zr_{0.5}Al_{0.5}N$	4.38	4.40[a]	4.32 [67]
$Hf_{0.5}Al_{0.5}N$	4.35	4.38 [68],4.35[a]	4.438 [69]
$V_{0.5}Al_{0.5}N$	4.11		4.12 [52]
$Nb_{0.5}Al_{0.5}N$	4.28	4.32 [70],4.30[a]	4.28 [70]
$Ta_{0.5}Al_{0.5}N$	4.28	4.28[a]	
$Zr_{0.5}Ti_{0.5}N$	4.44	4.46[a]	4.43 [71,72]
$Hf_{0.5}Ti_{0.5}N$	4.41	4.42[a]	
$V_{0.5}Ti_{0.5}N$	4.19	4.19 [60]	4.168 [73], 4.19 [74]
$Nb_{0.5}Ti_{0.5}N$	4.34	4.36 [60], 4.345 [75], 4.37[a]	4.32 [76], 4.41 [77]
$Ta_{0.5}Ti_{0.5}N$	4.35	4.35 [60], 4.35,[a] 4.34 [78]	4.35 [78], 4.32 [79]
$Zr_{0.33}Al_{0.33}Ti_{0.33}N$	4.35	4.34[a]	4.31 [53]
$Hf_{0.33}Al_{0.33}Ti_{0.33}N$	4.33	4.31[a]	
$V_{0.33}Al_{0.33}Ti_{0.33}N$	4.16		
$Nb_{0.33}Al_{0.33}Ti_{0.33}N$	4.27	4.28[a]	
$Ta_{0.33}Al_{0.33}Ti_{0.33}N$	4.27	4.27[a]	

[a] The linear fitted lattice constants obtained from data in Ref. [25].

Table 2
The *ab initio* calculated cubic elastic stiffness constants (C_{ij}) of binary, ternary and quaternary transition metal nitride alloys. $\overline{C}_{ij}$ denotes the cubic projected elastic stiffness constants. The values are given in GPa. The labels correspond to the notation used in Figs. 1–4 and 7.

	Label	C_{11}	C_{22}	C_{33}	C_{12}	C_{13}	C_{23}	C_{44}	C_{55}	C_{66}	$\overline{C}_{11}$	$\overline{C}_{12}$	$\overline{C}_{44}$
AlN		402	402	402	157	157	157	300	300	300	402	157	300
TiN		589	590	589	125	126	125	166	168	166	590	125	167
ZrN		530	532	530	109	111	109	121	119	121	531	110	120
HfN		633	635	633	90	92	90	164	160	164	634	91	163
VN		620	620	620	167	167	167	127	129	127	620	167	128
NbN		663	663	663	133	133	133	87	85	87	663	133	86
TaN		728	723	728	136	135	136	64	61	64	726	136	63
$Ti_{0.5}Al_{0.5}N$	(0)	456	425	460	161	152	160	201	211	198	447	158	203
$Zr_{0.5}Al_{0.5}N$	Zr(1)	391	374	378	154	149	141	156	174	156	381	148	162
$Zr_{0.33}Al_{0.33}Ti_{0.33}N$	Zr(2)	450	450	442	137	142	134	157	156	158	447(449)	138(151)	157(176)
$Zr_{0.5}Ti_{0.5}N$	Zr(3)	526	507	525	120	117	119	133	135	133	519	119	134
$Hf_{0.5}Al_{0.5}N$	Hf(1)	435	416	425	156	151	148	166	183	165	425	152	171
$Hf_{0.33}Al_{0.33}Ti_{0.33}N$	Hf(2)	470	470	467	136	142	137	166	164	165	469(473)	138(154)	165(182)
$Hf_{0.5}Ti_{0.5}N$	Hf(3)	552	535	554	120	118	121	138	141	138	547	120	139
$V_{0.5}Al_{0.5}N$	V(1)	481	487	460	154	176	168	187	191	187	476	166	188
$V_{0.33}Al_{0.33}Ti_{0.33}N$	V(2)	498	511	499	163	157	146	176	165	175	503(481)	155(163)	172(193)
$V_{0.5}Ti_{0.5}N$	V(3)	520	508	536	156	183	152	143	143	145	521	164	144
$Nb_{0.5}Al_{0.5}N$	Nb(1)	493	452	490	156	158	158	149	151	161	478	157	154
$Nb_{0.33}Al_{0.33}Ti_{0.33}N$	Nb(2)	516	525	508	150	153	141	153	146	151	516(500)	148(177)	150(170)
$Nb_{0.5}Ti_{0.5}N$	Nb(3)	583	551	593	158	136	149	121	119	119	576	148	120
$Ta_{0.5}Al_{0.5}N$	Ta(1)	515	459	513	148	161	164	149	152	157	496	158	153
$Ta_{0.33}Al_{0.33}Ti_{0.33}N$	Ta(2)	532	536	523	150	154	145	149	141	147	530(506)	150(170)	146(170)
$Ta_{0.5}Ti_{0.5}N$	Ta(3)	568	568	588	158	145	152	120	113	118	575	152	117

estimate the stiffness constants of the quaternary alloys for arbitrary x and y in the triangle.

From the projected elastic constants we see that the Born mechanical stability criteria (Eq. (3)) is fulfilled for all the considered alloys. $\overline{C}_{11}$ is the largest among the constants. Fig. 1 presents the projected cubic elastic constants, $\overline{C}_{11}$, $\overline{C}_{12}$ and $\overline{C}_{44}$, of ternary $X_{0.5}Al_{0.5}N$, $X_{0.5}Ti_{0.5}N$ and quaternary alloys $X_{0.33}Ti_{0.33}Al_{0.33}N$ where X can be Zr, Hf, V, Nb and Ta. The dashed lines show the elastic stiffness constants of $Ti_{0.5}Al_{0.5}N$. In general, with decreasing the AlN content the value of $\overline{C}_{11}$ increases significantly while the change in $\overline{C}_{44}$ and $\overline{C}_{12}$ is just minor. The largest increase is obtained for $Zr_{(1-x-y)}Ti_xAl_yN$ and $Hf_{(1-x-y)}Ti_xAl_yN$ alloys (X is a IVB metal in the periodic table) and in these two alloys one finds the possibility to synthesize alloys softer in $\overline{C}_{11}$ than the reference value of $Ti_{0.5}Al_{0.5}N$. The Vanadium-based quaternary alloys show only a minor error around 10%. The trend that $\overline{C}_{44}$ decreases with increasing Ti concentration can be explained by an increased $d-d$ orbital overlap between the first neighbor metal atoms [58–61]. Alloying a VB transition metal (increasing the number of d electrons) in $Ti_{0.5}Al_{0.5}N$ increases $\overline{C}_{11}$ significantly. The change in the elastic stiffness constants from 3d to 5d transition metals is negligible.

We derived the acoustic wave velocities through solving the

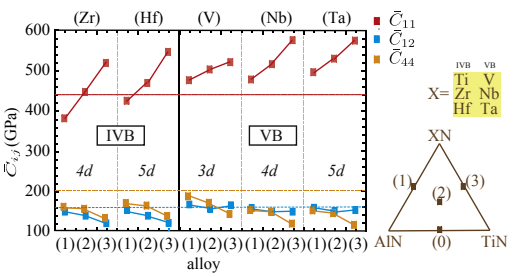

Fig. 1. The single crystal cubic elastic stiffness constants of quaternary $X_{(1-x-y)}Ti_xAl_yN$ alloys where X is Zr, Hf, V, Nb and Ta. The horizontal dashed lines denote the stiffness constants of $Ti_{0.5}Al_{0.5}N$ (0). The (1), (2) and (3) marked alloys are explained in the subdiagram.

Table 3
Calculated longitudinal acoustic sound velocities of binary, ternary and quaternary transition metal nitride alloys along the cubic high symmetry crystallographic directions [001, 110] and [111]. The values are given in m/s. The labels correspond to the notation used in Figs. 1–4 and 7.

	Label	v_{100}	v_{110}	v_{111}
AlN		9973	11974	12570
TiN		10520	9919	9710
ZrN		8591	7825	7552
HfN		6801	6191	5975
VN		10045	9212	8918
NbN		8977	7670	7182
TaN		6960	5741	5273
$Ti_{0.5}Al_{0.5}N$	(0)	9769	10389	10587
$Zr_{0.5}Al_{0.5}N$	Zr(1)	8132	8604	8756
$Zr_{0.33}Al_{0.33}Ti_{0.33}N$	Zr(2)	8926	8951	8959
$Zr_{0.5}Ti_{0.5}N$	Zr(3)	9054	8459	8251
$Hf_{0.5}Al_{0.5}N$	Hf(1)	6714	6982	7068
$Hf_{0.33}Al_{0.33}Ti_{0.33}N$	Hf(2)	7617	7613	7612
$Hf_{0.5}Ti_{0.5}N$	Hf(3)	7461	6934	6750
$V_{0.5}Al_{0.5}N$	V(1)	9682	10012	10120
$V_{0.33}Al_{0.33}Ti_{0.33}N$	V(2)	9869	9849	9842
$V_{0.5}Ti_{0.5}N$	V(3)	9554	9232	9123
$Nb_{0.5}Al_{0.5}N$	Nb(1)	8725	8666	8646
$Nb_{0.33}Al_{0.33}Ti_{0.33}N$	Nb(2)	9301	8989	8883
$Nb_{0.5}Ti_{0.5}N$	Nb(3)	9170	8388	8111
$Ta_{0.5}Al_{0.5}N$	Ta(1)	7044	6930	6891
$Ta_{0.33}Al_{0.33}Ti_{0.33}N$	Ta(2)	7916	7581	7465
$Ta_{0.5}Ti_{0.5}N$	Ta(3)	7440	6808	6584

Christoffel equation [62]. In Table 3 we show the longitudinal sound velocities in the three main crystallographic directions [100], [110], and [111] for all the alloys. One sees that the sound velocities decrease with the period number, that is with changing from 3*d* to 5*d* orbitals. Moreover, the longitudinal sound velocities decrease from lighter to heavier elements in the [111] direction and increase in [100]. The decrease of ν_{111} is connected to the decreasing $\overline{C}_{44}$ in Fig. 1, which is a clear indication of the decreased covalent bonding nature expressed also by a positive Cauchy pressure. The increase of ν_{100} is a consequence of stiffening $\overline{C}_{11}$. One sees that the sound velocity values show large similarities for X from the same period, that is, $Zr_{(1-x-y)}Ti_xAl_yN$ alloys have sound velocities close to the values of $Nb_{(1-x-y)}Ti_xAl_yN$, and similarly for the pair of $Hf_{(1-x-y)}Ti_xAl_yN$ and $Ta_{(1-x-y)}Ti_xAl_yN$.

3.1.3. Polycrystalline elastic constants and ductility

The values of the polycrystalline elastic constant are listed in Table 4 for all alloys. Fig. 2 shows a comparison of the Hill averaged Young's (*E*), shear (*G*) and bulk (*B*) moduli using the reference line of the value of $Ti_{0.5}Al_{0.5}N$. Since binary AlN has the lowest bulk modulus among the binary nitrides, it is reasonable to choose the Al content to guide our analysis. In general for each alloy *B* shows a monotonous increase with decreasing the Al content, which agrees with the results in Ref. [25]. In case of $V_{(1-x-y)}Ti_xAl_yN$, $Nb_{(1-x-y)}Ti_xAl_yN$ and $Ta_{(1-x-y)}Ti_xAl_yN$ quaternary alloys, *B* is above the reference value of 255 GPa. The value of *E* and *G* are below or close to the reference value in all cases. Further it is seen that *G* and *E* correlate. There is a distinct difference between alloying IVB or VB metal nitrides with $Ti_{0.5}Al_{0.5}N$. In case of IVB elements one observes a monotonous increase of *E* and *G* with the decrease of Al content. For VB transition metals both moduli have a maximum in the middle of the compositional triangle, where the TiN/AlN ratio is around 1. It also suggests that the *G*/*B* ratio shows a different behavior for the IVB and VB group. The *G*/*B* ratio is an accepted phenomenological criterion for estimation of the relative ductility and brittleness of materials [63]. A material is characterized as brittle if $G/B > 0.57$ otherwise one says that it is ductile (i.e, able to deform before breaking). With VB metal alloying we observe a significant decrease of *G*/*B* ratio with decreasing AlN content, indicating possible increase of the ductility.

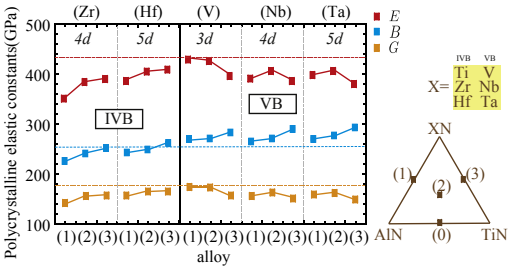

Fig. 2. The polycrystalline elastic constants of quaternary $X_{(1-x-y)}Ti_xAl_yN$ alloys where X is Zr, Hf, V, Nb and Ta. *E*, *B* and *G* denote the Young's, shear and bulk modulus, respectively.

Pettifor suggested the Cauchy pressure $(\overline{C}_{12} - \overline{C}_{44})$ as a measure of the angular bonding character in metals [64,65]. Negative Cauchy pressure indicates a directional character of atomic bonds, while a positive value means rather delocalized metallic bonds. Fig. 3 compares the alloys in terms of brittleness and bonding character. Cubic AlN is characterized with covalent bonding and a highly brittle behavior. In the other corner of the diagram, the cubic TaN is found as metallic and ductile material. $Ti_{0.5}Al_{0.5}N$ is found next to TiN in the middle of the diagram. One sees that mixing $Ti_{0.5}Al_{0.5}N$ with ZrN results in *G*/*B* values, which are similar to ZrN with negligible dependence on the mixing-strategies along the lines (0)–(1), (0)–(2) and (0)–(3). In case of $Hf_{(1-x-y)}Ti_xAl_yN$ alloys one predicts tendency towards ductile behavior though binary HfN is fairly brittle and being closer to AlN than to $Ti_{0.5}Al_{0.5}N$. There is a general tendency that along the (0)-(2)-(3) lines one observes

Table 4
Calculated Hill averaged polycrystalline elastic constants of quaternary $X_{(1-x-y}$ Ti_xAl_yN alloys where X is Zr, Hf, V, Nb and Ta. *B*, *G* and *E* denote the bulk, shear and Young's modulus. ν stands for the Poisson's ratio, and *A* is the Zener's anisotropic ratio. The elastic moduli are given in GPa. The labels correspond to the notation used in Figs. 1–4 and 7.

	Label	$(\overline{C}_{12} - \overline{C}_{44})$	B_H	G_H	G/B	E	ν	A	$E(111)/E(100)$
AlN		−143	239	210	0.88	486	0.16	2.45	2.02
TiN		−41	280	190	0.68	465	0.22	0.72	0.77
ZrN		−11	250	151	0.63	377	0.25	0.57	0.64
HfN		−72	272	200	0.74	482	0.20	0.60	0.67
VN		39	318	161	0.51	413	0.28	0.56	0.62
NbN		47	310	138	0.45	360	0.31	0.33	0.38
TaN		73	333	124	0.37	331	0.33	0.21	0.26
$Ti_{0.5}Al_{0.5}N$	(0)	−46	255	177	0.70	432	0.22	1.41	1.32
$Zr_{0.5}Al_{0.5}N$	Zr(1)	−14	226	142	0.63	352	0.24	1.39	1.32
$Zr_{0.33}Al_{0.33}Ti_{0.33}N$	Zr(2)	−20	241	156	0.65	385	0.23	1.01	1.01
$Zr_{0.5}Ti_{0.5}N$	Zr(3)	−15	252	157	0.62	391	0.24	0.67	0.72
$Hf_{0.5}Al_{0.5}N$	Hf(1)	−20	243	157	0.64	387	0.23	1.25	1.20
$Hf_{0.33}Al_{0.33}Ti_{0.33}N$	Hf(2)	−27	249	165	0.66	406	0.23	1.00	1.00
$Hf_{0.5}Ti_{0.5}N$	Hf(3)	−19	262	165	0.63	410	0.24	0.65	0.70
$V_{0.5}Al_{0.5}N$	V(1)	−22	270	174	0.65	430	0.23	1.22	1.17
$V_{0.33}Al_{0.33}Ti_{0.33}N$	V(2)	−17	271	173	0.64	427	0.24	0.99	0.99
$V_{0.5}Ti_{0.5}N$	V(3)	20	283	157	0.55	397	0.27	0.80	0.83
$Nb_{0.5}Al_{0.5}N$	Nb(1)	4	265	156	0.59	392	0.25	0.96	0.96
$Nb_{0.33}Al_{0.33}Ti_{0.33}N$	Nb(2)	−2	271	163	0.60	407	0.25	0.81	0.84
$Nb_{0.5}Ti_{0.5}N$	Nb(3)	28	290	151	0.52	387	0.28	0.56	0.61
$Ta_{0.5}Al_{0.5}N$	Ta(1)	5	270	159	0.59	399	0.25	0.90	0.92
$Ta_{0.33}Al_{0.33}Ti_{0.33}N$	Ta(2)	4	277	162	0.59	407	0.25	0.77	0.80
$Ta_{0.5}Ti_{0.5}N$	Ta(3)	37	293	149	0.51	381	0.28	0.55	0.61

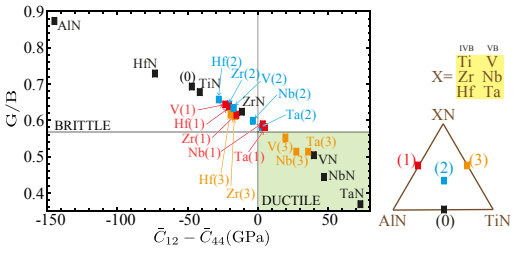

Fig. 3. The G/B vs. Cauchy pressure map of quaternary $X_{(1-x-y)}Ti_xAl_yN$ alloys where X is Zr, Hf, V, Nb and Ta.

increased ductility and the effect is much stronger for VB metals than for IVB ones. The same behavior is noticed along the (0)-(2)-XN lines. Furthermore, ductility is increasing with the increase of the period number, that is with changing from 3*d* transition metals to 5*d* ones. Decreasing the Cauchy pressure indicates tendency toward stronger covalency in the atomic bonds, which results in an increased resistance against shearing. The changes of shear modulus values, G in Fig. 2 correlate with the Cauchy pressure values in Fig. 3.

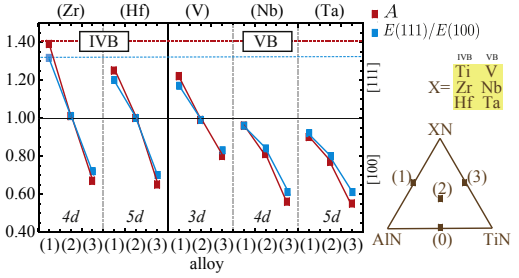

Fig. 4. The Zener's anisotropy ratio, A, and the Young's modulus ratio, $E(111)/E(100)$, of quaternary $X_{(1-x-y)}Ti_xAl_yN$ alloys where X is Zr, Hf, V, Nb and Ta.

3.1.4. Elastic anisotropy

Fig. 4 shows the derived Zener's elastic anisotropy, A, and the Young's modulus ratio, $E(111)/E(100)$, for all alloys. It is clear, that the two quantities correlate. One obtains $A \approx 1$ in the compositional triangle for ZrN, HfN and VN alloyed in $Ti_{0.5}Al_{0.5}N$. Moreover, in these quaternary alloys one has the possibility to engineer the elastic soft direction between the crystallographic [100] and [111] directions by a compositional variation. In contrast, in the NbN and TaN containing alloys, the [100] direction is always the elastically stiff direction. The largest freedom of tuning A is predicted in $Zr_{(1-x-y)}Ti_xAl_yN$.

In Fig. 5 one sees the directional dependence of the Young's modulus in each quaternary alloys. The figure underlines that the quaternary alloys are very close to be elastically isotropic by showing a spherical shaped $E_{\ell_1\ell_2\ell_3}$ distribution for mixing ZrN, HfN and VN with $Ti_{(1-x)}Al_xN$. It is clear that the sound velocity variations in Table 3 correlate with the Young's modulus distribution in each alloy. That is, in the case of $\nu_{100} < \nu_{110} < \nu_{111}$, one observes a Young's modulus variation characteristic for B1 AlN, while in case of $\nu_{100} > \nu_{110} > \nu_{111}$, $E_{\ell_1\ell_2\ell_3}$ has an elongated shape along [100].

3.2. Multilayers

The elastic constants of multilayer were derived using the linear-elasticity model of superlattices, see Eqs. (6)–(8). The error in Eq. (8), $\mathcal{O}(\delta C_{ij})$, is in the order of the error in the elastic constants δC_{ij}. That is, Eq. (8) propagates the error without accumulation. δC_{ij} is caused by excluding the lattice parameter difference and the altered chemistry (electronic effect) at the interface from the superlattice (SL) approach. We benchmark the SL approach by comparing the derived SL elastic constants with the *ab initio* calculated ones for TiN/$Ti_{(1-x)}Al_xN$(001) in Fig. 6. The computational error in the *ab initio* C_{ij} values is estimated to be less than 1 GPa. Accordingly, δC_{ij} in Fig. 6 is connected to the improper interface description in the SL approach. For example, one sees larger δC_{ij} s for TiN/AlN(001) corresponding to the large lattice mismatch between AlN and TiN; for the values see Table 1. Otherwise, δC_{ij} is below 8% for $C_{11}, C_{33}, C_{44}, C_{66}$ and distinguishably larger for C_{12} and C_{13}. It can be explained by the large lattice mismatch contribution. The similarity of the lattice parameters of the ternary

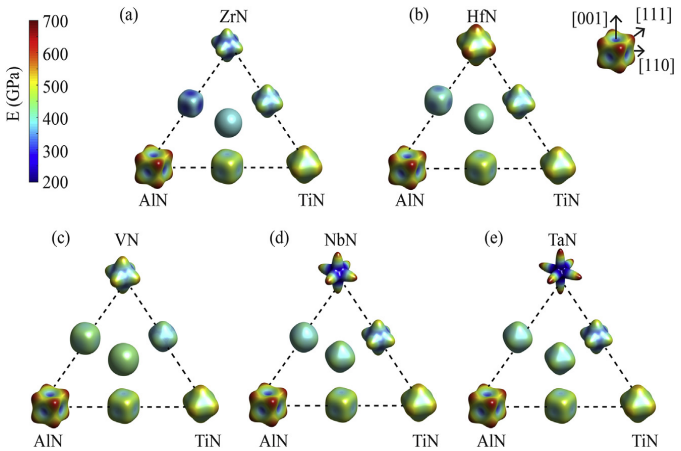

Fig. 5. Compositional maps of the directional dependence of the Young's modulus, E, in the quaternary $X_{(1-x-y)}Ti_xAl_yN$ alloys where X is Zr, Hf, V, Nb and Ta.

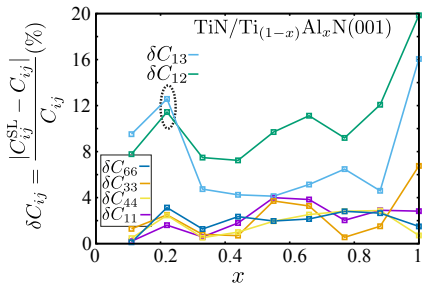

Fig. 6. The relative errors of the linearly derived superlattice (SL) elastic stiffness constants of TiN/$Ti_{(1-x)}Al_xN$(001) multilayers compared with the *ab initio* calculated values.

transition metal nitride alloys (see Table 1), combined with the derived smooth trends in the elastic constants of the quaternary alloys (see Figs. 1 and 5), allows to utilize the superlattice model to predict the Young's modulus of multilayers using Eq. (8).

Fig. 7 shows the Young's modulus $E_{\vec{n}}$ of ternary and quaternary alloys coherently multilayered with the most common TiN and ZrN binaries. It shows the values for a 1:1 fraction of the materials in the multilayer. These multilayered structures are commonly assumed to be formed in the gradient region during the spinodal decompositions of the alloys themselves. One sees in the figure that for all the multilayers, the variations of the multilayer $E_{\vec{n}}$ values follow the ones shown in Fig. 5 for the bulk alloys in addition to the fact that ZrN has lower Young's modulus values than TiN. HfN containing alloys in the (111) multilayers behave differently because binary HfN shows the largest Young's modulus along [111] (Fig. 5). In comparing the influence of alloying in the compositional triangles we see, that with the (111) interfacial orientation, $E_{\vec{n}}$ decreases with increasing TiN content, that is along the (1)-(2)-(3) line. On the contrary, $E_{\vec{n}}$ increases with an increasing TiN content in the [001] oriented multilayers. The dominant [001] directional high strength (Young's modulus) of all the transition metal nitrides determines the strength of the multilayers and results in higher

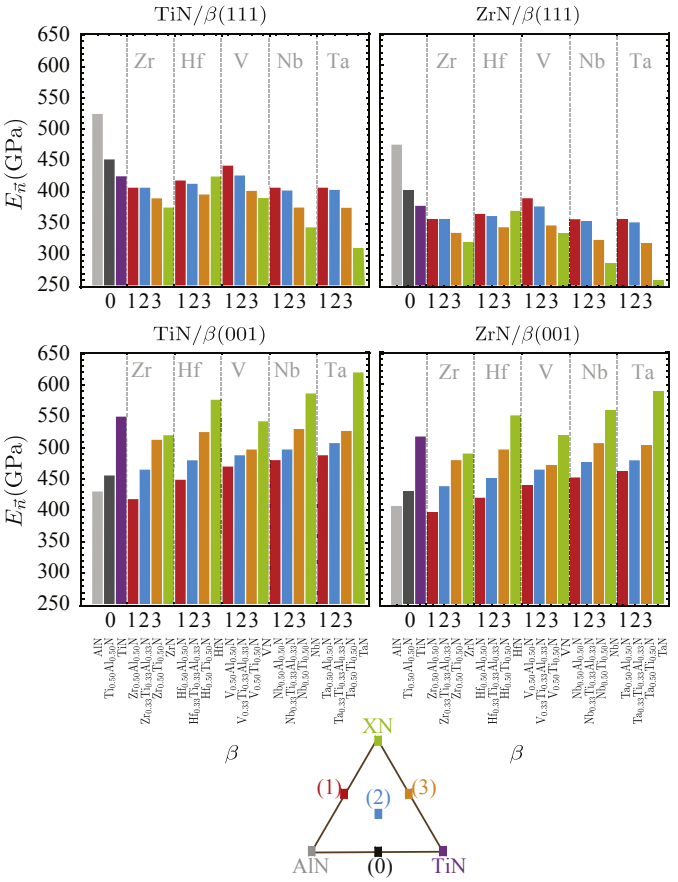

Fig. 7. The Young's modulus perpendicular to the interface in coherent (001) and (111) orientated TiN/$X_{(1-x-y)}Ti_xAl_yN$ and ZrN/$X_{(1-x-y)}Ti_xAl_yN$ multilayers where X is Zr, Hf, V, Nb and Ta.

Young's modulus values for the (001) multilayers. In summary, we establish that one can estimate the variation of $E_{\vec{n}}$ in the multilayers based on Fig. 5.

In Fig. 2 we have established that with increasing TiN content, along the (1)-(2)-(3) alloy samples, the bulk moduli of the alloys increase and G in general follows E. Using these facts we conclude that the [111] orientated multilayers can become more ductile with increasing the TiN content. On the other hand, the increase of the $E_{\vec{n}}$ values with the TiN content in the (001) multilayers results in larger G/B values, which predicts increased brittleness.

4. Summary and conclusions

In this study we analyzed the effects of multicomponent alloying and forming coherent multilayers on the elastic and mechanical properties in transition metal nitride materials. We calculated the change in the materials elastic constants and starting from the reference of $Ti_{0.5}Al_{0.5}N$ we suggested strategies to engineer the materials ductility/brittleness for thin film hard coating applications. The elastic stiffness constants of the alloys were derived using the cubic symmetry based projection technique. We showed that the bulk modulus increases in general with decreasing AlN content and that alloying a VB transition metals in $Ti_{0.5}Al_{0.5}N$ significantly increases $\bar{C}_{11}$. The sound velocities decreased in the [111] crystallographic direction with alloying from lighter to heavier elements and increase in [100]. In quaternary $X_{(1-x-y)}Ti_xAl_yN$ alloys with X as IVB transition metals both, the Young's modulus and shear modulus increased with the removal of AlN, while in case of X chosen from VB transition metals both moduli have a maximum. The ductility of alloys should increase with increasing the period number of X. We predicted that elastically isotropic materials can be obtained in case of mixing ZrN, HfN or VN with $Ti_{(1-x)}Al_xN$ alloys, and the largest freedom to tune the elastic properties was obtained in $Zr_{(1-x-y)}Ti_xAl_yN$. On the example of TiN/$Ti_{(1-x)}Al_xN$(001) we showed that a linear superlattice approach is capable to predict elasticity of coherent multilayers with sharp interfaces instead of performing computationally demanding *ab initio* calculations. We predicted that the multilayers of TiN or ZrN with quaternary transition metal alloys supports the increase of ductility (decreasing G/B ratio) in the case of the [111] interfacial orientation. On the other hand, we demonstrated that with the [100] growth direction, the compositional variation affects the material in such a way that it should become more brittle. The multilayers with the [111] interface showed higher materials strength (Young's modulus). We underlined in this work that the Young's moduli variation in the parent (bulk) quaternary nitride alloys gives an approximate tool to screen the Young's moduli in coherent multilayers in the framework of high-throughput methods to design coherent superlattices.

Acknowledgment

The authors would like to gratefully acknowledge the support from the Swedish Foundation for Strategic Research (SSF) project SRL Grant No. 10-0026. This work was also supported by the M-ERA.NET (2013-02355) funded Multiscale Computational-design of novel hard nanostructure Coatings (MC2) project. Fei Wang acknowledges funding received through Erasmus Mundus Joint European Doctoral Programme *DocMASE*. I.A.A. wishes to acknowledge the Swedish Research Council (VR) Grant No. 2015-04391, the Swedish Government Strategic Research Area in Materials Science on Functional Materials at Linköping University (Faculty Grant SFO-Mat-LiU No. 2009 00971), as well as the Grant of Ministry of Education and Science of the Russian Federation (Grant No. 14.Y26.31.0005). The calculations have been carried out through the Swedish National Infrastructure for Computing (SNIC) and performed at the Swedish National Supercomputer Center (NSC) for high performance computing in Linköping.

Appendix A. Supplementary data

Supplementary data related to this article can be found at http://dx.doi.org/10.1016/j.actamat.2017.01.017.

References

[1] M.W. Covert, E.M. Knight, J.L. Reed, M.J. Herrgard, B.O. Palsson, Integrating high-throughput and computational data elucidates bacterial networks, Nature 429 (2004) 92–96.
[2] J. Jeon, S. Nim, J. Teyra, A. Datti, J.L. Wrana, S.S. Sidhu, J. Moffat, P.M. Kim, A systematic approach to identify novel cancer drug targets using machine learning, inhibitor design and high-throughput screening, Genome Med. 6 (2014) 57.
[3] C.M. Stafford, S. Guo, C. Harrison, M.Y.M. Chiang, Combinatorial and high-throughput measurements of the modulus of thin polymer films, Rev. Sci. Instrum. 76 (2005) 062207.
[4] M. De Jong, W. Chen, T. Angsten, A. Jain, R. Notestine, A. Gamst, M. Sluiter, C. Krishna Ande, S. van der Zwaag, J.J. Plata, C. Toher, S. Curtarolo, G. Ceder, K.A. Persson, M. Asta, Charting the complete elastic properties of inorganic crystalline compounds, Sci. Data 2 (2015) 150009.
[5] H.A. Jehn, S. Hofmann, V.-E. Rückborn, W.-D. Münz, Morphology and properties of sputtered (Ti,Al)N layers on high speed steel substrates as a function of deposition temperature and sputtering atmosphere, J. Vac. Sci. Technol. A Vac. Surf. Film. 4 (1986) 2701.
[6] O. Knotek, M. Böhmer, T. Leyendecker, On structure and properties of sputtered Ti and Al based hard compound films, J. Vac. Sci. Technol. A Vac. Surf. Film. 4 (1986) 2695.
[7] A. Hörling, L. Hultman, M. Odén, J. Sjölén, L. Karlsson, Thermal stability of arc evaporated high aluminum-content $Ti_{1-x}Al_xN$ thin films, J. Vac. Sci. Technol. A Vac. Surf. Film. 20 (2002) 1815.
[8] U. Wahlström, L. Hultman, J.-E. Sundgern, F. Adibi, I. Petrov, J.E. Greene, Crystal growth and microstructure of polycrystalline $Ti_{1-x}Al_xN$ alloy films deposited by ultra-high-vacuum dual-target magnetron sputtering, Thin Solid Films 235 (1993) 62–70.
[9] B. Alling, A. Ruban, A. Karimi, O. Peil, S. Simak, L. Hultman, I. Abrikosov, Mixing and decomposition thermodynamics of c-$Ti_{1-x}Al_xN$ from first-principles calculations, Phys. Rev. B 75 (2007) 045123.
[10] B. Alling, A.V. Ruban, A. Karimi, L. Hultman, I.A. Abrikosov, Unified cluster expansion method applied to the configurational thermodynamics of cubic $Ti_{1-x}Al_xN$, Phys. Rev. B 83 (2011) 104203.
[11] N. Shulumba, O. Hellman, Z. Raza, B. Alling, J. Barrirero, F. Mücklich, I.A. Abrikosov, M. Odén, Lattice vibrations change the solid solubility of an alloy at high temperatures, Phys. Rev. Lett. 117 (2016) 205502.
[12] F. Tasnádi, I.A. Abrikosov, L. Rogström, J. Almer, M.P. Johansson, M. Odén, Significant elastic anisotropy in $Ti_{1-x}Al_xN$ alloys, Appl. Phys. Lett. 97 (2010).
[13] F. Tasnádi, M. Odén, I.A. Abrikosov, Ab initio elastic tensor of cubic $Ti_{0.5}Al_{0.5}$ N alloys: dependence of elastic constants on size and shape of the supercell model and their convergence, Phys. Rev. B - Condens. Matter Mater. Phys. 85 (2012).
[14] N. Shulumba, O. Hellman, L. Rogström, Z. Raza, F. Tasnádi, I.A. Abrikosov, M. Odén, Temperature-dependent elastic properties of $Ti_{1-x}Al_xN$ alloys, Appl. Phys. Lett. 107 (2015) 231901.
[15] L. Zhou, D. Holec, P.H. Mayrhofer, First-principles study of elastic properties of cubic $Cr_{1-x}Al_xN$ alloys, J. Appl. Phys. 113 (2013) 043511.
[16] D. Holec, F. Tasnádi, P. Wagner, M. Friák, J. Neugebauer, P.H. Mayrhofer, J. Keckes, Macroscopic elastic properties of textured ZrN-AlN polycrystalline aggregates: from ab initio calculations to grain-scale interactions, Phys. Rev. B 90 (2014) 1–9.
[17] A. Knutsson, J. Ullbrand, L. Rogström, N. Norrby, L.J.S. Johnson, L. Hultman, J. Almer, M.P. Johansson Jöesaar, B. Jansson, M. Odén, Microstructure evolution during the isostructural decomposition of TiAlN-A combined in-situ small angle x-ray scattering and phase field study, J. Appl. Phys. 113 (2013) 213518.
[18] P.H. Mayrhofer, A. Hörling, L. Karlsson, J. Sjölén, T. Larsson, C. Mitterer, L. Hultman, Self-organized nanostructures in the Ti-Al-N system, Appl. Phys. Lett. 83 (2003) 2049.
[19] N. Ghafoor, L.J.S. Johnson, D.O. Klenov, J. Demeulemeester, P. Desjardins, I. Petrov, L. Hultman, M. Odén, Nanolabyrinthine ZrAlN thin films by self-organization of interwoven single-crystal cubic and hexagonal phases, APL Mater 1 (2013) 022105.
[20] N. Ghafoor, I. Petrov, D.O. Klenov, B. Freitag, J. Jensen, J. Greene, L. Hultman, M. Odén, Self-organized anisotropic $(Zr_{1-x}Six)Ny$ nanocomposites grown by reactive sputter deposition, Acta Mater 82 (2015) 179–189.
[21] L. Johnson, L. Rogström, M. Johansson, M. Odén, L. Hultman, Microstructure evolution and age hardening in (Ti,Si)(C,N) thin films deposited by cathodic arc evaporation, Thin Solid Films 519 (2010) 1397–1403.

[22] G. Abadias, A. Michel, C. Tromas, C. Jaouen, S. Dub, Stress, interfacial effects and mechanical properties of nanoscale multilayered coatings, Surf. Coat. Technol. 202 (2007) 844–853.

[23] H. Lind, R. Forsén, B. Alling, N. Ghafoor, F. Tasnádi, M.P. Johansson, I.A. Abrikosov, M. Odén, Improving thermal stability of hard coating films via a concept of multicomponent alloying, Appl. Phys. Lett. 99 (2011) 091903.

[24] R. Forsén, M. Johansson, M. Odén, N. Ghafoor, Decomposition and phase transformation in TiCrAlN thin coatings, J. Vac. Sci. Technol. A Vac. Surf. Film. 30 (2012) 061506.

[25] D. Holec, L. Zhou, R. Rachbauer, P.H. Mayrhofer, Alloying-related trends from first principles: an application to the Ti-Al-X-N system, J. Appl. Phys. 113 (2013) 113510.

[26] V.I. Ivashchenko, P.E.A. Turchi, Phonon softening and the phase transition in VN, Phys. Rev. B 78 (2008) 224113.

[27] A.B. Mei, O. Hellman, N. Wireklint, C.M. Schlepütz, D.G. Sangiovanni, B. Alling, A. Rockett, L. Hultman, I. Petrov, J.E. Greene, Dynamic and structural stability of cubic vanadium nitride, Phys. Rev. B 91 (2015) 054101.

[28] P. Steneteg, O. Hellman, O. Vekilova, N. Shulumba, F. Tasnádi, I. Abrikosov, Temperature dependence of TiN elastic constants from ab initio molecular dynamics simulations, Phys. Rev. B 87 (2013) 094114.

[29] E. Mozafari, N. Shulumba, P. Steneteg, B. Alling, I.A. Abrikosov, Finite-temperature elastic constants of paramagnetic materials within the disordered local moment picture from ab initio molecular dynamics calculations, Phys. Rev. B 94 (2016) 054111.

[30] M. Stueber, H. Holleck, H. Leiste, K. Seemann, S. Ulrich, C. Ziebert, Concepts for the design of advanced nanoscale PVD multilayer protective thin films, J. Alloys Compd. 483 (2009) 321–333.

[31] A. Knutsson, M.P. Johansson, P.O.A. Persson, L. Hultman, M. Odén, Thermal decomposition products in arc evaporated TiAlN/TiN multilayers, Appl. Phys. Lett. 93 (2008) 143110.

[32] A. Knutsson, M.P. Johansson, L. Karlsson, M. Odén, Thermally enhanced mechanical properties of arc evaporated $Ti_{0.34}Al_{0.66}N$/TiN multilayer coatings, J. Appl. Phys. 108 (2010) 044312.

[33] F. Wang, I.A. Abrikosov, S.I. Simak, M. Odén, F. Mücklich, F. Tasnádi, Coherency effects on the mixing thermodynamics of cubic $Ti_{1-x}Al_xN$/TiN(001) multilayers, Phys. Rev. B 93 (2016) 174201.

[34] A. Zunger, S.H. Wei, L.G. Ferreira, J.E. Bernard, Special quasirandom structures, Phys. Rev. Lett. 65 (1990) 353–356.

[35] A.V. Ruban, I.A. Abrikosov, Configurational thermodynamics of alloys from first principles: effective cluster interactions, Rep. Prog. Phys. 71 (2008) 046501.

[36] P.E. Blöchl, Projector augmented-wave method, Phys. Rev. B 50 (1994) 17953–17979.

[37] G. Kresse, J. Furthmüller, Efficient iterative schemes for ab initio total-energy calculations using a plane-wave basis set, Phys. Rev. B 54 (1996) 11169–11186.

[38] J.P. Perdew, K. Burke, M. Ernzerhof, Generalized gradient approximation made simple, Phys. Rev. Lett. 77 (1996) 3865–3868.

[39] J.D. Pack, H.J. Monkhorst, Special points for Brillouin-zone integrations, Phys. Rev. B 16 (1977) 1748–1749.

[40] F. Tasnádi, F. Wang, M. Odén, I.A. Abrikosov, Special quasirandom structure method in application for advanced properties of alloys: a study on $Ti_{0.5}Al_{0.5}N$ and TiN/$Ti_{0.5}Al_{0.5}$ N multilayer, Comput. Mater. Sci. 103 (2015) 194–199.

[41] J.F. Nye, Physical Properties of Crystals, Oxford Science Publications, 1992, p. 1985 reprinted ed., Oxford Clarendon Press.

[42] L. Vitos, Computational Quantum Mechanics for Materials Engineers, Engineering Materials and Processes, Springer, London, 2007.

[43] J.T. Browaeys, S. Chevrot, Decomposition of the elastic tensor and geophysical applications, Geophys. J. Int. 159 (2004) 667–678.

[44] M. Moakher, A.N. Norris, The closest elastic tensor of arbitrary symmetry to an elasticity tensor of lower symmetry, J. Elast. 85 (2006) 215–263.

[45] M.A. Caro, S. Zhang, T. Riekkinen, M. Ylilammi, M.A. Moram, O. Lopez-Acevedo, J. Molarius, T. Laurila, Piezoelectric coefficients and spontaneous polarization of ScAlN, J. Phys. Condens. Matter 27 (2015) 245901.

[46] K. Huang, M. Born, Dynamical Theory of Crystal Lattices, Oxford University Press, London, 1954.

[47] H.M. Ledbetter, R.P. Reed, Elastic properties of metals and alloys, I. Iron, Nickel, and Iron-Nickel alloys, J. Phys. Chem. Ref. Data 2 (1973) 531.

[48] M. Grimsditch, F. Nizzoli, Effective elastic constants of superlattices of any symmetry, Phys. Rev. B 33 (1986) 5891–5892.

[49] M. Friák, D. Tytko, D. Holec, P.P. Choi, P. Eisenlohr, D. Raabe, J. Neugebauer, Synergy of atom-probe structural data and quantum-mechanical calculations in a theory-guided design of extreme-stiffness superlattices containing metastable phases, New J. Phys. 17 (2015) 93004.

[50] A. Cazzani, M. Rovati, Extrema of Young's modulus for elastic solids with tetragonal symmetry, Int. J. Solids Struct. 42 (2005) 5057–5096.

[51] P.H. Mayrhofer, R. Rachbauer, D. Holec, Influence of Nb on the phase stability of Ti-Al-N, Scr. Mater. 63 (2010) 807–810.

[52] F. Rovere, D. Music, S. Ershov, M.T. Baben, H.-G. Fuss, P.H. Mayrhofer, J.M. Schneider, Experimental and computational study on the phase stability of Al-containing cubic transition metal nitrides, J. Phys. D. Appl. Phys. 43 (2010) 035302.

[53] L. Chen, D. Holec, Y. Du, P.H. Mayrhofer, Influence of Zr on structure, mechanical and thermal properties of Ti-Al-N, Thin Solid Films 519 (2011) 5503–5510.

[54] R. Rachbauer, D. Holec, P. Mayrhofer, Increased thermal stability of Ti-Al-N thin films by Ta alloying, Surf. Coat. Technol. 211 (2011) 98–103.

[55] R. Rachbauer, D. Holec, M. Lattemann, L. Hultman, P.H. Mayrhofer, Electronic origin of structure and mechanical properties in Y and Nb alloyed Ti-Al-N thin films, Int. J. Mater. Res. 102 (2011) 735–742.

[56] R. Rachbauer, A. Blutmager, D. Holec, P. Mayrhofer, Effect of Hf on structure and age hardening of Ti-Al-N thin films, Surf. Coat. Technol. 206 (2012) 2667–2672.

[57] S. Glatz, R. Hollerweger, P. Polcik, R. Rachbauer, J. Paulitsch, P. Mayrhofer, Thermal stability and mechanical properties of arc evaporated Ti-Al-Zr-N hard coatings, Surf. Coat. Technol. 266 (2015) 1–9.

[58] P.H. Mayrhofer, D. Music, J.M. Schneider, Influence of the Al distribution on the structure, elastic properties, and phase stability of supersaturated $Ti_{1-x}Al_xN$, J. Appl. Phys. 100 (2006) 094906.

[59] D.G. Sangiovanni, V. Chirita, L. Hultman, Electronic mechanism for toughness enhancement in $TixM_{1-x}$ N(M=Mo and W), Phys. Rev. B - Condens. Matter Mater. Phys. 81 (2010) 1–7.

[60] D.G. Sangiovanni, L. Hultman, V. Chirita, Supertoughening in B1 transition metal nitride alloys by increased valence electron concentration, Acta Mater. 59 (2011) 2121–2134.

[61] D.G. Sangiovanni, V. Chirita, L. Hultman, Toughness enhancement in TiAlN-based quaternary alloys, Thin Solid Films 520 (2012) 4080–4088.

[62] R.E. Newnham, Properties of Materials: Anisotropy, Symmetry, Structure, first ed., Oxford University Press, USA, 2005.

[63] S. Pugh, Relations between the elastic moduli and the plastic properties of polycrystalline pure metals, Philos. Mag. Ser. 7 45 (1954) 823–843.

[64] D.G. Pettifor, Theoretical predictions of structure and related properties of intermetallics, Mater. Sci. Technol. 8 (1992) 345–349.

[65] K. Chen, L.R. Zhao, J.S. Tse, I. Introduction, Ab initio study of elastic properties of Ir and Ir3X compounds, J. Appl. Phys. 93 (2003) 2414–2417.

[66] Powder Diffraction Files 00-046-1200 (AlN), 03-065-0565 (TiN), 00-035-0768 (VN), 00-035-0753 (ZrN), 03-065-5011 (NbN), 00-033-0592 (HfN), 03-065-9404 (TaN), International Center for Diffraction Data, 2007. PDF-2/release.

[67] R. Lamni, R. Sanjinés, M. Parlinska-Wojtan, A. Karimi, F. Lévy, Microstructure and nanohardness properties of Zr-Al-N and Zr-Cr-N thin films, J. Vac. Sci. Technol. A 23 (2005) 593–598.

[68] B. Alling, A. Karimi, I. Abrikosov, Electronic origin of the isostructural decomposition in cubic $M_{1-x}Al_xN$ (M= Ti, Cr, Sc, Hf): a first-principles study, Surf. Coat. Technol. (2008) 883–886.

[69] B. Howe, J. Bareño, M. Sardela, J. Wen, J. Greene, L. Hultman, A. Voevodin, I. Petrov, Growth and physical properties of epitaxial metastable $Hf_{1-x}Al_xN$ alloys deposited on MgO(001) by ultrahigh vacuum reactive magnetron sputtering, Surf. Coat. Technol. 202 (2007) 809–814.

[70] D. Holec, R. Franz, P.H. Mayrhofer, C. Mitterer, Structure and stability of phases within the NbN-AlN system, J. Phys. D. Appl. Phys. 43 (2010) 145403.

[71] A. Hoerling, J. Sjölén, H. Willmann, T. Larsson, M. Odén, L. Hultman, Thermal stability, microstructure and mechanical properties of $Ti_{1-x}Zr_xN$ thin films, Thin Solid Films 516 (2008) 6421–6431.

[72] V.V. Uglov, V.M. Anishchik, S.V. Zlotski, G. Abadias, S.N. Dub, Structural and mechanical stability upon annealing of arc-deposited Ti-Zr-N coatings, Surf. Coat. Technol. 202 (2008) 2394–2398.

[73] M. Roldán, M. Alcalá, C. Real, Characterisation of ternary $Ti_xV_{1-x}N_y$ nitride prepared by mechanosynthesis, Ceram. Int. 38 (2012) 687–693.

[74] U. König, Deposition and properties of multicomponent hard coatings, Surf. Coat. Technol. 33 (1987) 91–103.

[75] Z.-Y. Jiao, P.-F. Tao, Ab initio study on the mechanical and electronic properties of the $Ti_{1-x}Nb_xN$ alloys, Eur. Phys. J. B 88 (2015) 33.

[76] K. Vasu, M.G. Krishna, K.A. Padmanabhan, Effect of Nb concentration on the structure, mechanical, optical, and electrical properties of nano-crystalline $Ti_{1-x}Nb_xN$ thin films, J. Mater. Sci. 47 (2012) 3522–3528.

[77] G.M. Matenoglou, L.E. Koutsokeras, C.E. Lekka, G. Abadias, C. Kosmidis, G.A. Evangelakis, P. Patsalas, Structure, stability and bonding of ternary transition metal nitrides, Surf. Coat. Technol. 204 (2009) 911–914.

[78] G.M. Matenoglou, C.E. Lekka, L.E. Koutsokeras, G. Karras, C. Kosmidis, G.A. Evangelakis, P. Patsalas, Structure and electronic properties of conducting, ternary $Ti_xTa_{1-x}N$ films, J. Appl. Phys. 105 (2009) 103714.

[79] G. Abadias, L.E. Koutsokeras, S.N. Dub, G.N. Tolmachova, A. Debelle, T. Sauvage, P. Villechaise, Reactive magnetron cosputtering of hard and conductive ternary nitride thin films: Ti-Zr-N and Ti-Ta-N, J. Vac. Sci. Technol. A Vac. Surf. Film. 28 (2010) 541.

Supplemental material

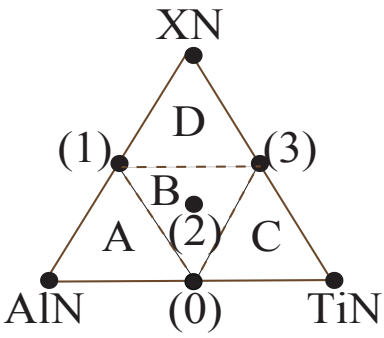

FIG. 1. (Color online) The triangle diagram with marked (0) $Ti_{0.5}Al_{0.5}N$, (1)$X_{0.5}Al_{0.5}N$, (2)$X_{0.33}Ti_{0.33}Al_{0.33}N$ and (3)$X_{0.5}Ti_{0.5}N$ alloys where X is Zr, Hf, V, Nb and Ta.

TABLE I. The derived a, b and c fitting parameters of the $a\,x + b\,y' + c\,\bar{C}_{ij} = d$ ($y' = (\sqrt{3}/2)y$) planes for each sub-triangles in the compositional triangle of quaternary $Zr_yTi_{(1-x-y)}Al_xN$ alloys. The fitting is made by using the binary and ternary 50-50% mid-point values.

$\bar{C}_{ij}$	Sub-triangle	a	b	c	d
$\bar{C}_{11}$	A	-19.4855	-21.75	-0.2165	-106.5211
	B	-59.7557	1.5	-0.2165	-126.6562
	C	-61.9208	0.25	-0.2165	-127.7387
	D	59.7557	-40.5	0.2165	109.7687
$\bar{C}_{12}$	A	-0.4330	-9.25	-0.4330	-68.4160
	B	12.5573	-26.75	-0.2165	-34.2080
	C	14.2894	-11.25	-0.2165	-27.0632
	D	-12.5573	11.75	0.2165	27.7128
$\bar{C}_{44}$	A	42.0022	-113.75	-0.4330	-87.9015
	B	12.1243	-41.5	-0.2165	-43.9507
	C	15.5884	-25.5	-0.2165	-36.1565
	D	-12.1243	14.0	0.2165	32.0429

TABLE II. The derived a, b and c fitting parameters of the $a\,x + b\,y' + c\,\bar{C}_{ij} = d$ ($y' = (\sqrt{3}/2)y$) planes for each sub-triangles in the compositional triangle of quaternary $Hf_yTi_{(1-x-y)}Al_xN$ alloys. The fitting is made by using the binary and ternary 50-50% mid-point values.

$\bar{C}_{ij}$	Sub-triangle	a	b	c	d
$\bar{C}_{11}$	A	-19.4855	0.25	-0.2165	-106.5211
	B	-52.8275	19.5	-0.2165	-123.1921
	C	-61.9208	14.25	-0.2165	-127.7387
	D	52.8275	-74.0	0.2165	99.5929
$\bar{C}_{12}$	A	-0.4330	-5.25	-0.4330	-68.4160
	B	13.8564	-27.0	-0.2165	-34.2080
	C	14.2894	-10.75	-0.2165	-27.0632
	D	-13.8564	22.5	0.2165	32.2594
$\bar{C}_{44}$	A	42.0022	-104.75	-0.4330	-87.9015
	B	13.8564	-40.0	-0.2165	-43.9507
	C	15.5884	-23.0	-0.2165	-36.1565
	D	-13.8564	-4.0	0.2165	24.8982

TABLE III. The derived a, b and c fitting parameters of the $a\,x + b\,y' + c\,\bar{C}_{ij} = d$ ($y' = (\sqrt{3}/2)y$) planes for each sub-triangles in the compositional triangle of quaternary $V_yTi_{(1-x-y)}Al_xN$ alloys. The fitting is made by using the binary and ternary 50-50% mid-point values.

$\bar{C}_{ij}$	Sub-triangle	a	b	c	d
$\bar{C}_{11}$	A	-19.4855	25.75	0.2165	-106.5211
	B	-19.4855	25.75	-0.2165	-106.5211
	C	-61.9208	1.25	-0.2165	-127.7387
	D	19.4855	-60.75	0.2165	91.3656
$\bar{C}_{12}$	A	-0.4330	8.75	-0.4330	-68.4160
	B	0.8660	2.5	-0.2165	-34.2080
	C	14.2894	11.25	-0.2165	-27.0632
	D	-0.8660	-1.0	0.2165	34.8575
$\bar{C}_{44}$	A	42.0022	-87.75	-0.4330	-87.9015
	B	19.0525	-40.5	-0.2165	-43.9507
	C	15.5884	-20.5	-0.2165	-36.1565
	D	-19.0525	19.0	0.2165	34.6410

TABLE IV. The derived a, b and c fitting parameters of the $a\,x + b\,y' + c\,\bar{C}_{ij} = d$ ($y' = (\sqrt{3}/2)y$) planes for each sub-triangles in the compositional triangle of quaternary $Nb_yTi_{(1-x-y)}Al_xN$ alloys. The fitting is made by using the binary and ternary 50-50% mid-point values.

$\bar{C}_{ij}$	Sub-triangle	a	b	c	d
$\bar{C}_{11}$	A	-19.4855	26.75	-0.2165	-106.5211
	B	-42.4352	40.0	-0.2165	-117.9959
	C	-61.9208	28.75	-0.2165	-127.7387
	D	42.4352	-68.0	0.2165	105.8716
$\bar{C}_{12}$	A	-0.4330	-0.25	-0.4330	-68.4160
	B	3.8971	-7.25	-0.2165	-34.2080
	C	14.2894	3.25	-0.2165	-27.0632
	D	-3.8971	9.75	0.2165	35.2905
$\bar{C}_{44}$	A	42.0022	-121.75	-0.4330	-87.9015
	B	14.7224	-50.0	-0.2165	-43.9507
	C	15.5884	-32.5	-0.2165	-36.1565
	D	-14.7224	25.5	0.2165	33.3419

TABLE V. The derived a, b and c fitting parameters of the $a\,x + b\,y' + c\,\bar{C}_{ij} = d$ ($y' = (\sqrt{3}/2)y$) planes for each sub-triangles in the compositional triangle of quaternary $Ta_yTi_{(1-x-y)}Al_xN$ alloys. The fitting is made by using the binary and ternary 50-50% mid-point values.

$\bar{C}_{ij}$	Sub-triangle	a	b	c	d
$\bar{C}_{11}$	A	-19.4855	35.75	-0.2165	-106.5211
	B	-34.2080	44.25	-0.2165	-113.8823
	C	-61.9208	28.25	-0.2165	-127.7387
	D	34.2080	-95.25	0.2165	91.7986
$\bar{C}_{12}$	A	-0.4330	0.75	-0.4330	-68.4160
	B	2.5980	-4.5	-0.2165	-34.2080
	C	14.2894	5.25	-0.2165	-27.0632
	D	-2.5980	9.5	0.2165	36.3730
$\bar{C}_{44}$	A	42.0022	-122.75	-0.4330	-87.9015
	B	15.5884	-52.0	-0.2165	-43.9507
	C	15.5884	-34.0	-0.2165	-36.1565
	D	-15.5884	36.0	0.2165	37.0225

Paper V

High temperature thermodynamics of spinodal decomposition in arc deposited $Ti_xNb_yAl_zN$ coatings

Ferenc Tasnádi
Lina Rogström
Jianqiang Zhu
Fei Wang
T.-W. Hsu
Hans Lind
Igor A. Abrikosov
M. P. Johansson-Jõesaar
Magnus Odén

V

Submitted to Materials and Design

High temperature thermodynamics of spinodal decomposition in arc deposited $Ti_xNb_yAl_zN$ coatings

F. Tasnádi[1,2], L. Rogström[1], J. Zhu[1], F. Wang[1], T.-W. Hsu[1], H. Lind[1], I.A. Abrikosov[1,2], M. P. Johansson-Jõesaar[1,3], and M. Odén[1]

[1]Department of Physics, Chemistry, and Biology (IFM), Linköping University, SE-581 83 Linköping, Sweden

[2]Materials Modeling and Development Laboratory, National University of Science and Technology 'MISIS', 119049 Moscow, Russia

[3]SECO Tools AB, SE-737 82 Fagersta, Sweden

Keywords: hard coating films; NbN; cathodic arc deposition; thermodynamic stability; hardness

Abstract

Using first principles calculations and experimental methods we show that B1 structured solid solution $Ti_xNb_yAl_zN$ can be grown. The mixing free energy surface indicates that the alloys should decompose. Theoretical analysis of the thermodynamic driving force towards the spinodal decomposition shows that the force can be different in alloys with equally low thermodynamic stability but different Nb content, indicating that the detailed picture of the decomposition should also be different. Electron microscopy and nanoindentation underlines different age hardening of the samples We demonstrate that an alloy with the optimized composition, $Ti_{0.42}Nb_{0.17}Al_{0.41}N$ combines high thermal stability and age hardening behavior.

High temperature metastable alloys define a class of materials, which are typically synthesized using the thin-films non-equilibrium growth techniques. They often demonstrate high thermal stability combined with high strength or improved oxidation and corrosion resistance [1]. The cutting tool industry focuses on the material's high-temperature stability and mechanical strength to increase the cutting rate [2]. Power plant gas turbine and aircraft engine blades are developed with focus on the materials' resistance to high-temperature corrosion, oxidation, and creep in order to stabilize its surface during harsh environment operation [3].

Low-temperature physical vapor deposition (PVD) is a method to successfully grow metastable thin films with high thermal stability. For example, cubic TiAlN alloy coatings have been developed with extraordinary hardness improvement at elevated temperature [4,5], which is explained by the microstructural changes caused by the material's isostructural spinodal decomposition [6]. However, in Ti_xAl_zN alloys, the high temperature phase transformation of cubic AlN to hexagonal AlN causes a drastic hardness drop and it should be suppressed in order to extend the thermal operation window of the coatings. Therefore, attempts to shift this phase transformation up to higher temperatures and stabilize the extended hardness value are highly motivated [7,8,9].

Nb has a low mass density and it is known to increase the creep resistance of steels [10]. Chemical alloying of refractory materials with Nb is a promising approach to achieve multiphase alloys with high temperature strength, toughness and oxidation resistance [11]. Mayrhofer et al. has investigated the effect of small (up to 12%) amount of Nb on the properties of (Ti-Al)N coatings especially around the composition $Ti_{0.4}Al_{0.6}N$ [12,13].

We use a combination of first principles calculations and experimental methods to evaluate the thermal stability of cubic $Ti_xNb_yAl_zN$ alloys in the predicted most interesting compositional region. The phase stability is simulated for the full range of Nb, Ti and Al contents. Based on the theoretical results, three compositions with similar thermodynamic stability, but different thermodynamic driving force towards the spinodal decomposition were selected. The corresponding coatings were grown by cathodic arc deposition and their stability were evaluated up to 1100 °C. The experimental results show that the detailed picture of the spinodal decomposition in the three alloys is indeed different, in accordance with the predicted theoretical trends. Robust decomposition tendency is observed in high-Nb-content coatings while the sample $Ti_{0.42}Nb_{0.17}Al_{0.41}N$ which belongs to the composition region of the slowly varying mixing free energy shows higher temperature stability upon annealing.

The Gibbs free energy *G* of $Ti_xNb_yAl_zN$ is calculated as:

$$G(x,y,z,T) = E_{chem+conf}(x,y,z) - TS_{conf}(x,y,z) + F_{vib}(x,y,z) + pV, \quad (1)$$

Here $E_{chem+conf}$ is the *chemical* internal energy of the alloy, which includes the effect of substitutional disorder, F_{vib} denotes its vibrational Helmholtz free energy and (x,y,z) gives the alloy composition. S_{conf} is the configurational entropy, p stands for pressure and V for volume. The configurational entropy was defined within the mean-field approximation. We observed that the electronic entropy has negligible contribution and therefore this term is neglected. Shulumba *et al.* [14] demonstrated the importance of the vibrational contribution to the description of the Ti_xAl_zN phase diagram. However, the methodology proposed in Ref. [14] is extremely computationally demanding and therefore in this work the vibrational contribution to the free energy is estimated within the Debye model [15] using the elastic constants of $Ti_xNb_yAl_zN$ calculated at temperature T=0 K [16] for selected compositions followed by their piece-wise linear interpolation over the compositional triangle.

The chemical internal energies were determined by first-principles density functional theory (DFT) calculations. For details see Supplemental materials.

$Ti_xNb_yAl_zN$ coatings were grown in an industrial cathodic arc deposition system (Metaplas MZR323), described in detail elsewhere [17]. Three cathodes with Ti:Nb:Al atomic ratios of 50:0:50, 33:33:34, and 0:50:50 were vertically mounted, top to bottom, on the chamber wall and polished WC-12wt%Co substrates (ISO SNUN120408) were placed in five horizontal rows on a rotating cylinder opposite to the cathodes. With this setup, five unique $Ti_xNb_yAl_zN$ coatings were obtained by plasma mixing. The metal content of the coatings positioned just in front of each of the cathode (three rows) is close to that of the specific cathode. The two compositions grown at intermediate positions in between the top-and-middle cathodes and middle-and-bottom cathodes, respectively, had a metal content caused by plasma mixing from the two nearest cathodes. Before deposition, the substrates were sputter cleaned with Ar ions. In order to minimize Co diffusion [4] into the coating during post-deposition annealing, a 300 nm thick TiN interlayer was deposited first followed by a ~3.5 µm thick $Ti_xNb_yAl_zN$ coating. Depositions were carried out at ~500 °C and 4.5 Pa nitrogen pressure with the substrate holder rotating at 3 rpm (single rotation) and a substrate bias of -30 V. A $Ti_{0.50}Al_{0.50}N$ reference coating was grown at 2 Pa N_2 pressure and a substrate temperature of 400 °C using a $Ti_{0.5}Al_{0.5}$ cathode and a substrate bias of -40 V. Post-deposition thermal treatments of the coatings were performed at a hold temperature between 800 and 1100 °C for 15 min in a vacuum furnace at total pressure below 7×10^{-4} Pa. A heating and cooling rate of 20 °C/min were used.

The coatings were studied by scanning electron microscopy, x-ray diffractometry, nanoindentation and analytical transmission electron microscopy. See Supplemental materials for details.

Figure 1 (a) and (b) show the mixing Gibbs free energy

$$\Delta G = G\left(Ti_xNb_yAl_zN\right) - xG(TiN) - yG(NbN) - zG(AlN) \quad (2)$$

of cubic $Ti_xNb_yAl_zN$ calculated at 1100 K and at zero-pressure relative to the cubic B1 phases of TiN, NbN, and AlN at 1100 K. Note that a solid solution is thermodynamically unstable against the phase separation if ΔG is positive. However, it can often still be synthesized in the thin film growth. It is important to underline that upon annealing an unstable solid solution undergoes the spinodal decomposition if the second derivative $\partial G^2/\partial\, v(x,y,z)^2$is negative, while the alloys are at least metastable if it is positive. The direction with the most negative value of the second derivative gives an estimation of the thermodynamic driving force towards the spinodal decomposition, and it determines the most probable local spinodal decomposition path.

One can see that the inclusion of the vibrational contribution stabilizes the solid solution. This observation is in agreement with conclusions presented in [14] for the Ti_xAl_zN quasi-binary system. NbN is known to have B1 structure at room temperature [18, 19], which is dynamically unstable at 0 K. We note that the mixing free energy of Nb_yAl_zN and Ti_xAl_zN is positive for all compositions, while it is negative for Ti_xNb_yN. The high positive value of the mixing Gibbs free energy in the Al-rich end of Nb_yAl_zN and the minimum value at equal Nb and Ti content in Ti_xNb_yN determine the topology of the mixing Gibbs free energy surface. In comparison, the Gibbs free energy landscapes of $Ti_xCr_yAl_zN$ [9] and $Ti_xZr_yAl_zN$ [20] were dominated by a single high maximum value at the Ti_xAl_zN and Zr_yAl_zN edges, respectively. Comparing $Ti_xNb_yAl_zN$ with the latter systems, a novel feature is observed where the mixing Gibbs free energy has a small positive value at the border between two distinct regions with positive and negative mixing free energy. We focus on this region of the composition space. Three

experimental samples, S1, S2, and S3 were deposited in the vicinity of this border with the following compositions, S1: $Ti_{0.42}Nb_{0.17}Al_{0.41}N$, S2: $Ti_{0.22}Nb_{0.36}Al_{0.42}N$, S3: $Ti_{0.03}Nb_{0.45}Al_{0.52}N$.

Note that the region on the diagram where the alloys are at least metastable is filled with open circles. The length of the arrows is proportional to the magnitude of the second derivative of the mixing Gibbs free energy, indicating the local strength of the tendency towards the spinodal decomposition. This approach has been successfully used for studies of the spinodal decomposition in $Ti_xCr_yAl_zN$ [9] and $Ti_xZr_yAl_zN$ [20]. Figure 1 shows the so determined most favorable local paths for the spinodal decomposition. Interestingly, while vibrational contribution strongly affects the thermodynamic stability of the solution phases, it does not change the favorable paths for the spinodal decomposition.

Considering three compositions S1, S2 and S3 suggested for the experimental studies, one sees that the values of ΔG are similar for all of them, while the local topology of the free energy surface is different for each sample, as indicated by the different behavior of the arrows in the vicinity of S1, S2, and S3 compositions. This suggests the different thermal stabilities for the samples against the spinodal decomposition.

Figure 2 shows x-ray diffractograms of the as-deposited and annealed coatings. The as-deposited coatings reveal a cubic B1 $Ti_xNb_yAl_zN$ solid solution with a lattice parameter close to that of B1 TiN that increases with increasing Nb-content. The coatings have a columnar structure with decreasing column width for increasing Nb-content as observed in SEM of fractured cross-sections (not shown). For the highest Nb-content the columns consist of small grains, attributed to the more intense impingement resulting from more energetic species arriving to the coating due to the higher average charge state of Nb-species in the plasma [21, 22]. It results in broader diffraction peaks for sample S3. During annealing, the diffraction peaks initially broaden, which is a sign of spinodal decomposition, followed by appearance of peaks originating from hexagonal h-AlN at 1000-1100 °C. Figure 3(a) shows a cross-sectional bright field TEM micrograph of the as-deposited S1 sample confirming the columnar structure. The coating has an artificial layered structure due to the sample fixture rotation and inhomogeneous distribution of the species with different atomic mass in the plasma [23]. This is a general feature of all the coatings studied in this work. EDS reveals thin, dark contrast Nb-enriched layers and thicker, bright contrast layers in which Ti, Nb and Al are distributed homogenously. Figures 3(b)-(c) and 3(d) show elemental contrast scanning TEM micrographs of the S1 and S2 samples annealed at 900 °C. In addition to the inherent layering, compare with Fig. 3(a), a nanoscale compositional modulation, homogeneously distributed in the entire coatings, has evolved during annealing, observed as dark and bright contrast elongated domains. An elemental profile in Fig. 3(e) shows that the dark contrast domains are Al-enriched while the bright contrast domains are enriched in Ti and Nb. Thus, spinodal decomposition occurs resulting in (TiNb)AlN and TiNb(Al)N domains (parenthesis indicate minority elements). According to Fig. 1. TiNb(Al)N has a slightly lower free energy than TiN while Al(TiNb)N has higher energy than AlN. The increasing length of the arrows towards the AlN-corner indicates a steep change of the energy. This change is smaller when the composition is close to the TiAlN edge.

Figure 4(a) shows the width of the cubic 200 diffraction peak as a function of annealing temperature. For all samples, the broadening at 800 °C indicates that decomposition has started. For the two coatings with highest Nb-content (S2 and S3), the width of the cubic 200 peak is the largest after annealing at 800 °C while coarsening of the (TiNb)AlN and TiNb(Al)N domains result in reduced peak width at higher temperatures. The small increase in peak width at 1000 °C can be assigned to re-nucleation of c-TiNb(Al)N grains. In comparison, the largest peak broadening is observed after annealing at 900 °C for the low Nb-content coating S1. This demonstrates that spinodal

decomposition occurs at a lower temperature for S2 and S3 as suggested by the results in Figure 1. Annealing at 1000 °C results in formation of h-AlN in S2 and S3, easiest observed in the insets in Figure 2. For S1, peaks from the h-AlN phase are first observed after annealing at 1100 °C, thus formation of h-AlN is delayed compared to the other samples. It underlines the expected robust decomposition with high Nb-content predicted by Figure 1.

Figure 4(b) presents the hardness of the as-deposited and annealed samples. The hardness of the as-deposited samples is related to the residual stress state, which is -2.3 GPa for S1, -2.1 GPa for S2 and -1.7 GPa for S3. For sample S3, the hardness is also affected by the smaller grain size in this coating, which acts to increase the hardness. All the three coatings show an initial increase in hardness up to 800 °C as a result of the compositional modulations evolving during the spinodal decomposition. In the case of S3, the strong decrease of hardness at temperatures above 800 °C is related to the formation and growth of h-AlN. This can be compared to the behavior of a $Ti_{0.50}Al_{0.50}N$ coating, for which the hardness drops dramatically above 900 °C due to formation and growth of h-AlN. For S1 the hardness remains high to annealing temperatures of 1000 °C due to the retained cubic structure. Above 1000 °C, growth of h-AlN causes the hardness to decrease rapidly for S1 and S2 too.

It is important to underline that the experimental results discussed above confirm the theoretical prediction. For $Ti_{0.33}Al_{0.67}N$ alloys, which is in the vicinity of the free energy maximum of Ti_xAl_zN with strong variation of $\partial^2 G/\partial x^2$, low thermal stability has been observed with an appearance of the hexagonal AlN phase at a relatively low temperature (1000 °C) causing a significant drop of the hardness [24]. On the other hand, for a $Ti_{0.13}Zr_{0.69}Al_{0.18}N$ sample from an extended region with slowly varying mixing free energy, a high temperature stabilization of the (metastable) solid solution has been shown [20]. From the point of view of hard coatings applications, a too limited strength toward the spinodal decomposition may reduce favorable age hardening, as it has been observed in Ti_zZr_yN [25].

In samples S2 and S3 notably amplified strength toward the decomposition into stable Ti_xNb_yN and metastable Ti_xAl_zN has been observed. In sample S1, where the Nb-content is low, the decomposition is suppressed. This is in agreement with our calculations. Indeed, they indicate that there is higher tendency towards the spinodal decomposition in S3, which should lead to significant age hardening but low thermal stability stability. For S1 thermal stability is predicted to be higher than for S2 and S3.

In summary, metastable solid solution cubic B1 structured $Ti_xNb_yAl_zN$ coatings with up to 45 at.% NbN-contents have been deposited using cathodic arc evaporation. Addition of Nb refines the grain size while a columnar structure is retained. The metastable $Ti_xNb_yAl_zN$ solid solution phase decomposes by spinodal decomposition, resulting in nanoscale compositional modulations, followed by formation and growth of h-AlN. After annealing at 1100 °C for 15 min, the coatings consisted of h-AlN and c- Ti_xNb_yN and no separation of TiN and NbN is observed which is understood by the ab initio calculated diagram of the Gibbs free energy of mixing. With increasing the Nb-content the detrimental mechanical effect of the h-AlN occurs at a lower temperature. However, with the right amount of Nb in the coatings, an extended high temperature stability of the hardness can be achieved.

The authors acknowledge the support provided by the Swedish Foundation for Strategic Research (SSF) program SRL Grant No. 10-0026 and 621-2012-4401, the Swedish Government Strategic Research Area in Materials Science on Functional Materials at Linköping University (Faculty Grant SFO-Mat-LiU No 2009-00971), Vinnova (M-ERA.NET project: Multi-scale computational-driven design

of novel hard nanostructured Coatings - MC2), and the Ministry of Education and Science of the Russian Federation (Grant No. 14.Y26.31.0005). The calculations have been carried out through the Swedish National Infrastructure for Computing (SNIC) and performed at the Swedish National Supercmputer Center (NSC) for high performance computing in Linköping.

[1] Ludvik Martinu et al., in Handbook of Deposition Technologies for Films and Coatings, Third Edition, Peter M Martin, Ed., Elsevier (2009).
[2] K. Bobzin, CIRP J. Manuf. Sci. Technol. In press https://doi.org/10.1016/j.cirpj.2016.11.004
[3] T.M Pollock, Nat. Mater **15** (2015) 809.
[4] A. Hörling, L. Hultman, M. Odén,J. Sjölén and L. Karlsson, J. Vac. Sci. Technol. A **20** (2002) 1815.
[5] A. Hörling, L. Hultman, M. Odén, J. Sjölén, L. Karlsson, Surf. Coat. Technol. **191** (2005) 384.
[6] P.H Mayrhofer, A. Hörling, L. Karlsson, J. Sjölén, T. Larsson, C. Mitterer, L. Hultman, Appl. Phys. Lett. **83** (2003) 2049.
[7] H. Lind, F. Tasnádi, I.A. Abrikosov, New. J. Phys. **15** (2013) 095010.
[8] N. Norrby, H. Lind, G Parakhonskiy, M P. Johansson, F. Tasnádi, L S. Dubrovinsky, N Dubrovinskaia, I.A. Abrikosov and M. Odén, J. Appl. Phys. **113** (2013) 053515.
[9] H. Lind, R. Forsén, B. Alling, N. Ghafoor, F. Tasnádi, M.P. Johansson, I.A. Abrikosov, M. Odén, Appl. Phys. Lett. **99** (2011) 091903.
[10] Fujita, T., Asakura, K., Sawada, T. et al. MTA (1981) 12: 1071.
[11] Y. Murayama and S. Hanada, Sci. Technol. Adv. Mater. 3 (2002) 145.
[12] P.H. Mayrhofer, R. Rachbauer and D. Holec, Scripta Mater. **63** (2010) 807.
[13] R. Rachbauer, D. Holec, M. Lattemann, L. Hultman and P.H. Mayrhofer, Int. J. Mat. Res. **102** (2011) 735.
[14] N. Shulumba, O. Hellman, Z. Raza, B. Alling, J. Barrirero, F. Mücklich, I.A. Abrikosov, and M. Odén, Phys. Rev. Lett. **117** (2016) 205502.
[15] G. Grimvall, Thermophysical properties of materials, Elsevier Science 1999.
[16] F. Wang, D. Holec, M. Odén, F. Mücklich, I.A. Abrikosov, F. Tasnádi, Acta Mater. **127** (2017) 124.
[17] A. Knutsson, M. P. Johansson, L. Karlsson and M. Odén, Surf Coat Tech **205** (2011) 4005-4010.
[18] A. I. Gusev, Phys. Status Solidi B **209** (1998) 267-286.
[19] S. J. Kim and H. F. Franzen, J Less-Common Met **143** (1988) 339-343.
[20] H. Lind, R. Pilemalm, L. Rogström, F. Tasnádi, N. Ghafoor, R. Forsén, L.J. S. Johnson, M.P. Johansson-Jöesaar, M. Odén, I.A. Abrikosov, AIP Advances **4** (2014) 127147.
[21] A. Anders, Phys. Rev. E **55** (1997) 969.
[22] A. Anders, Thin Solid Films **518** (2010) 4087.
[23] A. O. Eriksson, J. Q. Zhu, N. Ghafoor, M. P. Johansson, J. Sjölén, J. Jensen, M. Odén, L. Hultman and J. Rosen, Surf Coat Tech **205** (2011) 3923-3930.
[24] A. Knutsson, M.P. Johansson, L. Karlsson, M. Odén, J. Appl. Phys. **108** (2010) 044312.
[25] A Hörling, J. Sjölén, H. Willmann, T. Larsson, M. Odén and L. Hultman, Thin Solid Films **516** (2008) 6421.

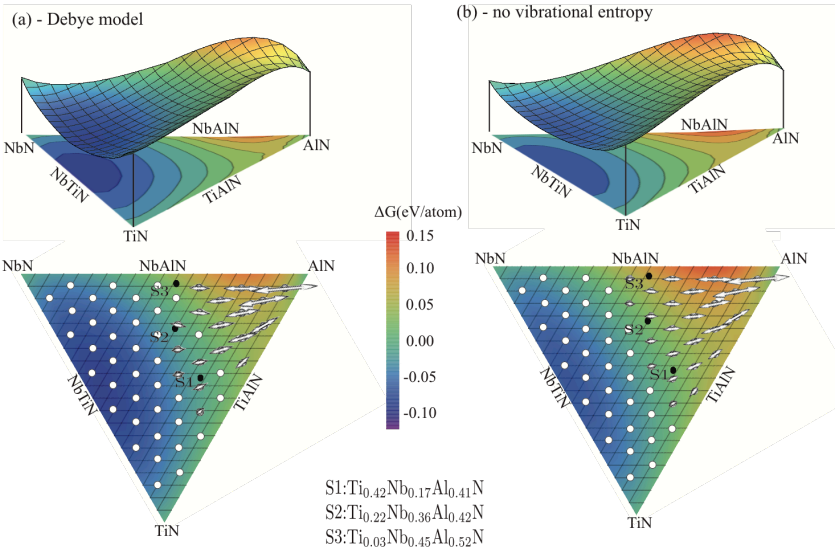

Figure 1 **:** (Color online) The mixing free energy ΔG surface together with the local tendencies for spinodal decomposition in cubic $Ti_XNb_YAl_ZN$ at 1100 K. (a) shows ΔG with the inclusion of phonon contribution approximated through the Debye model while (b) displays ΔG with configurational entropy only, for comparison. The arrows represent the most favorable directions of spinodal decomposition. The length of the arrows is proportional to the magnitude of $\partial^2 G/\partial v(x,y,z)^2$. The circles represent the thermodynamically stable compositions.

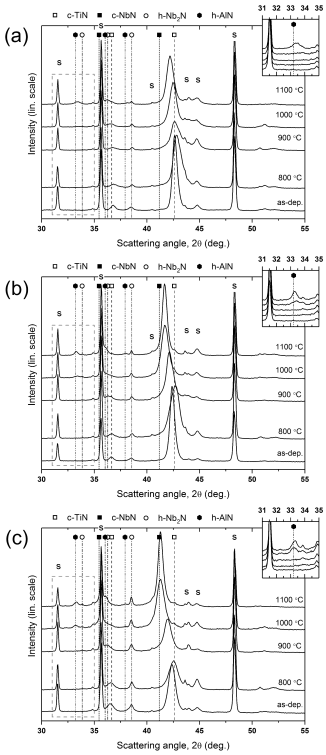

Figure 2 : *ϑ-2ϑ x-ray diffractograms of annealed samples; (a) S1, (b) S2, and (c) S3. The insets show a magnified part of the diffractogram.*

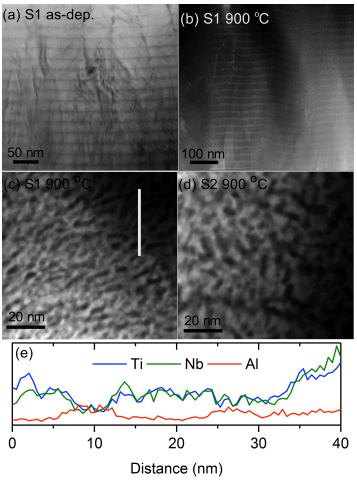

Figure 3 : (a) Bright field micrograph of the as-deposited S1 sample. (b,c,d) show elemental contrast STEM micrographs of samples S1 and S2 respectively, annealed at 900 C. (e) shows an elemental line profile from S1 annealed at 900 C as indicated in (c).

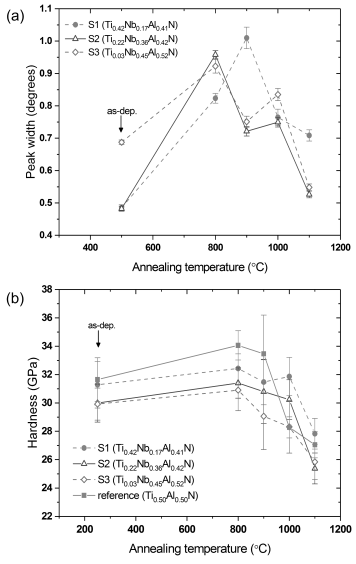

Figure 4 : (a) width of the TiNbAlN 200 peak and (b) hardness as a function of annealing temperature.

Paper VI

Thermal expansion of quaternary nitride coatings

Ferenc Tasnádi
Fei Wang
Magnus Odén
Igor A. Abrikosov

Submitted to APL materials

Thermal expansion of quaternary nitride coatings

Ferenc Tasnádi,[1,2,*] F. Wang,[3,4] Magnus Odén,[1] and Igor A. Abrikosov[1,2]

[1] *Department of Physics, Chemistry and Biology (IFM), Linköping University, SE-581 83 Linköping, Sweden*

[2] *Materials Modeling and Development Laboratory, National University of Science and Technology "MISIS", 119049 Moscow, Russia*

[3] *Materials Modeling and Development Laboratory, NUST "MISIS", 119049 Moscow, Russia*

[4] *Functional Materials, Materials Science and Engineering Department (MSE), Saarland University, P.O. Box 151150, 66041 Saarbrücken, Germany*

(Dated: January 4, 2018)

Abstract

Thermal expansion coefficient of technologically relevant multicomponent cubic nitride alloys are predicted using the Debye model with *ab initio* elastic constants calculated at 0 K and the isotropic approximation for the Grüneisen parameter. Our method is benchmarked against measured thermal expansion of TiN and $Ti_{(1-x)}Al_xN$ as well as against results of molecular dynamics simulations. We show that the thermal expansion coefficients of $Ti_{(1-x-y)}X_yAl_xN$ (X=Zr, Hf, Nb, V, Ta) solid solutions monotonously increase with the amount of alloying element X at all temperature except for Zr and Hf, for which they instead decrease for $y \gtrsim 0.5$.

Thermal expansion coefficient (TEC) of solids is a fundamental physical property with high technological relevance. Upon heating the anharmonic lattice vibrations[1] in the materials change the materials volume typically by expansion although some materials contract with temperature[2]. Coatings that are exposed to thermal load will be subjected to strain that is related to the difference in thermal expansion between substrate and coating. This strain may alter the function of the coating or even cause spallation. Therefore TEC is an important parameter in tailor-design multicomponent coatings. Recently, the Atomate computational materials science framework[3] has been extended with efficient high-throughput workflows for determining materials' properties, such as the Grünesien parameter and thermal expansion, derived from third and fourth order elastic tensors. To provide efficiency a quasi-harmonic Debye approximation has been implemented. In multicomponent solid solutions the high computational demands necessitate the application of efficient approximations with distinct carfulness. In this study we benchmark and utilize a simple approach to predict TEC of an extended class of multicomponent nitride coatings with high potential for industrial application.

Metallurgical alloying is a successful concept to improve the functionality of materials, such as extending the thermal stability of coatings for high temperature applications[6]. Multicomponent nitride solid solutions have been developed that outperform the inherent binary nitrides in terms of high temperature hardness, oxidation, wear resistance[7–9] and piezoelectricity[10,11]. However, upon alloying the materials TEC is altered which influences their mechanical integrity and reliability.

Advanced theoretical methods have been applied to predict the materials thermal expansion with the implicit or explicit inclusion of anharmonic atomic vibrations[12–14]. Recently, the temperature dependent effective potential method (TDEP)[12] has been applied to investigate the thermal stability, lattice expansion and elastic constants of $Ti_{(1-x)}Al_xN$ alloys[15–18]. These studies have underlined the significant effect of vibrations on the mixing thermodynamics in $Ti_{(1-x)}Al_xN$. The quasi-harmonic approximation (QHA) has been used to predict TEC of Cu[19] and Cr-Al-N coatings in agreement with experiments[20]. QHA calculation of the thermal expansion of 2-4 atoms large system requires around 25.000 core hours computational time . In a case of a system with around 20-30 atoms the same amount of computational effort is expected for a selected volume. The model system size of quaternary solid solutions with random configuration has to be at least around 100 atoms. Therefore, a systematic exploration of TEC in several alloys using TDEP or QHA is nowadays a computationally oversized research objective. On the other hand, the concept of high-throughput search has been utilized to select materials candidates for accurate and systematic investigations. The thermo-physical properties of TiC and TiN have been predicted using the Debye model to account for the effect of lattice vibrations[21]. The value of such simple approximation is in its efficiency, which is higly requested, e.g. in high-throughput search of materials that meet pre-defined conditions.

In this study we apply a quasi-harmonic Debye approximation for the vibrational contribution

to the free energy of a system and predict TEC of multicomponent cubic nitride alloys using *ab initio* elastic constants calculated at 0 K. Reliable calculations of the elastic constants for random alloys can be done nowadays relatively quickly[17,22]. Moreover, we foresee that 0 K elastic constants are getting available in data bases, see the recent paper by M. de Jong et al.[23]. We benchmark our approximation against more accurate methods for the reproduction of measured thermal expansion coefficients of TiN and $Ti_{(1-x)}Al_xN$.

The linear thermal expansion coefficient (TEC) is calculated as

$$\alpha(T) = \sum_r \frac{1}{3B} \left(\frac{\partial S_r}{\partial V} \right)_T , \tag{1}$$

where S_r stands for the different entropy contributions, V denotes the volume, T the temperature and B is the isotermal bulk modulus. The volume dependence of each entropy term can be written with the help of the Grüneisen parameter γ_r and the heat capacity at constant volume $(C_V)_r$. Considering only electronic (e) and phononic (phon.) entropies one writes

$$\alpha(T) = \frac{\gamma_{\text{el.}}(C_V)_{\text{el.}}}{3BV} + \frac{\gamma_{\text{phon.}}(C_V)_{\text{phon.}}}{3BV}. \tag{2}$$

The acoustic phononic Grüneisen parameter can be approximated as $\gamma_{\text{phon.}} = 3B/(2\rho B\bar{v}^2)$[24], where B is the 0 K bulk modulus, ρ is the mass density and $\bar{v}$ denotes the mean long-wavelength phase velocity of acoustic phonons calculated from the 0 K elastic stiffness constants. This approximation is based on the assumption that the solid is isotropic and the temperature T is lower than the Debye temperature Θ_{D}. Though, for the binary ZrN, HfN, VN, NbN and TaN significant elastic anisotropy has been shown their alloys with AlN can be approximated to the first order as isotropic materials[22]. The electronic Grüneisen parameter is calculated as $\gamma_{\text{el.}} = 5/3$ according to Ref.[25].

The heat capacities in Eq.(2) are approximated through the Debye model[2,25] as

$$\begin{aligned} (C_V)_{\text{el.}} &= \frac{2\pi^2}{3} k_{\text{B}}^2 T \times \text{DOS}(\epsilon_{\text{F}}), \\ (C_V)_{\text{phon.}} &= 9Nk_{\text{B}} \left(\frac{T}{\Theta_{\text{D}}} \right)^3 \int_0^{\Theta_{\text{D}}/T} \frac{t^4 e^t}{(e^t-1)^2}\, dt. \end{aligned} \tag{3}$$

The temperature dependence of the cubic lattice paremeter a can be represented in the form of

$$a(x,y,T) = a_0(x,y)\left(1 + \alpha_\infty(x,y)\Theta_{\text{D}} f_{\text{D}}(\Theta_{\text{D}}/T)\right) \tag{4}$$

with the Debye function

$$f_{\text{D}}(\tau) = 3\int_0^1 \frac{t^3}{e^{\tau t}-1}\, dt \tag{5}$$

as suggested in Ref.[26]. Here, a_0 gives the 0 K cubic lattice parameter and α_∞ is called the high temperature limit of TEC. Θ_{D} in Eqs.(3,4,5) is calculated through averaging the sound velocities obtained from the solution of the Christoffel equation[27].

To further increase the efficiency of the simulations, we base our study on a piece-wise linear representation of the quantities over the compositional triangle (x, y) as introduced in Ref.[22] for the elastic stiffness constants. That is, the set of compositional points $\{(0.0, 0.0)$, $(0.5, 0.0)$, $(1.0, 0.0)$, $(0.5, 0.0)$,$(0.5, 0.5)$, $(0.0, 1.0)\}$ split the (x, y) triangle into four sub-triangles in each of which linear interpolation is used. The *ab initio* calculated 0 K elastic stiffness constants are taken from Ref.[22]. The electronic density of state at the Fermi level DOS($\epsilon_{\rm F}$) is calculated for each queternary alloy only in the six compositional points given above using the structural models and calculational details given in Ref.[22].

Figure 1 shows the mixing energetics of $Ti_{(1-x)}Al_xN$ solid solutions calculated at 1500 K. In Figure 1 a) one sees a comparison of the Gibb's free energy obtained by TDEP[12] and by the quasi-harmonic Debye model using elastic constants calculated for $x = 0.0, 0.5$ and 1.0 at 0 K. In Figure 1b) one sees the vibrational contribution to $G_{\rm mix}$ in both, TDEP and the quasi-harmonic Debye model. The kink-like behavior in the case of the quasi-harmonic Debye model is an artifact of the piece-wise linear representation used for deriving the elastic constants. Despite it, the large part of the effect of lattice vibrations on the alloy free-energy is captured by the Debye model, and this motivates the application of the latter to greatly increase the efficiency of simulations of the broad class of multicomponent nitride coatings. A direct benchmark of the quasi-harmonic Debye model against TDEP in predicting TEC is shown in Figure 2. The figure shows a comparison of the theoretically and experimentally obtained temperature variation of the lattice parameter in TiN and $Ti_{0.5}Al_{0.5}N$ alloy. The theoretical values are derived with different approximation levels in the description of phonons. The experimental values were obtained by *in situ* high temperature x-ray diffraction measurements[18]. The figures show the lattice parameter expansions relative to the reference values at 300 K. The solid line shows our results using the Debye model. We observe that the electronic contribution to the thermal expansion in our model is negligible for all alloys. The figure shows that TDEP and QHA results give the best agreement with experiments yet the computationally efficient quasi-harmonic Debye model performs accurately for both, TiN and $Ti_{0.5}Al_{0.5}N$. The relative error between the measured value of the lattice parameter in $Ti_{0.5}Al_{0.5}N$ at 850 K and the one obtained within the Debye approximation is around 0.1%. We note that $\Theta_{\rm D}(Ti_{0.5}Al_{0.5}N) = 967$ K, see Table I, which means that our assumption for $\gamma_{\rm phon.}$ becomes less reliable above this temperature and therefore a somewhat larger discrepancy is expected between the experimental value and the result of the quasi-harmonic Debye approximation at high temperatures, T$\geq$1000 K. Yet, the extrapolation of the curves up to high temperatures is quite reasonable, and the use of the data is motivated in view of the need of these data in experimental investigation of metastable transition metal nitride solid solutions in high performance cutting applications.

The applicability of the quasi-harmonic Debye model for TiN and $Ti_{0.5}Al_{0.5}N$ allows us to

investigate the thermal expansion of industrially relevant TiN-based quaternary alloys, such as $Ti_{(1-x-y)}X_xAl_yN$, where X is Zr, Hf, V, Nb, Ta.

Based on a piece-wise linear representation of the quantities over the compositional triangle (x, y) proposed in Ref.[22], the linear thermal expansion coefficient $\alpha(x, y, T)$ can be derived through Eqs.(2,3) and using the values of Θ_D and DOS(ϵ_F) listed in Table I. Figure 3 shows the distribution of $\alpha(x, y, T)$ for $T = 600$, 900 and 1200 K. We establish that the value of α increases with temperature in each alloy. Furthermore, α shows a monotonous increase with the amount of alloying element X at all temperature except for Zr and Hf. In the latter case a decrease is obtained with increasing Hf content. For Zr and Hf alloying the highest value of TEC is observed around $Zr_{0.5}Al_{0.5}N$ and $Hf_{0.5}Al_{0.5}N$. A slowly varying value of $\alpha(x, y)$ is observed in the alloys with high V and Nb content at higher temperatures, 900 and 1200 K. A rapid increase of TEC can be seen for $Ti_{(1-x-y)}Ta_xAl_yN$ with high Ta contant, however binary TaN is highly anisotropic which is inconsistent with our approximation of $\gamma_{\text{phon.}}$.

Eq.(4) gives a simple representation of the lattice parameter variation with the compositions x, y and temperature T. Based on Eqs.(1,2,3) we calculated $a(x, y, T)$ on a 10×10 grid in (x, y) for 32 different temperatures up to 1200 K. In each compositional point (x_i, y_i) these 32 values were fitted to Eq.(4) using $a_0(x_i, y_i)$ and $a_\infty(x_i, y_i)$ as fitting parameters. Figure 4 shows the distribution of the fitted a_0 and α_∞ in each alloy. a_0 is found to agree with the values of the 0 K lattice parameters for each alloy. Furthermore, α_∞ correlates well with TEC at 1200 K in Fig. 2. The six corner point values of a_0 and α_∞ are listed in Table I, which allows one for the accurate reproduction of $a(x, y, T)$. One realizes that the behavior of α_∞ for ZrN and HfN is distinct from what one sees for VN, NbN and TaN. It corresponds to the observed deviation of TEC in Fig. 3. The approach of piece-wise plane approximation is obvious in the figure.

In summary we predicted the linear thermal expansion of quaternary nitride solid solutions using the quasi-harmonic Debye model, an isotropic approximation of the Grüneisen parameter and a piece-wise linear representation of the compositional variation of the elastic constants. We showed that TEC of $Ti_{(1-x-y)}X_yAl_xN$ (X=Zr, Hf, Nb, V, Ta) increase monotonously with the fraction of X at all temperature except for Zr and Hf. A piece-wise linear representation of the temperature variation of the cubic lattice parameter has been proposed to reproduce the thermal expansion at arbitrary temperature. We foresee that our approach can be effectively used for the high-throughput estimations of the thermal expansion in multicomponent alloys, one of the key parameters needed for computer based searches for new materials.

Acknowledgements

This work was supported by the Swedish Foundation for Strategic Research (SSF) program SRL Grant No. 10-0026 and 621-2012-4401, the competence center FunMat-II that is financially supported by Vinnova (grant no 2016-05156) the Swedish Government Strategic Research Area in Materials Science on Functional Materials at Linköping University (Faculty Grant SFO-Mat-LiU No 2009-00971), Vinnova (M-ERA.NET project: Multi-scale computational-driven design of novel hard nanostructured Coatings - MC2), and the Ministry of Education and Science of the Russian Federation (Grant No. 14.Y26.31.0005). This study was performed in the framework of . Fei Wang acknowledges funding received through Erasmus Mundus Joint European Doctoral Programme *DocMASE*. The calculations have been carried out through the Swedish National Infrastructure for Computing (SNIC) and performed at the Swedish National Supercomputer Center (NSC) for high performance computing in Linköping.

---

* Electronic address: tasnadi@ifm.liu.se

[1] Ziman JM. Principles of the Theory of Solids. Cambridge University Press; 1972.

[2] K. Takenaka, Sci. Technol. Adv. Mater. **13**, 013001 (2012).

[3] K. Mathew, et al., Comp. Mater. Sci. **139**, 140 (2017).

[4] D.R. Clarke DR and S.R. Phillpot, Mater. Today. **8**, 22 (2005).

[5] N. Yamamoto, E. Gdoutos, R. Toda, V. White, H. Manohara and C. Daraio, Adv. Mater. **26**, 3076 (2014).

[6] H. Lind, R. Forsén, B. Alling, N. Ghafoor, F. Tasnádi, M.P. Johansson, I.A. Abrikosov and M. Odén, Appl. Phys. Lett. **99**, 091903 (2011).

[7] A. Hörling, L. Hultman, M. Odén, J. Sjölén, L. Karlsson, J. Vac. Sci. Technol. A **20**, 1815 (2002).

[8] H. Lind, R. Pilemalm, L. Rogström, F. Tasnádi, N. Ghafoor, R. Forsén, L.J.S. Johnson, M.P. Johansson-Jöesaar, M. Odén and I.A. Abrikosov IA, AIP Advances **4**, 127147 (2014)

[9] X.Z. Ding, X.T. Zeng, Y.C. Liu, F.Z. Fang and G.C. Lim, Thin Solid Films **516**, 1710 (2008).

[10] F. Tasnádi, B. Alling, C. Höglund, G. Wingqvist, J. Birch, L. Hultman and I.A. Abrikosov, Phys. Rev. Lett. **104**, 137601 (2010).

[11] C. Tholander, F. Tasnádi, I.A. Abrikosov, L. Hultman, J. Birch and B. Alling, Phys. Rev. B. **92**, 174119 (2015).

[12] O. Hellman O, I.A. Abrikosov and S.I. Simak, Phys. Rev. B. **84**, 180301 (2011).

[13] D.B. Zhang, T. Sun and R.M. Wentzcovitch, Phys. Rev. Lett. **112**, 058501 (2014).

[14] M.P. Ljungberg and J. Íñiguez, Phys. Rev. Lett. **110**, 105503 (2013).

[15] N. Shulumba, O. Hellman, Z. Raza, B. Alling, J. Barrirero, F. Mücklich, I.A. Abrikosov and Odén, Phys. Rev. Lett. **117**, 205502 (2016).

[16] F. Tasnádi, I.A. Abrikosov, L. Rogström, J. Almer, M. Johansson and M. Odén, Appl. Phys. Lett. **97**, 231902 (2010).

[17] F. Tasnádi, M. Odén and I.A. Abrikosov, Phys. Rev. B. **85**, 144112 (2012).

[18] N. Shulumba, O. Hellman, L. Rogström, Z. Raza, F. Tasnádi, I.A. Abrikosov IA and M. Odén, Appl. Phys. Lett. **107**, 231901 (2015).

[19] S. Narasimhan and S. de Gironcoli, Phys. Rev. B. **65**, 064302 (2002).

[20] M. Bartosik, D. Holec, D. Aple, M. Klaus, C. Genzel, J. Keckes, M. Arndt, P. Polcik, C.M. Koller and P.H. Mayrhofer, Scr. Mater. **127**, 182 (2017).

[21] J. Kim and S. Kang, J. Alloys Compd. **528**, 20 (2012).

[22] F. Wang, D. Holec, M. Odén, F. Mücklich, I.A Abrikosov and F. Tasnádi, Acta Mater. **127**, 124 (2017).

[23] M. de Jong, W. Chen, R. Notestine, K. Persson, G. Ceder, A. Jain, M. Asta, A. Gamst, Sci. Rep. **6**, 34256 (2016).

[24] P.A. Korzhavyi, A.V. Ruban, S.I. Simak and Y.K. Vekilov, Phys. Rev. B **49**, 14229 (1994).

[25] G. Grimvall, Thermophysical properties of materials. Elsevier Science; 1999.

[26] S. Figge, H. Kröncke, D. Hommel and B.M. Epelbaum, Appl. Phys. Lett. **94**, 101915 (2009).

[27] R.E. Newnham. Properties of materials, Anisotropy, symmetry, Structure. Oxford University Press; 2005.

[28] N. Shulumba, Vibrations in solids: From first principles lattice dynamics to high temperature phase stability (PhD thesis). 2015.

Figures

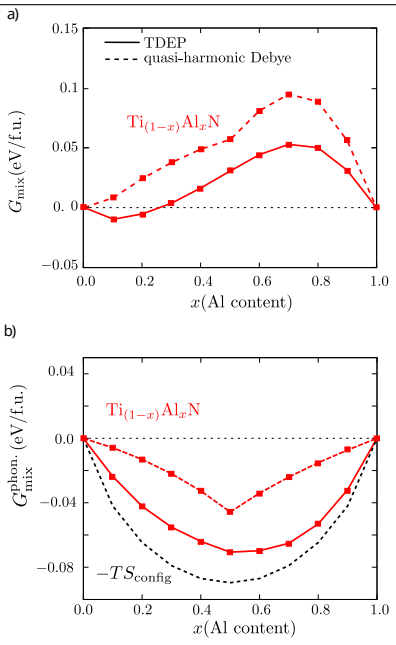

FIG. 1: Mixing energetics of $Ti_{(1-x)}Al_xN$ solid solutions calculated at 1500 K. a) shows G_{mix} obtained by TDEP method[12] with solid lines and the dashed lines show the results of the quasi-harmonic Debye model. In b) the lines display the vibration contribution to G_{mix} in both, TDEP and the present quasi-harmonic Debye model with elastic constants calculated for x=0.0, 0.5 and 1.0.

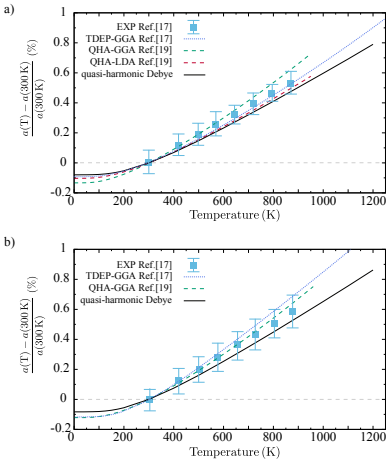

FIG. 2: Relative cubic lattice thermal expansion of a) TiN and b) $Ti_{0.5}Al_{0.5}N$ within different approximations. The values are given relative to the reference lattice parameters at 300 K. The square symbols display the experimental values[18]. The dashed lines show the values obtained by Bartosik et al.[20] using density functional theory with GGA and LDA approximation combined with quasi-harmonic description of vibrational contribution to free energy. The dotted line is obtained by TDEP[12].

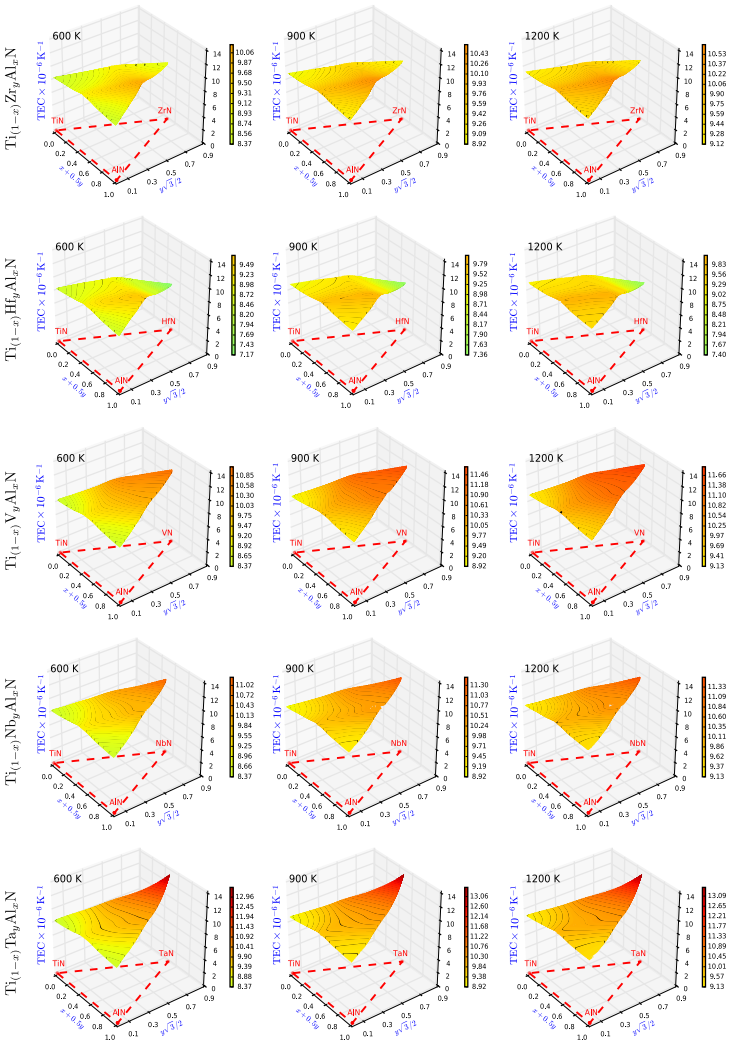

FIG. 3: The linear thermal expansion coefficients (TEC) of cubic quaternary $Ti_{(1-x)}X_yAl_xN$ (X=Zr, Hf, V, Nb, Ta) solid solutions at 600, 900 and 1200 K using the quasi-harmonic Debye approximation.

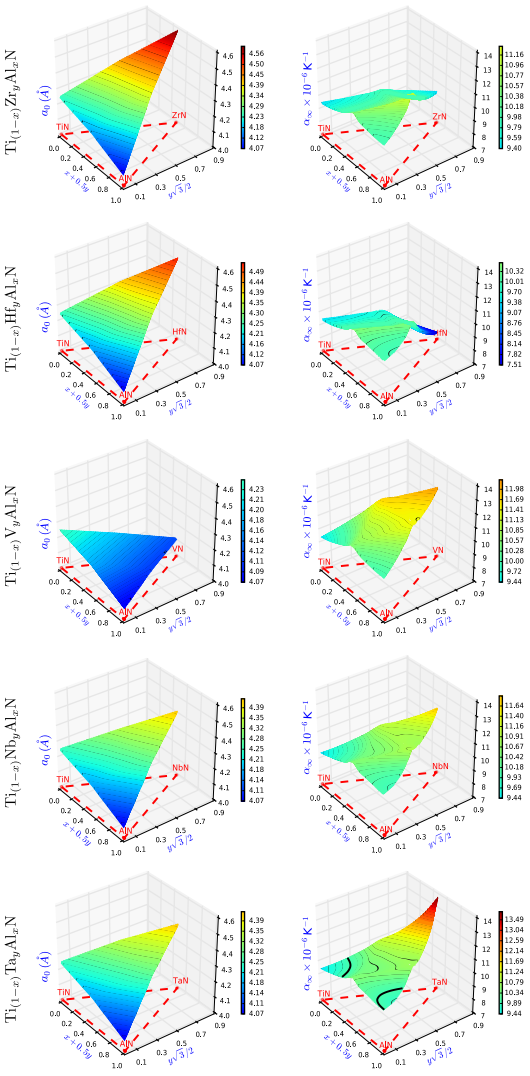

FIG. 4: a_0 and α_∞ coefficients to reproduce the cubic lattice parameter $a(T) = a_0(x,y)(1 + \alpha_\infty(x,y)\Theta_D f_D(\Theta/T))$ of the quaternary $Ti_{(1-x)}X_yAl_xN$ (X=Zr, Hf, V, Nb, Ta) solid solutions.

Tables

TABLE I: Density of states at Fermi levels (DOS(ϵ_F)), Debye temperatures (Θ_D) and the values of the fitting parameters a_0, α_∞ of the cubic lattice paremeters a (see Eq.(4)) for quaternary $Ti_{(1-x-y)}X_yAl_xN$ (X=Zr, Hf, Nb, V, Ta) solid solutions in six compositional (x, y) points.

composition: (x, y)	(1.0,0.0)	(0.5,0.0)	(0.0,0.0)	(0.5,0.5)	(0.0,0.5)	(0.0,1.0)
$Ti_{(1-x-y)}Zr_yAl_xN$						
DOS(ϵ_F) (eV/atom)	0.0	0.236	0.433	0.1506	0.4073	0.3632
Θ_D (K)	1137	967	923	745	738	653
a_0 (Å)	4.07	4.18	4.25	4.38	4.44	4.60
$\alpha_\infty \times 10^{-6}$ (K^{-1})	10.02	10.58	9.44	11.33	9.95	9.38
$Ti_{(1-x-y)}Hf_yAl_xN$						
DOS(ϵ_F) (eV/atom)	0.0	0.236	0.433	0.167	0.374	0.334
Θ_D (K)	1137	967	923	617	611	550
a_0 (Å)	4.07	4.18	4.25	4.35	4.41	4.53
$\alpha_\infty \times 10^{-6}$ (K^{-1})	10.05	10.58	9.44	10.51	9.67	7.47
$Ti_{(1-x-y)}V_yAl_xN$						
DOS(ϵ_F) (eV/atom)	0.0	0.236	0.433	0.7742	0.454	0.80
Θ_D (K)	1137	967	923	940	827	818
a_0 (Å)	4.07	4.18	4.25	4.11	4.19	4.12
$\alpha_\infty \times 10^{-6}$ (K^{-1})	10.05	10.58	9.44	11.52	11.74	12.25
$Ti_{(1-x-y)}Nb_yAl_xN$						
DOS(ϵ_F) (eV/atom)	0.0	0.236	0.433	0.182	0.412	0.458
Θ_D (K)	1137	967	923	772	713	597
a_0 (Å)	4.07	4.18	4.25	4.28	4.34	4.42
$\alpha_\infty \times 10^{-6}$ (K^{-1})	10.05	10.58	9.44	10.95	11.01	11.92
$Ti_{(1-x-y)}Ta_yAl_xN$						
DOS(ϵ_F) (eV/atom)	0.0	0.236	0.433	0.1723	0.386	0.4035
Θ_D (K)	1137	967	923	617	573	407
a_0 (Å)	4.07	4.18	4.25	4.28	4.35	4.42

$\alpha_\infty \times 10^{-6}\,(\mathrm{K}^{-1})$	10.05	10.58	9.44	10.75	11.12	13.95